Chiroptical Spectroscopy of Biomolecules Using Chiral Plasmonic Nanostructures

Calum Jack

University of Glasgow

Submitted in fulfilment of the requirements for the Degree of Doctor of Philosophy

July 2016

School of Chemistry

College of Science and Engineering

University of Glasgow

Abstract

This thesis explores the potential of chiral plasmonic nanostructures for the ultrasensitive detection of protein structure. These nanostructures support the generation of fields with enhanced chirality relative to circularly polarised light and are an extremely incisive probe of protein structure. In chapter 4 we introduce a nanopatterned Au film (Templated Plasmonic Substrate, TPS) fabricated using a high through-put injection moulding technique which is a viable alternative to expensive lithographically fabricated nanostructures. The optical and chiroptical properties of TPS nanostructures are found to be highly dependent on the coupling between the electric and magnetic modes of the constituent solid and inverse structures. Significantly, refractive index based measurements of strongly coupled TPSs display a similar sensitivity to protein structure as previous lithographic nanostructures. We subsequently endeavour to improve the sensing properties of TPS nanostructures by developing a high through-put nanoscale chemical functionalisation technique. This process involves a chemical protection/deprotection strategy. The protection step generates a self-assembled monolayer (SAM) of a thermally responsive polymer on the TPS surface which inhibits protein binding. The deprotection step exploits the presence of nanolocalised thermal gradients in the water surrounding the TPS upon irradiation with an 8ns pulsed laser to modify the SAM conformation on surfaces with high net chirality. This allows binding of biomaterial in these regions and subsequently enhances the TPS sensitivity levels. In chapter 6 an alternative method for the detection of protein structure using TPS nanostructures is introduced. This technique relies on mediation of the electric/magnetic coupling in the TPS by the adsorbed protein. This phenomenon is probed through both linear reflectance and nonlinear second harmonic generation (SHG) measurements. Detection of protein structure using this method does not require the presence of fields of enhanced chirality whilst it is also sensitive to a larger array of secondary structure motifs than the measurements in chapters 4 and 5. Finally, a preliminary investigation into the detection of mesoscale biological structure is presented. Sensitivity to the mesoscale helical pitch of insulin amyloid fibrils is displayed through the asymmetry in the circular dichroism (CD) of lithographic gammadions of varying thickness upon adsorption of insulin amyloid fibril spherulites and fragmented fibrils. The proposed model for this sensitivity to the helical pitch relies on the vertical height of the nanostructures relative to this structural property as well as the binding orientation of the fibrils.

Contents

Abstract ii

Contents iii

List of Tables viii

List of Figures ix

Acronyms and Abbreviations xvi

Publications xviii

Acknowledgements xix

Authors Declaration xx

Chapter 1: Introduction

1.1 Background 1

1.2 Thesis Overview 3

1.3 References 6

Chapter 2: Theory

2.1 Chirality 8

2.1.1 Molecular Chirality 8

2.1.2 Optical Activity 8

2.1.3 Models of Chirality 12

2.1.4 “Superchiral Fields” 14

2.2 Fundamentals of Plasmonics 16

2.2.1 Plasmon Oscillations 16

2.2.2 Surface Plasmon Polaritons (SPPs) 19

2.2.3 Localised Surface Plasmon Resonances (LSPRs) 23

2.2.4 Decay of SPPs and LSPRs 24

2.2.5 Surface Plasmon Resonance Refractive Index Sensitivity 24

2.2.6 Surface Plasmon Hybridisation 25

2.2.7 Interference Phenomena 27

2.3 Second Harmonic Generation (SHG) 30

2.3.1 Nonlinear Susceptibility 31

2.3.2 Polarisation Dependent SHG from Molecular Systems 38

2.3.3 SHG from Nanostructures 40
2.4 References 47

Chapter 3: Experimental

3.1 Introduction 52
3.2 Nanostructure Fabrication 52
3.2.1 Electron Beam Lithography (EBL) 52
3.2.2 Templated Plasmonic Substrates (TPS) 55
3.3 Microscopy 58
3.3.1 Scanning Electron Microscopy (SEM) 59
3.3.2 Atomic Force Microscopy (AFM) 59
3.4 Spectroscopic Measurements 61
3.4.1 Polarisation Microscope 61
3.4.2 Plasmonic Polarimetry 64
3.4.3 Second Harmonic Generation (SHG) 66
3.4.4 Circular Dichroism (CD) 68
3.5 Surface Functionalisation 69
3.5.1 Polyethylene glycol (PEG)-thiol Self Assembled Monolayer (SAM) Functionalisation 69
3.5.2 Nitrilotriacetic Acid (NTA) Thiol Functionalisation 70
3.6 Analyte Measurement and Preparation 71
3.6.1 Microfluidic Cell 71
3.6.2 Protein Solution Preparation 71
3.6.3 5-enolpyruvylshikimate-3-phosphate (EPSP) Synthase Preparation 72
3.7 Polarised Optical Microscopy of Insulin Amyloid Fibril Spherulites 72
3.8 Numerical Simulations 72
3.8.1 Finite Element Modelling Methods 72
3.8.2 Numerical Simulations of Chiral Plasmonic Nanostructures 77
3.8.3 Electromagnetic Field Simulations 77
3.8.4 Thermal Simulations 78
3.9 References 78

Chapter 4: Linear Optical Study of Templated Plasmonic Substrates (TPS) with Tuneable Chirality

4.1 Introduction 79

4.1.1 Nanostructure Fabrication by Direct Nanopatterning 80

4.1.2 Nanostructure Fabrication by Replicative Nanopatterning 81

4.2 Results and Discussion 82

4.2.1 Geometric Characterisation 82

4.2.2 Linear Optical Properties 84

4.2.3 Au Thickness Dependence of Optical Properties 86

4.2.4 Au Thickness Dependence of Shuriken EM Fields 88

4.2.5 Au Thickness Dependence of TPS Chirality and Optical Activity 91

4.2.6 Hybridisation Scheme 95

4.2.7 Comparison with Lithographically Fabricated Nanostructures 98

4.2.8 Protein Spectroscopy using TPS Nanostructures 100

4.3 Conclusion 103

4.4 References 104

4.5 Appendix 105

Chapter 5: Nanoscale Control of TPS Surface Chemistry through Nanolocalised Water Heating

5.1 Introduction 107

5.1.1 Sub-Micron Control of Chemical Functionalisation 108

5.2 Results and Discussion 109

5.2.1 TPS Shuriken Chiroptical Properties 109

5.2.2 Simulations of TPS Shuriken Thermal behaviour 110

5.2.3 Chemical Functionalisation of TPS Shuriken Surface 115

5.2.4 Sample Geometry During Irradiation 117

5.2.5 Sensitivity to PEG-TPS Surface Chemistry 119

5.2.6 Manipulation of Surface Chemistry using Nanolocalised Water Heating 121

5.2.7 Influence of Nanoscale Chemical Functionalisation on Biosensing 126

5.2.8 Nanoscale Spatial Control of TPS Surface Chemical Functionalisation 131

5.3 Conclusion 133

5.4 References 134

5.5 Appendix 135

Chapter 6: Mediation of TPS Mode Hybridisation by Protein Secondary Structure

6.1 Introduction 137

6.1.1 Hybridisation in Plasmonic Metamaterials 138

6.1.2 Nonlinear Optical Activity of Nanostructures 138

6.2 Results and Discussion 139

6.2.1 Gammadion Morphology and Hybridisation Scheme 139

6.2.2 Characterisation of Linear Optical Properties 141

6.2.3 Linear Spectroscopic Measurements of Gammadions Upon Adsorption of Biomolecules 145

6.2.4 Characterisation of Gammadion Nonlinear Optical Properties 148

6.2.5 Nonlinear Spectroscopic Measurements of Gammadions Upon Adsorption of Biomolecules 152

6.2.6 Molecular Mediation of TPS Mode Hybridisation to Detect Protein Structure 159

6.3 Conclusion 161

6.4 References 163

6.5 Appendix 164

Chapter 7: Detection of Mesoscale Biological Structure using Chiral Plasmonic Nanostructures

7.1 Introduction 171

7.1.1 Formation and Structural Characterisation of Amyloid Fibrils 172

7.1.2 Formation and Structure of Amyloid Fibril Spherulites 173

7.2 Results and Discussion 174

7.2.1 Polarised Optical Microscopy of Insulin Amyloid Fibril Spherulites 174

7.2.2 Gammadion Geometry and CD Spectra 175

7.2.3 Spectroscopic Measurements of Insulin Amyloid Fibril Spherulites 177

7.2.4 Spectroscopic Measurements of Fragmented Insulin Amyloid Fibrils 182

7.2.5 Detection of Fibril Helical Pitch 184

7.3 Conclusion 186

7.4 References 188

Summary and Future Outlook 190

List of Tables

Table 2.01: Second order susceptibility tensors associated with f_i, g_i and h_i for a chiral and achiral isotropic surface where the surface is in the x-y plane.

Table 4.01: Resonance positions of the maximum and minimum ORD peaks and peak to peak heights of five separate substrates measured in 10mM tris buffer. The bottom row displays the standard deviation for each column.

Table 6.01: Fitting coefficients to equation 2.62 for p-polarised SH emission from the front face in the presence of tris buffer. Errors are derived from a standard deviation of four measurements.

Table 6.02: Fitting coefficients to equation 2.62 for p-polarised SH emission from the back face in the presence of tris buffer. Errors are derived from a standard deviation of four measurements.

Table 6.03: Fitting coefficients to equation 2.62 for s-polarised SH emission from the front face in the presence of tris buffer. Errors are derived from a standard deviation of four measurements.

Table 6.04: Fitting coefficients to equation 2.62 for s-polarised SH emission from the back face in the presence of tris buffer. Errors are derived from a standard deviation of four measurements.

Table 6.05: Fitting parameters to equation 2.62 for the s-polarised SH signal generated from Au gammadions in the presence of air, 10mM tris buffer and 8M Guanidine Hydrochloride.

Table 6.06: Fitting parameters to equation 2.62 for the s-polarised SH signal generated from LH gammadions in the presence of air, 10mM tris buffer and 8M Guanidine Hydrochloride.

Table 6.07: Fitting parameters to equation 2.62 for the s-polarised SH signal generated from RH gammadions in the presence of air, 10mM tris buffer and 8M Guanidine Hydrochloride.

Table 6.08: Values of ζ for RH and LH gammadions upon adsorption of biomolecules. The α-helical biopolymers are highlighted purple, red and blue; β-sheet structures are highlighted peach colour and the disordered structures is highlighted green.

.

List of Figures

Figure 2.01: Propagation of a linearly polarised beam consisting of equal amplitude RH and LH circularly polarised components through: **(a)** an achiral medium; **(b)** a chiral medium with different refractive indices for RH and LH CPL (optical rotation) and **(c)** a chiral medium with different absorption coefficients for RH and LH CPL (circular dichroism). $\mathbf{E_L}$ and $\mathbf{E_R}$ are the electric field vectors of RH and LH circularly polarised beams and **E** is the electric field vector of the resultant linearly polarised beam. Figure adapted from reference [1]

Figure 2.02: Optical rotation and corresponding ellipticity around the region of the electronic absorption wavelength λ_j.

Figure 2.03: **(a)** Pictorial representation of a single helical oscillator and coupled oscillator models of chirality. In the coupled oscillator model θ represents the angle the two oscillators are inclined at and h is the separation distance.

Figure 2.04: Schematic representation of a bulk plasma oscillation in a metal. The action of an electric field E induces the deviation of the free electron gas from its equilibrium position in **(a)** by a distance x in **(b)**. The positive ion cores induce a restoring force to move the electron cloud back to its original position, causing a collective oscillatory motion of the electron gas around the equilibrium position.

Figure 2.05: **(a)** Schematic representation of metal charge distribution and the resultant electric fields in the metal and dielectric due to surface plasma oscillations (surface plasma polaritons). **(b)** Electric field strength perpendicular to the surface. δ_d and δ_m are the electric field decay lengths in the dielectric and metal respectively and $|E_z|$ is the electric field strength in the z direction.

Figure 2.06: **(a)** Dispersion relation for light in a vacuum and a SPP. Otto configuration **(b)** and Kretschmann configuration **(c)** for excitation of a SPP at a metal-dielectric interface.

Figure 2.07: Graphic illustration of noble metal nanorod upon excitation of **(a)** dipolar longitudinal LSPR and **(b)** dipolar transverse LSPR.

Figure 2.08: Hybridisation scheme adapted from reference [28] representing coupling between dipoles of two nanodimers aligned end to end and separated by a small gap.

Figure 2.09: Schematic representation of energy levels of a three level atom. ω_p and ω_c are the frequency of the probe and pump beams respectively.

Figure 2.10: **(a)** Coupled oscillator model for the interference between an optically bright and dark mode. The mass m_1 is the optically bright mode and m_2 represents the dark mode. **(b)** Hypothetical representation of the resonance lineshape for an optically bright (ω_1) and optically dark (ω_2) mode. **(c)** Fano resonance lineshape generated by the interference of an optically bright and dark mode. ω is the frequency and φ is the amplitude of the resonance.

Figure 2.11: Experimental geometry employed in SHG measurements. k_{in} and k_{ref} are the incident and reflected wave vectors for the IR and SH beams respectively both of which are in the x-z plane. The angle of incidence is denoted θ_{in}. The electric field polarisation of

the IR and SH beams are denoted using p_i (x-z plane polarisation) and s_i (polarised in y direction).

Figure 2.12: Qualitative representation of the effect on the shape of the polarisation dependent profile for vertically polarised SHG and corresponding equation 62 fitting parameters as a spherical nanoparticle (radius~5nm) is rendered less centrosymmetric. The form of the SH profiles and fitting parameters were chosen to reflect the general trend of the results reported in reference 82-84. Zero degrees corresponds to vertically polarised incident light.

Figure 2.13: Graphical representation of electric dipole, electric quadrupole, magnetic dipole and higher order terms of equation 62 for **(a)** s-polarised and **(c)** p-polarised SH radiation. Zero degrees correspond to s-polarised incident light. **(b)** and **(d)** display experimental geometry and polarisation states for s-polarised and p-polarised SHG respectively. k_{in} and k_{ref} are the incident and reflected wave vectors for the IR and SH beams respectively both of which are in the x-z plane.

Figure 3.01: Complete process for the fabrication of lithographic gammadions used in chapter 7.

Figure 3.02: Photograph of array of lithographically fabricated gammadions on quartz.

Figure 3.03: Comparison of nanostructure fabrication with single resist layer and resist bilayer.

Figure 3.04: Photograph of Engel Victory 28 hydraulic injection moulder.

Figure 3.05: **(a)** Graphic representation of the injection moulder tool. **(b)** Overview of the steps required for fabrication of injection moulded nanostructures.

Figure 3.06: Photograph of nanopatterned polycarbonate slide before metal deposition and after evaporation of 100nm Au to form the TPS.

Figure 3.07: Schematic of viewing angle that is used to define the numerical aperture of a lens.

Figure 3.08: Schematic representation of AFM operation.

Figure 3.09: Graphic depiction of the effect of the tip sharpness on the accuracy of the measured AFM height profile (red line).

Figure 3.10: Labelled photograph of polarisation microscope.

Figure 3.11: Schematic of polarisation microscope components.

Figure 3.12: Image of field of view of polarisation microscope for TPS substrates.

Figure 3.13: Example of plasmonic polarimetry measurement upon adsorption of biomaterial using RH (blue) and LH (red) chiral plasmonic nanostructures. Solid lines are ORD recorded in buffer and dashed lines are measured after adsorption of biomaterial.

Figure 3.14: Labelled diagram of SHG experimental set-up.

Figure 3.15: CMOS camera image of the IR beam on nanostructure arrays during sample alignment.

Figure 3.16: Depiction of experimental geometry during CD measurements.

Figure 3.17: Poly-ethylene glycol methyl ether thiol (PEG-thiol) structure, n≈ 150.

Figure 3.18: Diagram of NTA thiol formation, Ni (II) sulphate functionalisation and His-tagged protein binding

Figure 3.19: Labelled image of microfluidic cell.

Figure 3.20: Two triangular elements with two common nodes (2 and 3).

Figure 3.21: Depiction of tetrahedral mesh and hexahedral mesh.

Figure 4.01: SEM of **(a)** 100nm Au TPS, **(b)** 20nm Au TPS and **(c)** 20nm Au TPS measured with 30^{o} tilt. AFM images and their corresponding height profiles for **(d)** a 20nm film and **(e)** 100nm film. Coloured lines overlaying the images correspond to the regions where height profiles were measured.

Figure 4.02: **(a)** Perspective and side views of TPS geometry before metal deposition. Shurikens are imprinted into the surface of a polycarbonate slide to a depth of 80nm. **(b)** Perspective and side views of TPS geometry after metal deposition. The continuous Au film containing the inverse structure is labelled the top surface whilst the shuriken shaped nanostructures at the bottom of these voids is the bottom surface.

Figure 4.03: ORD and reflectance spectra of RH (blue) and LH (red) shurikens recorded in 10mM tris buffer with corresponding SEM images. The polarisation of the incident light during reflectance measurements is denoted in by the black arrow.

Figure 4.04: **(a)** ORD of 100nm Au measured through the back face of the TPS slide (blue) and from 100nm Au on an Si wafer (black). **(b)** ORD of LH gammadions from five different TPSs measured in 10mm tris buffer.

Figure 4.05: Dependence of RH (blue) and LH (red) shurikens reflectivity **(a)** and ORD **(b)** on Au film thickness.

Figure 4.06: EM modelling of 100nm **(b)** and 30nm **(d)** TPS shuriken ORD spectra and comparison with experimentally obtained results **(a, c)**. The arrows in **(d)** and **(b)** indicate the wavelength at which the z components of the Ez **(e-h)** and Hz **(i-l)** fields were modelled for the 30nm and 100nm Au films respectively. The black arrow in **(e)** represents the polarisation of the incident field for all simulations **(e-l)**. The units for the side bar of the Ez fields are (MV/m) and for the Hz fields are ($1x10^{-4}$ A/m). The colour range is limited to create comparable scales for all plots.

Figure 4.07: Effect of Au thickness on reflectance **(a)** and ORD **(b)** collected from LH TPS shurikens immersed in 10mM tris buffer. Graphic representation of **(c)** SHO and **(d)** Born-Kuhn (coupled oscillator) models of chirality. Pink highlighted region corresponds to ORD lineshapes typical of the Kauzman model and non-highlighted region relate to ORD lineshapes associated with Born-Kuhn model.

Figure 4.08: Simulation of chirality of z component of EM field **(a-d)** and associated Ez **(e-h)** and Hz **(i-l)** field strength and distribution of top and bottom surfaces. The upper half contains plots for 100nm Au TPS shurikens and the lower half corresponds to 30nm Au TPS shurikens. Scale of chirality normalized to values of circularly polarised light, units for the Ez fields are (MV/m) and for the Hz fields are ($1x10^{-4}$ A/m). The black arrow in (A) indicates electric field polarisation of incident EM wave for all plots. The colour range is limited to create comparable scales for all plots.

Figure 4.09: Qualitative representation of effect due to varying the Au thickness on hybridisation between electric modes (red) and magnetic modes (purple). Δ is the energy separation between the bright and dark modes.

Figure 4.10: Illustration representing the distribution of individual dipoles of the shuriken for **(a)** the E_1 dipolar mode and **(b)** the E_2 quadrupole mode.

Figure 4.11: ORD spectra and corresponding SEM images for RH (blue) and LH (red) shurikens fabricated using **(a)** electron beam lithography and **(b)** injection moulding. ORD spectra are recorded in 10mM tris buffer. The scale bar for SEM images is 500nm in length.

Figure 4.12: **(a)** Resonant wavelength as a function of increasing refractive index for RH (blue) and LH (red) shurikens. **(b)** $\Delta\Delta\lambda$ values for shurikens as a function of increasing difference in refractive index between salt solution and water.

Figure 4.13: ORD spectra for **(a)** 100nm Au TPS and **(b)** 30nm Au TPS. Red lines correspond to LH shurikens and blue lines correspond to RH shurikens. The solid lines are measurements taken in 10mM tris buffer and dotted lines are measured when the sample is immersed in 1mg/ml Con A solution. The solid vertical bars highlight the position of measurement for the buffer and dotted vertical bars are the position for the Con A. ΔΔλ values are also given. EM modelling of the optical chirality of the top and bottom surface combined for **(c)** 100nm and **(d)** 30nm Au films are given for the wavelengths indicated in figure 4.06. Chirality values have been normalised to those of LH circularly polarised light.

Figure 5.01: Plots of temperature gradients at the pulse end generated in TPS shurikens upon irradiation with an incident beam of different pulse widths. In both cases the fluence of the incident beam is 15mJcm^{-2}.

Figure 5.02: **(a)** Side view of surface plot of the thermal gradients generated in the Au and water upon pulse end (8ns). Labels denote the temperature of the surrounding water. **(b)** Stacked surface plots of water temperature within the shuriken moving up the z axis. **(c)** Graph following the temperature of water moving from the central region to the tips of the arms at different heights of the substrate.

Figure 5.03: **(a)** Modelling of the temporal thermal behaviour of the nanostructure and surrounding water for various time intervals after the pulse end. **(b)** Surface plots of water temperature in the shuriken at a height of z=60nm after the pulse end. Graph of average temperature of water in arms and central region for 10nm<z≤70nm **(c)** and average temperature in Au nanostructure for z<0nm **(d)**. D_t is the thermal diffusivity of water and Au.

Figure 5.04: Molecular structure and corresponding Newman projection of **(a)** gauche and **(b)** trans conformation of polyethylene glycol methyl ether thiol (PEG-thiol). Red highlighted area represents the section of the molecule displayed in the Newman projection.

Figure 5.05: Reflectance spectra and corresponding experimental geometry for TPS irradiation from **(a,b)** the front face and **(c,d)** the back face. The red line in the reflectance spectra corresponds to the bandwidth of the 8ns pulse 1064 Nd:YAG laser.

Figure 5.06: Experimental geometry during irradiation of nanostructures with nanosecond pulsed laser.

Figure 5.07: ORD spectra of a LH Peg-TPS after: **(a)** heating to 358K in water; **(b)** washing with Butan-1-ol at 293K; **(c)** heating to 323K in water and **(d)** heating to 358K in air. Magnitude and direction of the resonance shifts are given. The blue line corresponds

to the PEG-TPS ORD before modification and the red line is the subsequent ORD. All ORD spectra are measured in 10mM tris buffer.

Figure 5.08: ORD spectra of LH shuriken after **(a)** irradiation of a PEG-TPS in water with an 8ns pulsed 1064nm laser at 15mJcm^{-2} for 60s and **(b)** varying time durations of laser irradiation. **(c)** Modelled average temperature of the surrounding water between z=20 and z=30 in the shuriken arms and central region after 60s irradiation at 15mJcm^{-2}. Effect on the LH shuriken ORD spectra after: **(d)** irradiation of a PEG-TPS in water with a 400 μs pulsed laser at 20mJcm-2 for 60s; **(e)** irradiation of a plain TPS in water with an 8ns pulsed laser at 15mJcm^{-2} for 60s and **(f)** irradiation of a PEG-TPS in air with an 8ns pulsed laser at 15mJcm^{-2} for 60s. In all ORD spectra the blue line is the ORD measured before irradiation and the red line is the ORD post irradiation. The magnitude and direction of resonance shifts are indicated below each spectrum.

Figure 5.09: **(a)** Magnitude of the LH shuriken ORD shift as a function of increasing laser fluence. **(b)** Modelled average temperature of the water in the shuriken arms and central region with increasing fluence.

Figure 5.10: SEM images collected for a plain and PEG-TPS before irradiation **(a,c)** and after irradiation with an 8ns laser **(b,d)**.

Figure 5.11: RH (blue) and LH (red) shuriken ORD spectra with corresponding asymmetry parameters upon adsorption of Concanavalin A on: a plain TPS **(a)**; a PEG-TPS before irradiation **(b)** and PEG-TPS after irradiation **(c)**. Solid lines are buffer measurements and dashed lines are Concanavalin A measurements.

Figure 5.12: Asymmetry parameter (ΔΔλ) for Concanavalin A adsorption on shurikens as a function of increasing laser fluence.

Figure 5.13: RH (blue) and LH (red) shuriken ORD spectra with corresponding asymmetry parameters upon adsorption of EPSP synthase on PEG TPS after irradiation **(a)** and a plain TPS **(b)**. Solid lines are buffer measurements and dashed lines are EPSP synthase measurements.

Figure 5.14: Pictorial representation of protection/deprotection strategy and subsequent functionalisation of shuriken nanostructures. The protection step is the formation of a thermally responsive PEG-SAM on the surface. The deprotection step involves irradiation of the PEG-SAM with a ns pulsed laser which generates nanolocalised thermal gradients within the surrounding water. This leads to a conformational change of the PEG-thiol in selective regions of the nanostructure which subsequently facilitates the binding of biomaterial to the surface.

Figure 6.01: **(a)** SEM of gammadions **(b)** Pictorial representation of gammadion geometry and surfaces.

Figure 6.02: Gammadion hybridisation scheme representing a qualitative interpretation of the coupling between electric/magnetic modes. Δ is the energy separation between the bright and dark mode.

Figure 6.03: Linear reflectance and ORD measurements of RH and LH gammadions in the presence of 10mM tris HCl buffer recorded through the front and back face. For nonlinear measurements the red and green highlighted regions represent the bandwidth of the fundamental and SH beam respectively.

Figure 6.04: Back face illuminated experimental **(a)** and simulated **(b)** reflectance spectra and normalized chirality surface plots for the top **(c)** and bottom surface **(d)**. Front face illuminated experimental **(e)** and simulated **(f)** reflectance spectra and normalized chirality surface plots for the top **(g)** and bottom surface **(h)**.

Figure 6.05: Reflectance spectra of RH and LH gammadions for front face protein experiments. Blue lines are for buffer, dotted red show results with protein solutions and the solid red line is the protein solution data blue shifted to overlap with the buffer to allow clearer comparison of lineshapes.

Figure 6.06: Qualitative representation of the changes in hybridisation of the electric and magnetic modes between buffer (black) and upon protein adsorption (red). Δ is the energy separation between the bright and dark modes.

Figure 6.07: Normalised s and p-polarised SHG profiles of 100nm Au TPS gammadions and a flat Au surface measured from the front and back face in the presence of 10mM tris buffer. Blue squares are experimental data and the red solid line is the fit to equation 66 in chapter 2.

Figure 6.08: **(a)** Relationship between resonance position and refractive index for reflectance spectra recorded through the front face. **(b)** Reflectance spectra measured through the back face in the presence of air (n=1.00) and 8M guanidine hydrochloride (n=1.48).

Figure 6.09: Normalised back face s-polarised SH profiles for gammadions and Au collected in the presence of air, (black) 10mM tris buffer (blue) and 8M Guanidine Hydrochloride (red). Zero degrees in the polar plots corresponds to s-polarised incident light.

Figure 6.10: Normalised intensity of S-polarised SH signal as a function of the incident polarisation angle (θ) for arrays of right and left handed gammadions in the presence of tris buffer (blue) and protein solution(red). Squares represent the measured experimental data; solid lines are the fit to equation (2.62); blue and red shaded lobes correspond to the fit of only the dipolar term (α) of equation (2.62). Zero degrees in the polar plots corresponds to s-polarised incident light.

Figure 6.11: Normalised intensity of S-polarised SH signal as a function of the incident polarisation angle (θ) for arrays of right and left handed gammadions in the presence of tris buffer (blue) and Lysine solution(red). Squares represent the measured experimental data; solid lines are the fit to equation (2.62); blue and red shaded lobes correspond to the fit of only the dipolar term (α) of equation (2.62).

Figure 7.01: **(a)** Schematic diagram of spherulite with a disordered core at the centre, radially oriented fibrils emanating from the core and a thin outer layer formed by the ends of fibrils that fold back onto the structure. **(b)** Representation of individual amyloid fibril with a nanometre scale helical pitch and **(c)** layout of constituent cross β strands**.**

Figure 7.02: Cross polarised microscope images of **(a)** insulin amyloid fibril spherulites and **(b)** sonicated insulin amyloid fibril spherulites. The biomaterial is adsorbed onto the surface of gammadions in both images. The lighter green area in **(a)** is the gammadion Au surface and the orange area in **(b)** corresponds to the gammadion Au surface.

Figure 7.03: SEM image of 100nm Au LH gammadions.

Figure 7.04: CD spectra of RH (blue) and LH (red) gammadions of varying Au thickness recorded in the presence of 10mM tris buffer.

Figure 7.05: **(a)** SEM image of an insulin amyloid fibril spherulite. **(b)** Pictorial representation of a spherulite bound to the substrate surface. **(c)** Magnified view of spherulite fibrils bound with their long axis perpendicular to the sample surface. The relative size of the gammadions and spherulite are not to scale.

Figure 7.06: CD spectra of RH (blue) and LH (red) gammadions of varying Au thickness recorded in the presence of 10mM tris buffer (solid) and insulin amyloid fibril spherulite solution (dashed).

Figure 7.07: **(a)** Calculated difference spectra upon adsorption of insulin amyloid fibril spherulites for RH (blue) and LH (red) gammadions of varying Au thickness. **(b)** Values of the asymmetry calculated using equation 1.

Figure 7.08: **(a)** SEM image of sonicated spherulites on a metal surface. **(b)** Pictorial representation of fragmented insulin amyloid fibrils bound to the sample surface where the long axis of the fibril is parallel to the surface.

Figure 7.09: CD spectra of RH (blue) and LH (red) gammadions of varying Au thickness recorded in the presence of 10mM tris buffer (solid) and fragmented insulin amyloid fibrils(dashed).

Figure 7.10: **(a)** Calculated difference spectra upon adsorption of fragmented insulin amyloid fibrils for RH (blue) and LH (red) gammadions of varying Au thickness. **(b)** Values of the asymmetry calculated using equation 1.

Abbreviations and Acronyms

AFM	Atomic Force Microscopy
BSE	Back Scattered Electrons
BSA	Bovine Serum Albumin
CCD	Charge-coupled Device
CD	Circular Dichroism
CPL	Circularly Polarised Light
CMOS	Complementary metal-oxide-semiconductor
EBL	Electron Beam Lithography
EELS	Electron Energy Loss Spectroscopy
EIT	Electromagnetically Induced Transparency
EM	Electromagnetic
EPSP	5-enolpyruvylshikimate-3-phosphate
FEM	Finite Element Methods
HWP	Half Wave Plate
I.R.	Infra-Red
IM	Injection Moulding
IOC	Integrated Optical Chirality
IPA	Iso-propyl Alcohol
LH	Left Handed
LSPR	Localised Surface Plasmon Resonance
MIBK	Methyl Iso Butyl Ketone
MACE:ID	Molecular Assembly Controlled by Electron beam Induced Deposition
NTA	Nitrilotriacetic acid
NRT	Nonlinear Response Tensor
NMR	Nuclear Magnetic Resonance
NA	Numerical Aperture
OR	Optical Rotation
ORD	Optical Rotatory Dispersion
PML	Perfectly Matched Layers
PEG	Poly ethylene glycol

PMMA	Poly methylmethacrylate
ROA	Raman Optical Activity
RIU	Refractive Index Unit
RH	Right Handed
SEM	Scanning Electron Microscopy
SE	Secondary Electrons
SH	Second Harmonic
SHG	Second Harmonic Generation
SHRS	Second Harmonic Rayleigh Scattering
SAM	Self-Assembled Monolayer
SHO	Single Helical Oscillator
SERS	Surface Enhanced Raman Spectroscopy
SPP	Surface Plasmon Polariton
SP	Surface Plasmon
SPR	Surface Plasmon Resonance
TPS	Templated Plasmonic Substrate
TEM	Transmission Electron Microscopy
U.V.	Ultra-Violet

Publications

- Nadia Abdulrahman, Christopher D. Syme, Calum Jack, Affar Karimullah, Laurence D. Barron, Nikolaj Gadegaard and Malcolm Kadodwala
  "The Origin of Off-Resonance Non-Linear Optical Activity of a Gold Chiral Nanomaterial"
  Nanoscale, 2013. **5**, 12651-12657

- Affar Karimullah, Calum Jack, Ryan Tullius, Vincent M. Rotello. Graeme Cooke, Nikolaj Gadegaard, Laurence D. Barron and Malcolm Kadodwala
  "Disposable Plasmonics: Templated Plasmonic Metamaterials with Tuneable Chirality"
  Advanced Materials, 2015. **27** (37), 5610-5616

- Calum Jack, Affar Karimullah, Ryan Tullius. Larousse Khorashad, Marion Rodier, Brian Fitzpatrick, Laurence D. Barron, Nikolaj Gadegaard, Adrian J. Lapthorn, Vincent M. Rotello, Graeme Cooke, Alexander O. Govorov, and Malcolm Kadodwala
  "Spatial Control of Chemical Processes on Nanostructures through Nano-Localized Water Heating"
  Nature Communications, 2016. **7**, 10946

- Calum Jack, Affar Karimullah, Ross Leyman, Ryan Tullius, Vincent M. Rotello, Graeme Cooke, Nikolaj Gadegaard, Laurence D Barron, Malcolm Kadodwala
  "Biomacromolecular Stereostructure Mediates Mode Hybridisation in Chiral Plasmonic Nanostructures"
  Nano Letters, **16**, 5806-5814

Acknowledgements

Firstly, I am indebted to my supervisor Professor Malcolm Kadodwala for offering me the chance to undertake my post-graduate studies within his research group. I would like to thank him for offering his consistent support and encouragement without which this project would not have been possible. I would also like to extend my sincere thanks to our Post-Doc, Dr Affar Karimullah whose expertise across a whole range of aspects covered in this project was invaluable. In addition, the help and encouragement provided by fellow PhD students Ryan Tullius and Marion Rodier is much appreciated. Finally, I thank the numerous project students who have worked in our lab throughout my thesis namely, Melissa Simonet, Alex Ramsay and Chris Kelly.

I would like to also express my thanks to the academic staff within the School of Chemistry at Glasgow. In particular, Dr Adrian Lapthorn for his advice and expertise in all things protein related and Dr Sharon Kelly for help with circular dichroism measurements. Moreover, I express my gratitude to Dr Chris Syme for his guidance during the initial stages of my research. I am thankful to the technical staff including Stuart McKay, Arlene Douglas and Jim Gallagher for their assistance when things went wrong. I would like to express my gratitude to the staff and users of the JWNC and the various members of the Gadegaard group in the School of Engineering for their time and effort with regards to sample fabrication and microscopy. My thanks also go to Professor Alexander Govorov and Dr Larousse Khorashad at Ohio University for their contributions to numerical simulations used in chapter 5 of this thesis.

During my PhD I spent a total of four months at the Institute for Molecular Science in Okazaki, Japan. A great deal of thanks is due to Professor Hiromi Okamoto for allowing me to work in his laboratory and his significant efforts in making my stay as enjoyable as possible. I am also extremely grateful to the various members of the Okamoto group namely, Dr Tetsuya Narushima, Dr Yoshio Nishiyama, Shun Hashiyada, Akiko Ishikawa and Emiko Nomura for making me feel welcome and assisting me whenever possible throughout my stay.

Many thanks must also go to my family for their infinite patience and support throughout my time at university. Last but not least I would like to thank my girlfriend Kate and my friends David, Mark and Robin and the countless others I have forgotten.

Authors Declaration

I declare that, except where explicit reference is made to the contribution of others, this thesis is the result of my own work and has not been submitted for any other degree at the University of Glasgow or any other institution.

Calum Jack

July 2016

Chapter 1: Introduction

1.1 Background

The study of photonic metamaterials has increased exponentially in recent years as advances in fabrication techniques allow for the generation of ever more complex systems. Unlike bulk materials, the optical and electronic properties of metamaterials are not determined by the intrinsic properties of the constituent chemical elements but rather they rely on the structural properties of components within the system. This characteristic gives rise to the term “meta” which translates as “beyond” since the unique properties of these systems are literally “beyond” those displayed by bulk materials[1]. The elemental structures which constitute photonic metamaterials are precision engineered nanostructures. Depending on the elemental material, these nanostructures often facilitate the generation of plasmonic resonances associated with the structure. In this thesis one of the constituent materials of our nanostructures is Au therefore these structures support the generation of plasmonic modes. The optical properties of plasmonic nanostructures can be tightly controlled by manipulating the size, shape and arrangement of the constituent nanoscale structures[2-5]. Hence, the field of plasmonic metamaterials contains vast potential as it allows scientists to study and exploit the unique physical properties of these materials for use in areas such as sensing[6], optics[7] and photovoltaics[8].

In this thesis we are concerned with the application of plasmonic nanostructures to enhance the sensitivity limits of chiroptical spectroscopy. For a number of years chirally sensitive spectroscopies such as circular dichroism (CD) and optical rotation (OR) have lagged significantly behind other spectroscopic techniques such as Surface Enhanced Raman Spectroscopy (SERS)[9] and surface plasmon resonance (SPR) spectroscopy[10] with regards to their absolute sensitivity. This severely limits the study of biological molecules which relies on chiroptical techniques to identify various levels of structure and chirality. Preliminary experimental and theoretical studies into using plasmonic nanostructures to improve CD measurements have achieved sensitivity enhancements up to two orders of magnitude[11, 12]. However, this enhancement is relatively modest whilst it is also severely limited by the requirement for complementary nanoparticle and molecular resonances.

In recent years, a new paradigm in chiroptical spectroscopy has been introduced which has the potential to revolutionise the spectroscopy of biomolecules. This technique is based on

initial theoretical studies whereby it was proposed that electromagnetic fields that are more inherently chiral than circularly polarised light (CPL) may exist[13]. It was further suggested that the application of such chiral fields in chirally sensitive spectroscopies would be significantly more sensitive to biological structure than CPL. The first experimental demonstration of chiroptical spectroscopy using fields of enhanced chirality was demonstrated by Kadodwala et al at the University of Glasgow[14]. It was found that chiral fields were generated in the near-field of chiral plasmonic nanostructures and that these sculpted EM fields were sensitive to different protein structural motifs. The most significant result of this initial study was the enhanced sensitivity limits of chiroptical measurements using chiral evanescent fields compared with conventional techniques. These measurements were able detect picogram quantities of biomaterial which represents an enhancement of six orders of magnitude. Subsequent studies into the sensing properties of chiral evanescent fields have found that unlike CD/OR measurements these fields are also sensitive to higher order protein structure (tertiary structure)[15]. Thus, chiroptical spectroscopy of biomolecules using chiral EM fields is a more incisive probe than CPL with regards to both its sensitivity limits and the level of structure that may be detected.

Despite these considerable benefits of sensing with nanostructure chiral fields, this technique suffers from several drawbacks which means at present it is confined to fundamental laboratory studies. The most significant drawback is the inherent problems that arise from the fabrication method used to produce these structures. The preferred method of fabrication for plasmonic nanostructures is through electron beam lithography. However, this fabrication technique is costly and suffers from an extremely low through-put whereby it takes several days to produce a small number of substrates. Furthermore, lithographically fabricated nanostructures are extremely fragile and are not suitable for repeated use in biological measurements due to the degradation of the structures during the cleaning process. As a result of these aforementioned issues, sensing with chiral plasmonic nanostructures is currently unsuitable for commercial applications until a viable alternative fabrication method is found. This method must achieve cheap, high-throughput nanostructure fabrication whilst equalling or exceeding the sensitivity limits of lithographically fabricated nanostructures.

1.2 Thesis Overview

In the first results chapter (chapter 4) we introduce novel polycarbonate chiral plasmonic nanostructures, referred to as templated plasmonic substrates (TPS), fabricated using a cheap, high-throughput injection moulding (IM) technique. IM presents a viable alternative to lithographic fabrication and may potentially allow nanostructures to be mass produced at low cost for commercial applications. This fabrication technique has previously been employed to generate simple nanoscale structures such as gratings[16] and biomimetic structures[17]. However, complex architectures such as those employed in this thesis have never before been fabricated using IM therefore our work represents the first investigation into the viability of polycarbonate nanostructures. Firstly, the morphology of TPSs is investigated whereby it is found that IM is able to consistently reproduce high quality nanoscale features. The most important structural aspect of these nanostructures is that they are hybrid structures that possess symmetry equivalent solid and inverse structures in close spatial proximity. Evaluation of the linear optical and chiroptical properties in tandem with electromagnetic field simulations allows us to rationalise the physical behaviour of this hybrid system. The optical properties of the TPS nanostructures are found to be highly dependent on the coupling between the electric and magnetic modes associated with the solid and inverse structures respectively. This coupling is controlled by varying the Au film thickness. Thin Au films (≤30nm) result in weak coupling and reflectance lineshapes typical of a weak interference phenomenon whilst thick films (≥40nm) generate strong coupling and a reflectance lineshape associated with strong interference. This electric/magnetic coupling results in the generation of hybrid plasmonic modes which are rationalised using a plasmon hybridisation scheme. Overall, we find that the Au thickness determines the strength of the electric/magnetic coupling (hybridisation) which in turn modulates the interference between a bright and a dark hybrid plasmonic mode and this interference controls the TPS optical properties [18]. In addition, the extent of electric/magnetic coupling also controls the level of chirality associated with the structures. Strong coupling results in the nanostructures displaying large levels of chirality associated with the single helical oscillator model of chirality. In contrast poor coupling generates low levels of chirality associated with the coupled oscillator chirality model. Finally, similar to the initial measurements by Kadodwala et al[14], refractive index based measurements using TPS nanostructures are shown to be

incisive probes of β-sheet secondary structure and may detect picogram quantities of biomaterial.

Following the confirmation of TPS nanostructures as a viable alternative to lithographically fabricated structures, chapter 5 endeavours to answer another fundamental problem associated with sensing using photonic nanostructures. The effectiveness of applying such materials for biosensing depends on maximizing the interaction of biomaterial with the intense EM fields associated with the nanostructures. These areas of concentrated EM fields, known as plasmonic "hotspots", are typically found in nanoscale regions of the metamaterial. Therefore, it is desirable to selectively place biomaterial in such hotspots. Selective placement of biomaterial can be achieved through nanoscale chemical functionalisation of the nanostructure surface. However, current techniques such as direct laser patterning[19] and dip-pen lithography[20] are severely limited due to the need to functionalise nanoscale areas individually. This renders these nanoscale functionalisation techniques extremely low through-put and unsuitable for widespread applications in sensing. In collaboration with colleagues at the University of Ohio we present a novel high through-put technique that allows for the nanoscale chemical functionalisation of large arrays of TPS nanostructures. This method is analogous to a chemical protection/deprotection strategy commonly found in organic synthesis and is employed to enhance the sensitivity of chiroptical measurements. Firstly, the protection step requires functionalisation of the TPS surface with a thermally responsive polymer which inhibits the binding of biomaterial. The deprotection step involves exploitation of nanolocalised thermal gradients generated in the water surrounding the nanostructure upon irradiation with a nanosecond pulsed laser. These localised thermal gradients are used to modify the structural conformation of the polymer in particular areas of the TPS with the desired EM field properties. This allows biomaterial to be selectively placed in these nanoscale regions which subsequently enhances the sensitivity of the TPSs to β-sheet protein structure.

In chapters 4 and 5, spectroscopic measurements using TPS nanostructures to detect protein structure effectively combine the structural sensitivity of chiroptical spectroscopy with the detection levels of plasmonic refractive index based measurements. This new paradigm in chiroptical sensing has allowed for the detection and characterisation of protein structure, specifically β-sheets, on a sub-picogram level. However, despite these advantages this

method remains fundamentally limited as measurements do not directly probe protein structure, rather they are sensitive to the anisotropy of β-sheets within the molecule [14]. This renders such measurements insensitive to a vast array of protein structures particularly α-helical motifs which are isotropically arranged in proteins. An alternative and more structurally incisive spectroscopic technique is proposed in chapter 6 whereby it is possible to unequivocally identify α-helical, β-sheet and unfolded secondary structure motifs using TPS nanostructures. The foundation of this technique lies in the dependence of the TPS optical and chiroptical properties on the coupling (hybridisation) between the electric and magnetic modes of the solid and inverse structures (chapter 4). In a new development, we find that adsorption of structured protein molecules can modulate this electric/magnetic hybridisation in weakly coupled TPSs. An increased sensitivity to protein secondary structure, particularly α-helical motifs, is observed which we attribute to the electric dipole-magnetic dipole origin of this effect. Importantly, this effect does not depend on the effective refractive index of chiral molecules in nanostructure chiral fields nor is there a prerequisite for these fields to possess an enhanced chirality relative to CPL. Initial investigations are conducted in the linear regime whereby subtle changes in the reflectance lineshape upon protein adsorption indicate a modulation of the electric/magnetic hybridisation however the magnitude of this effect is relatively small. Following this, chiroptical spectroscopic measurements are performed in the nonlinear regime using second harmonic generation (SHG). The effects of protein adsorption on the TPS mode hybridisation in the nonlinear regime results in a variation of the chirally sensitive electric dipole SHG contribution whereby α-helical, β-sheet and unfolded structures elicit vastly differing effects on this SH element. This study represents a fundamental step forward in the understanding of the interaction between chiral molecules and TPS nanostructures whilst it significantly expands the toolkit for the detection of protein structure.

Finally, a preliminary investigation into the application of lithographic chiral plasmonic nanostructures for the detection of biological mesoscale structure is introduced in chapter 7. The mesoscale occupies the range between molecular structures (tens of nanometres) and the size of individual cells (tens of microns). Conventional techniques (such as CD) are insensitive to this higher order biological structure therefore there is an increasing need for a simple, incisive, spectroscopic probe of this structural lengthscale. The potential of detecting

this structural domain with chiral EM fields generated around lithographic gammadions is investigated using insulin amyloid fibrils. The mesoscale structure that we aim to probe in these biomolecules is the helical pitch of the fibril which measures 70-120nm. The detection and structural characterisation of such fibrils is now considered to be vitally important. The accumulation of these structures in vivo is linked to various amyloidosis diseases such as Alzheimer's caused by accumulation of Aβ protein in the brain [21] and Type II Diabetes caused by Amylin deposits in the pancreas[22]. Spectroscopic measurements are performed using gammadions of varying Au thickness and measuring the asymmetry in the changes of the RH and LH CD spectra upon adsorption of insulin amyloid fibril spherulites and bundles of fragmented insulin amyloid fibrils. The use of two distinct forms of insulin amyloid fibrils is essential due to the nature through which the fibrils bind to the substrate surface. Fibrils in spherulites bind with their long axis perpendicular to the surface whilst fragmented fibrils bind with their long axis parallel to the surface. It was found that an asymmetric CD response was highly dependent on this orientation of the fibril at the surface and the Au thickness. Due to the preliminary nature of this study a comprehensive model accounting for these experimental observations has yet to be constructed. However, we propose an initial model whereby the sensitivity to the helical pitch arises due to a combination of factors including: the orientation of fibrils with respect to the nanostructure surface and the length of the fibril helical pitch with respect to the vertical height of the gammadions. These measurements highlight the potential of applying chiral plasmonic nanostructures for spectroscopic measurements of biological structure on a much larger scale however it is important to emphasize that this remains an early preliminary investigation.

1.3 References

1. Y. Liua, X.Z., *Metamaterials: a new frontier of science and technology.* Chemical Society Reviews, 2011. **40**: p. 2494-2507.
2. M. Rycenga, C.M.C., J. Zeng, W. Li, C.H. Moran, Q. Zhang, D. Qin, Y. Xia, *Controlling the synthesis and assembly of silver nanostructures for plasmonic applications.* Chemical Reviews, 2011. **111**(6): p. 3669-3712.
3. W.A. Murray, W.L.B., *Plasmonic materials.* Advanced Materials, 2007. **19**: p. 3771-3782.
4. E.Petryayeva, U.J.K., *Localized surface plasmon resonance: Nanostructures, bioassays and biosensing—A review.* Analytica Chimica Acta, 2011. **706**: p. 8-24.
5. M. Hu, J.C., Z.Y Li, L. Au, G.V. Hartland, X. Li, M. Marqueze, Y. Xia, *Gold nanostructures: engineering their plasmonic properties for biomedical applications.* Chemical Society Reviews, 2006. **35**: p. 1084-1094.
6. K.A.Willets, R.P.V.D., *Localized surface plasmon resonance spectroscopy and sensing.* Annual Review of Physical Chemistry, 2007. **58**: p. 267-297.

7. Stockman, M.I., *Nanofocusing of optical energy in tapered plasmonic waveguides.* Physical Review Letters, 2011. **106**: p. 019901.
8. H.A. Atwater, A.P., *Plasmonics for improved photovoltaic devices.* Nature Materials, 2010. **9**: p. 205-213.
9. K. Kneipp, Y.W., H. Kneipp, L.T. Perelman, I. Itzkan, R. R. Dasari, M.S. Feld, *Single molecule detection using surface-enhanced raman scattering (SERS).* Physical Review Letters, 1997. **78**(9): p. 1667-1670.
10. Homola, J., *Surface plasmon resonance sensors for detection of chemical and biological species.* Chemical Reviews, 2008. **108**: p. 462-493.
11. I. Lieberman, G.S., T. Fried, E. M. Kosower, G. Markovich, *Plasmon resonance enhanced absorption and circular dichroism.* Angewandte Chemie, 2008. **47**: p. 4855-4857.
12. H. Zhang, A.O.G., *Giant circular dichroism of amolecule in a region of strong plasmon resonances between two neighboring gold nanocrystals.* Physical Review B, 2013. **87**: p. 075410.
13. Y. Tang, A.E.C., *Optical chirality and its interaction with matter.* Physical Review Letters, 2010. **104**: p. 163901.
14. E. Hendry, T.C., L. D. Barron, J. Johnston, N. Gadegaard,M. Popland, M. Kadodwala, *Ultrasensitive detection and characterization of biomolecules using superchiral field.* Nature Nanotechnology, 2010. **5**: p. 783-787.
15. R. Tullius, A.S.K., M. Rodier, B. Fitzpatrick, N. Gadegaard, L. D. Barron, V. M. Rotello, G. Cooke, A. Lapthorn, M. Kadodwala, *"Superchiral" spectroscopy: Detection of protein higher order hierarchical structure with chiral plasmonic nanostructures.* Journal of American Chemical Society, 2015. **137**: p. 8380-8383.
16. S. H. Yoon, N.G.C., J. S. Lee, J.G. Park, D. J. Carter, J. L. Mead, C.M.F. Barry, *Effect of processing parameters, antistiction coatings, and polymer type when injection molding, Microfeatures.* Polymer Engineering and Science, 2010. **53**: p. 116-122.
17. N. Gadegaard, S.M., N.B Larsen, *Biomimetic polymer nanostructures by injection molding.* Macromolecular Materials and Engineering, 2003. **288**: p. 76-83.
18. E. Prodan, C.R., N. J. Halas, P. Nordlander, *A hybridization model for the plasmon response of complex nanostructures.* Science, 2003. **302**: p. 419-422.
19. J.H. Slater, J.S.M., S.S. Yu , J.L. West *Fabrication of multifaceted micropatterned surfaces with laser scanning lithography.* Advanced Functional Materials, 2011. **21**: p. 2876-2888.
20. R.D. Piner, J.Z., F. Xu, S. Hong, C. A. Mirkin, *"Dip-Pen" Nanolithography.* Science, 1999. **283**: p. 661-663.
21. Z. Xu, R.P., M.J. Buehler, *Alzheimer's Ab(1-40) amyloid fibrils feature size-dependent mechanical properties.* Biophysical Journal, 2010. **98**: p. 2053-2062.
22. G. Lee, W.L., H. Lee, C. Y. Lee, K. Eom, T. Kwon, *Self-assembled amyloid fibrils with controllable conformational heterogeneity.* Scientific Reports, 2015. **5**: p. 16220.

Chapter 2: Theory

2.1 Chirality

An object is described as possessing chirality if it is of sufficiently low symmetry that it is not superimposable on its mirror image. A chiral object and its mirror image are referred to as enantiomers whilst a non-chiral object is designated as achiral. In terms of group theory, Barron states "for an object to be chiral, it must not possess symmetry elements such as centre of inversion, reflection planes, or rotation-reflection axes"[1]. This means that a chiral object must belong to one of the following point groups: C_n, D_n, *O, T or I.* In addition, chirality may also be observed in electromagnetics whereby circular polarisation of an EM wave results in the electric and magnetic field precessing in either a right handed or left handed helix about the propagation axis. In this thesis we are primarily concerned with the manifestation of chirality on the nanoscale both in natural and engineered systems.

2.1.1 Molecular Chirality

The importance of chirality in molecular systems has been recognized for well over a century[2-4]. Arguably the most significant manifestation of molecular chirality is found in biology wherein the vast majority of naturally occurring biological molecules possess a particular handedness. This chirality influences the structure of biomolecules which in turn controls their function in biological systems. Naturally occurring amino acids (except glycine) are L-amino acids whilst their synthetic enantiomeric partners are D-amino acids. In contrast the natural form of sugars is the D-enantiomer whilst the L-form is synthetic. The chirality of nature also has significant repercussions for the synthesis of pharmacological compounds as whilst one enantiomer may induce therapeutic effects the mirror image molecule may be extremely harmful[5]. Consequently, it is of great importance to be able to distinguish between molecular enantiomers and identify their higher order structure. This is achieved by exploiting another unique property of chiral molecules known as optical activity.

2.1.2 Optical Activity

A system is described as possessing natural optical activity if it displays a differential response to right handed (RH) and left handed (LH) circularly polarised light (CPL) in the absence of external influences such as an applied magnetic field[1]. In the linear optical regime, it is possible to measure both electronic and vibrational optical activity. Electronic optical activity facilitates the observation of circular dichroism (CD) and optical rotation (OR)

in the U.V/visible range whilst vibrational optical activity gives rise to Raman optical activity (ROA) and CD in the I.R region. This thesis is mainly concerned with chiroptical spectroscopy in the visible region therefore we will subsequently explore only electronic natural optical activity.

The propagation of an electromagnetic wave through a medium is dictated by the refractive index (n) and the extinction coefficient (k) of the medium. The extinction coefficient relates to the extent of absorption (or scattering) within the medium and determines the amplitude of the emerging electromagnetic (EM) field. The refractive index describes the speed of propagation of an EM wave through the medium. In a chiral medium these physical properties depend on the polarisation of the incident light whereby the medium possesses different values of n and k for RH and LH CPL i.e. it displays optical activity. Optical activity is measured using a linearly polarised light beam which can be interpreted as a superposition of RH and LH CPL beams with equal amplitude. The polarisation state of the resultant electric field vector (**E**) after propagation through a chiral medium depends on the relative phase and amplitude of the two circularly polarised beams $\mathbf{E_L}$ and $\mathbf{E_R}$. In achiral media the phase relationship remains fixed whilst there is no difference in absorption of $\mathbf{E_L}$ and $\mathbf{E_R}$ therefore the emerging beam remains linearly polarised along the same axis (figure 2.01a).

Firstly, we will discuss optical activity in terms of the differential refractive index (n) which gives rise to the phenomenon of optical rotation (OR) (figure 2.01b). A linearly polarised light beam of angular frequency $\omega = 2\pi c/\lambda$ enters a transparent chiral medium at z=0. At a point in time, the E-field vectors $\mathbf{E_L}$ and $\mathbf{E_R}$ at z=0 have traversed equal distances with respect to the axis parallel to **E**. At the same instant, at a point z=*l* in the optically active media $\mathbf{E_L}$ and $\mathbf{E_R}$ have traversed different distances and the E-field vectors are inclined at angles of:

$$\theta_R = -2\pi cl/\lambda v_R \qquad (1)$$

$$\theta_L = 2\pi cl/\lambda v_L \qquad (2)$$

with respect to the axis parallel to **E** at z=0. v_R and v_L are the velocities of the RH and LH CPL components in the medium. The angle of rotation of the linearly polarised light beam in terms of the differential CPL velocities in a chiral medium may then be expressed as:

$$\alpha = \frac{1}{2}(\theta_R + \theta_L) = \frac{\pi cl}{\lambda}\left(\frac{1}{v_L} - \frac{1}{v_R}\right) \qquad (3)$$

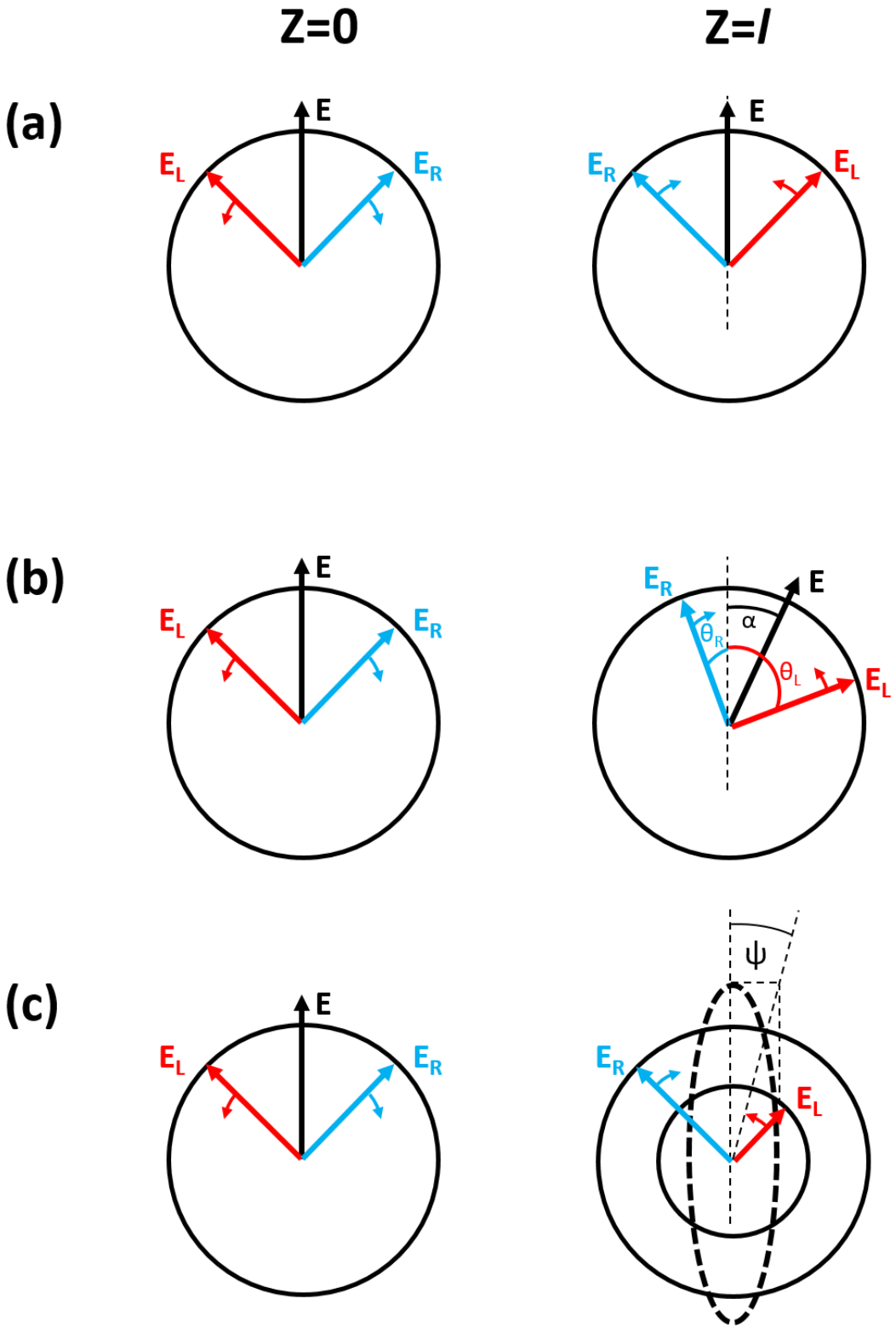

Figure 2.01: Propagation of a linearly polarised beam consisting of equal amplitude RH and LH circularly polarised components through: **(a)** an achiral medium; **(b)** a chiral medium with different refractive indices for RH and LH CPL (optical rotation) and **(c)** a chiral medium with different absorption coefficients for RH and LH CPL (circular dichroism). $\mathbf{E_L}$ and $\mathbf{E_R}$ are the electric field vectors of RH and LH circularly polarised beams and **E** is the electric field vector of the resultant linearly polarised beam. Figure adapted from reference [1].

In terms of the refractive index where $n = c/v$, equation 3 may be written as:

$$\alpha = \frac{\pi l}{\lambda}(n_L - n_R) \qquad (4)$$

For the example in figure 2.01b the chiral medium has a larger refractive index for $\mathbf{E_L}$ therefore the medium displays circular birefringence. When viewed towards the light source, a chiral compound that rotates the linear polarisation clockwise is referred to as dextro-rotatory whilst anti-clockwise rotation is referred to as levo-rotatory.

If the refractive index of a chiral medium is different for $\mathbf{E_L}$ and $\mathbf{E_R}$ at transparent frequencies, then it becomes apparent that the absorption of $\mathbf{E_L}$ and $\mathbf{E_R}$ will be different at absorbing frequencies. The differential absorption of $\mathbf{E_L}$ and $\mathbf{E_R}$ is known as circular dichroism (CD) and a simplified pictorial description is provided in figure 2.01c. Unlike optical rotation, $\mathbf{E_L}$ and $\mathbf{E_R}$ have the same phase velocity in chiral media therefore $\alpha = 0$. However, $\mathbf{E_L}$ and $\mathbf{E_R}$ now display a discrepancy in their relative amplitudes due to differential absorption in the medium. This results in elliptical polarisation since $\mathbf{E_L}$ is absorbed to a greater extent than $\mathbf{E_R}$. The ellipticity (ψ) is parametrised through simple calculation of the ratio of the major and minor axes of the ellipse:

$$tan\psi = \frac{(\mathrm{E}_R - \mathrm{E}_L)}{(\mathrm{E}_R + \mathrm{E}_L)} \qquad (5)$$

The intensity of CD spectra is commonly referred to in terms of these units with proteins typically displaying values on the order of hundreds of millidegrees. Alternatively, CD may be expressed as the differential absorbance of $\mathbf{E_L}$ and $\mathbf{E_R}$ where $A = log\frac{I_0}{I_l} = \epsilon lc$. Typical values for ΔA_{L-R} are on the order of 0.1%[6]. A final dimensionless parameter that is widely used to measure the enatioselectivity of a system is the dissymmetry factor[7]:

$$g \equiv \frac{(A^L - A^R)}{\frac{1}{2}(A^L + A^R)} \qquad (6)$$

This parameter can be described as the ratio of CD to the conventional absorption. Typical values of g for proteins are on the order of 10^{-3} at U.V./visible wavelengths.

Refractive and absorptive effects of a medium depend on the wavelength of incident light therefore optical rotation and circular dichroism display a wavelength dependence whereby

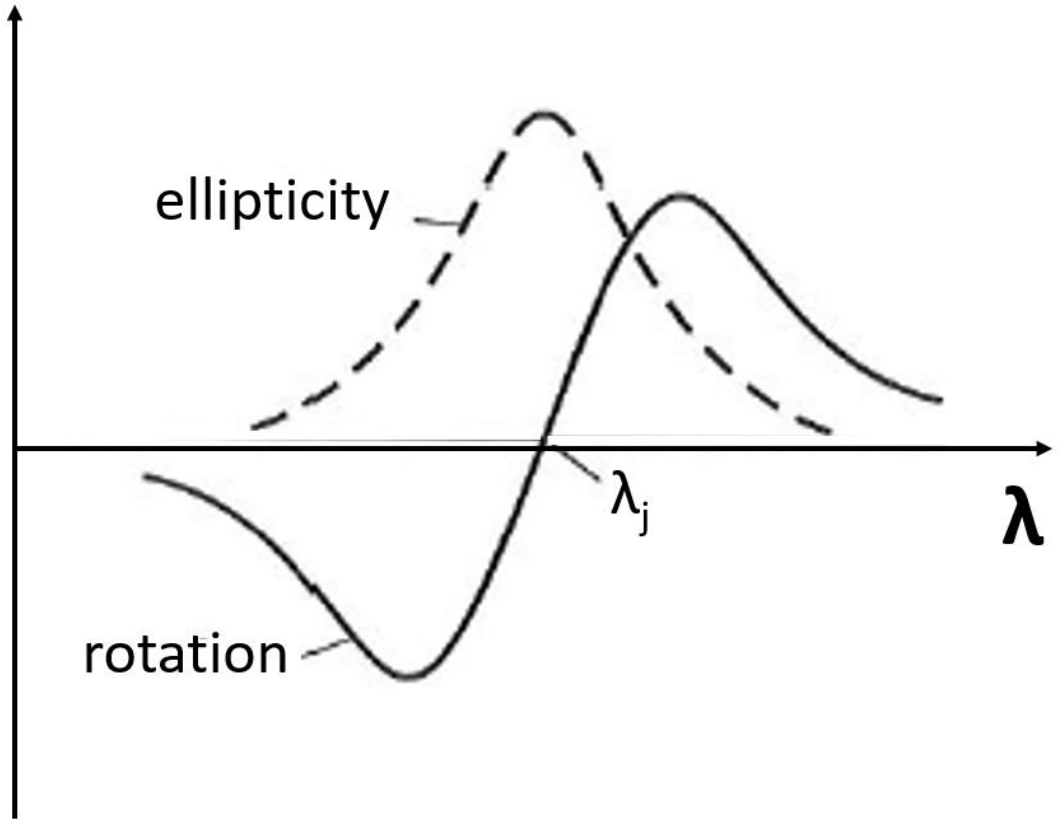

Figure 2.02: Optical rotation and corresponding ellipticity around the region of the electronic absorption wavelength λ_j.

both effects may be observed simultaneously at particular wavelengths (figure 2.02). Since circular dichroism is an absorptive process, the ellipticity maximum will coincide with electronic absorption bands; therefore; CD effects are associated with specific energies. For proteins this absorption is strongest in the far U.V. region due to $n - \pi^*$ and $\pi - \pi^*$ transitions of the peptide bond. Due to being a refractive effect OR may in theory occur with different intensities over all wavelengths. Measurement of the OR as a function of wavelength is known as the optical rotatory dispersion (ORD). In the absorption region the ORD and CD are closely related through a phenomenon known as the Cotton effect (figure 2.02). The ORD displays a bisignate profile with a point of inflection at the ellipticity maximum whilst the ORD maxima and minima are either side of the CD peak.

2.1.3 Models of Chirality

The electronic optical activity of circular dichroism and optical rotation originates from higher order effects, primarily electric dipole-magnetic dipole interactions and electric dipole-electric-quadrupole interactions. In an isotropic media of chiral molecules electric dipole-electric quadrupole interactions average to zero[1] therefore in this section we will

focus on electric dipole-magnetic dipole contributions to optical activity. Through extensive quantum mechanical computations it was found that the magnitude of ORD and CD effects is related to the rotatory power[9, 10]:

$$R_{ab} = \mu . m \qquad (7)$$

Where a and b are molecular states μ is the electric dipole transition moment and m is the magnetic transition dipole moment. Equation 8 dictates that in order for ORD and CD to occur, μ and m must have components parallel to each other. The physical models of chirality which adequately satisfy equation 7 have been widely discussed over the past century. The general consensus allows for the application of two distinct models to account for the optical activity of a chiral system: the single helical oscillator (SHO) also known as the Kauzman model[10] and the coupled oscillator often referred to as the Born-Kuhn model[11]. The single helical oscillator model is illustrated in figure 2.03 whereby a single electron is constrained to move along a helical path. The vertical translatory motion gives rise to the electric dipole transition moment and the rotatory motion gives rise to a magnetic dipole moment. These will be parallel or anti-parallel depending on the handedness of the helical pitch. Reversing the chirality of the helical motion changes the

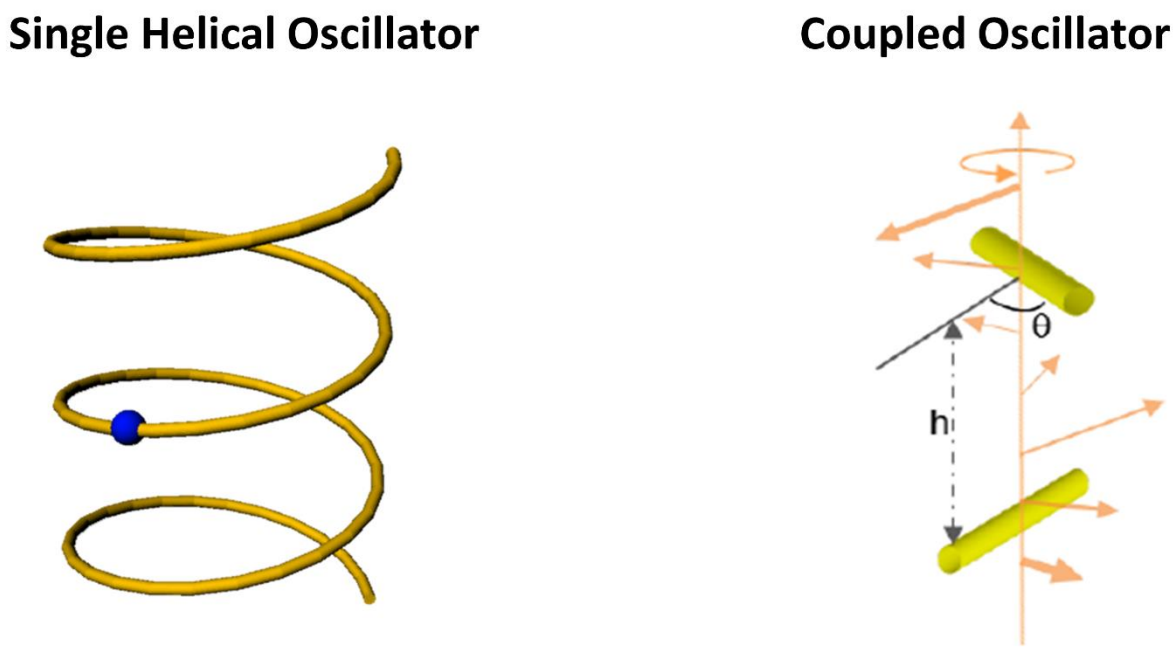

Figure 2.03: (a) Pictorial representation of a single helical oscillator and coupled oscillator models of chirality. In the coupled oscillator model θ represents the angle the two oscillators are inclined at and h is the separation distance.

sign of m and consequently R_{ab}. This reversal of R_{ab} means the resultant ORD and CD spectra will be inverted. In contrast, the Born-Kuhn model is based upon the interaction of two separate charges inclined at an angle of θ and separated by a distance h wherein the optical activity arises due to the geometric arrangement. An incident wave induces an oscillating dipole in the upper oscillator which is confined along the long axis. Coupling of the upper oscillator with the lower one induces an oscillation of charge along the long axis of this lower component. An electric field is associated with both the upper and lower oscillators and the resultant electric field of the system as a whole follows a helical path. Hence, movement of charge in this system is constrained to move along a helical path generating parallel components of μ and m resulting in optical activity.

2.1.4 "Superchiral" Fields

As discussed, optical activity in an isotropic system arises due to the interaction between electric and magnetic dipole moments. However, pure electric dipole excitations occur with far greater frequency and with equal probability for RH and LH CPL in the linear regime. Thus, the dominant light-matter interaction is achiral meaning ORD and CD effects in chiral molecules are extremely small. Furthermore, when chiral light-matter interactions do occur they are found to be extremely weak. The helicity of a circularly polarised EM wave is dependent on the wavelength whereby the optical field twists 360^{o} over one wavelength, typically hundreds of nanometres in the U.V./visible regime. This lengthscale is considerably larger than the tens of nanometres over which molecular chirality is manifested meaning the EM field undergoes a barely perceptible twist over molecular lengthscales. This large mismatch in chiral lengthscale and the low probability of electric dipole-magnetic dipole interactions renders optically active effects extremely weak. Indeed, the sensitivity limits of conventional chiroptical spectroscopies is on the order of micrograms which is extremely poor compared with that of other spectroscopic techniques.

In 1964 Lipkin introduced a series of conserved quantities (known as "zilch") to describe an electromagnetic field in a vacuum which are independent of energy-momentum[12]. Originally, these properties were dismissed as physically irrelevant[13, 14] and Lipkin stated there was "lack of any ready physical interpretation for the quantities that are found to be conserved". Recently, in an attempt to provide a more complete description of chirality in EM fields Tang and Cohen[15] recognized the requirement for a time even pseudoscalar for

such a description. The authors identified one of Limpkin's simple zilch quantities as fulfilling this requirement and subsequently named this quantity the optical chirality parameter, C. This quantity describes the chirality of an EM field independent of its interaction with matter:

$$C = \frac{\varepsilon_0}{2} E \cdot \nabla \times E + \frac{1}{2\mu_0} B \cdot \nabla \times B \qquad (8)$$

where ε_0 is the permittivity of free space, μ_0 is the permeability of free space and E and B are the time dependent electric and magnetic field vectors respectively. For the EM field simulations in this thesis, values of C are normalised to circularly polarised light where $C = +1$ corresponds to LH CPL and $C = -1$is RH CPL. Subsequently, the authors in reference [15] demonstrated that the CD dissymmetry factor g (equation 6) may be rewritten to incorporate equation 9:

$$g = g_{cpl} \frac{cC}{2U_e \omega} \qquad (9)$$

Where g_{cpl} is the dissymmetry factor under circular polarisation, c is the speed of light, U_e is the local electric energy density of the surrounding field, ω is the angular frequency and C is the optical chirality. In contrast to equation 6, it is found that the magnitude of the CD dissymmetry factor (g) no longer solely depends on the absorptive properties of matter but is also dependent on the chirality C of the incident light[16]. Therefore, it may be possible to generate fields with $|C| > 1$ in some regions of space in order to enhance g. Such fields are commonly known as "*superchiral*" fields i.e. EM fields that have a greater helicity than ordinary CPL at the same frequency.

The application of plasmonic nanostructures is currently the simplest pathway that leads to an enhancement of C [17]. The coupling of plasmonic nanostructures with EM radiation in the visible/I.R. region may generate strong electric and magnetic fields in the near field of such systems. In order to generate an enhancement of C, the arrangement of the constituent components of the structure must be chiral and designed so as to optimize the coupling of parallel electric and magnetic fields[18]. The application of chiral plasmonic nanostructures in the spectroscopy of biomolecules has resulted in reports of dissymmetry factor enhancements up to 10^5 [19] which corresponds to the detection of picogram (10^{-12})

amounts of material. Thus, chiroptical spectroscopy with chiral plasmonic nanostructures provides a route for the detection of chiral molecules at very low concentrations such as those found in physiological systems and has the potential to be applied for enhanced sensing and diagnostic technologies.

2.2 Fundamentals of Plasmonics

As discussed, the generation of EM fields with an enhanced C exploits the phenomenon of plasmon oscillations generated around metal nanostructures therefore; in this section a brief overview of the field of plasmonics is provided. The electrical, thermal and optical properties of metals are interpreted using the very simple free electron gas model otherwise known as the plasma model. Due to their large distance from the nucleus, the valence electrons of metal ions are weakly bound to the positive cores. When metal atoms are brought closer together in a periodic arrangement such as a crystal lattice, valence electrons experience the potential energy due to all nuclei and other valence electrons in the system[20]. This generates an electrically neutral medium whereby valence electrons move about a fixed background of positive ion cores generating an electron plasma. In noble metals the density of this free electron plasma is approximately $1x10^{23}cm^{-3}$. In the absence of an applied electric field the electrons propagate throughout the entire volume of the lattice in a random motion similar to an ideal gas wherein electron-electron collisions are neglected.

2.2.1 Plasmon Oscillations

At equilibrium there are equal numbers of positive ions and negative electrons at all points in the system therefore the total charge inside the metal is zero. When an electric (or electromagnetic) field is applied to an isotropic metal, the free electron gas is displaced by a distance x from its equilibrium position as illustrated in figure 2.04. There is now an excess of negative charge on the right and an excess of positive charge on the left which produces a charge density. Consequently, the positive ionic cores of the lattice induce a restoring force which pulls the electrons back to their equilibrium position. This oscillatory motion of the electron gas is known as plasma oscillation with a corresponding plasma frequency ω_p. Using Newton's second law and electrostatic relationships it is possible to obtain ω_p[21]. The volume charge density is given as:

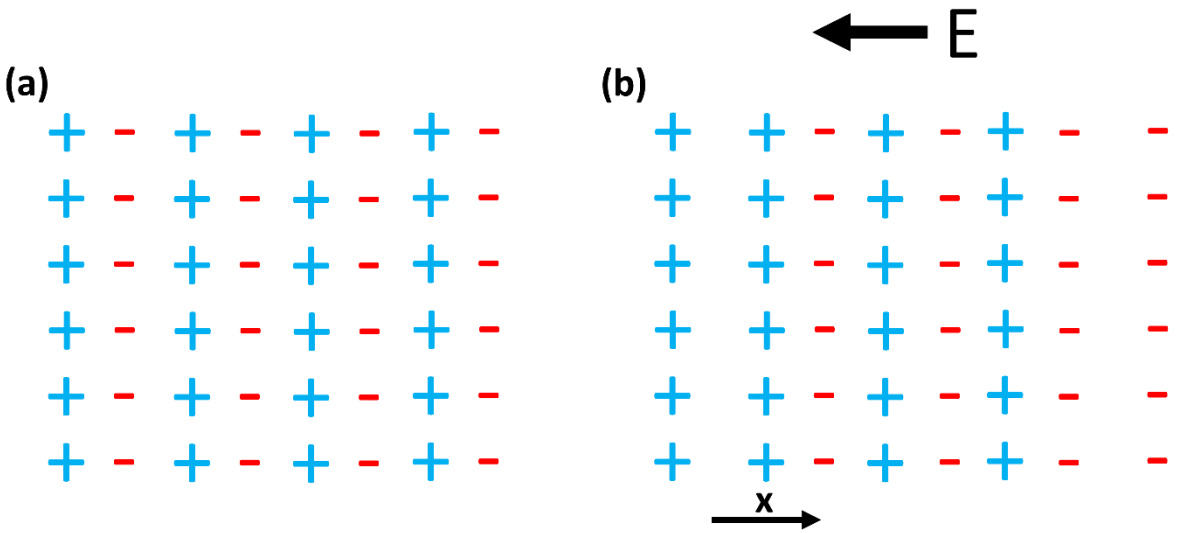

Figure 2.04: Schematic representation of a bulk plasma oscillation in a metal. The action of an electric field E induces the deviation of the free electron gas from its equilibrium position in **(a)** by a distance x in **(b)**. The positive ion cores induce a restoring force to move the electron cloud back to its original position, causing a collective oscillatory motion of the electron gas around the equilibrium position.

$$\rho = \sigma\delta(x) \tag{10}$$

where σ is the surface charge density of an infinite plane $\delta(x)$. The integral form of Gauss's law is:

$$\int_v \frac{\rho}{\varepsilon_0} dv = \oint \vec{E} \cdot d\vec{A} \tag{11}$$

where the permittivity of the medium is ε_0 and $\vec{E} \cdot d\vec{A}$ is the area integral of the electric field over a closed surface. In order to find the total charge, we can simply write equation 11 in the form:

$$\frac{\sigma A}{\varepsilon_0} = EA + EA \tag{12}$$

The electric field can then be expressed as:

$$E = \frac{\sigma}{2\varepsilon_0} \tag{13}$$

Written in terms of charge number density (n), electron charge (e) and charge displacement (x) in a system with two interfaces equation 13 has the form:

$$E = \frac{2nex}{2\varepsilon_0} \tag{14}$$

Upon perturbation of the charge equilibrium, the force experienced by the electrons is $-eE$. From Newton's second law we know that $F = ma$ therefore:

$$-eE = m_e a \tag{15}$$

Replacing E with equation 14 gives us:

$$-e.\frac{2(en_e)(x)}{2\varepsilon_0} = m_e a \tag{16}$$

$$= -\frac{(e^2 n_e)(x)}{\varepsilon_0} = m_e a \tag{17}$$

Expressing the acceleration as a differential equation and some simple manipulation of equation 17 yields:

$$\frac{d^2x}{dt^2} + \frac{(e^2 n_e)}{m_e \varepsilon_0} x = 0 \tag{18}$$

The equation for simple harmonic oscillation is of the form:

$$\ddot{x} + \omega^2 = 0 \tag{19}$$

where ω is the angular frequency of oscillation. Thus, we can write the frequency of electron plasma oscillations as:

$$\omega_p = \sqrt{\frac{(e^2 n_e)}{m_e \varepsilon_0}} \tag{20}$$

Throughout this thesis we will often refer to plasma oscillations using the quantum mechanical term "plasmons". This quantum mechanical treatment of the collective plasma oscillation considers this phenomenon as quasi-particle with energies $\hbar\omega_p$ analogous to the quantization of EM radiation using photons.

Figure 2.04 corresponds to a longitudinal excitation i.e. the plasma oscillation is vibrating in the same direction as the applied electric field. EM radiation is a transverse wave hence the plasma oscillation depicted in figure 2.04 may not be excited by electromagnetic fields. These oscillations of the electron charge density across the whole crystal lattice of the metal are known as bulk or volume plasmons i.e. a plasma oscillation in the bulk of the material. The properties of bulk plasmons have been extensively investigated through electron energy

loss spectroscopy (EELS) whereby electrons are inelastically scattered losing energy in quanta of $\hbar\omega_p$due to the excitation of bulk plasmons. Typically for most metals this energy ranges between 2-15eV[22].

2.2.2 Surface Plasmon Polariton (SPP)

In the previous section we have described bulk plasmons as a quantised charge density fluctuation within an isotropic media between two interfaces that cannot be excited by a transverse wave. However, generation of a plasmonic resonance by EM radiation is possible at a metal-dielectric interface. This combined excitation consisting of a surface plasmon and an electromagnetic wave is called a surface plasmon polariton (SPP) and is illustrated graphically in figure 2.05a. In simple terms, incident EM radiation induces a surface charge oscillation which propagates along the metal dielectric interface giving rise to an electric field perpendicular to the interface. At shorter wavelengths (U.V./visible), the SPP resonance frequency of a metal is related to ω_p through:

$$\omega_{spp=}\omega_p/\sqrt{2} \qquad (21)$$

Hence, surface plasmon polaritons are excited at energies below that of the bulk plasmon.

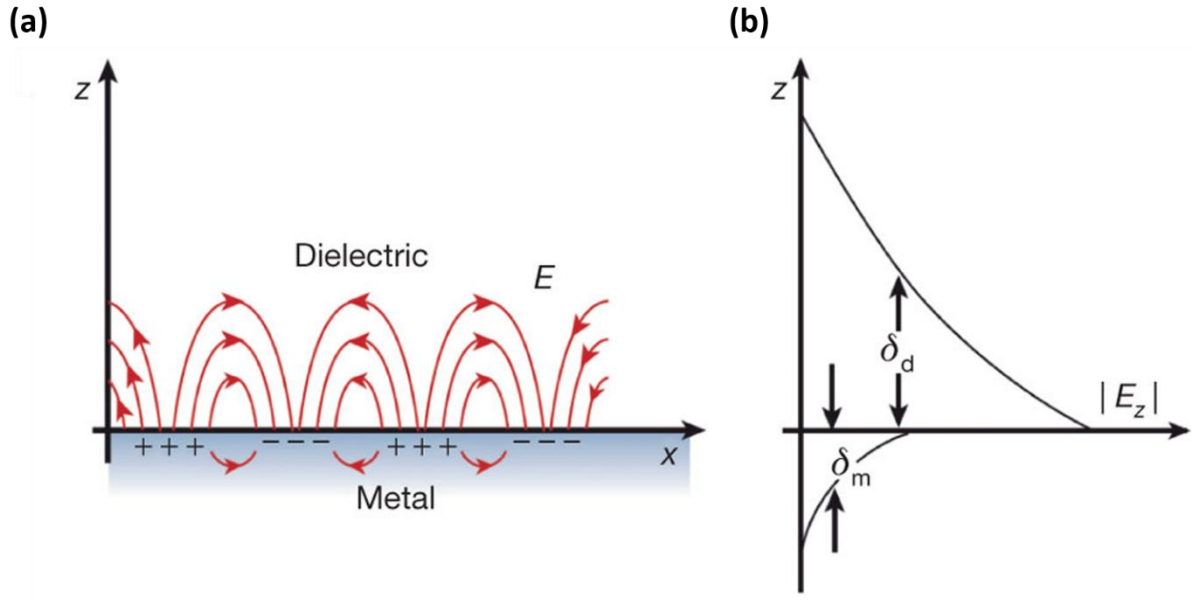

Figure 2.05: (a) Schematic representation of metal charge distribution and the resultant electric fields in the metal and dielectric due to surface plasma oscillations (surface plasma polaritons). **(b)** Electric field strength perpendicular to the surface. δ_d and δ_m are the electric field decay lengths in the dielectric and metal respectively and $|E_z|$ is the electric field strength in the z direction. Figure taken from reference [25].

As a consequence of this interaction between surface charges and EM radiation, the effects of SPPs are evident in both the metal and the dielectric. In the metal the SPP primarily exists as charge fluctuations excited by incident EM radiation. Once the energy of the incident light has been converted into an SP mode, the plasma oscillation will propagate along the surface and gradually attenuate due to ohmic losses in the metal. As discussed, surface plasmon oscillations result in the generation of an electric field (a surface wave) perpendicular to the metal surface which protrudes into both the dielectric and the metal. This surface wave is characterised by three different lengths. Firstly, the surface wave will propagate along the metal surface in the x direction and gradually attenuate with the damping of the plasma oscillation to which it is inextricably linked. Relevant to this thesis the typical propagation distance for surface waves along the Au-vacuum interface at optical frequencies is tens of microns[23]. In contrast to the propagating SPP modes along the surface, the field components perpendicular to the interface exhibit exponential decay as the distance from the metal surface increases (figure 2.05b). The field along this axis is said to be evanescent and is otherwise known as the near-field. The generation of these non-radiative evanescent fields is a result of the surface plasmon modes being bound to the surface of the metal. The near-field protrudes into both the metal and the dielectric however the field decay in the dielectric is considerably larger. In the metal the field decay length is approximately equivalent to the skin depth which is ~15nm in Au at 633nm. For surface waves at optical frequencies in the dielectric the decay length is typically on the order of half the wavelength of light (hundreds of nanometres). As a result of the surface bound, non-radiative nature of SPPs confinement of light at the metal surface generates large field intensities at SPP frequencies which have been widely exploited for applications in sensing and optics.

In order for the excitation of SPP modes to occur several physical prerequisites must be satisfied. An important parameter is the surface plasmon dispersion relation which is obtained by solving Maxwell's equations under the appropriate boundary conditions and is expressed as[24]:

$$k_{sp} = k_0 \sqrt{\frac{\varepsilon_d \varepsilon_m}{\varepsilon_d + \varepsilon_m}} \qquad (22)$$

This function describes the frequency dependent surface plasmon wave vector (k_{sp}) in terms of the wave vector of a photon in free space (k_0) and the frequency dependent metal (ε_m) and dielectric (ε_d) relative permittivity. In order for a plasmonic resonance to exist at an interface, ε_m must be large and negative whilst ε_d must be small and positive. This condition is satisfied at optical and infra-red frequencies for metal/air or metal/liquid interfaces as ε_m is large and negative in this frequency range[25]. For example, the ε_m of Au at 600nm is -12.7 and the ε_d of air at the same wavelength is 1.00 therefore $k_{sp} \cong 1.09.k_0$. However, the wave vector associated with the surface plasmon (k_{sp}) is larger than that of a photon of the same frequency in free space (k_0). This leads to the second prerequisite for surface plasmon excitation.

In quantum mechanics, interactions involving photons must obey the law of conservation of momentum. This means for SPP excitation, the momentum of the surface plasmon and incident photon of the same frequency must match. The wave vector k may be related to the momentum through:

$$\rho = \hbar k \qquad (23)$$

Consequently, in the above example of plasmon excitation at the Au/air interface there exists a mismatch in the momentum between the surface plasmon and a photon in free space. This mismatch in momentum can be illustrated graphically by plotting the dispersion relation for an SPP at a metal surface and a photon in a vacuum (figure 2.06a). Evidently, the SPP dispersion curve is below the photon dispersion at all frequencies therefore SPPs cannot be excited by EM waves incident through the dielectric as surface plasmon modes of the same frequency have a larger momentum. In order to satisfy the requirement of conservation of momentum and excite an SPP, additional momentum must somehow be provided to the incident wave. In practice, this is done by propagating the incident light through a high refractive index medium which infers additional momentum since:

$$\rho = \hbar k = \frac{nhf}{c} \qquad (24)$$

where n is the refractive index of the medium and f is the frequency. The two common experimental setups employed to achieve this are the Otto configuration and the Kretschmann configuration (figure 2.06b-c). In the Otto configuration a small gap between

the prism and the metal surface is necessary as otherwise the SPP dispersion will also be altered whilst the metal film in the Kretschmann configuration must be extremely thin to allow light to propagate through the film to the metal-dielectric interface.

An alternative method for inferring additional momentum allowing for the generation of a SPP is the scattering of incident light from a periodic grating or features on the metal surface[26]. In chapters 4, 5 and 6 we exploit this phenomenon in order to generate SPPs in nanostructured Au films. Photons incident on a metal surface can scatter from the grating/features which increases or decreases the component of its wave vector by integer multiples of the grating wave vector:

$$k_g = 2\pi/\lambda_g \tag{25}$$

with λ_g representing the grating wavelength. This phenomenon gives rise to diffracted orders (υ). Thus, matching of the momentum between the wave vector of a photon in free space and an SPP occurs whenever the following condition is met:

$$k_{sp} = k_0 \pm \upsilon k_g \tag{26}$$

where υ is an integer value. The use of periodic gratings/features is advantageous as it allows direct excitation of an SPP mode by a photon incident from free space. Furthermore, the coupling strength can now be easily controlled by selection of the appropriate grating periodicity/excitation wavelength and groove depth of the metal surface.

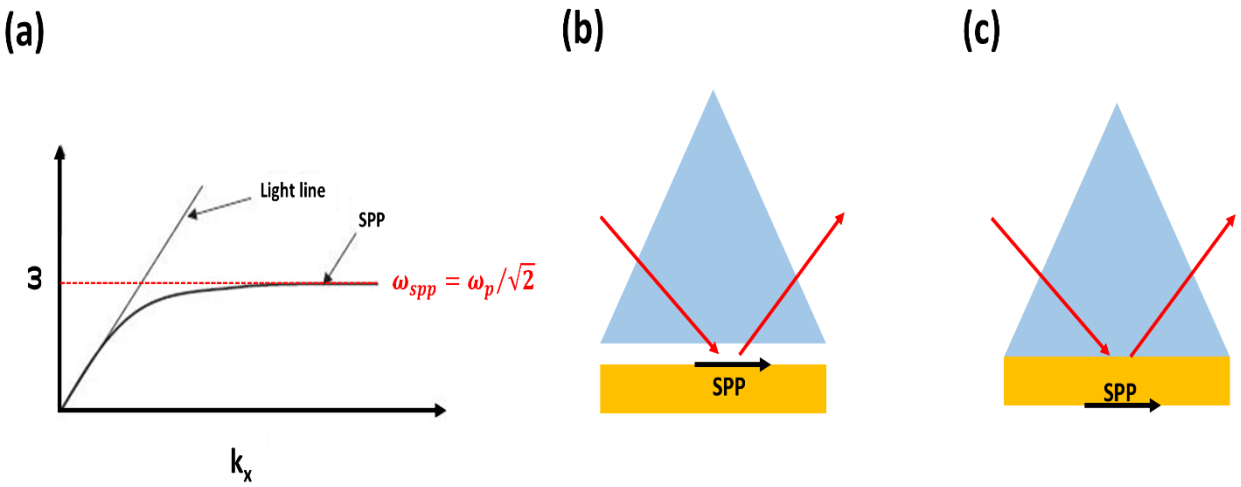

Figure 2.06: (a) Dispersion relation for light in a vacuum and a SPP. Otto configuration **(b)** and Kretschmann configuration **(c)** for excitation of a SPP at a metal-dielectric interface.

2.2.3 Localised Surface Plasmon Resonances (LSPR)

The oscillation of the surface charge density in nanostructures that are a similar lengthscale to the incident light is known as a localised surface plasmon resonance (LSPR). The closed geometry of the nanostructure constrains the plasma oscillation within the boundaries of the structure therefore unlike SPPs which propagate along the surface, LSPRs are stationary surface charge density oscillations. As in the case of bulk plasmon excitation an incoming electric field perturbs the valence electrons from their equilibrium position and the positively charged background acts as the restoring force thus a coherent plasma oscillation is generated (figure 2.07). Since the SP mode is no longer propagating along the metal/dielectric interface but is well localised within the physical boundaries of the structure, the momentum matching condition is satisfied. This strong field localization around the nanostructure allows EM radiation to be confined into volumes below the diffraction limit. Furthermore, sub-wavelength confinement of electric fields results in strong field enhancements around the structure which are much greater than those found in SPPs [27]. This is a result of the significantly shorter evanescent field decay length of LSPRs which is highly dependent on the nanostructure geometry and is typically tens of nanometres [28].

Due to the non-propagating nature of LSPRs, excitation of these modes depends only on the energy and polarisation of the incident EM wave whilst the finite geometry of the noble metal nanostructures determines the LSPR resonance frequency (ω_{spp}). In recent years a wide variety of nanostructure shapes and geometries have been studied ranging from

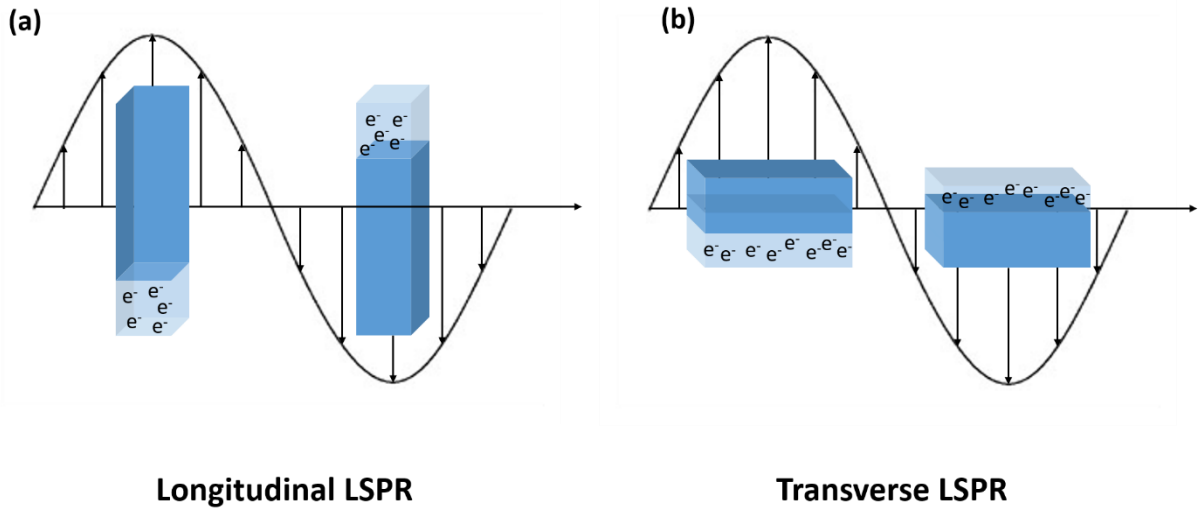

Figure 2.07: Graphic illustration of noble metal nanorod upon excitation of **(a)** dipolar longitudinal LSPR and **(b)** dipolar transverse LSPR.

simple spherical nanoparticles to more complex shapes such as gammadions. As the complexity of the nanostructure architecture increases, the plasmonic modes associated with the system become increasingly difficult to decipher.

2.2.4 Decay of SPPs and LSPRs

In this thesis we exploit the presence of both SPPs on a nanostructured Au film and LSPRs in nanostructures to perform spectroscopic measurements of biomolecules. In addition to the resonant frequency, the main feature of nanostructured Au film SPPs and nanostructure LSPRs is the spectral linewidth otherwise known as the quality factor (Q). A theoretical analysis by Y.R. Shen [29] surprisingly concludes that this parameter is almost entirely determined by the dielectric constant of the metal which relates to the damping of plasma oscillations. This damping is either radiative (emission of a photon) or non-radiative. Radiative decay in nanostructures and nanostructured surfaces occurs via spontaneous emission of photons and is a process that requires a quantum mechanical treatment that is beyond the scope of this thesis[21, 30]. Non-radiative decay arises due to scattering events of individual conduction electrons with phonons, lattice cores or other conduction electrons. This decay pathway also occurs through intraband excitations within the conduction band or through interband excitations caused by transitions between other bands (d-bands) and the conduction band. Hence, once the desired resonance frequency and metal have been selected there is little that can be done to modify the spectral linewidth.

2.2.5 Surface Plasmon Resonance Refractive Index Sensitivity

Referring to equation 22 we know that the resonant wavelength at which SPPs and LSPRs oscillate is dependent on ε_d, the relative permittivity of the surrounding medium. Since ε_d is related to the refractive index through $\varepsilon_d = n^2$, the wavelength at which a surface plasmon oscillates is determined by the refractive index of the medium at the metal-dielectric interface. This effect has been exploited using SPPs and more recently LSPRs to perform highly sensitive refractive index dependent measurements. Surface plasmon based refractive index sensors display extraordinary sensitivity primarily due to the strongly localised and enhanced fields at the metal surface. The confinement of these intense non-propagating fields at the interface facilitates a much stronger light-matter interaction making SPs a particularly incisive probe of molecular species at the interfacial region.

Through experimental curve fitting of SPP data Campbell et al derived a simple quantitative formulism for the interpretation of the surface plasmon response[31]:

$$\Delta\lambda = m\Delta n\left[1 - \exp(^{-2_d}/_{l_d})\right] \quad (27)$$

Where m is a constant relating to a sensitivity factor, Δn is the change in refractive index, *d* is the thickness of the molecular layer at the surface and l_d is the spatial evanescent decay of the local field at the interface. The most important aspect of expression 27 to appreciate with regards to this thesis is the linear dependence of Δn on the resonant wavelength. Consequently, an increases in the refractive index of the surrounding dielectric results in a red-shift of the surface plasmon wavelength. The sensitivity factor m is measured in units of nanometres per refractive index unit (nm/RIU) and is highly dependent on the thickness of the Au film and nature of the particular SP mode. The value of m for SPPs is around $2x10^6$ nm/RIU [32] whilst for LSPRs this is typically around 200-400 nm/RIU[33, 34]. Despite this large discrepancy, refractive index sensing with LSPRs offer several advantages over SPPs. This is a result of the relative decay lengths of the evanescent fields which as previously stated is ~200nm for SPPs and tens of nanometres for LSPRs. Due to the long decay length of SPPs the resonant wavelength shift is highly dependent on the refractive index of the bulk solution. In contrast, the short decay length of LSPRs means the effective sensing volume is much smaller therefore the observed resonant shifts are more closely related to the species directly adsorbed on the metal surface. From equation 27 we also find that as l_d decreases the LSPR wavelength shift increases. This increased spectral response from a smaller sensing volume in LSPRs renders this technique as an ideal candidate for ultrasensitive detection of molecular interactions in the nanometre lengthscale such as those found in biology[35-37].

2.2.6 Surface Plasmon Hybridisation

The discussion of SPPs and LSPRs until this point has focussed on the excitation of an isolated nanostructure. However, in most plasmonic metamaterials the constituent nanostructures are arranged periodically to form large arrays. When the inter-particle separation is sufficiently small between constituent plasmonic nanostructures (typically within the decay length of the electric field) it is possible for plasmonic modes to couple via a coulomb interaction which leads to a dramatic modification in the metamaterial optical properties[38]. Coupling between plasmonic modes in solid-solid [39], inverse-inverse [40]

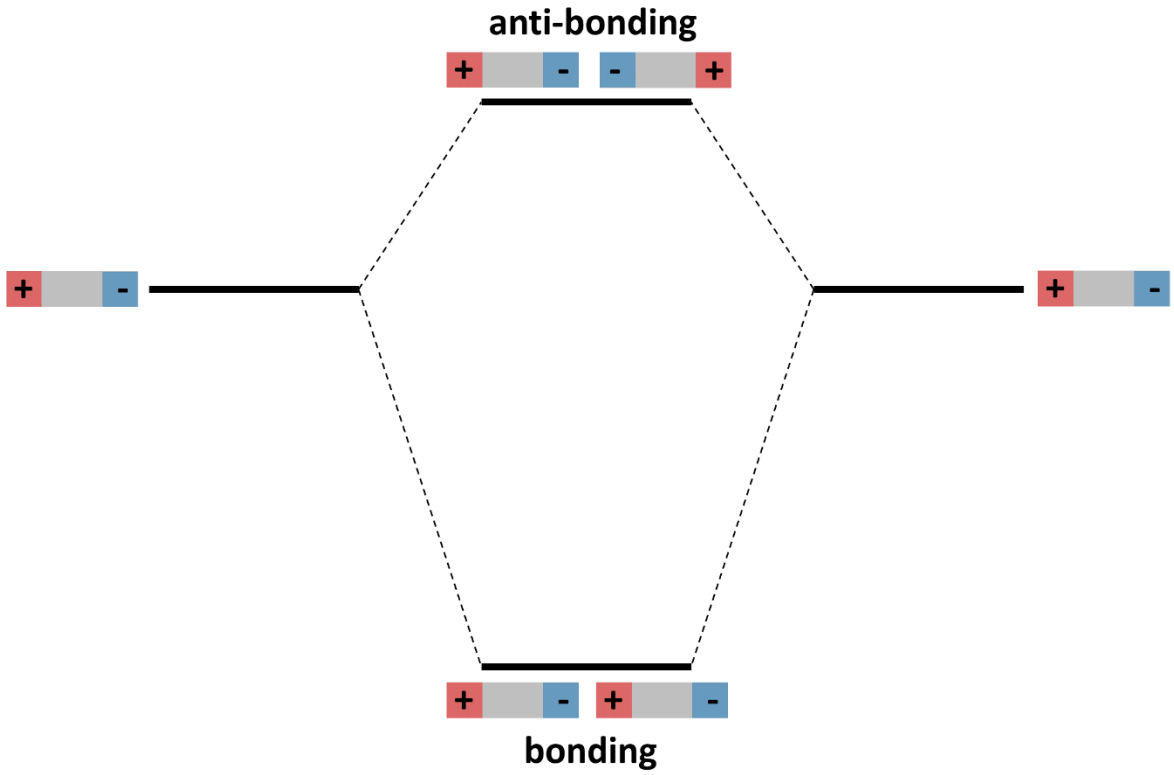

Figure 2.08: Hybridisation scheme adapted from reference [28] representing coupling between dipoles of two nanorods aligned end to end and separated by a small gap.

and solid-inverse nanostructured systems have recently been reported [41]. In all three systems it was revealed that sufficiently strong coupling between dipole (or quadrupole) plasmonic modes leads to the generation of hybrid plasmonic modes[42].

A simple, intuitive model to characterize the hybridisation of nanostructure plasmonic modes was introduced by Provan et al [43] wherein this interaction can be interpreted through an electromagnetic analogue of molecular orbital hybridisation. One of the simplest hybridisation models is coupling between nanodimers aligned end to end separated by a small gap[44]. The single particle dipole plasmon modes may oscillate either in-phase or out-of-phase which corresponds to bonding and anti-bonding molecular orbitals (figure 2.08). Note that analogous to molecular orbitals the bonding (in-phase) orbitals are lower in energy than the anti-bonding (out-of-phase) orbitals. This results in the generation of two hybrid plasmons that are distinct from the dipole modes of individual nanorods. The in-phase (bonding) hybrid plasmon is lower in energy and produces a large EM field enhancement in the particle gap known as a “hotspot”. The out-of-phase (anti-bonding) plasmon is excited at higher energies and the EM field strength is negligible between the

particle gap. This hybridisation model allows the plasmonic resonances of complex nanostructures to be explained in terms of the well-known plasmonic modes supported by the basic entities (rods, spheres etc) that form the overall structure[43]. In chapter 4 we follow this precedent by applying a hybridisation model to interpret the plasmonic modes of solid-inverse shuriken nanostructures.

2.2.7 Interference Phenomena

In this thesis, interference phenomena are of great significance in our plasmonic metamaterials, therefore, in this section we will discuss these phenomena in terms of atomic systems and then with respect to metamaterials. Firstly we will discuss interference phenomena with regards to electromagnetically induced transparency (EIT) which was originally observed in atomic systems of strontium vapour[45]. In simple terms, an electronic transition induced by an incident EM field is inhibited if the electron is driven by two sinusoidal forces of opposite phase[46]. This phenomenon results in the appearance of a spectrally narrow transmission band within an absorption band. Figure 2.09 displays the simplest and most common three level set up for EIT in an atomic system whereby there exists two dipole allowed transitions and one dipole forbidden transition. The system is irradiated by a probe beam and a couple beam with angular frequencies ω_p and ω_c respectively. In the absence of the couple beam, the system will give rise to a typical

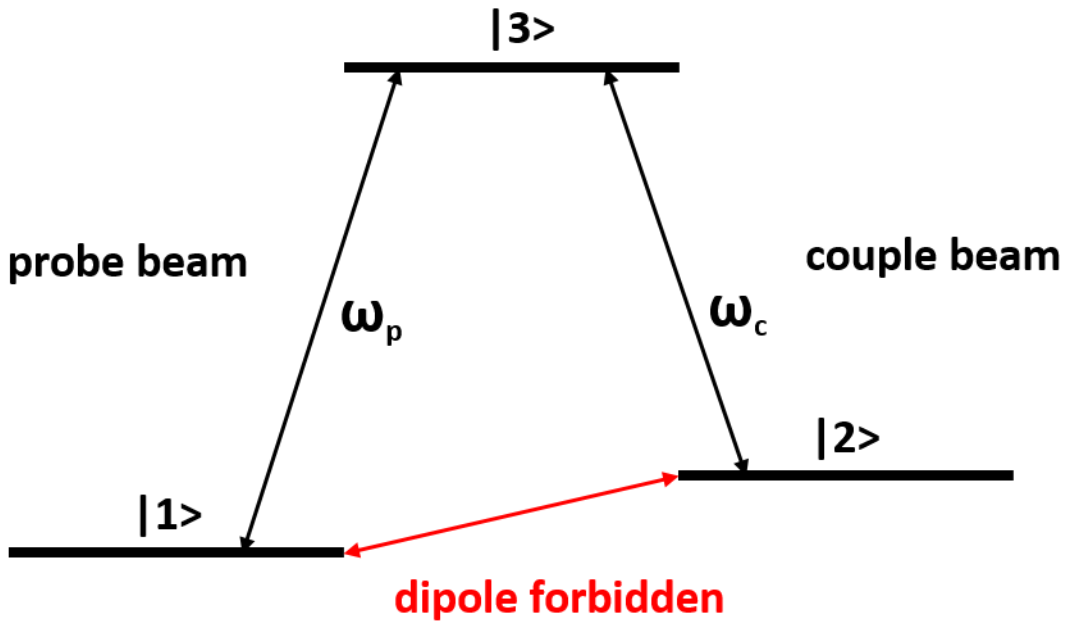

Figure 2.09: Schematic representation of energy levels of a three level atom. ω_p and ω_c are the frequency of the probe and pump beams respectively.

absorption profile around the probe beam frequency due to electronic transitions from |1> → |3>. However, if the system is also irradiated with the couple beam, a sharp transparency window arises within this resonance. Upon irradiation with this beam there are now two pathways by which an electron can move from the ground state to the excited state: the original |1> → |3> pathway or from |1> → |3> → |2> → |3>. Quantum mechanics dictates that when two excitation pathways exist, interference between their probability amplitudes will occur[46, 47]. One driving term is proportional to the probability amplitude of the ground state|1>. The other term is oppositely phased and proportional to the probability amplitude of state |2>. Hence, due to their opposite phase, these probability amplitudes cancel out over a narrow spectral region leaving the probability amplitude of an electron being excited into state 3 as zero.

A similar interference phenomenon is that of Fano resonances which as opposed to producing a conventional lorentzian resonance lineshape gives rise to a distinct asymmetric absorption/reflectance profile. The Fano lineshape is generated through the interference between two scattering amplitudes: scattering within a continuum of states (background process) and scattering due to excitation of a discrete state (resonant process)[48, 49]. The phenomenon of Fano resonances was originally discovered in quantum interference effects such as autoionization[50]. In order for interference between the discrete state and the continuum state to occur these states must have overlapping energies. For energies far from the resonant energy the background scattering process (continuum) dominates. As the system approaches the resonant energy, the background scattering amplitude varies slowly with energy whilst the resonant scattering amplitude displays significant changes in both phase and amplitude. At the resonant energy, this phase change results in destructive and constructive interference phenomena between the discrete and continuum states over an extremely narrow spectral range. This gives rise to a maximum and minimum absorption within this narrow range which generates a Fano lineshape [51].

In recent years, interference phenomena have become increasingly important in metamaterials[41, 48, 52, 53]. As opposed to interference between the quantum states of an atom, Fano/EIT effects in plasmonic systems arise due to interference between plasmonic modes. From figure 2.08 it is clear that only the bonding mode in the plasmonic nanorods may be excited by an incident EM wave and has an overall dipole moment hence

this is described as the “bright mode” or the continuum. Dipolar resonances in metal nanoparticles of a similar lengthscale to the incident EM radiation commonly display spectrally broad resonances due to extensive radiative damping[54]. In contrast, the anti-bonding plasmon oscillation has a net dipole moment of zero and cannot be excited by far field incident EM radiation thus it is dark and may be viewed as the discrete state[55]. Excitation of this mode may only occur through a near-field interaction between neighbouring nanostructures. For the case of symmetric rods this is achieved through asymmetric excitation using localised point like dipole sources[55] and focussed excitation beams[56].These dark modes generate spectrally narrow resonances due to an absence of radiative damping with the loss mechanism being almost exclusively due to losses in the metal[53].

Interference phenomena in nanostructured plasmonic systems is determined by the geometry of the constituent structures. When a broad optically bright plasmonic mode

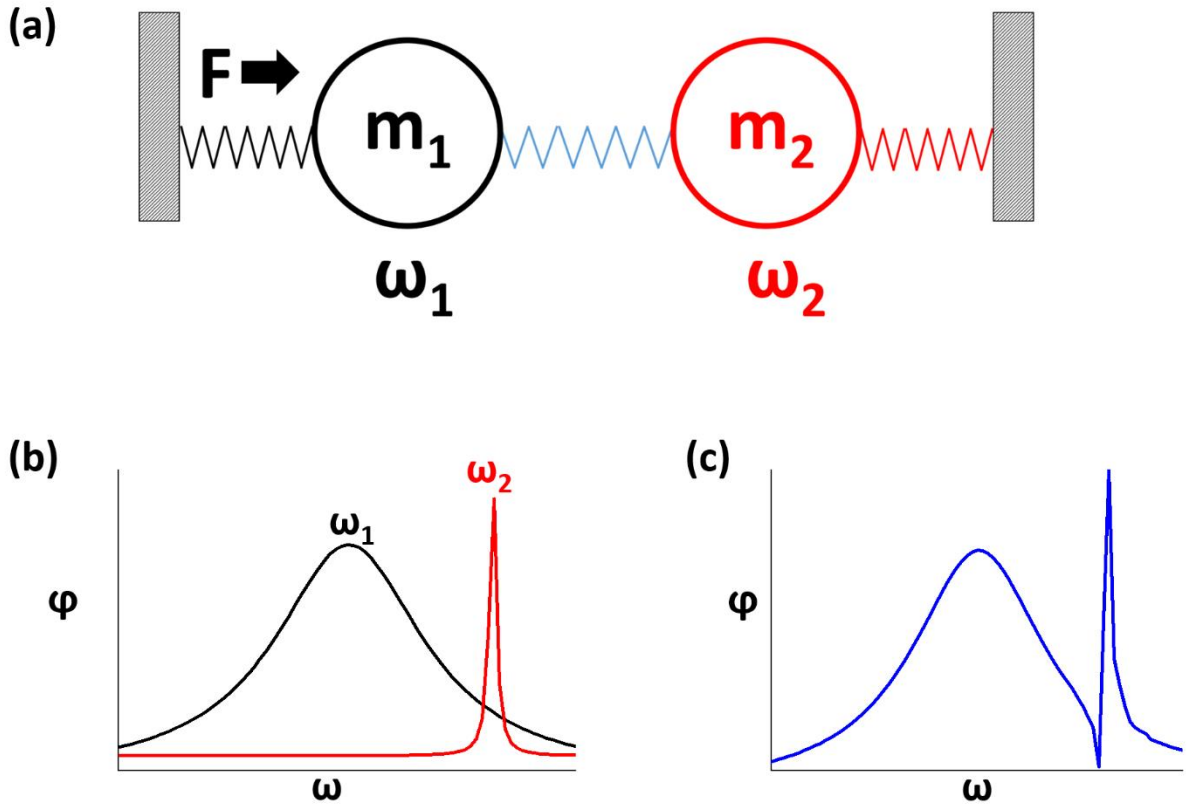

Figure 2.10: (a) Coupled oscillator model for the interference between an optically bright and dark mode. The mass m_1 is the optically bright mode and m_2 represents the dark mode. **(b)** Hypothetical representation of the resonance lineshape for an optically bright (ω_1) and optically dark (ω_2) mode. **(c)** Fano resonance lineshape generated by the interference of an optically bright and dark mode. ω is the frequency and φ is the amplitude of the resonance.

(continuum state) spectrally overlaps with a narrow dark mode (discrete state) they may interfere to generate an EIT-like effect or Fano resonance. The physical mechanism for the appearance of these effects in metamaterials is the same [57, 58] wherein EIT only arises when there is coherent coupling between bright and dark modes with similar resonant amplitudes whilst Fano resonances appear for systems that are weakly coupled[48].

The physical origin of Fano resonances and EIT in metamaterials can be understood through the very simple analogy of a system of coupled oscillators driven by a force applied to one of the oscillators[59] (figure 2.10a). An external force is applied to m_1 causing the mass to oscillate at a frequency of ω_1. This is analogous to the bright dipolar mode whereby the external force is an EM field which induces an in-phase dipole oscillation in the coupled nanorods. When the resonant frequency of m_1 and m_2 spectrally overlap, the oscillation of m_1 will induce a strong oscillation in m_2 at a frequency of ω_2 (figure 2.10b). This oscillation of m_2 corresponds to the dark mode of the nanorod as it is not induced by the applied external force but may only be excited by the movement of m_1 (the bright dipolar mode). Generation of EIT/Fano phenomena is highly dependent on the relative phase of the two coupled oscillators. For a single oscillator driven by an external field the phase difference of the oscillator (ψ) may be expressed as [59]:

$$\psi(\omega) = tan^{-1}\left(\frac{\omega\gamma}{\omega_0^2-\omega^2}\right) \qquad (28)$$

where ω is the frequency of the driving field, ω_0 is the resonant frequency and γ is the damping parameter. From equation 28 we see that the phase of the oscillation of m_1 changes by π when the frequency of the oscillator goes through ω_0. This means that at frequencies below ω_0 the oscillator and the external force are in-phase and at frequencies above ω_0 they are out-of-phase. Consequently, at the resonance frequency of the second oscillator (ω_2) there are effectively two driving forces acting on m_1. These driving forces will be out-of-phase and therefore interfere destructively generating the Fano lineshape (figure 2.10c) or suppression of absorption (EIT).

2.3 Second Harmonic Generation (SHG)

In chapter 6 of this thesis the nonlinear optical properties of a chiral plasmonic metamaterial are investigated through second harmonic generation. In order to understand the nonlinear behaviour of this system, the following sections provide a comprehensive

discussion of the nonlinear optical properties of chiral molecules and chiral metamaterials. We begin by introducing the nonlinear susceptibility tensor which allows the microscopic nonlinear polarisation in the medium to be related to the macroscopic SH response. It is important to first discuss this material property in terms of chiral molecules as this provides a basis for subsequent discussions of SHG from chiral nanostructured systems. An explanation as to the procedure for elucidating the magnitude of individual chiral/achiral tensor elements from chiral molecules is provided. We subsequently introduce a function to fit polarisation dependent SHG measurements of chiral molecules which allows the relative intensity of electric dipole/higher order SH contributions to be measured.

This method for the nonlinear study of chiral molecules is then adapted for SHG measurements from chiral metamaterials. Due to highly localised EM hotspots and a varying nonlinear susceptibility across the nanostructure surface, the procedure for the analysis of polarisation dependent SHG studies of molecular systems cannot be directly applied to nanostructures. Hence, two methods which are broadly similar to the analysis of molecular systems are proposed. These methods differ slightly from analysis of molecular systems in that as opposed to relating the microscopic nonlinear susceptibilities of the medium to the overall SH signal, they directly relate the polarisation state of the input and output beams. Both methods allow us to neglect the spatial inhomogeneity of the EM fields and nonlinear susceptibility across the sample surface and provide a simple means for interpreting the metamaterial SH response.

2.3.1. Nonlinear Susceptibility

As an electromagnetic wave propagates through a medium it exerts a force on the loosely bound valence electrons resulting in a polarisation of the medium. The dipole moment per unit volume (or polarisation) depends on the material properties and the electric field strength of the electromagnetic wave. In linear optics the induced polarisation (P) can be expressed as follows:

$$P(t) = \epsilon_0 \, \chi^{(1)} \, \tilde{E}(t) \tag{29}$$

Where ϵ_0 is the permittivity of free space, $\chi^{(1)}$ is the linear electric susceptibility and $\tilde{E}$ is the electric field strength. From equation 29 we see that the induced polarisation is linearly

proportional to the electric field strength. The induced polarisation is often expanded by expressing $P(t)$ as a power series to include higher order nonlinear terms:

$$P(t) = \epsilon_0\left[\chi^{(1)}\,\tilde{E}(t) + \chi^{(2)}\,\tilde{E}^2(t) + \chi^{(3)}\,\tilde{E}^3 \ldots\right] \qquad (30)$$

The $\chi^{(2)}$ and $\chi^{(3)}$ terms are labelled the second order and third order nonlinear susceptibilities respectively and require high amplitude fields generated by laser light in

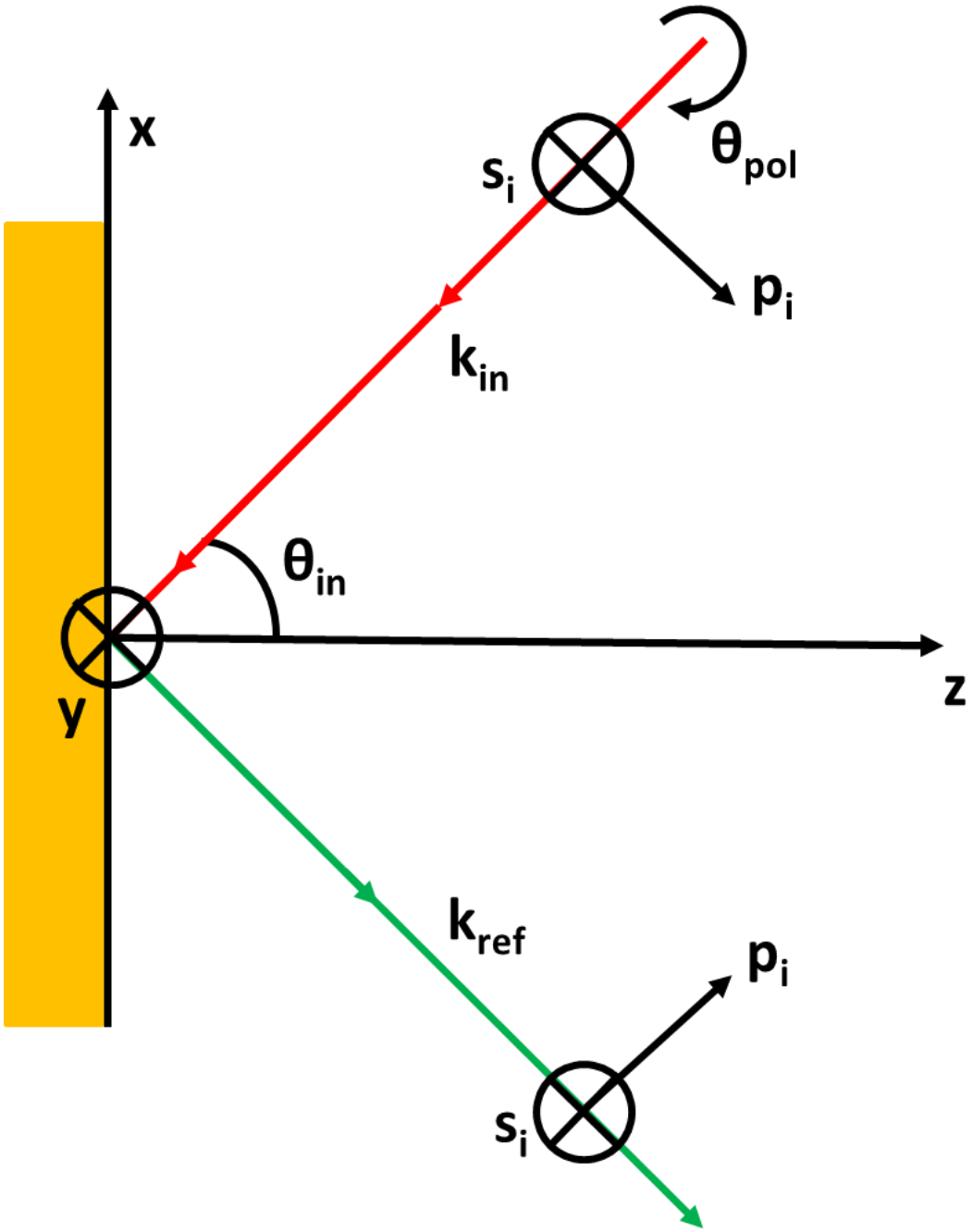

Figure 2.11: Experimental geometry employed in SHG measurements. k_{in} and k_{ref} are the incident and reflected wave vectors for the IR and SH beams respectively both of which are in the x-z plane. The angle of incidence is denoted θ_{in}. The electric field polarisation of the IR and SH beams are denoted using p_i (x-z plane polarisation) and s_i (polarised in y direction).

order to elicit a noticeable response. At present, the medium is assumed to be isotropic therefore the terms $P(t)$ and $\tilde{E}(t)$ are treated as scalar quantities. The aforementioned higher order terms are described as being "nonlinear" in the sense that the nonlinear response of a medium depends upon the intensity of the incident electromagnetic field in a nonlinear manner. Consequently, the intensity of second order nonlinear optical phenomena such as Second Harmonic Generation (SHG) increase quadratically with the intensity of the incident field.

Second harmonic generation described in terms of photons is the annihilation of two photons at the fundamental frequency into one photon with twice the frequency and half the wavelength. Franken et al [60] were the first to discover this phenomenon through focussing pulses of ruby laserlight (694.3 nm) onto a quartz crystal producing a small amount of ultraviolet light of wavelength 347.15 nm. The experimental geometry employed for SHG measurements in this thesis is illustrated in figure 2.11.

Firstly, we will discuss the nonlinear response in terms of the electric dipole approximation. In physics, this approximation considers only the oscillating dipoles induced by the electric field of an electromagnetic wave and neglects the much weaker magnetic and electric quadrupole effects. Therefore, within the electric dipole approximation the second harmonic response can be expressed using the nonlinear induced polarisation:

$$P_i(2\omega) = \epsilon_0 \chi^2 \tilde{E}^2(\omega) \qquad (31)$$

Where i is either p or s polarised light. The electric field strength of a laser may be written as:

$$\tilde{E}(t) = Ee^{-i\omega t} + c.c \qquad (32)$$

with c.c. being the complex conjugate. It is immediately apparent that substituting equation (32) for $\tilde{E}^2$ in equation (31) generates a component at twice the fundamental frequency since $\left(Ee^{-i\omega t}\right)^2$ is equivalent to $\left(Ee^{-2i\omega t}\right)$ hence frequency doubled radiation (SHG) is emitted.

The symmetry properties of the medium are also extremely important when considering SHG under the electric dipole approximation. If we change the sign of the applied electric

field $\tilde{E}(\omega)$ the sign of $P_i(2\omega)$ must also change if the medium is centrosymmetric hence the relation must be:

$$-P_i(2\omega) = \epsilon_0 \chi^2 [-\tilde{E}(\omega)]^2 \quad (33)$$

This generates:

$$-P_i(2\omega) = \epsilon_0 \chi^2 \tilde{E}^2 \quad (34)$$

For centrosymmetric media $-P_i$ must equal P_i which can only occur if:

$$-P_i = P_i = 0 \quad (35)$$

meaning χ^2=0 for centrosymmetric media. SHG is therefore forbidden in crystals possessing inversion symmetry. However, SH emission may be generated from the surface of centrosymmetric crystals as inversion symmetry is broken approaching the crystal surface which renders SHG a highly sensitive probe of surfaces and interfaces down to atomic layer thicknesses [61-63]. Due to this sensitivity to the symmetry of surfaces and media SHG is employed as a highly sensitive probe of chirality [64, 65].

Until this point, the present discussion has relied on the assumption of an isotropic media whereby the polarisation and electric field strength are spatially invariant therefore the material properties are uniform in all directions. However, a vast majority of materials possess optical properties that are orientationally dependent, in other words, they are birefringent. As a result, the induced polarisation depends not only on the strength of the applied electric field but also on the polarisation direction. This means that the linear and nonlinear electric susceptibilities are also anisotropic hence they cannot be represented by a single χ value. Anisotropic media possess distinct electric susceptibilities along their coordinate axes therefore the relationship between the incident field and the induced polarisation is treated using a tensor description for each component:

$$P(t) = \epsilon_0 \begin{bmatrix} \chi_x & 0 & 0 \\ 0 & \chi_y & 0 \\ 0 & 0 & \chi_z \end{bmatrix} \tilde{E}(t) \quad (36)$$

The above function represents the linear electric susceptibility tensor for an ideal system wherein the dipoles are perfectly aligned along the coordinate axes. More often dipoles are aligned between axes meaning an electromagnetic wave polarised along the X axis may also

induce a dipole along the Y or Z directions. Consequently, the linear electric susceptibility tensor is written more generally as:

$$\begin{bmatrix} \chi_{xx} & \chi_{xy} & \chi_{xz} \\ \chi_{yx} & \chi_{yy} & \chi_{yz} \\ \chi_{zx} & \chi_{zy} & \chi_{zz} \end{bmatrix} \quad (37)$$

The above matrix is the commonly known form of the linear susceptibility tensor and is a rank 2 tensor as it depends on the polarisation of the applied field and the induced polarisation in the medium.

In the case of higher order nonlinear susceptibility tensors, the matrix expansion becomes significantly more complicated. The second order nonlinear susceptibility is a third rank tensor with 27 components:

$$\begin{bmatrix} \chi_{xxx} & \chi_{xyy} & \chi_{xzz} & \chi_{xyz} & \chi_{xzy} & \chi_{xzx} & \chi_{xxz} & \chi_{xxy} & \chi_{xyx} \\ \chi_{yxx} & \chi_{yyy} & \chi_{yzz} & \chi_{yyz} & \chi_{yzy} & \chi_{yzx} & \chi_{yxz} & \chi_{yxy} & \chi_{yyx} \\ \chi_{zxx} & \chi_{zyy} & \chi_{zzz} & \chi_{zyz} & \chi_{zzy} & \chi_{zzx} & \chi_{zxz} & \chi_{zxy} & \chi_{zyx} \end{bmatrix} \quad (38)$$

The last two subscript terms denote the polarisation of the incident beam and the first term is the induced polarisation of the nonlinear source. In SHG under the electric dipole approximation, the number of components may be reduced to 18 since only a single incident beam is used therefore in some cases the last two terms are equivalent (e.g. χ_{xxz}=χ_{xzx}) :

$$\begin{bmatrix} \chi_{xxx} & \chi_{xyy} & \chi_{xzz} & \chi_{xyz} & \chi_{xxz} & \chi_{xxy} \\ \chi_{yxx} & \chi_{yyy} & \chi_{yzz} & \chi_{yyz} & \chi_{yxz} & \chi_{yxy} \\ \chi_{zxx} & \chi_{zyy} & \chi_{zzz} & \chi_{zyz} & \chi_{zxz} & \chi_{zxy} \end{bmatrix} \quad (39)$$

The number of tensor components can be further simplified depending on the symmetry of the crystal surface [66]. In the case of an in-plane isotropic chiral sample (C_∞ symmetry or C_n symmetry) χ^2 can be reduced to [67, 68]:

$$\begin{bmatrix} 0 & 0 & 0 & \chi_{xyz} & \chi_{xxz} & 0 \\ 0 & 0 & 0 & \chi_{yyz} & -\chi_{yxz} & 0 \\ \chi_{zxx} & \chi_{zyy} & \chi_{zzz} & 0 & 0 & 0 \end{bmatrix} \quad (40)$$

where χ_{xzz}=χ_{yzz}, χ_{xxz}=χ_{yyz} and χ_{xyz}= $-\chi_{yxz}$. Individual electric susceptibility tensor elements may be measured experimentally by applying the appropriate polarisation combinations of the fundamental and SH beam. Referring to figure 2.11 we find that in p-

polarised light the electric field is polarised horizontally (i.e. in the xz plane) therefore only elements associated with this incident beam polarisation will be non-vanishing:

$$\begin{bmatrix} 0 & 0 & 0 & 0 & \chi_{xxz} & 0 \\ 0 & 0 & 0 & 0 & -\chi_{yxz} & 0 \\ \chi_{zxx} & 0 & \chi_{zzz} & 0 & 0 & 0 \end{bmatrix} \quad (41)$$

Similarly, for S-polarised incident light, the only non-vanishing tensor elements are associated with the electric field polarised in the y direction:

$$\begin{bmatrix} 0 & 0 & 0 & 0 & 0 & 0 \\ 0 & 0 & 0 & 0 & 0 & 0 \\ 0 & \chi_{zyy} & 0 & 0 & 0 & 0 \end{bmatrix} \quad (42)$$

It is important to note that the second order nonlinear electric susceptibility tensor (equation 39) may possess several chiral terms. Under the electric dipole approximation these chiral tensor elements are components containing three different terms i.e. χ_{yxz} which are non-zero for chiral media. Measurement of the opposite enantiomer should result in a change in sign of this chiral tensor element ($-\chi_{yxz}$). Hence, selection of the appropriate input and output polarisations allows the chiral contributions to the SH signal to be probed.

The study of a wide range of surfaces has highlighted the need to consider the nonlinear response beyond the electric dipole approximation[69, 70]. In the majority of SH studies it is common practice to group these terms under the generic label of "magnetic terms" (χ^{mee}, χ^{eem}) as due to symmetry restrictions it is extremely challenging to experimentally separate the microscopic magnetic dipole and electric quadrupole contributions[71-73]. Unlike electric dipole SH emission, magnetic contributions to SHG are not forbidden in centrosymmetric media therefore such nonlinear sources may arise from the surface and bulk[74]. A tensor analysis of these magnetic susceptibilities may be conducted in a similar fashion as was done for the purely electric dipole susceptibility in order to relate the microscopic SHG elements to the overall macroscopic response. Unlike tensor elements associated with the electric dipole, none of the "magnetic" tensors are equivalent therefore the original 27 element tensor (equation 38) must be employed. However, the symmetry of the surface does result in several vanishing terms. For an in-plane isotropic C_4 surface the χ^{eem} components are:

$$\begin{bmatrix} 0 & 0 & 0 & \chi_{xyz} & \chi_{xzy} & \chi_{xzx} & \chi_{xxz} & 0 & 0 \\ 0 & 0 & 0 & \chi_{yyz} & \chi_{yzy} & -\chi_{yzx} & -\chi_{yxz} & 0 & 0 \\ \chi_{zxx} & \chi_{zyy} & \chi_{zzz} & 0 & 0 & 0 & 0 & \chi_{zxy} & -\chi_{zyx} \end{bmatrix} \quad (43)$$

As with the electric dipole tensor setting the appropriate incident and SH beam polarisation conditions allows particular tensor elements to be probed. For magnetic tensors, when the electric field is polarised in the x and z directions the magnetic component will be polarised in the y direction. For p-polarised incident radiation (with respect to the electric field) the nonvanishing elements are:

$$\begin{bmatrix} 0 & 0 & 0 & 0 & \chi_{xzy} & 0 & 0 & 0 & 0 \\ 0 & 0 & 0 & 0 & \chi_{yzy} & 0 & 0 & 0 & 0 \\ 0 & 0 & 0 & 0 & 0 & 0 & 0 & \chi_{zxy} & 0 \end{bmatrix} \quad (44)$$

Likewise, for s-polarised incident radiation:

$$\begin{bmatrix} 0 & 0 & 0 & \chi_{xyz} & 0 & 0 & 0 & 0 & 0 \\ 0 & 0 & 0 & \chi_{yyz} & 0 & 0 & 0 & 0 & 0 \\ 0 & 0 & 0 & 0 & 0 & 0 & 0 & 0 & -\chi_{zyx} \end{bmatrix} \quad (45)$$

This analysis is repeated for the second magnetic tensor χ^{mee}:

$$\begin{bmatrix} 0 & 0 & 0 & \chi_{xyz} & \chi_{xzy} & \chi_{xzx} & \chi_{xxz} & 0 & 0 \\ 0 & 0 & 0 & \chi_{yyz} & \chi_{yzy} & -\chi_{yzx} & -\chi_{yxz} & 0 & 0 \\ \chi_{zxx} & \chi_{zyy} & \chi_{zzz} & 0 & 0 & 0 & 0 & 0 & 0 \end{bmatrix} \quad (46)$$

For p-polarised light this tensor is reduced to:

$$\begin{bmatrix} 0 & 0 & 0 & 0 & \chi_{xzy} & 0 & 0 & 0 & 0 \\ 0 & 0 & 0 & 0 & \chi_{yzy} & 0 & 0 & 0 & 0 \\ 0 & 0 & 0 & 0 & 0 & 0 & 0 & 0 & 0 \end{bmatrix} \quad (47)$$

And for s-polarised light:

$$\begin{bmatrix} 0 & 0 & 0 & \chi_{xyz} & 0 & 0 & 0 & 0 & 0 \\ 0 & 0 & 0 & \chi_{yyz} & 0 & 0 & 0 & 0 & 0 \\ 0 & 0 & 0 & 0 & 0 & 0 & 0 & 0 & 0 \end{bmatrix} \quad (48)$$

Magnetic tensor elements are also associated with chirality whereby elements containing two or more identical terms are defined as chiral i.e. xxx, xxz, yyz etc. We can see that both magnetic susceptibility tensors contain chiral terms therefore these contributions to the chiral SH signal must be taken into account. Similar to the electric susceptibility tensor

analysis, selection of the appropriate polarisation states allows for individual magnetic tensor elements to be probed.

Performing a detailed examination of nonlinear behaviour allows the microscopic origins of SHG (the magnitude of individual tensor elements) from molecular systems to be related to the overall macroscopic SHG signal. Evidently, the symmetry properties of the nonlinear medium and the incident beam electric field are vitally important for the study of SHG from both achiral and chiral molecular systems. Furthermore, studies of molecular SHG highlight the significance of SHG sources beyond the electric dipole approximation. Hence, these factors must be carefully considered in later studies of SHG from chiral metamaterials.

2.3.2. Polarisation Dependent SHG from Molecular Systems

Polarisation dependent SHG is a method that is commonly used to quantify the relative intensities of electric dipole/higher order chiral and achiral SHG contributions in a molecular system. This technique involves varying the incident beam polarisation about 360° and measuring the intensity of the vertically or horizontally polarised SH beam [72, 75-77]. The intensity of SH radiation generated from a surface may be expressed as:

$$I(2\omega) = \left|fE_p(\omega)E_p(\omega) + gE_s(\omega)E_s(\omega) + hE_p(\omega)E_s(\omega)\right|^2 \qquad (49)$$

Where E_p and E_s are the p and s-polarised components of the incident field respectively. The f, g and h coefficients correspond to linear combinations of the electric (χ^{eee}) and magnetic (χ^{mee}, χ^{eem}) second order susceptibility tensors discussed in section 2.3.1 The nature of the f, g, and h coefficients depend on the symmetry of the surface (table 1). Since p-polarised waves can be represented by $E_p = E\cos\theta$ and s-polarised waves by $E_s = E\sin\theta$ where E is the intensity of the electric field and θ is the angle of the E-field vector with respect to the scattering plane(θ_{pol} in figure 2.11), equation 49 can be written as:

$$I(2\omega) = |f_i E\cos\theta(\omega)\, E\cos\theta(\omega) + g_i E\sin\theta(\omega)\, E\sin\theta(\omega) + h_i E\cos\theta(\omega)\, E\sin\theta\,(\omega)|^2 \qquad (50)$$

This is rewritten as:

$$I(2\omega) = E^4(\omega)|f_i\cos^2\theta + g_i\sin^2\theta + h_i\cos\theta\sin\theta|^2 \qquad (51)$$

Expanding this function gives:

$$I(2\omega) = E^4(\omega)\Big|\big|f_i^2\big|\cos^4\theta + f_i g_i \cos^2\theta \sin^2\theta + f_i h_i \cos^3\theta \sin\theta + g_i f_i \sin^2\theta \cos^2\theta + \big|g_i^2\big|\sin^4\theta + g_i h_i \cos\theta \sin^3\theta + h_i f_i \cos^3\theta \sin\theta + h_i g_i \cos\theta \sin^3\theta + \big|h_i^2\big|\cos^2\theta \sin^2\theta\Big| \quad (52)$$

Combining like terms yields:

$$I(2\omega) = E^4(\omega)\Big|\big|f_i^2\big|\cos^4\theta + \big|g_i^2\big|\sin^4\theta + (f_i h_i + h_i f_i)\cos^3\theta\, sin\theta + (g_i h_i + h_i g_i)\cos\theta\, sin^3\theta + (f_i g_i + g_i f_i + \big|h_i^2\big|)\cos^2\theta \sin^2\theta\Big| \quad (53)$$

We simplify equation 53 by defining real coefficients as:

$$\alpha_i = E^4(\omega)\big|f_i^2\big|$$

$$\beta_i = E^4(\omega)(f_i g_i + g_i f_i + \big|h_i^2\big|)$$

$$\gamma_i = E^4(\omega)\big|g_i^2\big|$$

$$\delta_i = E^4(\omega)(f_i h_i + h_i f_i)$$

$$\varepsilon_i = E^4(\omega)(g_i h_i + h_i g_i)$$

Therefore, we write equation 53 as:

$$I_i(2\omega) = \alpha_i cos^4\theta + \beta_i sin^2 cos^2\theta + \gamma_i sin^4\theta + \delta_i sin\theta cos^3\theta + \varepsilon_i sin^3\theta cos\theta \quad (54)$$

In the case of a chiral fourfold symmetric surface, the nonvanishing electric dipole and magnetic tensor elements are found in tensors 40, 43 and 46 respectively. A theoretical derivation of the SH response from a chiral surface by Maki et al [72] identified which of these tensor elements are associated with f_i, g_i and h_i (table 2.01).

Recall from section 2.3.1. that chiral electric tensor elements must have three different terms whilst chiral magnetic terms must possess at least two terms that are the same. Looking at the elements present in each f, g and h coefficient we find that only f_s, g_s and h_p contain chirally sensitive tensor elements. Thus, in s–polarised light all five coefficients of equation 58 are chirally sensitive whilst for p-polarised light only β, δ, and ε display sensitivity to chirality.

	Independent non-vanishing tensor elements	
	Isotropic and achiral	**Isotropic and chiral**
f_s		$\chi_{xyz,}^{eee}\ \chi_{xzx}^{eem},\ \chi_{xzx}^{mee},$ $-\chi_{zxx}^{mee},-\chi_{zzz}^{mee}$
g_s	-	$\chi_{xxz}^{eem},\chi_{zxx}^{mee}$
h_s	$\chi_{xxz}^{eee},-\chi_{xzy}^{eem},-\chi_{xyz}^{eem},\ \chi_{xyz}^{mee}$	-
f_p	$\chi_{xxz}^{eee},\ \chi_{zxx}^{eee},\chi_{zzz}^{eee},\ \chi_{xyz}^{mee}$ $\chi_{xzy}^{eem},-\chi_{zxy}^{eem}$	-
g_p	$\chi_{zxx}^{eee},\ \chi_{xyz}^{eem},-\chi_{zxy}^{eem}$	-
h_p	-	$\chi_{xyz}^{eee},\ \chi_{xxz}^{eem},\chi_{xzx}^{eem},\chi_{zxx}^{eem},$ $-\chi_{zzz}^{eem},\ \chi_{xxz}^{mee}$

Table 2.01: Second order susceptibility tensors associated with f_i, g_i and h_i for a chiral and achiral isotropic surface where the surface is in the x-y plane.

2.3.3. SHG from Nanostructures

The technique of polarisation dependent SHG to ascertain the electric dipole/higher order origins of chirality in chiral molecular systems is relevant as this method may be adapted for similar studies of chiral metamaterials. Hence, in this thesis we perform a modified version of polarisation dependent SHG for chiral plasmonic nanostructures to probe the electric dipole/higher order origins of the nanostructure nonlinear chiroptical response.

Analysis of the SHG properties of molecular systems in section 2.3.1. and 2.3.2. assumes a uniform local nonlinearity (χ^2) and electric field distribution across the surface. This assumption is valid as the size of molecules is significantly smaller than the wavelength of the incident or SH radiation. A uniform local nonlinearity means the microscopic nonlinear polarisation induced in the molecule can be directly related to the macroscopic SH signal. However, as the size of the nonlinear system approaches a similar lengthscale to that of the incident wavelength this assumption begins to break down. This is due to the generation of highly localised EM hotspots around metallic nanostructures which results in a large spatial variation of χ^2 on a lengthscale similar to that of the incident wavelength.

In order to overcome this difficulty, the molecular approach is modified to produce a more general interpretation of SHG from arrays of nanostructures. Currently, there are two reported methods for the analysis of polarisation dependent SHG measurements from which a fitting function of the same form can be derived. However, the inherent difference in these two methods is the interpretation of the coefficients in the function. Both of these methods are broadly similar to a molecular SHG tensor analysis wherein the macroscopic electric dipole/higher order nature of the nanostructure SH signal is probed. However, the nonlinear susceptibility χ^2 is integrated over the entire structure due to the spatial inhomogeneity of this material property in such nanostructured systems. This means we cannot relate the individual χ^{eee}, χ^{mee}, χ^{eem} terms to the macroscopic SH response as is done for molecular entities. Alternatively, we analyse the polarisation properties of the fundamental and SH radiation which provides an insight into the electric dipole/multipole character of the SH signal. This approach is favourable as it provides a convenient way to describe the nonlinear optical response of nanostructures without having to be concerned with the nanoscale inhomogeneities in the nonlinear susceptibility and EM field distribution.

We will now look at these two related methods that have been proposed to deduce the nature of SH radiation from nanostructures. Firstly, Kauranen et al [78] introduced the macroscopic nonlinear response tensor (NRT) whereby the input and output fields are expressed as:

$$E_i(2\omega) = \sum_{jk} A_{ijk} E_j(\omega)\, E_k(\omega) \tag{55}$$

This function bears a resemblance to equation 35 which relates the polarisation of the nonlinear source to the incident field. However, the important differences are that the term on the left hand side of equation 55 describes the measureable SH field as opposed to the source polarisation (P_i). Moreover, the nonlinear susceptibility χ^2 is replaced by the NRT (A) which accounts for all dipolar and multipolar nonlinear contributions. The subscript i corresponds to the polarisation of the measured SH signal whilst j and k are the polarisation of the incident beam. If we assume that the fundamental field has two transverse plane wave components, then using the coordinate system in figure 2.11 we can express the SH field as:

$$E_i(2\omega) = A_{ixx}E_x^2(\omega) + A_{iyy}E_y^2(\omega) + A_{ixy}E_x(\omega)E_y(\omega) \quad (56)$$

Where $i = x, y$. Similar to section 2.3.2 p-polarised waves can be represented as $E_x = E\cos\theta$ and s-polarised waves as $E_y = E\sin\theta$ where E is the electric field intensity and θ is the angle between the incident wave and the scattering plane. Hence, if we write equation 56 in terms of the intensity of the detected SH signal we get:

$$I(2\omega) = \left|A_{ixx}E\cos\theta(\omega)\,E\cos\theta(\omega) + A_{iyy}E\sin\theta(\omega)\,E\sin\theta(\omega) + A_{ixy}E\cos\theta(\omega)\,E\sin\theta\,(\omega)\right|^2 \quad (57)$$

Equation 57 may be rewritten as:

$$I(2\omega) = E^4(\omega)\left|A_{ixx}\cos^2\theta + A_{iyy}\sin^2\theta + A_{ixy}\cos\theta\sin\theta\right|^2 \quad (58)$$

Similar to the molecular tensor analysis we expand this expression which gives:

$$\begin{aligned} I(2\omega) = E^4(\omega)\Big|&\left|A_{ixx}^2\right|\cos^4\theta + A_{ixx}A_{iyy}\cos^2\theta\sin^2\theta + A_{ixx}A_{ixy}\cos^3\theta\sin\theta + \\ &A_{iyy}A_{ixx}\sin^2\theta\cos^2\theta + \left|A_{iyy}^2\right|\sin^4\theta + A_{iyy}A_{ixy}\cos\theta\sin^3\theta + \\ &A_{ixy}A_{ixx}\cos^3\theta\sin\theta + A_{ixy}A_{iyy}\cos\theta\sin^3\theta + \left|A_{ixy}^2\right|\cos^2\theta\sin^2\theta\Big| \end{aligned} \quad (59)$$

If we combine like terms the final expression obtained is:

$$\begin{aligned} I(2\omega) = E^4(\omega)\Big|&\left|A_{ixx}^2\right|\cos^4\theta + (A_{ixx}A_{iyy} + A_{iyy}A_{ixx} + \left|A_{ixy}^2\right|)\cos^2\theta\sin^2\theta \\ &+ \left|A_{iyy}^2\right|\sin^4\theta + (A_{ixx}A_{ixy} + A_{ixy}A_{ixx})\cos^3\theta\,sin\theta + (A_{iyy}A_{ixy} \\ &+ A_{ixy}A_{iyy})\cos\theta\,sin^3\theta\Big| \end{aligned} \quad (60)$$

Evidently, the form of the final expression to which the measured SHG signal is fitted has the same form as that used for molecular systems. It is important to understand the inherent differences between these two functions. For molecular systems, the coefficients f, g and h correspond to different combinations of the χ^{eee}, χ^{mee}, χ^{eem} tensor elements (table 1). However, the NRT (A) directly describes the polarisation properties of the incident and SH light. This means that through manipulation of the polarisation of the input and output radiation it is possible to probe particular coefficients of the NRT. The dipolar NRT terms will be of the form $i = j = k$ (i.e. A_{xxx}) whereas the higher order contributions are included in the other terms (i.e. A_{xyy}). The main drawback of this approach is that whilst the electric

dipole SH sources can be identified, the higher order terms are all grouped together hence electric quadrupole and magnetic terms cannot be distinguished.

The second reported method for the interpretation of polarisation dependent SHG from nanostructures does not involve the use of tensors to quantify the dipolar/higher order contributions. Alternatively, the far-field polarisation dependent SH emission pattern may be used to infer the dipolar/multipolar character of the SH response[79]. Thus, an alternative, phenomenological approach involves the direct analysis of the shape of the polarisation dependent SH profile. This analysis is broadly similar to the NRT approach whereby both methods involve fitting the SH profile to an equation of the same form. However, as will be discussed, the inherent difference between these two methods is the interpretation of the coefficients in this function.

Inferring the SHG nature through analysis of the shape of the far-field radiation pattern was first developed by Dadap et al[80, 81] through a theoretical assessment of SHG from perfectly spherical nanoparticles much smaller than the incident wavelength. The authors calculate the contributions to the SH signal in terms of the fundamental field interactions where E1 is an electric dipole and E2 is an electric quadrupole. The leading order contribution is the purely local electric dipole emission E1+E1→E1. In this notation the left hand terms denote the nature of the excitation and the right hand term is the electric dipole SH response. However, this purely local electric dipole excitation is forbidden in centrosymmetric media. This can be understood intuitively by considering the spherical symmetry of the nanoparticle. The incident beam induces mutually cancelling polarisations at opposite sides of the centrosymmetric particle hence electric dipole emission is not observed. The next leading order contributions were found to be E1+E2→E1 and E1+E1→E2, which relate to a nonlocal excitation of an electric dipole and the local excitation of an electric quadrupole respectively. It is possible to separate these odd and even multipolar contributions to the SH response by collecting the SH signal at 90^{o} to the incident beam and selecting the appropriate polarisation of the SH radiation[80]. For vertically polarised SH light only the E1+E1→E2 excitation is possible whereas only the E1+E2→E1 signal is measured for horizontally polarised SHG. Simulations of the nanoparticle polarisation dependent SH response at 90^{o} were in complete agreement with the theoretical model. A four lobed profile was obtained for vertically polarised SHG which agrees with the predicted

local electric quadrupole nonlinear response (E1+E1→E2 excitation) whereas a two lobed profile was produced for horizontally polarised SHG which is commensurate with the expected nonlocal dipolar SH signal (E1+E2→E1). Thus, the shape of the SH profile can be used to provide a broad insight into the nature of the SH response.

The understanding of this framework was theoretically and experimentally expanded through second harmonic Rayleigh scattering (SHRS) measurements of vertically polarised SHG from Au and Ag nanoparticles. Initial experimental polarisation dependent measurements of the vertically polarised SH signal produced a predominantly dipolar SH profile which was in complete disagreement with the theoretically predicted four lobed SH response[82]. The origin of this dipolar profile was due to the imperfect spherical shape of the nanoparticles. This imperfection means the SH generated from local electric dipole excitations at the surface (E1+E1→E1) do not cancel out in the far field. In order to understand the effect of deformations on the nature of the SH response Brevet et al modelled the vertically polarised SHG of nanoparticles with varying degrees of ellipsoidal structure [82-84]. Figure 2.12 provides a generalised view of the effect of this geometric distortion on the polarisation dependent SH profiles. As the nanoparticle shape is deformed, it is no longer centrosymmetric therefore electric dipole SH emission occurs. Hence, the shape of the SH profile transforms from a four lobed profile to a gradually more dipolar form. The extent of the dipolar/quadrupolar SHG was parameterized by fitting SH profiles to the classical polarisation dependence relationship for an oscillating dipole:

$$I_i(2\omega) = \alpha_i cos^4\theta + \beta_i sin^2 cos^2\theta + \gamma_i sin^4\theta \qquad (61)$$

where θ is the input polarisation angle relative to the vertically or horizontally polarised SH beam and α, β, γ, are real coefficients. The magnitude of these coefficients relates the different electric dipole, electric quadrupole and magnetic dipole contributions to the macroscopic SHG signal. For perfectly spherical nanoparticles, the β term was found to dominate hence this coefficient relates to the magnitude of the electric quadrupole SH contribution. As the nanoparticle was rendered less centrosymmetric, the electric dipole contribution increased and α becomes more prominent therefore this term accounts for electric dipole SHG. As γ relates to components at 90^o to α it is assumed that this coefficient accounts for magnetic dipole SH sources. However, as the diameter of nanoparticles

approaches a similar lengthscale to the fundamental wavelength, SH profiles can no longer be fitted to equation 61 and two additional parameters are introduced to give equation 62:

$$I_i(2\omega) = \alpha_i cos^4\theta + \beta_i sin^2 cos^2\theta + \gamma_i sin^4\theta + \delta_i sin\theta cos^3\theta + \varepsilon_i sin^3\theta cos\theta \quad (62)$$

These additional δ and ε terms account for higher order SH contributions that arise due to the presence of localised EM hotspots on the nanoparticle surface. Equation 62 was also shown to be applicable to nanostructure arrays by Capretti et al [85] through measurements of the nonlinear response of resonantly excited arrays of planar nanocylinders with dimensions similar to that of the incident beam.

Evidently, equation 62 is of the same form as equation 60 and both provide a general macroscopic description of the SH signal in terms of the input and output beams. However, it is important to again emphasize the differences between the coefficients in each case. The NRT method established by Kauranen et al[78] approaches the problem of nanostructure SHG through a broad tensor analysis of the input and output beams. Each coefficient relates to a particular fundamental/SH polarisation combination allowing the

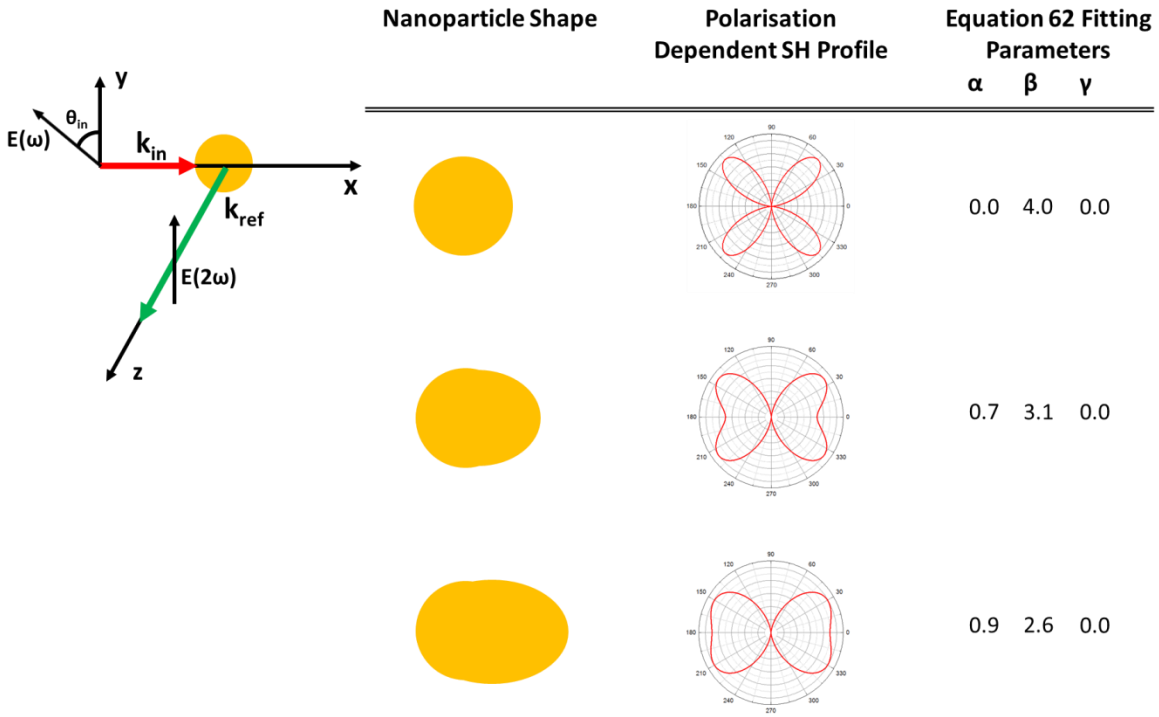

Figure 2.12: Qualitative representation of the effect on the shape of the polarisation dependent profile for vertically polarised SHG and corresponding equation 62 fitting parameters as a spherical nanoparticle (radius~5nm) is rendered less centrosymmetric. The form of the SH profiles and fitting parameters were chosen to reflect the general trend of the results reported in reference [82-84]. Zero degrees corresponds to vertically polarised incident light.

electric dipole/higher order SH contributions to be realised. The phenomenological approach developed from the SHG of nanoparticles represents a simpler method to generate a macroscopic overview of the SH response. This scheme assigns the electric dipole/higher order nature of the coefficients primarily through an intuitive analysis of the shape of the polarisation dependent SH profile. Hence, due to the simplicity and intuitive nature of this phenomenological approach experimental data in this thesis is fitted to equation 62.

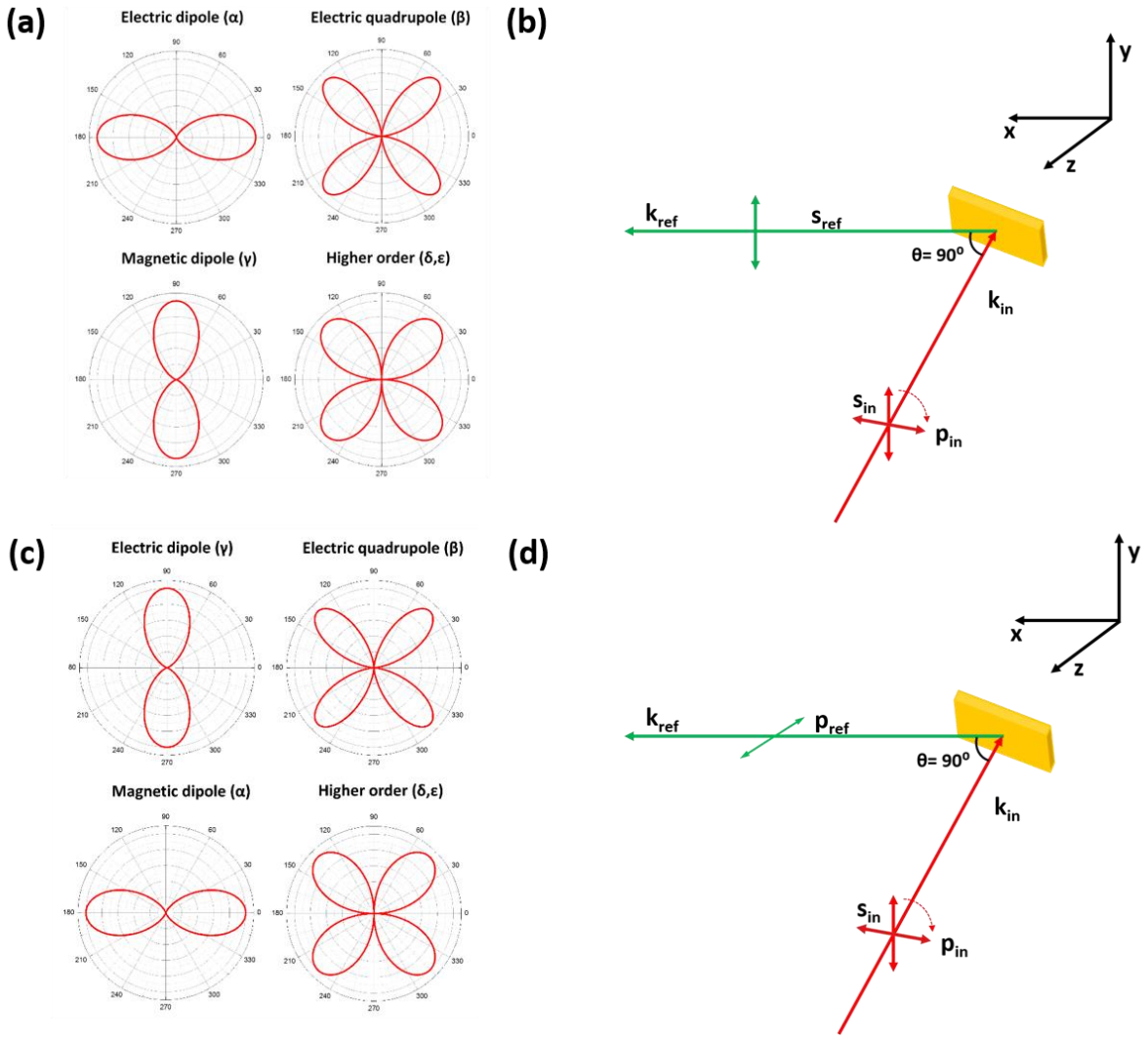

Figure 2.13: Graphical representation of electric dipole, electric quadrupole, magnetic dipole and higher order terms of equation 62 for **(a)** s-polarised and **(c)** p-polarised SH radiation. Zero degrees correspond to s-polarised incident light. **(b)** and **(d)** display experimental geometry and polarisation states for s-polarised and p-polarised SHG respectively. k_{in} and k_{ref} are the incident and reflected wave vectors for the IR and SH beams respectively both of which are in the x-z plane.

In the majority of our SHG experiments the s-polarised SH signal is measured, 0^o in the polar plots corresponds to s-polarised incident light therefore from figure 2.13 we conclude that α is the electric dipole contribution since the SH field and incident field are polarised in the same plane. The four lobed nature of the β term indicates this is the electric quadrupole contribution. The component at 90^o to the SH electric field polarisation is attributed to magnetic dipole contributions therefore the γ term accounts for this element. It is important to note that if the polarisation of the SH signal is p-polarised then α would be the magnetic dipole and γ the electric dipole. Finally, since the nanostructures employed in this study are of a similar lengthscale to the incident beam, higher order contributions are accounted for by the δ and ε terms. Through application of this function, the relative strength of the electric dipole, electric quadrupole, magnetic dipole and higher order contributions to the gammadion SH response are quantified.

2.4 References

1. Barron, L.D., *Molecular Light Scattering and Optical Activity*. 2nd ed. 2004, Cambridge U.K.: Cambirdge University Press.
2. Mason, S.F., *Molecular Optical Activity and the Chiral Discriminations*. 1982, Cambridge U.K.: Cambridge University Press.
3. B. Kahr, O.A., *Arago's Best Paper.* ChemPhysChem, 2012. **13**: p. 79-88.
4. R. S. Cahn, C.I., V. Prelog, *Specification of Molecular Chirality.* Angewandte Chemie International Edition, 1966. **5**(4): p. 385-415.
5. I. Hargittai , M.H., *Symmetry through the Eyes of a Chemist* 1995, New York and London: Plenum Press
6. S. M. Kelly, N.C.P., *The application of circular dichroism to studies of protein folding and unfolding.* Biochimica et Biophysica Acta, 1997. **1338**: p. 161-185.
7. J. S. Choi, M.C., *Limitations of a superchiral field.* Physical Review A, 2012. **86**: p. 063834.
8. Penzkofer, A., *Optical rotatory dispersion measurement of D-glucose with fixed polarizer analyzer accessory in conventional spectrophotometer.* Journal of Analytical Sciences, Methods and Instrumentation, 2013. **3**: p. 234-239.
9. Hicks, J.M., *The Physical Chemistry of Chirality*. 2002, Washington: American Chemical Society.
10. Condon, E.U., *Theories of Optical Rotatory Power.* Reviews of Modern Physics, 1937. **9**: p. 432-457.
11. Kirkwood, J.G., *On the Theory of Optical Rotatory Power.* The Journal of Chemical Physics, 1937. **5**: p. 479-491.
12. Lipkin, D.M., *Existence of a new conservation law in electromagnetic theory.* Journal of Mathematical Physics, 1964. **5**(5): p. 696-700.
13. Kibble, T.W.B., *Conservation laws for free fields.* Journal of Mathematical Physics, 1965. **6**: p. 1022-1026.
14. M. Przanowski, B.R., J.Tosiek, *On some conservation laws in the maxwell electrodynamics in vacuum.* Acta Physica Polonica B, 1994. **25**(7): p. 1065-1077.
15. Y. Tang, A.E.C., *Optical chirality and its interaction with matter.* Physical Review Letters, 2010. **104**: p. 163901.

16. M. Schaeferling, D.D., M. Hentschel, H. Giessen, *Tailoring enhanced optical chirality: Design principles for chiral plasmonic nanostructures.* Physical Review X, 2012. **2**: p. 031010.
17. N. Meinzer, E.H., W. L. Barnes, *Probing the chiral nature of electromagnetic fields surrounding plasmonic nanostructures.* Physical Review B, 2013. **88**: p. 041407.
18. E. Hendry, R.V.M., L. D. Barron, M. Kadodwala, T. J. Davis, *Chiral electromagnetic fields generated by arrays of nanoslits.* Nano Letters, 2012. **12**: p. 3640-3644.
19. E. Hendry, T.C., J. Johnston, M. Popland, R. V. Mikhaylovskiy, A.J. Lapthorn, S.M. Kelly, L. D. Barron, N. Gadegaard, M. Kadodwala, *Ultrasensitive detection and characterization of biomolecules using superchiral field.* Nature Nanotechnology, 2010. **5**: p. 783-787.
20. G. Grosso, G.P.P., *Solid State Physics*. 2014, Oxford: Elsevier Science.
21. S. Enoch, N.B., *Plasmonics: From Basics to Advanced Topics*. Vol. 167. 2012, Berlin: Springer.
22. Egerton, R.F., *Electron energy-loss spectroscopy in the TEM.* Reports on progress in Physics, 2009. **72**: p. 016502.
23. P. G. Etchegoin, E.C.L.R., M. Meyer, *An analytic model for the optical properties of gold.* The Journal of Chemical Physics, 2006. **125**: p. 164705.
24. J.R. Sambles, G.W.B., F. Yang, *Optical excitation of surface plasmons: An introduction.* Contemporary Physics, 1991. **32**(3): p. 173-183.
25. Adachi, S., *The handbook on optical constants of metals*. 2012, Japan.
26. Maier, S.A., *Plasmonics: Fundamentals and Applications*. 2007, New York City, NewYork: Springer.
27. D. Lis, F.C., *Localized surface plasmon resonances in nanostructures to enhance nonlinear vibrational spectroscopies: towards an astonishing molecular sensitivity.* Belstein Journal of Nanotechnology, 2014. **5**: p. 2275-2292.
28. J.N. Anker, W.P.H., O. Lyandres, N.C. Shah, J.Zhao, R.P. Van Duyne, *Biosensing with plasmonic nanosensors.* Nature Materials, 2008. **7**: p. 442-453.
29. Shen, F.W.a.Y.R., *General properties of local plasmons in metal nanostructures.* Physical Review Letters, 2006. **97**: p. 206806.
30. T. Kokkinakis, A.A., *Observation of radiative decay of surface plasmons in small silver particles* Physical Review Letters, 1972. **28**(25): p. 1632-1634.
31. L. S. Jung, C.T.C., T. M. Chinowsky, M. N. Mar, S. S. Yee, *Quantitative interpretation of the response of surface plasmon resonance sensors to adsorbed films.* Langmuir, 1998. **14**: p. 5636-5648.
32. Barbillon, G., *Determination of evanescent electric field decay length of metallic nanodisks by using localized surface plasmon spectroscopy.* Journal of Materials Science and Engineering, 2010. **4**(11): p. 69-74.
33. L. J. Sherry, R.J., C. A. Mirkin, G. C. Schatz, R. P. Van Duyne, *Localized surface plasmon resonance spectroscopy of single silver triangular nanoprisms.* Nano Letters, 2006. **6**(9): p. 2060-2065.
34. G. Barbillon, J.L.B., J.S. Bouillard J. Plain, M. L. De La Chapelle, P.M. Adam, P. Royer, *Detection in near-field domain of biomolecules adsorbed on a single metallic nanoparticle.* Journal of Microscopy, 2008. **229**(2): p. 270-274.
35. L. Soares, A.C., J. Jatschk, W. Fritzsche, O. Flores, R. Franco, E. Pereira, *Localized surface plasmon resonance (LSPR) biosensing using gold nanotriangles: detection of DNA hybridization events at room temperature.* Analyst, 2014. **139**: p. 4964-4973.
36. A. J. Haes, R.P.V.D., *A nanoscale optical biosensor: Sensitivity and selectivity of an approach based on the localized surface plasmon resonance spectroscopy of triangular silver nanoparticles.* Journal of American Chemical Scoiets, 2002. **124**: p. 10596-10604.
37. A. J. Haes, L.C., W. L. Klein, R. P. Van Duyne, *Detection of a biomarker for alzheimer's disease from synthetic and clinical samples using a nanoscale optical biosensor.* Journal of American Chemical Scoiets, 2004. **127**: p. 2264-2271.

38. T. Maurer, P.M.A., G. Lévêque, *Coupling between plasmonic films and nanostructures: from basics to applications.* Nanophotonics, 2015. **4**: p. 363-382.
39. P. K. Jain, M.A.E.-S., *Plasmonic coupling in noble metal nanostructures.* Chemical Physics Letters, 2010. **487**: p. 153-164.
40. A. Artar, A.A.Y., H. Altug, *Multispectral lasmon induced transparency in coupled meta-atoms.* Nano Letters, 2011. **11**: p. 1685-1689.
41. M. Hentschel, T.W., S. Bagheri, H. Giessen, *Babinet to the half: Coupling of solid and inverse plasmonic structures.* Nano Letters, 2013. **13**: p. 4428-4433.
42. W.A. Murray, W.L.B., *Plasmonic Materials.* Advanced Materials, 2007. **19**: p. 3771-3782.
43. E. Prodan, C.R., N. J. Halas, P. Nordlander, *A hybridization model for the plasmon response of complex nanostructures.* Science, 2003. **302**: p. 419-422.
44. Park, W., *Optical interactions in plasmonic nanostructures.* Nano Convergence, 2014. **1**(2): p. 1-27.
45. K.J. Boiler, A.I., S.E. Harris, *Observation of electromagnetically induced transparency.* Physical Review Letters, 1991. **66**(20): p. 2593-2596.
46. Harris, S.E., *Electromagnetically induced transparency.* Physics Today, 1997. **50**(7): p. 36-42.
47. M. Fleischhauer, A.I., J. P. Marangos, *Electromagnetically induced transparency: Optics in coherent media.* Reviews of Modern Physics, 2005. **77**: p. 663-672.
48. B. Luk'yanchuk, N.I.Z., S.A. Maier, N.J. Halas, P.Nordlander, H. Geissen, C.T. Chong, *The Fano resonance in plasmonic nanostructures and metamaterials.* Nature Materials, 2010. **9**: p. 707-715.
49. B. Gallinet, A.L., T. Siegfried, H. Sigg, O.J.F. Martin, *Fano resonant plasmonic systems: Functioning principles and applications.* AIP Conference Proceedings, 2012. **1475**: p. 18-20.
50. Fano, U., *Interaction between configurations with several open shells.* Physical Reviews, 1965. **140**: p. A67-A75.
51. A.E. Miroshnichenko, S.F., Y.S. Kivshar, *Fano resonances in nanoscale structures.* Reviews of Modern Physics, 2010. **82**(3): p. 2257.
52. N. Liu, T.W., Martin Mesch, L. Langguth, U. Eigenthaler, M. Hirscher, C. Sonnichsen, H. Geissen, *Planar metamaterial analogue of electromagnetically induced transparency for plasmonic sensing.* Nano Letters, 2010. **10**: p. 1103-1107.
53. N. Liu, L.L., T. Weiss, J. Kästel, M. Fleischhauer, T. Pfau, H. Giessen, *Plasmonic analogue of electromagnetically induced transparency at the Drude damping limit.* Nature Materials, 2009. **8**: p. 758-762.
54. K. K. Madoyan, A.H.M., H. R. Minassian, *Radiation damping of surface plasmons in a pair of nanoparticles and in nanoparticles near interfaces.* The Journal of Physical Chemistry C, 2012. **116**: p. 16800-16805.
55. M. Liu, T.W.L., S.K. Gray, P. G-S, M. Pelton, *Excitation of dark plasmons in metal nanoparticles by a localized emitter.* Physical Review Letters, 2009. **102**: p. 107401.
56. J. S. Huang, J.K., P. Geisler, P. Weinmann, M. Kamp, A. Forchel, P. Biagioni, B. Hecht, *Mode imaging and selection in strongly coupled nanoantennas.* Nano Letters, 2010. **10**: p. 2105-2110.
57. S. Hayashi, D.V.N., Z. Sekkat, *Fano resonance and plasmon induced transparency in waveguide-coupled surface plasmon resonance sensors.* Applied Physics Express, 2015. **8**(2): p. 022201.
58. Song Han, R.S., Longqing Cong, H. Yang, *Engineering the fano resonance and electromagnetically induced transparency in near-field coupled bright and dark metamaterial.* Journal of Physics D: Applied Physics, 2014. **48**: p. 035104.
59. Y.S. Joe, A.M.S., C. S. Kim, *Classical analogy of Fano resonances.* Physica Scripta, 2006. **74**: p. 259-266.
60. P.A. Franken, A.E.H., C.W. Peters, G.Weinreich, *Generation of optical harmonics.* Physical Review Letters, 1961. **7**(4): p. 118-120.

61. C.K. Chen, T.F.H., D. Ricard, Y.R. Shen, *Detection of molecular monolayers by optical second harmonic generation.* Physical Review Letters, 1981. **46**(15): p. 1010-1012.
62. Shen, Y.R., *Optical second harmonic generation at interfaces.* Annual Review of Physical Chemistry, 1989. **40**: p. 327-350.
63. McGilp, J.F., *Optical second-harmonic generation for studying surfaces and interfaces.* Journal of Physcis: Condensed Matter, 1989. **1**: p. 85-92.
64. J. M. Hicks, T.P.-M., J. D. Byers, *Consequences of chirality in second-order non-linear spectroscopy at surfaces.* Faraday Discussions, 1994. **99**: p. 341-357.
65. M. Kauranen, T.V., A. Persoons, *Second-order nonlinear optical signatures of surface chirality.* Journal of Modern Optics, 1998. **45**(2).
66. J. E. Sipe, D.J.M., H. M. van Driel, *Phenomenological theory of optical second and third harmonic generation from cubic centrosymmetric crystals.* Physical Review B, 1987. **35**(3): p. 1130-1141.
67. V. K. Valev, A.V.S., W. Gillijns, O. A. Aktsipetrov, V. V. Moshchalkov, T. Verbiest, *Asymmetric second harmonic generation in chiral optical metamaterials.* Proc. of SPIE, 2010. **7711**: p. 77111S.
68. V. K. Valev, A.V.S., N. Verellen, W. Gillijns, P. Van Dorpe, O. A. Aktsipetrov, G. A. E. Vandenbosch, V.V. Moshchalkov, T. Verbiest, *Asymmetric optical second-harmonic generation from chiral G-shaped gold nanostructures.* Physical Review Letters, 2010. **104**: p. 127401.
69. F. J. Rodríguez, F.X.W., B. K. Canfield, S. Cattaneo, M. Kauranen, *Multipolar tensor analysis of second-order nonlinear optical response of surface and bulk of glass.* Optics Express, 2007. **15**(14): p. 8695-8701.
70. M. Zdanowicz, S.K., H. Husu, M. Kauranen, *Effective medium multipolar tensor analysis of second-harmonic generation from metal nanoparticles.* New Journal of Physics, 2011. **13**(023025).
71. F. Hache, H.M., M. C. Schanne-Klein, *Application of classical models of chirality to surface second harmonic generation.* Journal of Chemical Physics, 2001. **115**: p. 6707.
72. J.J. Maki, M.K., A. Persoons, *Surface second-harmonic generation from chiral materials.* Physical Review B, 1995. **51**(3): p. 1425-1434.
73. M. Kauranen, T.V., J. J. Maki, A. Persoons, *Second-harmonic generation from chiral surfaces.* Journal of Chemical Physics, 1994. **101**: p. 8193.
74. P. Guyot-Sionnest, Y.R.S., *Bulk contribution in surface second-harmonic generation.* Physical Review B, 1988. **38**(12): p. 7985-7989.
75. M. Kauranen, T.V., J.J. Maki,A. Persoons, *Second harmonic generation from chiral surfaces.* Journal of Chemical Physics, 1994. **101**: p. 8193-8199.
76. J.J. Maki, T.V., M. Kauranen, S. Van Elshocht, A. Persoons, *Comparison of linearly and circularly polarized probes of second order optical activity of chiral surfaces.* Journal of Chemical Physics, 1996. **105**.
77. M. Kauranen, J.J.M., T. Verbiest, S. Van Elshocht, A. Persoons, *Quantitative determination of electric and magnetic second-order susceptibility tensors of chiral surfaces.* Physical Review B, 1996. **55**(4): p. 1985-1988.
78. B.K. Canfield, S.K., K. Jefimovs, Y. Svirko, J. Turunen, M. Kauranen, *A macroscopic formalism to describe the second-order nonlinear optical response of nanostructures.* Journal of Optics A, 2006. **8**: p. 278-284.
79. S. Kujala, B.K.C., M. Kauranen, *Multipole interference in the second-harmonic optical radiation from gold nanoparticles.* Physcial Review Letters, 2007. **98**: p. 167403.
80. J. I. Dadap, J.S., K. B. Eisenthal, T. F. Heinz, *Second harmonic rayleigh scattering from a sphere of centrosymmetric material.* Physical Review Letters, 1999. **83**(20): p. 4045.

81. J. I. Dadap, J.S., T. F. Heinz, *Theory of optical second-harmonic generation from a sphere of centrosymmetric material: small-particle limit.* Journal of the Optical Society of America, 2004. **21**(7): p. 1328.
82. J. Nappa, G.R., I. Russier-Antoine, E. Benichou, C. Jonin, P. F. Brevet, *Electric dipole origin of the second harmonic generation of small metallic particles.* Physical Review B, 2005. **71**: p. 165407.
83. I. Russier-Antoine, E.B., G. Bachelier, C. Jonin, P. F. Brevet, *Multipolar contributions of the second harmonic generation from silver and gold nanoparticles.* Journal of Physical Chemistry C, 2007. **111**: p. 9044.
84. G. Bachelier, I.R.-A., E. Benichou, C. Jonin, P.F. Brevet, *Multipolar second-harmonic generation in noble metal nanoparticles.* Journal of Optical Society of America B, 2008. **25**(6): p. 955-960.
85. A. Capretti, G.F.W., S.Minissale, J. Trevino, C. Forestiere, G.Miano, L. Dal Negro, *Multipolar second harmonic generation from planar arrays of Au nanoparticles* .Journal of Optical Society of America, 2012. **20**(14): p. 15797.

Chapter 3: Experimental

3.1 Introduction

This chapter provides an outline of the fabrication processes used to produce chiral plasmonic nanostructures, the techniques employed to perform experimental measurements and a brief overview of the procedures for EM field simulations. All fabrication and microscopy was performed in the James Watt Nanofabrication Centre (JWNC) and School of Engineering at the University of Glasgow. Spectroscopic measurements and protein preparation were carried out in the School of Chemistry at Glasgow unless otherwise specified. Electromagnetic field simulations were performed at the University of Glasgow by Dr Affar Karimullah in collaboration with Dr. Larousse Khosravi Khorashad and Professor Alexander O. Govorov of the School of Physics and Astronomy at Ohio University.

3.2 Nanostructure Fabrication

Two distinct nanofabrication techniques are used to produce the nanostructured substrates: injection moulding and electron beam lithography. Injection moulding is used as a high-throughput method to fabricate the templated plasmonic substrates (TPSs) used in chapters 4, 5 and 6. The substrates employed in chapter 7 are fabricated using electron beam lithography.

3.2.1 Electron Beam Lithography (EBL)

The gammadion nanostructures employed in chapter 7 are produced through a lithographic process using an electron beam writer (figure 3.01). A 1mm thick quartz substrate (25x25mm) is cleaned and sonicated using acetone, methanol and iso-propyl alcohol (IPA) before it is dried under a stream of N_2 gas and undergoes a round of oxygen plasma cleaning (180W for 60s). A PMMA (poly methylmethacrylate, Elvacite Lucite International) resist bilayer is then spin coated onto the surface to a thickness of approximately 300nm. The resist bilayer consists of 200nm PMMA (MW=2010) as the bottom layer and 100nm PMMA (MW=2041) atop this layer. After each resist layer is spin coated onto the quartz surface, the substrate is left to bake in a 180^{o}C oven for 5 minutes in order to evaporate the solvent each time. The resist bilayer is coated with 10nm Al in an electron beam evaporator (Plassys MEB-400s) to offset the effects of substrate charging during the electron beam writing process. The CAD designed nanopattern (L-edit v6.4) is now written into the sample by the

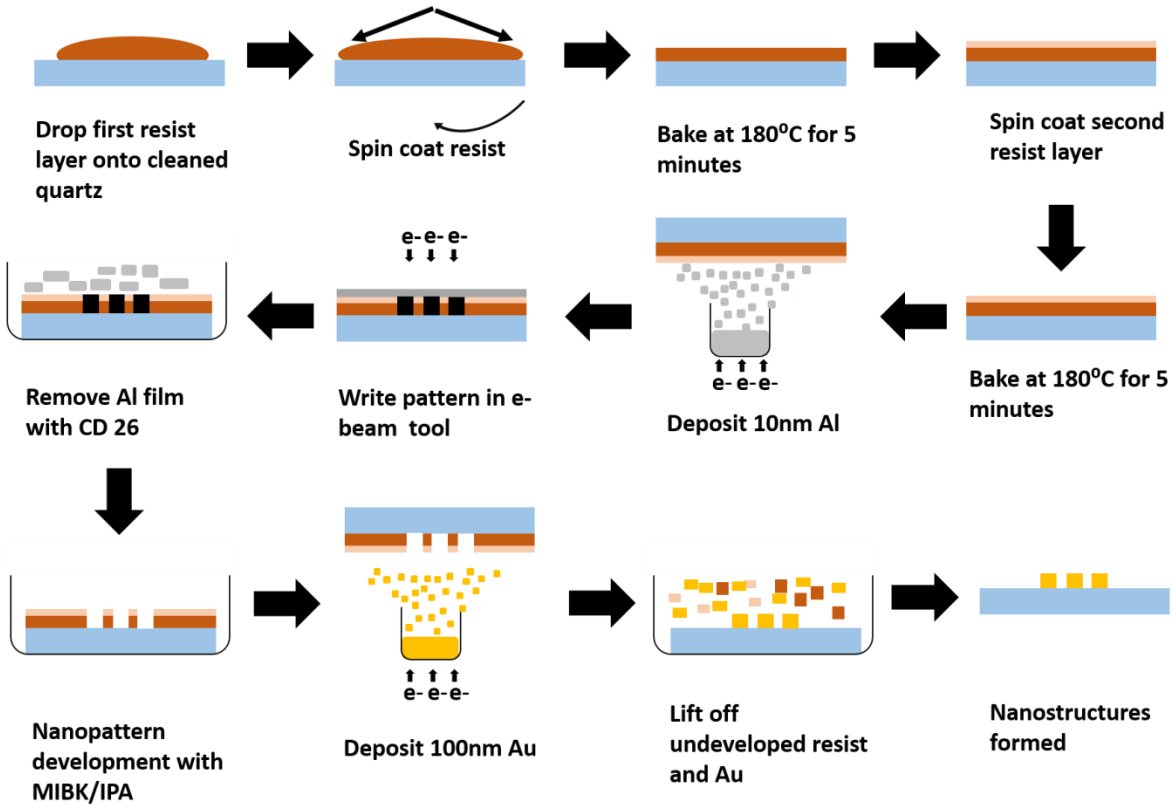

Figure 3.01: Complete process for the fabrication of lithographic gammadions used in chapter 7.

electron beam writer (Vistec VB6) over the course of approximately 30 minutes. The Al layer is removed by placing the sample in a solution of 49:1 RO water: Tetramethylammonium hydroxide (also known as CD 26) for 60s before washing the sample with small amounts of RO water to remove any solvent from the surface and dried using N_2 gas. The nanopattern is then developed by submerging the substrate in 2.5:1 methyl isobutyl ketone (MIBK): IPA solution at 25°C for 60s and the substrate is subsequently washed with small amounts of RO water and dried under a stream of N_2 gas. A 5nm Ti adhesion layer followed by 100nm Au is evaporated onto the developed resist using the Plassys MEB-400s evaporator. The sample is left in Acetone at 50°C for approximately 1 hour in order to remove the undeveloped resist layers and Au lying atop this layer. Finally, the completed sample is washed with a small amount of IPA then dried under a stream of N_2 gas (figure 3.02).

For the lithographic fabrication of gammadions in this section, a resist bilayer is chosen as the preferred method of resist coating. This procedure is selected as it enhances the effectiveness of the lift-off step and allows the generation of sharper nanostructure features. Figure 3.03 displays an illustration of the resultant structure after lift-off for a

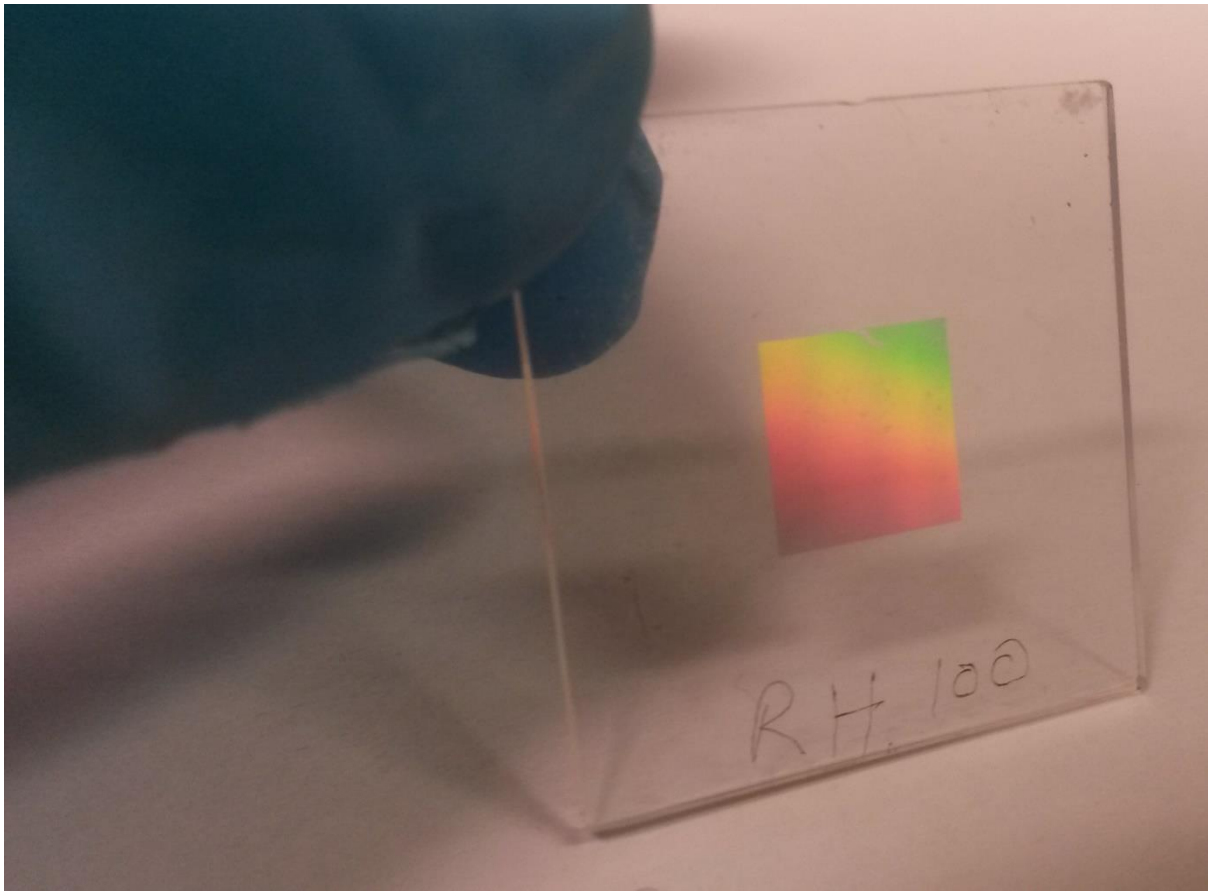

Figure 3.02: Photograph of array of lithographically fabricated gammadions on quartz.

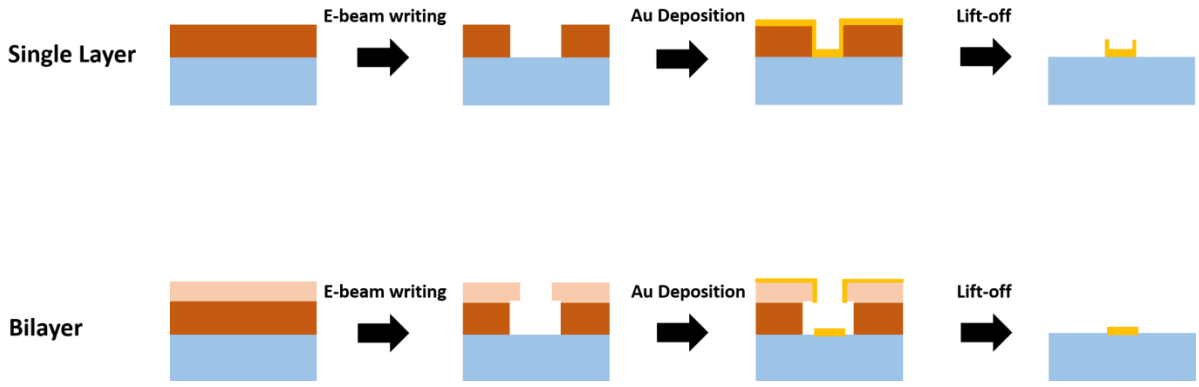

Figure 3.03: Comparison of nanostructure fabrication with single resist layer and resist bilayer.

single resist layer and a resist bilayer. Fabrication with a single resist layer may result in the deposition of excess Au around the edges and sides of the nanostructure. This may potentially affect the metamaterial performance as it modifies the nanostructure from the desired geometry. Using a resist bilayer, it is possible to limit this effect providing a more well defined structure. Due to its lower molecular weight, the bottom resist layer is developed faster and to a greater extent than the upper layer. Upon Au deposition this results in the formation of an “undercut” structure. During the lift-off stage this structure

allows the solvent to spread beneath the upper resist layer upon which the excess Au is bound. Consequently, this allows for a more effective removal of the excess Au generating sharper nanostructure features.

3.2.2 Templated Plasmonic Substrates (TPS)

The process required to generate the TPSs involves two distinct steps: fabrication of a metal nanopatterned master (known as a shim) and high-throughput replications of the master pattern using injection moulding. It is important to note that it is not necessary to fabricate a new shim for each new batch of polycarbonate substrates. The same shim may be used multiple times over a number of years provided it is stored and cleaned appropriately. Before and after each injection moulding session the shim is washed with rounds of ethanol and iso-propyl alcohol (IPA) and cleaned with oxygen plasma in order to remove any polymer residues and dirt. When not in use the shim is stored in a clean room environment.

The procedure for fabrication of the shim follows a similar process as that used for fabrication of lithographic nanostructures. A Si wafer is cleaned using several rounds of solvent washing (acetone, methanol and IPA) and sonication before it is dried under a stream of N_2 gas. A PMMA (MW=2010) resist layer is then spin coated onto the surface to a thickness of 100nm. Proper designation of this thickness is important as this defines the depth to which the master will imprint the nanopattern during the injection moulding stage. After the resist layer is spin coated onto the Si wafer, the substrate is left to bake in a 180^{o}C

Figure 3.04: Photograph of Engel Victory 28 hydraulic injection moulder.

oven for 5 minutes in order to evaporate the solvent. The resist is patterned with the desired nanostructure arrays using an electron beam writer (Vistec VB6). After electron beam writing the resist is developed using IPA and Methyl Isobutyl Ketone (MIBK) 2.5:1 ratio at 25°C for 60s. Ni is then electroplated (1mm) onto the developed substrate. Acetone is used to strip off the remaining PMMA which subsequently allows separation of the nanopatterned Ni shim from the Si wafer. The metal shim is fabricated using Ni due to the low surface roughness of this metal (<5nm) which is important for limiting defects and distortions in the injection moulded nanopatterned surface. In addition, Ni has a large thermal conductivity which is important for rapid cooling of the polymer during the injection moulding stage.

The machinery used to fabricate all injection moulded samples was an Engel Victory 28 hydraulic injection moulder (figure 3.04). Injection moulded samples are produced using

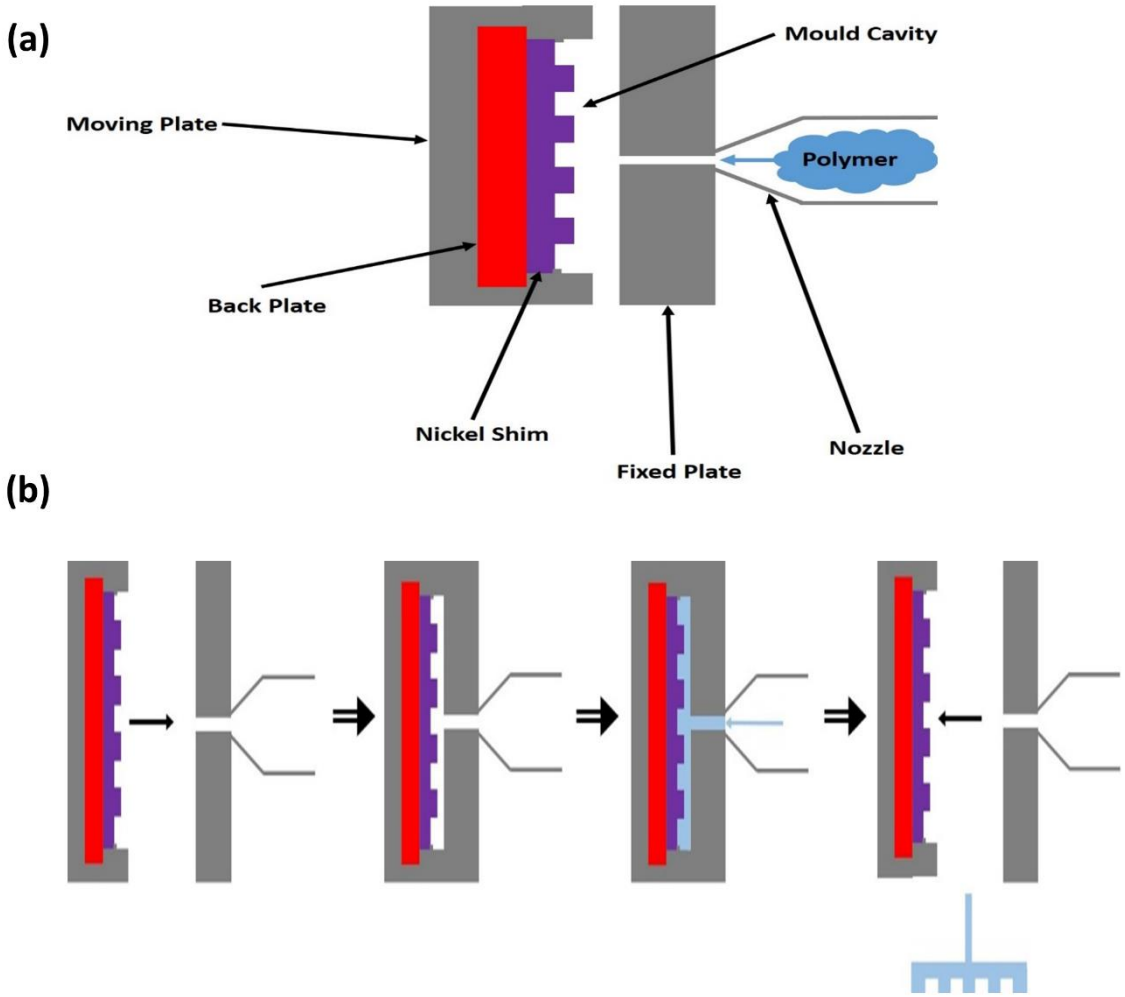

Figure 3.05: (a) Graphic representation of the injection moulder tool. **(b)** Overview of the steps required for fabrication of injection moulded nanostructures.

polycarbonate (Makrolon OD 2015). Polycarbonate is employed for fabrication as it is known to have the best ability to replicate nanofeatures. A typical injection moulding session will last approximately 2-3 hours producing upwards of 200 samples at a rate of approximately one sample every 10 seconds. The Ni shim is fitted into the injection moulder at the "tool" (figure 3.05a) and the appropriate temperature and flow parameters are then set. Selection of the appropriate operating parameters is vitally important to ensure the polycarbonate flows into the features of the shim properly and generates high quality substrates. Polycarbonate beads measuring a few millimetres in diameter are fed into the machine and brought to their melting point (280^{o}C) at the tool. Figure 3.05b displays the basic mechanics of the tool during the injection moulding process. The moving plate extends towards the fixed plate at which point the molten polymer is injected under pressure into the cavity wherein the temperature is kept below the polymer's glass transition temperature (T_g, 145^{o}C). The thermoplastic rapidly cools upon contact with the nickel shim producing the solid nanopatterned surface. The moving plate is then retracted allowing the substrate to be retrieved. Once the sample is retrieved the moving plate is again extended towards the fixed plate at the nozzle and the injection process is repeated. The polymer injection and sample retrieval process are fully automated and the machine is simply set to produce the desired number of substrates.

After fabrication, each slide is cleaned using methanol and IPA before being dried under a stream of N_2 gas. The clean slides are placed in an electron beam metal evaporator (Plassys MEB-400s) where the desired thickness of Au is coated onto the nanopatterned surface at a rate of ≈0.3 nm s^{-1}. This generates the final TPSs which are cleaned in an oxygen plasma asher (Plasmaprep 5) for 30 seconds at 160W (figure 3.06).

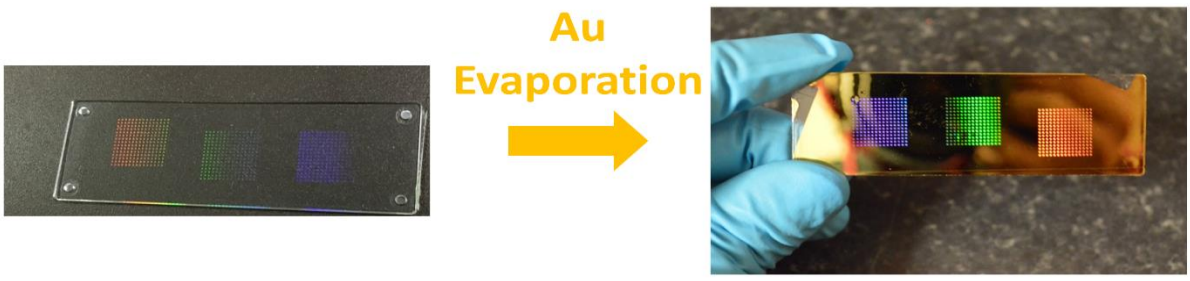

Figure 3.06: Photograph of nanopatterned polycarbonate slide before metal deposition and after evaporation of 100nm Au to form the TPS

3.3 Microscopy

The study of nanoscale systems using optical microscopy is fundamentally limited due to the well-known diffraction limit. Rayleigh defined this spatial resolution mathematically as:

$$r = 0.61\frac{\lambda}{NA}$$

where r is the lateral distance between two objects, and λ is the wavelength of incident light. The numerical aperture (NA) of a lens is a dimensionless number which defines the range of angles over which a lens can accept light (figure 3.07). This is calculated as:

$$NA = nsin\theta$$

Where n is the refractive index of the media surrounding the lens and θ is defined in figure 3.07. At a fixed wavelength the NA determines the resolving power of the system whereby a larger NA increases the resolution limit. The NA of typical objective lenses ranges from ~ 0.1 to 0.6 whilst most measurements are commonly performed in air (n=1.00). Consequently, the theoretical resolution limit of imaging systems at optical wavelengths is typically several hundred nanometres. Despite this sub-micron resolution limit for optical systems, high resolution imaging of nanoscale features cannot be achieved. Accurate measurement of the nanoscale surface morphology and topography requires two distinct microscopy techniques; scanning electron microscopy (SEM) and atomic force microscopy (AFM).

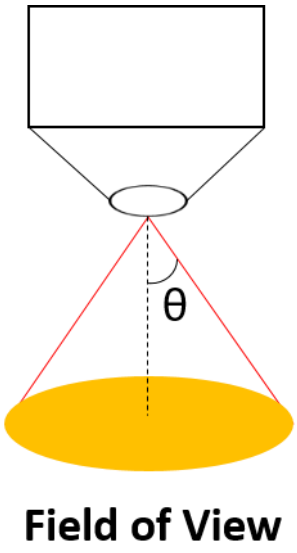

Figure 3.07: Schematic of viewing angle that is used to define the numerical aperture of a lens.

3.3.1 Scanning Electron Microscopy (SEM)

A SEM provides high resolution images by scanning a focussed electron beam across the surface which allows for the characterisation of surface morphology. The SEM operates under vacuum conditions and the instruments employed in this thesis are capable of resolving features as small as 5-10nm. Upon striking the surface, the primary electron beam penetrates the sample to a depth of a few microns depending on the accelerating voltage and density of the material. The nature of the signal generated from the primary electron beam-sample interaction depends on the depth at which this interaction occurs. At the surface, the primary electron beam collides inelastically with the sample resulting in the ionization of the constituent atoms. This generates secondary electrons (SE) which have an energy significantly lower than that of the primary beam. Electrons that collide elastically with atoms in the sample are known as back scattered electrons (BSE). This process occurs at greater depths within the sample and strongly depends on the density of the material therefore BSE are more commonly employed for the elemental analysis of samples. As a result of the poorer surface resolution of BSE images, SE are the primary method for analysis of nanoscale materials. Finally, it is important to note that in order to provide high resolution and greater contrast in SEM images the sample must be electrically conductive. This prevents the build-up of charge in small areas which can lead to distortions in nanostructure geometry and ultimately destruction of the sample.

SEM images in this thesis were recorded using an FEI Nova 630 NanoSEM and a Hitachi S4700 SEM in the JWNC at the University of Glasgow. SEM images are produced through measurement of secondary electrons with typical operating parameters of 5-10kV and 5-8nA. The resolution limit of the FEI Nova 630 NanoSEM is ~ 5nm at 10keV and is therefore used to collect high quality SEM images of the final nanostructured substrates. The Hitachi S4700 has a resolution limit of ~10nm at 10keV and is predominantly used to quickly monitor the quality of substrates at several stages throughout the fabrication processes.

3.3.2 Atomic Force Microscopy (AFM)

AFM is a highly incisive probe of surface topography and may resolve features with sub nanometre accuracy. The AFM operates by measuring the forces interacting with a probe as it is brought into close proximity with the sample. These forces include dipole-dipole interactions, electrostatic interactions and London forces. The probe consists of a sharp tip

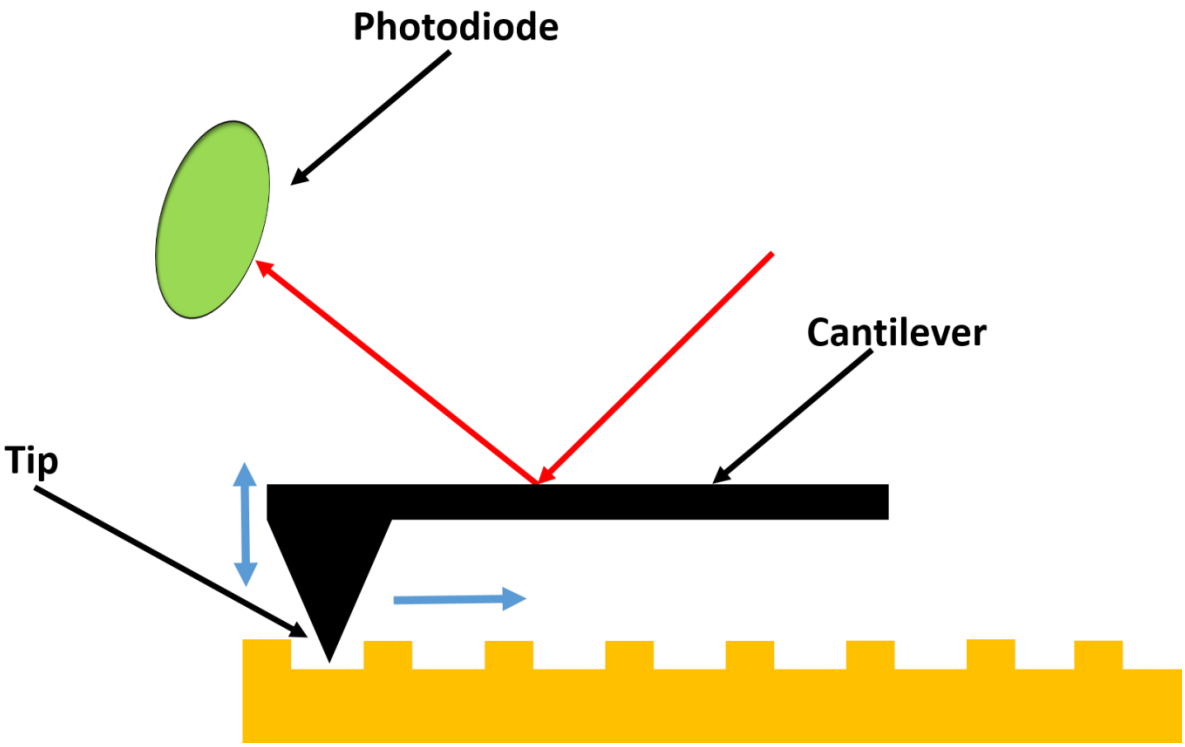

Figure 3.08: Schematic representation of AFM operation.

situated at the end of a cantilever which is dragged across or brought into very close proximity with the surface depending on the mode of operation. AFM data are collected using a Bruker Dimension Icon Atomic Force Microscope operating in tapping mode. In this mode the tip is not continuously dragged over the surface, rather, an image is produced through intermittent contact of the tip with the sample surface. Specifically, the cantilever is driven to oscillate at its resonant frequency with a constant amplitude, the amplitude of this oscillation decreases as the tip approaches and contacts the surface. The height of the cantilever is continuously adjusted to maintain constant oscillation amplitude which in turn modulates the reflection of the laser off the top of cantilever (figure 3.08). This modification in reflection is detected by the photodiode which provides information on the change in amplitude and phase of the cantilever allowing a topographic image to be generated. The vertical noise of the apparatus is <30 pm which allows a vertical resolution on a sub nanometre scale with limits of around 0.1nm. The lateral resolution of AFM measurements is highly dependent on the sharpness of the AFM tip and the effect of tip-sample convolution (figure 3.09). All AFM images are a convolution of the tip and sample however a less sharp tip results in features indented into the surface appearing narrower and shallower as the oversized probe cannot penetrate sufficiently deep enough into the

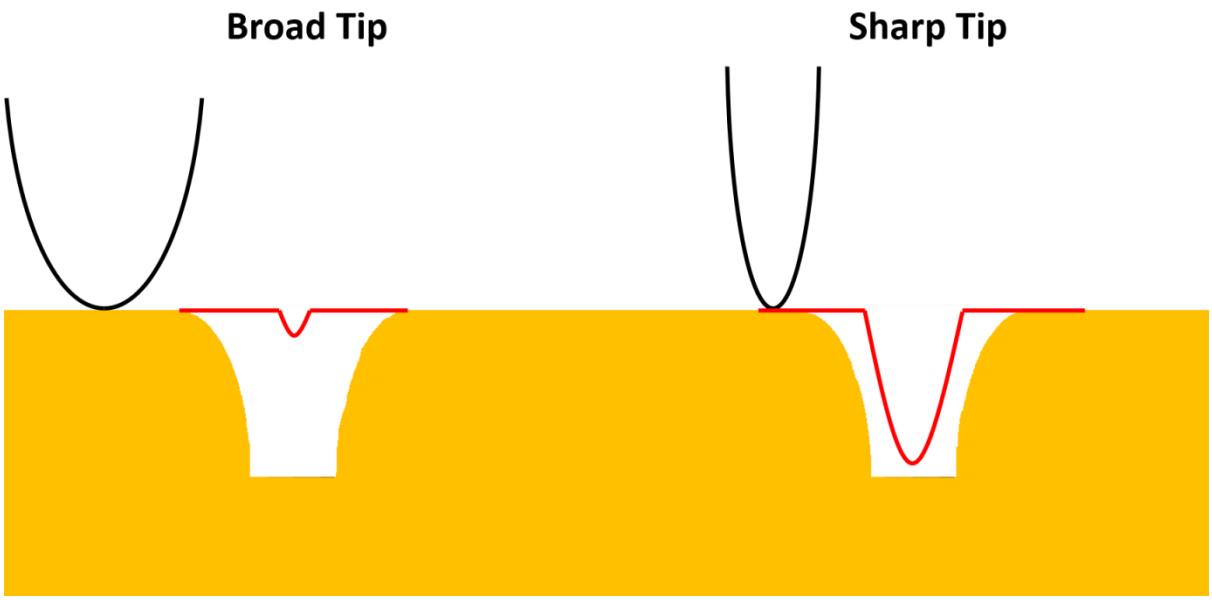

Figure 3.09: Graphic depiction of the effect of the tip sharpness on the accuracy of the measured AFM height profile (red line).

features. The lateral resolution limits of AFM measurements in this thesis is typically ~20-30nm.

3.4 Spectroscopic Measurements

Both linear and nonlinear spectroscopic techniques are utilized to probe the nanostructure optical properties and their biosensing capabilities. Linear spectroscopic measurements of the TPSs are carried out using a custom built polarization microscope to measure the optical rotatory dispersion (ORD) and relative reflectance whilst the TPS nonlinear optical properties are investigated using second harmonic generation (SHG). Spectroscopic analysis of lithographically fabricated substrates is conducted through circular dichroism (CD) measurements.

3.4.1 Polarisation Microscope

Linear optical measurements of TPSs (ORD and relative reflectance) were collected in reflectance using a custom built polarization microscope pictured in figure 3.10. A schematic diagram of the microscope set up can be found in figure 3.11. An unpolarised 50W tungsten halogen lamp (Thorlabs) provides the broadband lightsource which propagates through a collimating lens and a Glan-Thomson polarizer generating a vertically polarized collimated beam. This polarised collimated beam is directed down normally with respect to the sample surface by a 50:50 beamsplitter before a 10x objective lens (Olympus 0.16 N.A.) focuses the beam on the appropriate nanostructures. The reflected radiation propagates back through

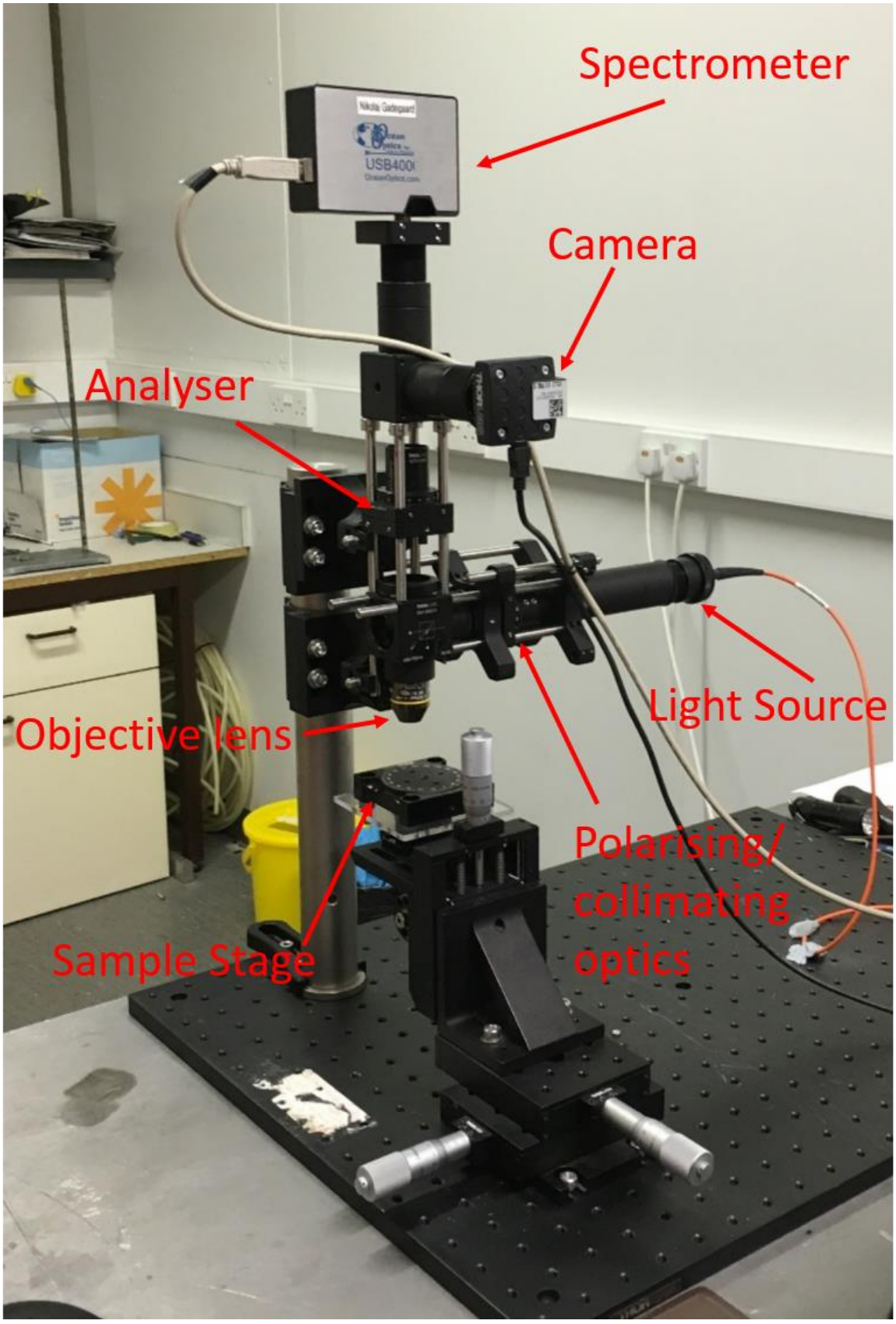

Figure 3.10: Labelled photograph of polarisation microscope.

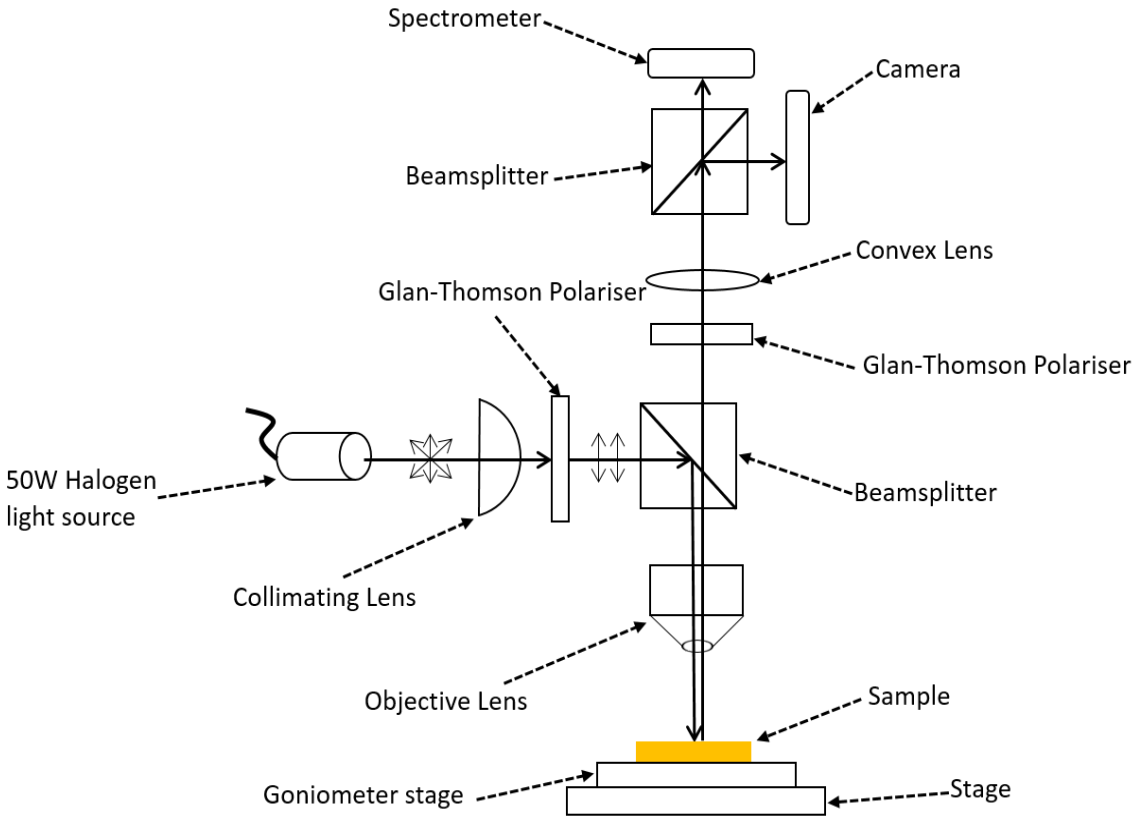

Figure 3.11: Schematic of polarisation microscope components.

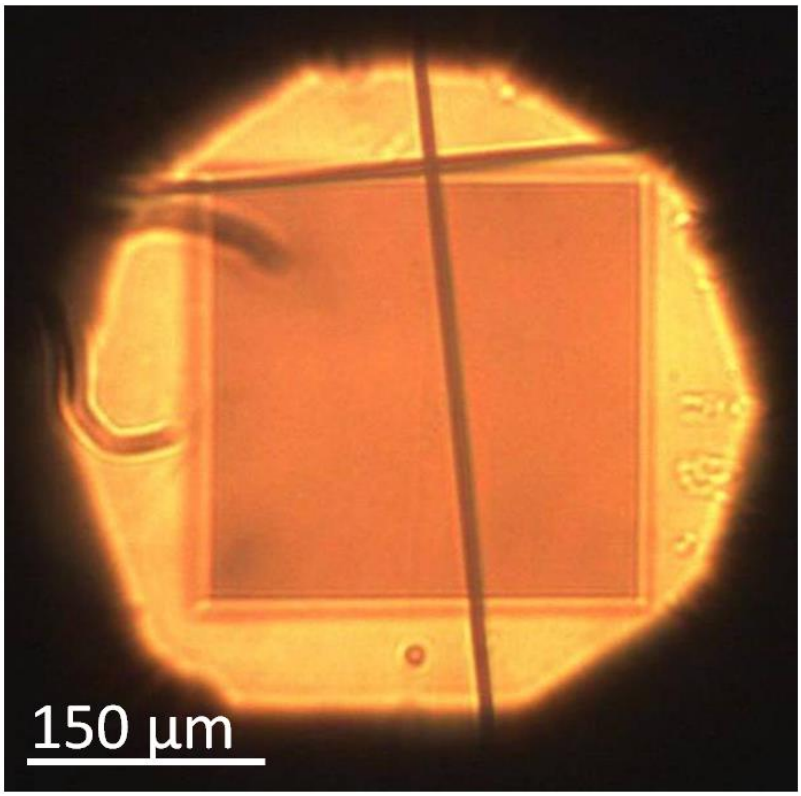

Figure 3.12: Image of field of view of polarisation microscope for TPS substrates.

the beamsplitter, a Glan-Thomson analyzer and a further beamsplitter before a convex lens focuses the beam into the spectrometer (Ocean Optics USB400). The spectral range of the spectrometer is approximately 300-1000nm. The field of view during spectroscopic measurements is approximately $90x10^3$ μm^2 (figure 3.12).

Positioning of the sample is achieved using a camera (Thorlabs DCC1645C) located after the analyser which provides clear visualisation of the beam on the nanostructure arrays. The angle of the sample and hence the angle of reflectance is controlled by adjusting the tilt of the goniometer stage. The goniometer stage tilt is fine-tuned to ensure the reflected beam propagates normal to the surface and passes through the centre of the analyser. The sample is considered to be aligned when nanostructure enantiomers generate mirror image ORD spectra and near identical reflectance spectra lineshapes.

Using Stokes methods the intensity of light at four polarisation angles on the analyser (0°, 45°, 90°, 135° with respect to the incident polarisation) are recorded and the ORD is calculated as:

$$ORD = \frac{1}{2} tan^{-1} \frac{(I_{45} - I_{135})}{(I_0 - I_{90})} \quad (1)$$

ORD spectra are measured on the RH and LH nanostructured surface and the unstructured flat Au. The flat Au ORD is subtracted from the nanostructure ORD in order reduce background noise. Reflectance spectra are generated by measuring the reflected light with the analyser angle at 0° and calculating:

$$Relative\ Reflectance = \left(\frac{Nanostructure\ Reflectance\ Intensity}{Flat\ Au\ Reflectance\ Intensity}\right) \quad (2)$$

For both the ORD and reflectance spectra, an average of four measurements is taken in order to reduce background noise.

3.4.2 Plasmonic Polarimetry

In this thesis we introduce a novel spectroscopic technique, known as plasmonic polarimetry, for the detection of the molecular and macromolecular structure of proteins absorbed onto the surface of TPS nanostructures (figure 3.13). The basis of this technique involves measurement of the ORD of RH and LH chiral plasmonic nanostructures around a

particular plasmonic resonance. For nanostructure enantiomers, the ORD are equal and opposite and arise due to the excitation of a plasmonic mode which results in the generation of chiral evanescent fields around the nanostructure. The net chirality of these evanescent fields (RH or LH) is also equal and opposite for nanostructure enantiomers. The wavelength at which nanostructure plasmonic modes resonate depends on the refractive index of the surrounding dielectric (section 2.2.4). For achiral molecules the refractive index is isotropic therefore it possesses the same value in RH and LH chiral fields meaning the magnitude of the ORD shift will be equivalent for RH and LH nanostructures. However, the dielectric properties of chiral molecules are anisotropic meaning the refractive index will differ depending on the handedness of the chiral fields with which the molecules interact. Plasmonic polarimetry exploits this anisotropy in the refractive index of chiral molecules to measure asymmetric resonance shifts in the RH and LH ORD spectra which allows different structural properties of proteins to be probed.

Firstly, the ORD from RH and LH nanostructures is recorded in 10mM tris buffer and the peak position of the first peak/trough is recorded for each (λ_{buffer}). The desired biomaterial is then adsorbed onto the Au surface and the spectral position of the same peak/trough is again measured ($\lambda_{analyte}$). The resonance shifts for RH and LH nanostructures due to the refractive index of the analyte are defined as:

$$\Delta\lambda = \lambda_{(analyte)} - \lambda_{(buffer)} \quad (3)$$

Analogous to conventional optical rotation, chiral molecules adsorbed on RH and LH nanostructures display slightly differing indices of refraction due to the chirality of the evanescent field associated with the nanostructure. This differential refractive index value will result in an asymmetric resonance shift between RH and LH shurikens ($\Delta\lambda_{RH} \neq \Delta\lambda_{LH}$). We parameterise this asymmetry using:

$$\Delta\Delta\lambda = \Delta\lambda_{RH} - \Delta\lambda_{LH} \quad (4)$$

This $\Delta\Delta\lambda$ parameter is directly related to the optical rotation measured in conventional polarimetry. Comparison of the magnitude and direction of the $\Delta\Delta\lambda$ parameter of a range of proteins allows a correlation between particular structural motifs and $\Delta\Delta\lambda$ values to be ascertained.

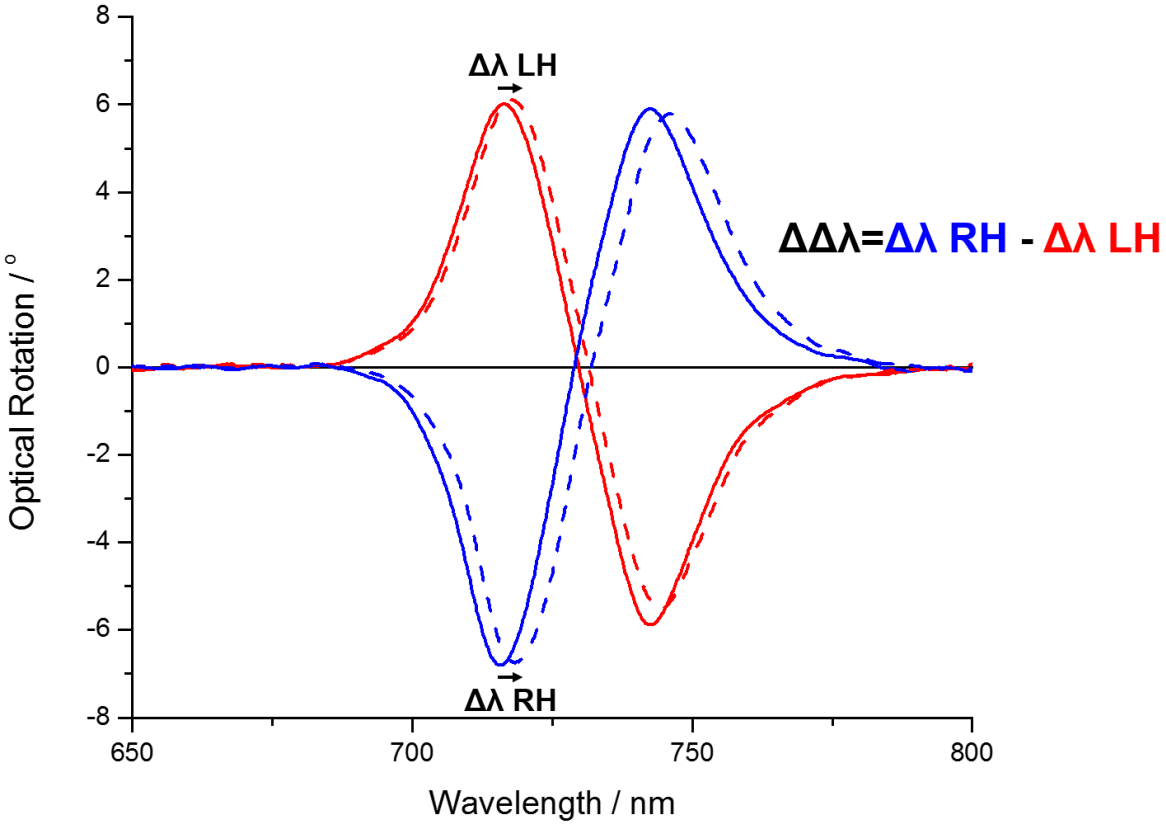

Figure 3.13: Example of plasmonic polarimetry measurement upon adsorption of biomaterial using RH (blue) and LH (red) chiral plasmonic nanostructures. Solid lines are ORD recorded in buffer and dashed lines are measured after adsorption of biomaterial.

3.4.3 Second Harmonic Generation (SHG)

A schematic of the experimental set up used in nonlinear spectroscopic measurements presented in chapter 5 is displayed in figure 3.14. A modelocked Yb:YAG fiber laser (MenloSystems) provides the incident beam at fundamental wavelength 1050nm (bandwidth ~80nm) with a pulse duration of approximately 100 fs and a 100 MHz repetition rate. The average power of the laser before the optical elements is 130mW and the fundamental beam is initially p-polarised before passing through a half wave plate (HWP) to control the incident polarisation. An IR band pass filter is positioned immediately after the HWP to remove any unwanted harmonic light from optical components. The beam is then focussed onto the sample surface with a convex lens producing a spot of approximately 200 µm in diameter. The IR light is incident on the sample at an angle of 45° with respect to the surface normal with an average power 120 mW. The SH beam generated at an angle of 45° with respect to the surface normal passes through the analyser, IR filter and 532nm band pass filter. The IR filter and 532nm band pass filter are employed to remove any radiation

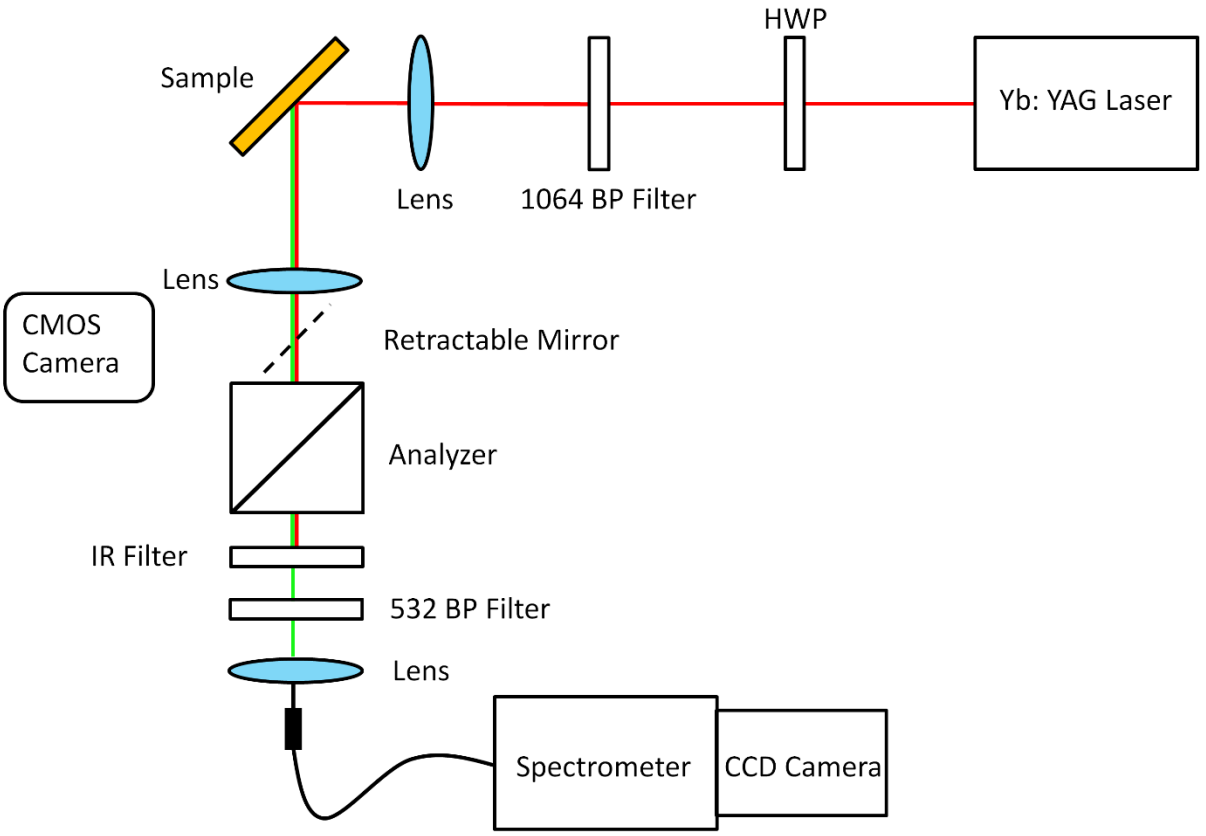

Figure 3.14: Labelled diagram of SHG experimental set-up.

that is not associated with SH emission from the sample. A retractable mirror is positioned after the sample to reflect the IR light into a CMOS camera (Thorlabs) which allows for visualization of the IR spot on the sample surface during alignment (figure 3.15). The SH signal is focussed into an optical fibre attached to the spectrometer (Andor Shamrock SR 303i) which is linked to an ungated CCD camera (Andor Newton EMCCD).

Sample alignment is achieved by first positioning the laser spot on the appropriate nanostructures using the CMOS camera (figure 3.15). The reflected beam is aligned into the fibre by adjusting the pitch and angle of the sample stage until the maximum SH signal intensity is obtained. The experimental SH signal is amplified by the ungated CCD camera and collected continuously over a period of 100 milliseconds. Background spectra collected in the absence of laser light are automatically subtracted from the SH signal by the data acquisition software in order to reduce the background noise levels. SH profiles are obtained by varying the ingoing polarisation around 360° and measuring the vertically/horizontally polarised SHG signal intensity at 5° intervals. Four SH spectra are averaged for each 5° interval in order to further reduce background noise.

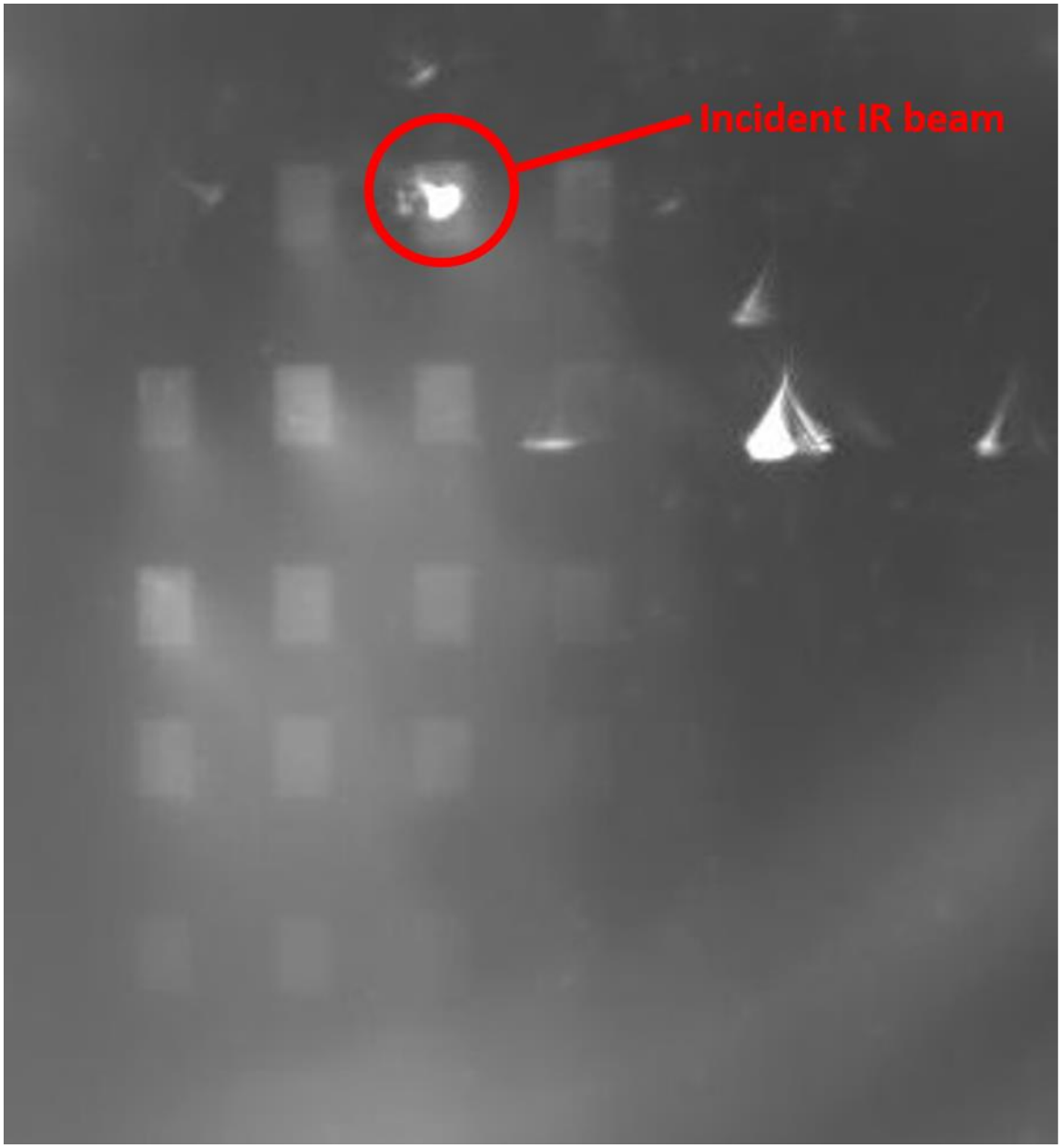

Figure 3.15: CMOS camera image of the IR beam on nanostructure arrays during sample alignment.

3.4.4 Circular Dichroism (CD)

CD measurements in chapter 7 of gammadions lithographically fabricated on quartz are performed using a commercial spectropolarimeter (JASCO J-810). The nanostructure CD is measured over a wavelength range of 190nm-900nm with data points recorded every 0.2nm. Nanostructure substrates are incorporated into a microfluidic cell of volume 20µl using a glass cover slip. The back face of the substrates (i.e. the Au/quartz interface) faces the detector, in other words, the incident light propagates through the buffer/insulin amyloid fibril solution and is then incident on the Au nanostructures (figure 3.16). Surface

adsorption of spherulites is achieved by dropping 20µl of spherulite solution (4.2 mg/ml) onto the nanostructure surface and leaving for 1 hour before CD measurements are recorded.

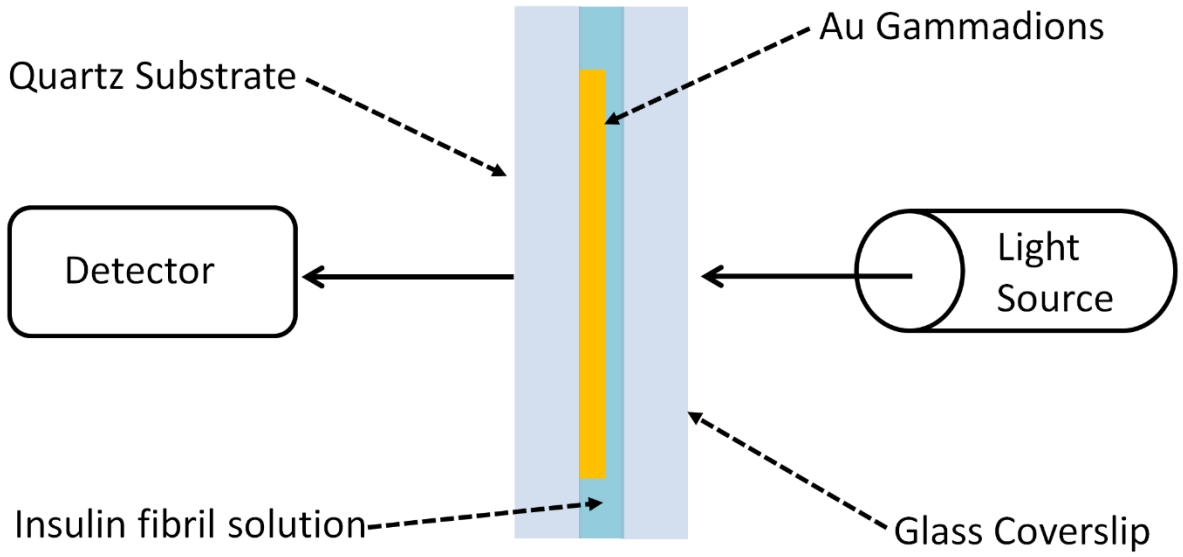

Figure 3.16: Depiction of experimental geometry during CD measurements.

3.5 Surface Functionalisation

The surface of TPSs are chemically modified in chapter 5 to allow for further investigation into the biosensing capabilities of the nanostructured system. Chemical modification may be employed to inhibit protein binding, promote specific binding of a molecule or direct protein adsorption to particular areas of the nanostructure.

3.5.1 Polyethylene glycol (PEG)-thiol Self Assembled Monolayer (SAM) Functionalisation

PEG-thiol (Poly (ethylene glycol)) methyl ether thiol (mw=6000, Sigma-Aldrich) was used to make an 833 uM solution in 95% ethanol. The TPS is immersed in the PEG-thiol solution for

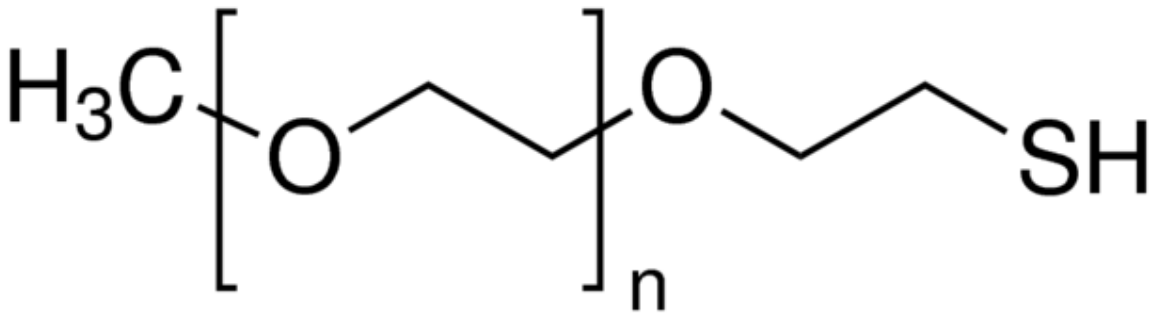

Figure 3.17: Poly-ethylene glycol methyl ether thiol (PEG-thiol) structure, n≈ 150.

18 hours to allow full assembly of an ordered PEG thiol monolayer. This involves breaking of the SH bond and formation of a new S-Au bond at the sample surface. After being removed from solution, the TPSs were washed with 5ml water and dried under a stream of nitrogen.

3.5.2 Nitrilotriacetic Acid (NTA) Thiol Functionalisation

The preparation of the nitrilotriacetic acid-thiol (NTA-thiol)/triethylene glycol mono-11-mercaptoundecyl (EG thiol) monolayer was performed in a similar manner to that described by Sigal et al [1]. The TPS substrates are submerged in 95% ethanol solution containing 0.1mM NTA thiol and 0.9mM EG-thiol spacer giving a total thiol concentration of 1mM and bubbled with N_2 for five minutes. The samples are left to incubate for 16-20 hours to allow a self-assembled monolayer to form then subsequently removed from solution and rinsed with 5ml 95% ethanol. The samples are then incubated in 1mM NaOH solution for 5 minutes before being immersed in 40mM Nickel Sulphate for 1 hour. Finally, the TPSs are washed with 5ml water and dried under a stream of N_2 gas. Figure 3.18 displays a schematic representation of the NTA thiol functionalisation, subsequent binding of Ni (II) sulphate and His-tagged protein binding.

After formation of the Ni^{2+} NTA thiol on the Au surface, the functionalised substrates are immersed in a solution of the desired His-tagged protein (5-enolpyruvylshikimate-3-phosphate (EPSP) Synthase). The Ni^{2+} chelate has a high affinity for the Nitrogen group of

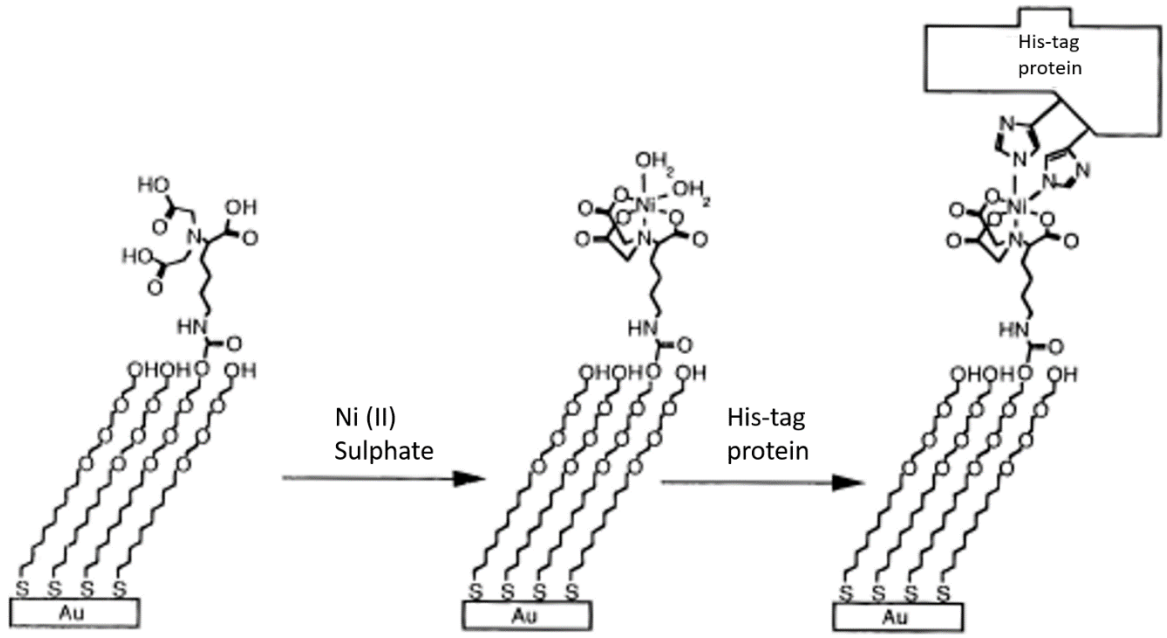

Figure 3.18: Diagram of NTA thiol formation, Ni (II) sulphate functionalisation and His-tagged protein binding

the His-tag therefore the protein is bound to the NTA SAM through two Ni^{2+}-Histidine bonds with the loss of two water molecules. The specific binding of Ni^{2+} to the His-tag at the N terminus of the protein means the protein molecules will be oriented in a consistent manner across the surface of the substrate.

3.6 Analyte Measurements and Preparation

An integral element of this thesis is the viability of plasmonic nanostructures as a technology for biosensing. In order to explore this a number of proteins possessing a variety of primary, secondary, tertiary and quaternary structures were studied.

3.6.1 Microfluidic Cell

When performing TPS spectroscopic measurements for a liquid layer the sample is incorporated into a simple microfluidic cell with an approximate volume of 200µl (figure 3.19). This cell is created by placing a glass coverslip on top of the substrate and sealing the edges of the coverslip and TPS together using silicon. Two hypodermic needles are inserted into the cell to allow the injection/extraction of the liquid analyte with a syringe.

3.6.2 Protein Solution Preparation

The buffer used in all protein experiments unless otherwise stated is tris (hydroxymethyl) aminomethane buffer of concentration 10mM adjusted to a pH of 7.4 using hydrochloric acid. All protein solutions are prepared to a concentration of 1mg/ml in 10mM tris HCl buffer unless otherwise specified. Solutions of insulin amyloid fibril spherulites used in chapter 7 were prepared to a concentration of 4.2mg/ml in 10mM tris HCl buffer by the MacPhee group in the School of Physics and Astronomy at the University of Edinburgh.

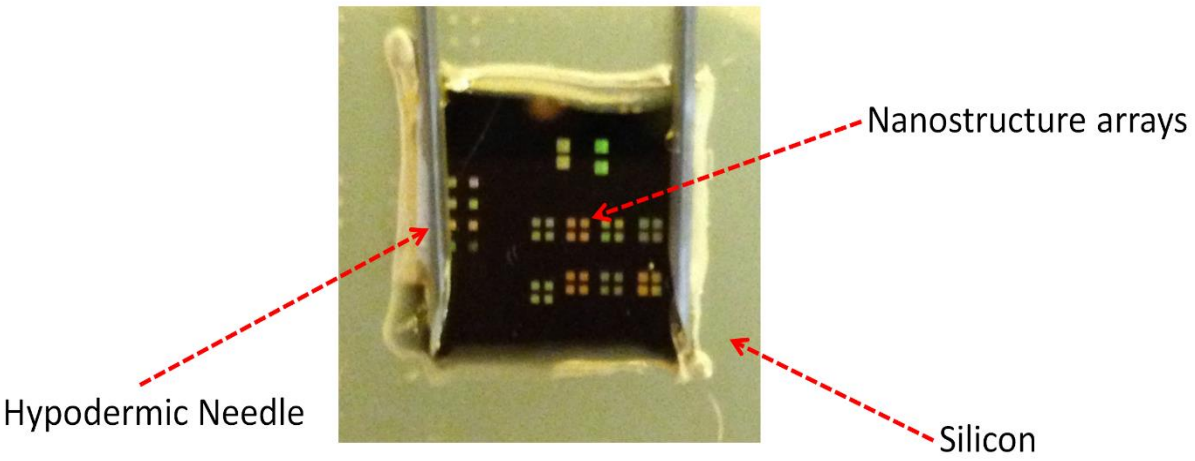

Figure 3.19: Labelled image of microfluidic cell.

3.6.3 5-enolpyruvylshikimate-3-phosphate (EPSP) Synthase Preparation

An existing His-tagged Escherica Coli gene was inserted and over-expressed in BL21 star cells. Liquid Luria Broth (LB) media was used to grow the cells and protein expression was induced with isopropyl β-D-1-thiogalactopyranoside (IPTG). The cells were harvested after three hours by centrifugation before being suspended in 50mM tris HCl buffer at pH 7.8. Sonication is employed to break down the cell membrane (cell lysis) and insoluble matter was removed by centrifugation at 20000 rpm. The protein is then purified from the cell lysate by Ni(II) affinity chromatography and the EPSP synthase eluted using 300mM imidazole and 300mM NaCl in 100mM tris HCl buffer. Finally, the protein is purified and concentrated by centrifuging and buffer exchange dialysis to yield a final solution concentration of 20mg/ml EPSP synthase.

3.7 Polarised Optical Microscopy of Insulin Amyloid Fibril Spherulites

Images of insulin amyloid fibril spherulites and sonicated insulin amyloid fibril spherulites are captured using a cross polarised microscope (Leica DM500) with a 5x (0.3 NA) objective lens. Insulin amyloid fibril solutions of volume 50µl are deposited on the gammadion nanostructures and left for 1 hour to allow surface adsorption before images were recorded.

3.8 Numerical Simulations

In order to fully understand the interaction of plasmonic metamaterials with electromagnetic waves and the thermal behaviour of these substrates it is necessary to perform numerical simulations. The numerical simulations presented in this thesis were performed by Dr Affar Karimullah of the University of Glasgow in collaboration with Dr. Larousse Khosravi Khorashad and Professor Alexander O. Govorov of Ohio University. In the following section a brief explanation of the numerical field simulation techniques used to produce the modelled data presented in chapters 4,5 and 6 is provided.

3.8.1 Finite Element Modelling Methods

Excitation of chiral plasmonic nanostructures by an electromagnetic wave results in the generation of complex electric and magnetic fields which have unique properties (such as a chiral asymmetry) depending on the geometry and constitution of the structures. In order to understand the observed experimental behaviour of the chiral nanostructures used in this thesis it is necessary to model the intensity, distribution and chirality of these

electromagnetic fields. The evolution of electromagnetic fields is described by Maxwell's equations which reflect the interaction between electric and magnetic fields whereby a change in one field with time leads to the evolution of the other. Modelling of the electromagnetic fields and thermal behaviour of nanostructures in this study is performed using the finite element method (FEM).

The mathematical modelling of many different physical phenomena such as electrodynamics require the introduction of partial differential equations (Maxwell's equations) which describe multiple independent variables associated with electromagnetic fields. The equations under consideration are often so complicated that numerical approximations have to be employed in order to obtain a viable solution. A particular class of numerical techniques to obtain these finite approximations of partial differential equations and generate an appropriate physical model are finite element methods. The basic premise of FEM involves several distinct computational steps. Firstly, the system that is to be modelled is divided into an equivalent system of many smaller units (elements) interconnected at points common to two or more element boundaries (nodes). The unknown field variable is solved for each individual node. The values of the field variable within the volume of each element are then expressed in terms of an interpolation function using the nodal values which renders the overall model an approximation. The resultant equations for each element are then assembled into a global system of equations which are calculated to give the desired field quantities.

The fundamental idea underpinning FEM is that it is simply a methodology for breaking up a complex domain into smaller elements and finding suitable approximating functions in each element. This process of dividing a large system into smaller elemental components is known as meshing. Figure 3.20 displays a basic example of this elemental meshing and the position of nodes for two triangular elements. The main advantage of this elemental meshing is that the problem of calculating the field quantities at every point in the body is replaced by only finding the values for a finite number of points, namely the nodes. The unknown field quantity Ψ is firstly calculated at the elemental nodes. An interpolation function (often a polynomial) is then applied to approximate the values of the field at any point within the element. Each small element possesses its own interpolation function therefore for each element, the unknown field within may be expressed as:

$$\Psi^e = \sum_{i=1}^{m} N_i \Psi_i \qquad (5)$$

Where m is the total number of nodes in a given element, N_i is the interpolation function,i stands for each node in the element and Ψ_i is the value of the field quantity at the node. From figure 3.20 we see that certain nodes are shared by two elements due to a common boundary. This commonality is important as it allows the calculation of related field quantities across the element boundaries. In order to yield approximate values of Ψ^e that more accurately reflect the real field quantities a larger number of elemental nodes and smaller meshing elements may be employed. However, as a result of this more complex node distribution the computational time may significantly increase.

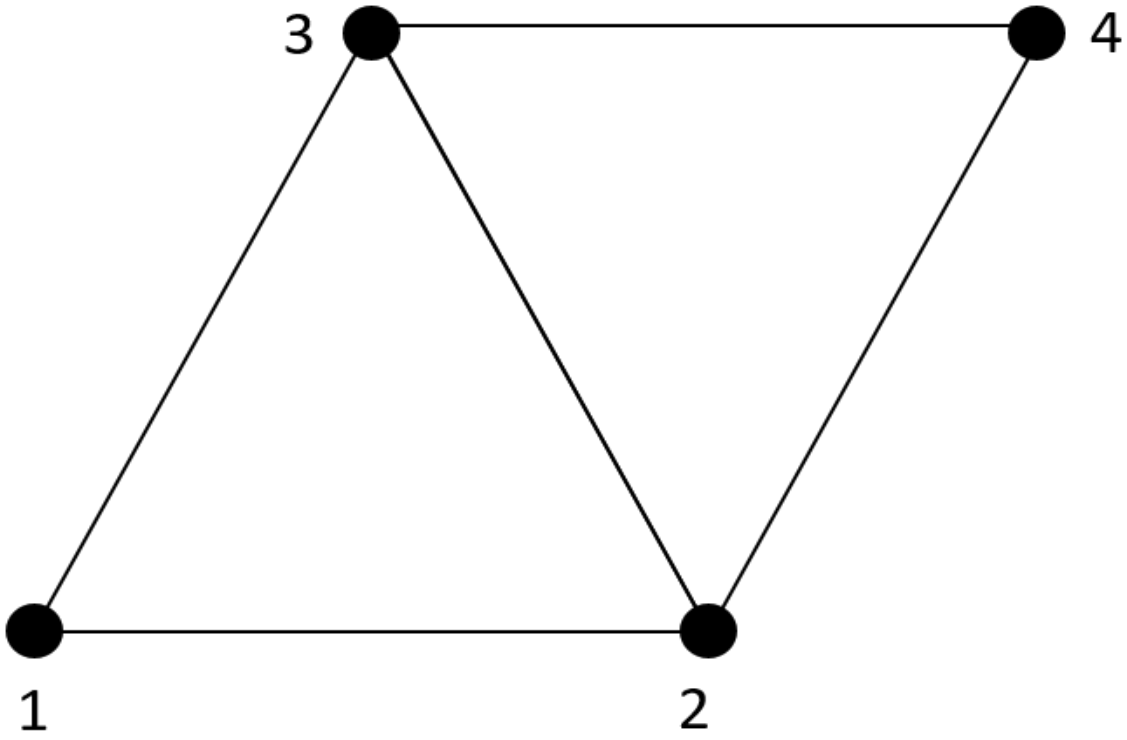

Figure 3.20: Two triangular elements with two common nodes (2 and 3).

The most important aspect of this stage to ensure accurate field simulations is selection of the appropriate mesh. The example in figure 3.20 may only be applied for two dimensional systems whereas for the three dimensional geometries employed in this thesis the meshing elements must also be three dimensional (e.g. tetrahedron, square based pyramid, triangular prisms or hexahedrons). The main determinant for selection of the appropriate meshing element is the geometry of the system. Tetrahedral meshes are the most

commonly used element for physical modelling as these can be employed for any three dimensional volumes. Furthermore, the aspect ratio of this element is close to unity therefore the accuracy of the solution in all directions is approximately equal. Application of other meshing elements is determined by the geometry of the system and the accuracy required in the simulation. These elements often have high aspect ratios and are employed when it is known that the solution will significantly change in one direction and only slightly in another (figure 3.21). The short axis (which will have smaller spacing between each node) is aligned in the direction of significant variation since these calculations will require greater accuracy. In contrast, the long axis is aligned along the direction of decreased variation as a smaller number of nodes per unit area is required. Finally, the importance of swept meshes must not be overlooked. This meshing technique is applied to thin three dimensional regions whereby the 2D mesh on one surface is swept (extended) into the 3D volume towards another similar surface producing hexahedral elements. This technique is employed primarily to reduce the number of elements compared with applying a tetrahedral mesh which has a tendency to "over-mesh" such regions therefore the computational time can be significantly reduced.

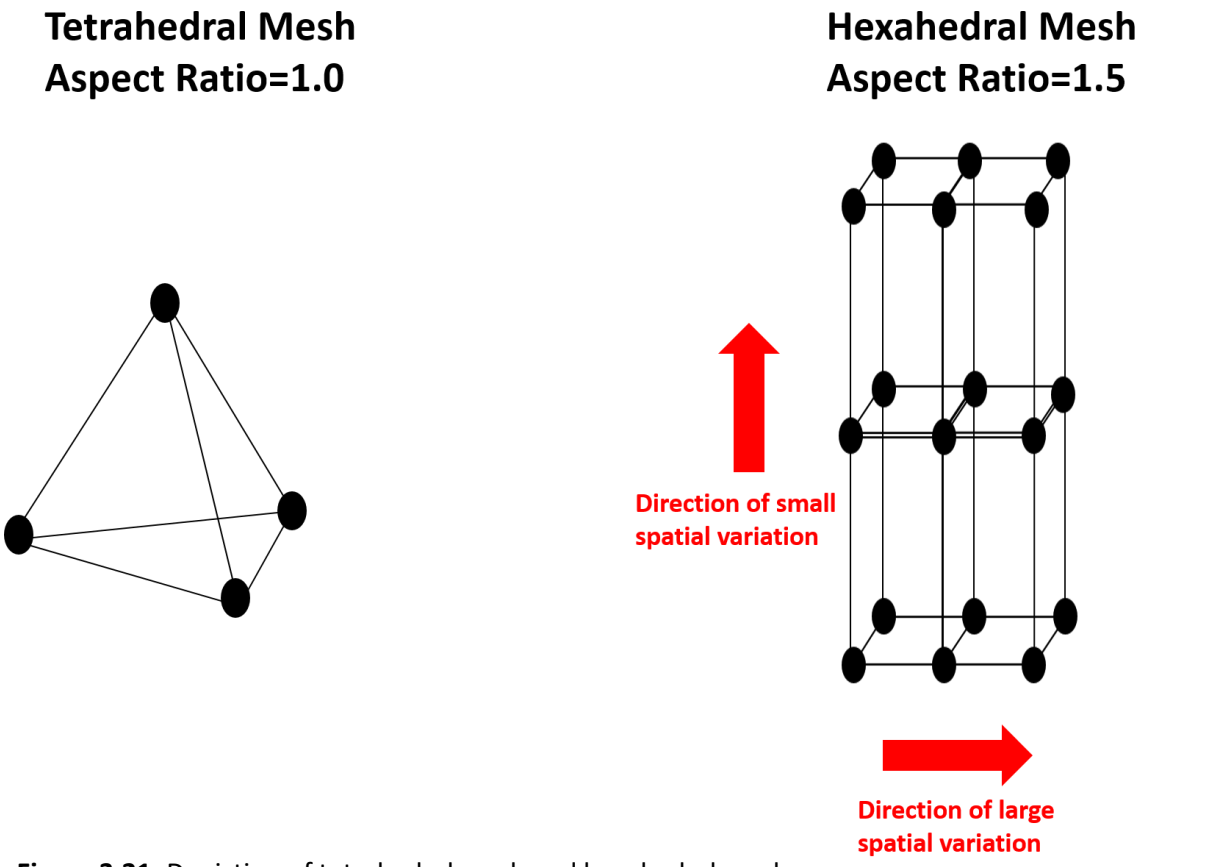

Figure 3.21: Depiction of tetrahedral mesh and hexahedral mesh.

In FEM, selection of the appropriate governing differential equations (field quantities to be calculated), meshing elements and interpolation functions allows the desired field quantity to be calculated in each element. The calculations for each individual element may therefore be solved and “glued” together to provide the solution for the overall system. However, this is an extremely inefficient approach which means simulations are not carried out this way. The connectivity of elements through commonly shared nodes allows an alternative and more computationally economical approach whereby the resultant equations for each element are assembled into global matrix equations. Formation of this global matrix allows calculation of a solution for individual elements whilst also linking across shared elemental nodes to produce a global solution. Moreover, the matrix order of these equations can be reduced due to the presence of shared nodes meaning this method is also more computationally efficient.

Before the global matrix elements can be solved, an integral part of FEM is the application of boundary conditions. For the electromagnetic field simulations performed in this thesis the most important boundary conditions relate to defining the properties and spatial extent of the space surrounding the plasmonic nanostructure. The first boundary condition that needs to be addressed is that of infinity. This boundary arises as, although the nanostructure has finite dimensions in the x, y and z directions, the space surrounding the modelled system extends to infinity. Thus, we must define the boundaries of the surrounding space in order for a well-defined solution to the desired field quantities to be calculated. This is achieved by the introduction of purely artificial boundaries which limit the computational domain to a finite size. However, it is necessary to prevent optical fields that propagate out from the modelled system towards this unnatural boundary being reflected back into the modelled domain. Consequently, boundary conditions are made to be absorbing to avoid this unnatural reflection with the most common technique employed to achieve this being perfectly matched layers (PML). Hence, PML is applied in the numerical simulations presented in this thesis. The other important feature of nanostructure arrays that must be considered when performing FEM simulations is the effect of the metamaterial periodicity. The periodicity of the structures has a significant effect on the scattering of light from the nanostructures in addition to the distribution and intensity of EM fields across the metamaterial surface. Thus, boundary conditions at all four boundaries of the nanostructure

must be introduced to account for the sample periodicity. The boundary conditions applied to FEM simulations in this thesis are Floquet periodic boundary conditions. These boundary conditions involve application of Floquet theory which allows solutions for periodic partial differential equations to be calculated.

3.8.2 Numerical Simulations of Chiral Plasmonic Nanostructures

Numerical simulations are performed using a commercial finite element package (COMSOL v4.4 Multiphysics software) using the Wave Optics and Heat Transfer modules. Simulations of the EM fields and ORD spectra discussed in chapters 4, 5 and 6 were performed by Dr Affar Karimullah in the School of Chemistry at Glasgow University. Modelling of the TPS thermal behaviour in chapter 5 was performed by Dr Affar Karimullah at Glasgow in collaboration with Dr. Larousse Khosravi Khorashad and Professor Alexander O. Govorov of the School of Physics and Astronomy at Ohio University.

3.8.3 Electromagnetic Field Simulations

EM field simulations were carried out to solve Maxwell's equations in order to obtain accurate simulations of the intensity, spatial distribution and chiral asymmetry of EM fields generated across the TPS. Floquet periodic boundary conditions were applied to all four boundaries to account for the periodicity of the nanostructure with perfectly matched layers behind the input and output ports. Swept mesh is used for the perfectly matched layers and tetrahedral meshing for the nanostructures and its surrounding media with automated meshing limited to a maximum element size of 18nm in the metal and 30 nm in the surrounding media. The electric field of the normally incident light was s-polarised and ORD spectra were calculated by evaluating the far field components for the reflected light and applying Stokes equations. The refractive index of Au was taken from Johnson and Christy [2]; the refractive index of water from Hale et al [3] and finally the refractive index of polycarbonate from a report by Sultanova et al [4]. The chiral asymmetry of EM fields is parametrised using the optical chirality parameter C proposed by Tang et al [5] (section 2.1.4) and is calculated as shown by Meinzer et al[6]. All positive and negative values of the optical chirality parameter are defined to represent left handed and right handed EM fields respectively.

3.8.4 Thermal Simulations

In chapter 5 modelling of the thermal gradients induced in the nanostructure and surrounding dielectric upon pulsed laser irradiation of the substrate is performed (section 5.2.2). The COMSOL heat transfer module allows the total heat dissipation from the electromagnetic field modelling to be used as a heat source. A time dependent function is then applied to the total heat dissipation to create a heat source that would replicate a square shaped laser pulse as the source for EM heating. After solving Maxwell's equations to determine the EM field intensities and distributions, the time dependent partial differential heat equation is solved to determine local electrical heating in the system. The parameters such as thermal conductivity, density and specific heat capacity used in these simulations can be found in section 5.5. Finally, the local heat and temperature distributions at the various time instances and laser fluence employed in the experiment are modelled.

3.9 References

1. G. B. Sigal, C.B., A. Barberis, J. Strominger, G. M. Whitesides, *A self-assembled monolayer for the binding and study of Histidine-tagged proteins by surface plasmon resonance.* Analytical Chemistry, 1996. **68**: p. 490-497.
2. P. Johnson, R.C., *Optical Constant of Noble Metals.* Physical Review B, 1972. **6**: p. 4370.
3. G.M. Hale, M.R.Q., *Optical Constants of Water in the 200-nm to 200-um wavelength region.* Applied Optics, 1973. **12**: p. 555.
4. N. Sultanova, S.K., I. Nikolov, , *Dipersion properties of optical polymers.* Acta Physica Polonica, 2009. **116**: p. 585-587.
5. Y. Tang, A.E.C., *Optical chirality and its interaction with matter.* Physical Review Letters, 2010. **104**: p. 163901.
6. N. Meinzer, E.H., W.L. Barnes, *Probing the chiral nature of electromagnetic fields surrounding plasmonic nanostructures.* Physical Review B, 2013. **88**: p. 041407.

Chapter 4: Linear Optical Study of Templated Plasmonic Substrates (TPS) with Tuneable Chirality

4.1 Introduction

The application of chiral plasmonic nanostructures in chiroptical spectroscopy represents a promising technique for the ultrasensitive detection of protein structure [1, 2]. Fabrication of nanostructured systems for such biosensing applications is primarily achieved through electron beam lithography (EBL) which is extremely costly and has a low through-put. Furthermore, the post-fabrication control of optical properties in such substrates is challenging as this requires modification of the whole nanostructure geometry. Hence, the exploitation of nanostructures for a commercial biosensing nanotechnology requires a cheap, high through-put nanofabrication technique.

In this chapter we introduce a nano-indented polycarbonate slide coated with a thin film of Au known as a templated plasmonic substrate (TPS). The polycarbonate nanostructures are fabricated using a cost effective, high through-put injection moulding (IM) method. The TPSs consist of hybrid nanostructures whereby a solid nanostructure has an identical shaped void (inverse structure) situated directly above it. The optical properties of these substrates are probed through linear spectroscopic measurements (reflectance and optical rotatory dispersion (ORD)) and electromagnetic (EM) field simulations. Through variation of the Au film thickness, we are able to control the optical and chiroptical properties. The reflectance spectrum displays a lineshape associated with interference phenomenon whereby a Fano resonance is observed for thin film (Au≤30nm) substrates and an electromagnetically induced transparency (EIT)-like effect for thicker films (Au≥40nm). This arises as the Au film thickness modulates the coupling between the electric modes associated with the solid structure and magnetic modes associated with the inverse structure. This electric/magnetic coupling gives rise to hybrid plasmonic modes therefore; analogous to molecular orbital hybridisation a plasmon hybridisation scheme is generated. Ultimately, it is the interference between a bright dipolar hybrid mode and a dark quadrupolar hybrid mode that gives rise to the Fano/EIT effect in the reflectance. In terms of the chiroptical properties, strong electric/magnetic coupling in the thick Au film substrates (Au≥40nm) is found to facilitate large levels of chirality and the nanostructure displays optical activity analogous to an inherently chiral system. Conversely, weak electric/magnetic coupling in substrates with

Au≤30nm gives rise to low levels of chirality in the TPS and optical activity analogous to a weakly chiral system. Finally, we investigate the biosensing properties of strongly and weakly coupled TPSs using plasmonic polarimetry wherein only strongly coupled TPSs are sensitive to protein secondary structure. Thus, TPS nanostructures represent a viable alternative to lithographically fabricated substrates for biosensing applications.

4.1.1 Nanostructure Fabrication by Direct Nanopatterning

Currently, the vast majority of nanostructure fabrication is performed by direct nanopatterning whereby thousands of structures are written individually onto a substrate. The most common direct nanopatterning technique is electron beam lithography (EBL) and a full description of this fabrication process can be found in section 3.2.1. Fabrication of nanostructures using EBL is advantageous as it enjoys an extremely high resolution allowing fabrication of complex nanostructures with precision approaching the atomic scale [3, 4]. In addition, EBL fabrication can be performed on a wide variety of substrates such as quartz and silicon which allows this technique to be applied for a wide range of applications across a number of scientific fields.

Despite the obvious benefits of EBL for nanoscale fabrication there are a number of factors which render it unsuitable for applications beyond fundamental laboratory studies[5]. Firstly, EBL suffers from an extremely low throughput as the overall process consists of an extensive number of steps which may only be completed over long time periods. Consequently, the timescale for the fabrication of a single substrate is at least several days. Lithographic fabrication processes are also extremely sensitive to environmental factors (temperature, pH, concentration, time) meaning sample reproducibility can be potentially challenging. Hence, EBL requires highly controlled environments. The requirement for a tightly regulated environment and the high equipment costs of electron beam writers renders nanoscale lithography extremely costly. Indeed, these costs often exceed thousands of pounds for a single sample. Lithographic substrates are also unsuitable for performing spectroscopic measurements that require adsorption of molecular species onto the surface. This is due to the degradation of structural features upon repeated cleaning of the surface which renders these substrates inappropriate for biosensing applications. Therefore, whilst lithographic substrates are extremely valuable in providing an insight for the academic study of

nanostructures, the high expense and low through-put nature of this technique inhibits the application for commercial purposes.

4.1.2 Nanostructure Fabrication by Replicative Nanopatterning

An alternative to lithographic nanopatterning is replicative nanofabrication. The basic premise of this technique involves the fabrication of a single nanopatterned master from which a large amount of replicas, containing nanoscale features, can be cheaply and easily produced. The replicative nanopatterning technique employed in this thesis is injection moulding (IM) whereby a molten polymer flows around the nanopatterned master and rapidly solidifies producing a nanopatterned polymer slide. A complete description of this IM process can be found in section 3.2.2. IM is a long established technique for the industrial scale manufacture of a wide range of cheap, thermoplastic consumables from basic products such as toothbrushes and combs, to more modern data storage technologies such as Blue Ray DVDs. The effectiveness of this method lies in its simplicity whereby only a small amount of simple cost-effective steps after fabrication of the master are required. The ability to adapt this technique for the fabrication of nanoscale features renders injection moulding as the prime candidate for the industrial scale production of nanostructures. Several promising preliminary studies into the use of IM nanostructures have been conducted in fields such as optics[6, 7] and biomimetics[8] whereby features as small as 4nm have been successfully generated. However, the viability of IM nanostructures with more complex geometries has yet to be explored.

Despite the significant advantages of IM, certain aspects of this process must be taken into consideration for nanoscale fabrication. Upon contact with the master the molten polymer rapidly cools and solidifies. The rate at which thermal energy flows from the molten polymer to the master is so rapid that it leads to the formation of a frozen “skin” layer which forms before the polymer melt can fill the cavities in the master [9, 10]. Due to this rapid cooling, fabrication of “raised” polymer nanostructures (features protruding from the surface) is extremely challenging. The preferred solution to this problem is the Variothermal technique whereby the flow of energy into the master is controlled. Control methods range from laser mediated heating of the master [11] to heating of the surface by electrical induction[12]. However, the Variothermal technique is currently limited to simple structural motifs such as micro/nano pillars[9] therefore complex nanostructures protruding from the surface (as

formed with EBL) cannot be produced using injection moulding. In contrast, rapid polymer cooling does not hinder the formation of holes or nanopatterned features indented into the surface plane [13] as it is easier for the polymer to flow around the master before it solidifies. Consequently, the complex injection moulded nanostructures employed in this thesis consist of a nanopattern indented into the surface of the polymer slide.

4.2 Results and Discussion

4.2.1 Geometric Characterisation

The chiral nanostructures imprinted into the surface of the polycarbonate slide are six-fold symmetric right handed and left handed (RH/LH) "shuriken" structures which consist of a circular central region with six equally spaced curved arms emanating from the centre (figure 4.01a). The bare polycarbonate slide is coated with a thin film of Au ranging from 20nm-100nm to form the templated plasmonic substrates (TPS). The distance from the end of opposite arms is 500nm whilst the thickness of individual arms is 32nm for the 100nm Au

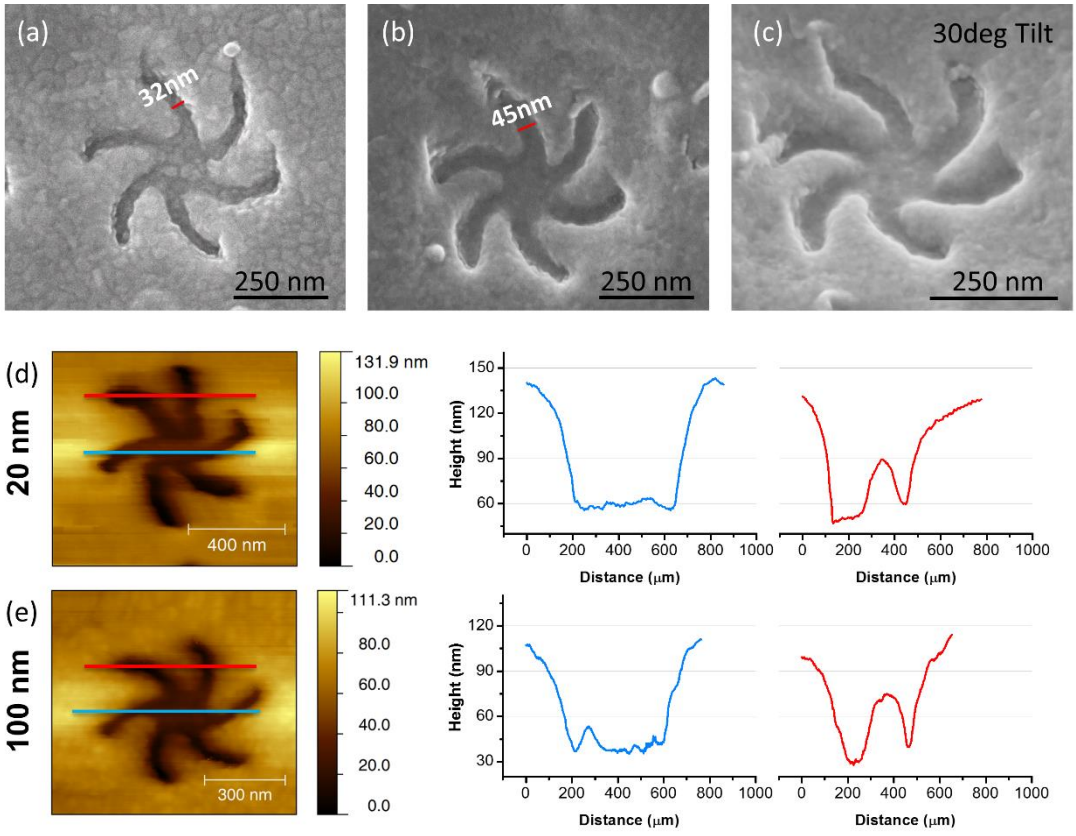

Figure 4.01: SEM of **(a)** 100nm Au TPS, **(b)** 20nm Au TPS and **(c)** 20nm Au TPS measured with 30° tilt. AFM images and their corresponding height profiles for **(d)** a 20nm film and **(e)** 100nm film. Coloured lines overlaying the images correspond to the regions where height profiles were measured.

film and 45 nm for the 20nm film. The discrepancy in the arm width between the 20nm and 100nm Au film is due to greater build-up of Au on the vertical walls for the thicker Au films. The periodicity of the array is 700nm and shurikens are imprinted into the surface to a depth of 80nm (figure 4.01d-e). The RH and LH shuriken arrays measure 300µm x 300µm with 430 shurikens along each side giving 184900 nanostructures per array. From the AFM data we find that the height profile does not drop off suddenly as the cantilever encounters the shuriken shaped void. This indicates that the vertical walls of the structures are not perfectly sharp but slope gradually down to the surface at an angle of approximately 30° (figure 4.01d-e). The continuous nature of the Au film is evidenced by the lack of charging in the SEM images for both the thickest and thinnest Au films. The absence of charging for the 20nm Au film measured at a 30° tilt confirms that the vertical walls of the indentations are completely coated with Au. This means the TPS can be described as a continuous Au film

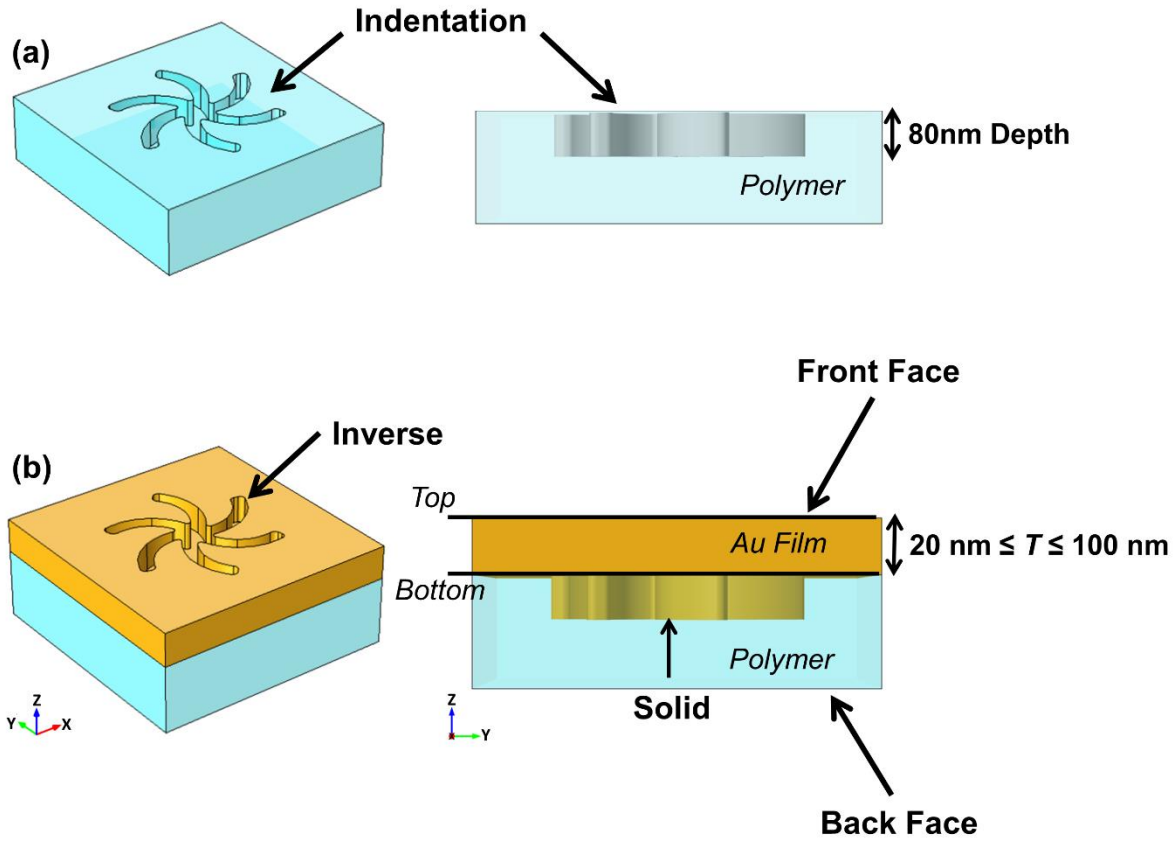

Figure 4.02: (a) Perspective and side views of TPS geometry before metal deposition. Shurikens are imprinted into the surface of a polycarbonate slide to a depth of 80nm. **(b)** Perspective and side views of TPS geometry after metal deposition. The continuous Au film containing the inverse structure is labelled the top surface whilst the shuriken shaped nanostructures at the bottom of these voids is the bottom surface.

punctuated by periodic shuriken shaped voids wherein a solid shuriken shaped nanostructure is found at the bottom of these voids. The presence of both solid and inverse constituent structures means the TPS shurikens may be described as a "hybrid" nanostructured system. Before proceeding to subsequent discussion concerning the optical properties of the system it is necessary to clarify the terminology we employ to define the various surfaces of the substrate (figure 4.02). The "top surface" is defined as the continuous Au film containing the shuriken voids whilst the "bottom surface" is the surface at the bottom of the void where the solid shaped nanostructure is found. The front face is the nanopatterned side of the polycarbonate slide coated with the Au film whilst the back face is the uncoated side of the TPS slide which does not have a nanopattern imprint.

4.2.2 Linear Optical Properties

Shuriken linear optical properties were investigated through measurement of the reflectance spectrum and optical rotatory dispersion (ORD) in the presence of 10mM tris buffer using the home built polarisation microscope described in section 3.4. Figure 4.03 displays the reflectance and ORD spectra for RH and LH shurikens covered with a 100nm Au film. As expected, RH and LH shurikens rotate linearly polarised light with the same magnitude but in the opposite sense hence the ORD spectra are mirror images. Shuriken enantiomer reflectance spectra are almost identical wherein both structures possess several resonances in the visible and NIR region with each resonance corresponding primarily to excitation of a plasmonic mode associated with the nanostructure. The polarisation of the incident light for reflectance measurements is indicated by the black arrow in figure 4.03. Subtle differences in the reflectance lineshape between RH and LH structures are attributed to nanoscale sample defects. The broad nature of the resonance at ~550nm may in part be attributed to d-sp interband transitions for Au at this wavelength and/or excitation of a bulk plasmon. The NIR resonance at ~1000nm is near the spectral limits of the spectrometer therefore subsequent discussion will focus on the highlighted asymmetric resonance at ~740nm.

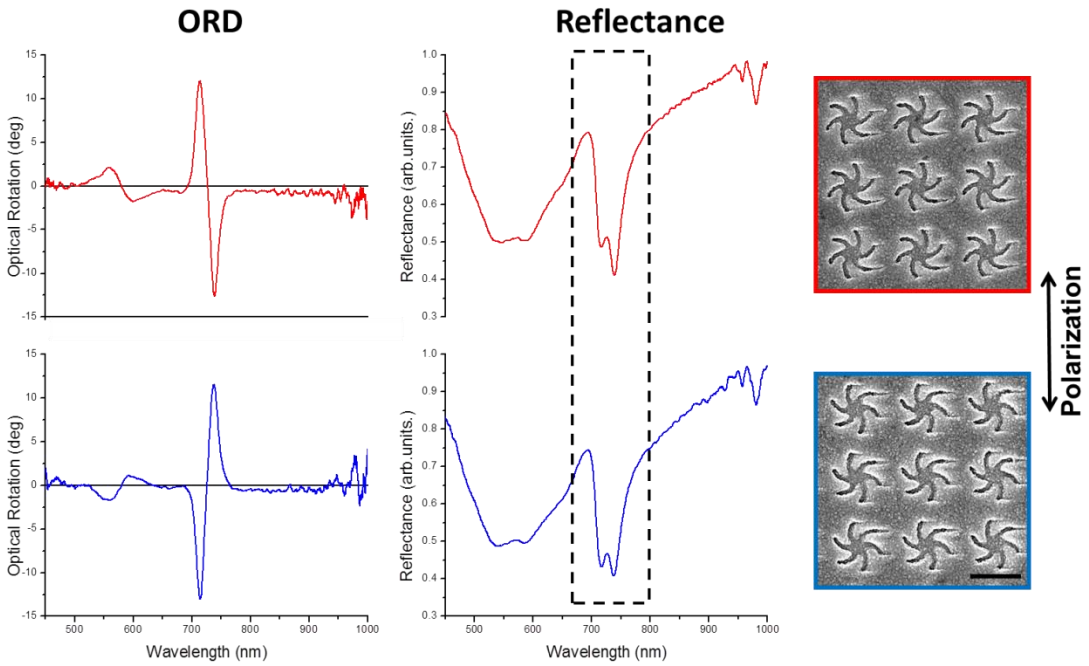

Figure 4.03: ORD and reflectance spectra of RH (blue) and LH (red) shurikens recorded in 10mM tris buffer with corresponding SEM images. The polarisation of the incident light during reflectance measurements is denoted in by the black arrow. The resonance of interest in the reflectance spectra is highlighted.

The polycarbonate from which the nanostructures are fabricated may potentially be birefringent due to the nature of the injection moulding process. To determine whether this effect is present in TPS nanostructures we measure the ORD of the flat Au at ~650-900nm measured through the back face i.e. the incident light propagates through the polycarbonate before reflecting off the Au surface. These results are compared with the ORD measured from an Au film on amorphous Si over the same wavelength range (figure 4.04a). The difference in lineshape between the ORD of Au on polycarbonate and Si is found to be minimal. We conclude that there is an absence of polymer birefringence in our region of interest therefore this negates the possibility that the TPS optical activity is a product of the optical anisotropy of the polymer substrate.

The reproducibility of nanostructure fabrication was tested by measuring the ORD in tris buffer of five different substrates (figure 4.04b, table 4.01). The standard deviation of the ORD peak position is approximately ± 2nm whilst the deviation in peak to peak height between samples is ± 3^{o}. The deviation in resonance positions and peak height are most likely due to variations in nanoscale sample defects and slight differences in the alignment of the microscope for each sample. The extremely small variations in the ORD spectra and

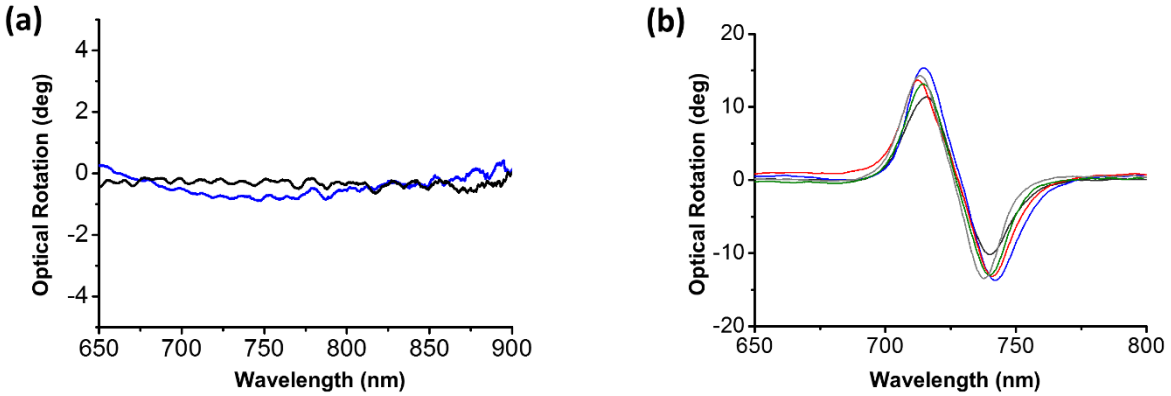

Figure 4.04: (a) ORD of 100nm Au measured through the back face of the TPS slide (blue) and from 100nm Au on an Si wafer (black). **(b)** ORD of LH gammadions from five different TPSs measured in 10mm tris buffer.

Sample	Peak 1	Peak 2	ORD pp
1	715.6	740.1	22.2
2	714.9	742.2	28.98
3	712.4	740.9	26.9
4	714.5	740.0	26.2
5	713.4	737.7	27.92
Std. dev.	1.3	1.6	2.6

Table 4.01: Resonance positions of the maximum and minimum ORD peaks and peak to peak heights of five separate substrates measured in 10mM tris buffer. The bottom row displays the standard deviation for each column.

negligible birefringence effects verify the reproducibility of the injection moulding process and confirm the suitability of polycarbonate TPS nanostructures as a candidate for a high-throughput mass produced nanotechnology.

4.2.3 Au Thickness Dependence of Shuriken Reflectance Spectra

The optical properties of the TPS shurikens are found to be highly dependent on the thickness of the Au film. The Au thickness dependence of the reflectance spectra for the resonance centred on ~740nm is displayed in figure 4.05a. For Au thickness of ≤30nm there exists an asymmetric reflectance dip for RH and LH shurikens which is characteristic of a Fano resonance. As discussed in section 2.2.7 a Fano resonance in plasmonic systems arises due to the destructive interference between a spectrally overlapping broad optically bright

mode and a narrow dark mode. Furthermore, for interference phenomena in metamaterials the appearance of a Fano lineshape is typically associated with low levels of interference. For Au film thickness ≥40nm the reflectance spectra continue to display an asymmetric dip,

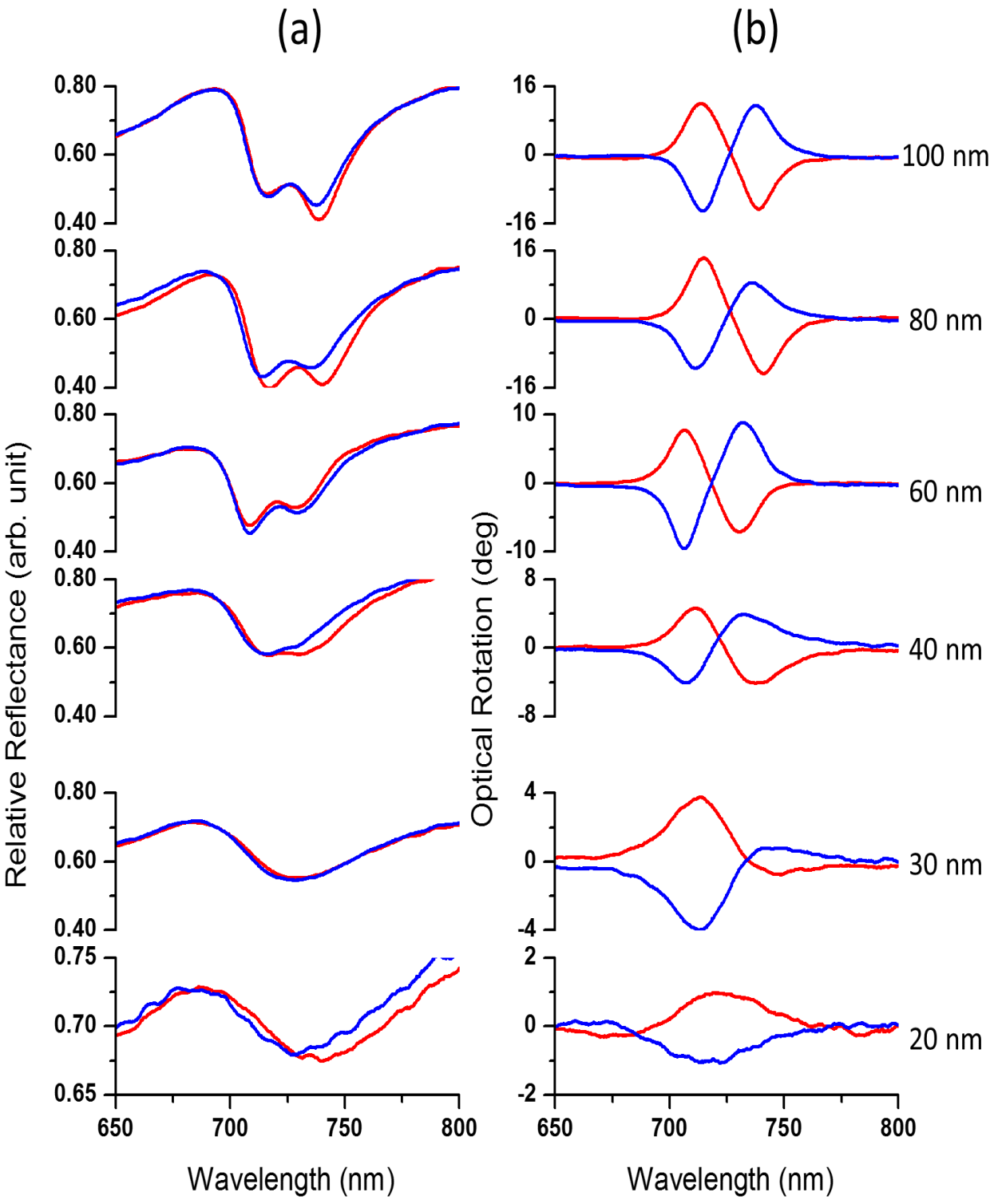

Figure 4.05: Dependence of RH (blue) and LH (red) shurikens reflectivity **(a)** and ORD **(b)** on Au film thickness.

however, a peak of enhanced reflectivity within this dip is observed which becomes increasingly apparent as the Au film thickness increases. As discussed in section 2.2.7 the appearance of such dips have been previously reported in a solid-inverse plasmonic system and are attributed to an electromagnetically induced transparency (EIT)–like phenomenon[14]. In photonic metamaterials this EIT-like effect is closely associated with the appearance of Fano resonances and arises due to large levels of interference between bright and dark modes. Thus, we propose that TPS shurikens with Au ≤30nm generate a Fano resonance whilst substrates with Au ≥40nm induce a plasmonic EIT effect.

In order to understand this thickness dependency in the reflectance spectra, it is necessary to consider the interaction between the solid and inverse structures that constitute the hybrid TPS shuriken. Generally, solid structures are interpreted in terms of electric modes and inverse structures in terms of magnetic modes[14]. This is an intuitive model; EM radiation incident on a solid structure invokes a polarisation within the medium generating a resultant electric field associated with the nanostructure. In contrast, EM radiation incident on an inverse structure invokes a ring current flowing around the nanostructure shaped void which generates a magnetic moment within the inverse structure. Hence, coupling between structures in solid-solid and inverse-inverse plasmonic systems can be easily understood through the interaction of electric and magnetic modes respectively. For hybrid TPS shurikens, solid structures are spatially located directly below inverse structures and both possess the same symmetry. This means coupling between the electric modes of the solid structure and magnetic modes of the inverse structure occurs. Thus, the thickness dependency of the reflectance lineshape can be explained in terms of the strength of this electric/magnetic coupling. Thin Au films (≤30nm) possess weak coupling between electric/magnetic modes whilst thick Au films (≥40nm) display strong electric/magnetic coupling. Consequently, the lineshape variations in figure 4.05 reveal that through varying the Au thickness we can control the strength of the electric/magnetic coupling which mediates the level of interference between the bright/dark modes of the TPS. The explicit nature of these bright and dark modes of the shuriken is discussed in section 4.2.6.

4.2.4 Au Thickness Dependence of Shuriken EM Fields

The thickness dependence of the electric/magnetic mode coupling is also manifested in the intensity and distribution of the EM fields associated with the constituent solid/inverse

structures. The presence of strong electric and magnetic fields and subsequent coupling of these fields renders the interpretation of TPS shuriken modes more complex. In order to simplify this problem we follow the approach of Hentschel et al [14] when modelling solid-inverse systems and interpret the coupling of electric and magnetic modes primarily in terms of their associated electric fields as this provides a clearer visualization of coupling between structures.

The simulated z component of the electric field (Ez) and magnetic field (Hz) distribution within the vicinity of the nanostructures for the top and bottom surfaces of a 30nm Au TPS is displayed in figure 4.06. As expected, for the top surface the Ez fields (g) are located on the metal film surrounding the inverse structure whilst the Hz fields (k) are strongest in the shuriken shaped void. Conversely the Ez field of the bottom surface (h) is mainly within the solid nanostructure whilst the Hz field (l) is more significant outside the solid shuriken. From figure 4.06 we find that the overall strength of the Hz field is much greater than that of the Ez field which is not altogether unexpected as the excitation field is initially incident upon the inverse structure therefore a significant amount of energy is absorbed before the EM wave is incident on the solid structure. Evidently, the top and bottom surfaces display different spatial distributions and phase for both the Ez and Hz components in substrates with Au ≤30nm. This is symptomatic of weak coupling between the electric/magnetic modes of the TPS as the thin Au film means Ez of the solid and inverse structure and Hz of the solid and inverse structure only weakly interact. Despite the continuous Au film connecting the top and bottom surfaces, the constituent structures are effectively behaving as two separate systems therefore there exists low levels of coupling between electric/magnetic modes.

As discussed, for Au thickness ≥40nm there is greater coupling of electric/magnetic modes. The spatial distribution and field strength of Ez and Hz in a 100nm Au TPS is displayed in figure 4.06. Similar to the thin films, the Ez fields are associated with the solid nanostructure/top Au surface whilst the Hz fields are more strongly associated with the shuriken void. The Ez fields of the top and bottom surface (e,f) now have matching spatial distributions but are out of phase whilst the Hz fields of the top and bottom surface (i,j) also have matching spatial distributions but are in phase. These out of phase Ez fields and in phase Hz fields are symptomatic of optimal coupling between the solid and inverse

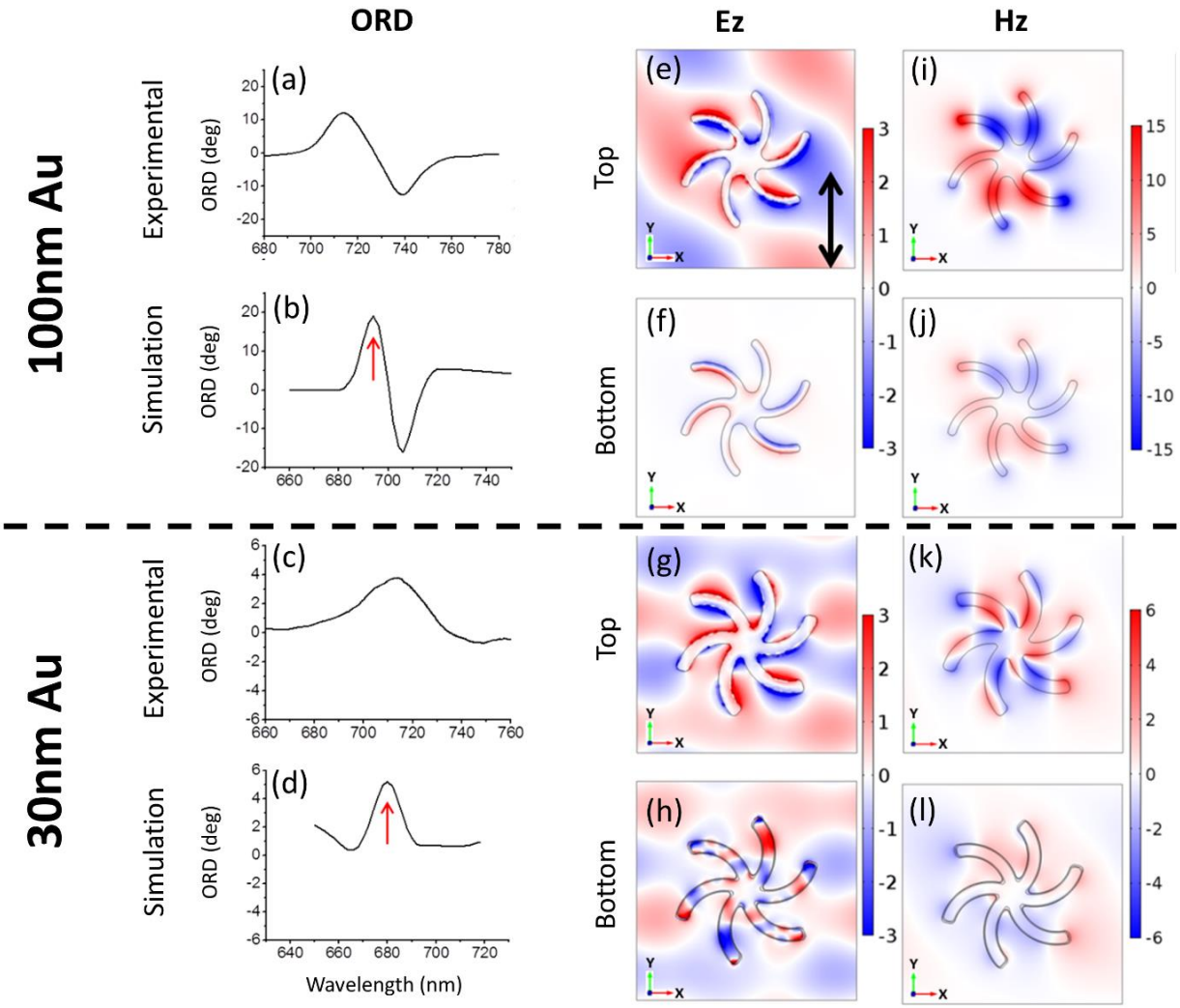

Figure 4.06: EM modelling of 100nm **(b)** and 30nm **(d)** TPS shuriken ORD spectra and comparison with experimentally obtained results **(a, c)**. The arrows in **(d)** and **(b)** indicate the wavelength at which the z components of the Ez **(e-h)** and Hz **(i-l)** fields were modelled for the 30nm and 100nm Au films respectively. The black arrow in **(e)** represents the polarisation of the incident field for all simulations **(e-l)**. The units for the side bar of the Ez fields are (MV/m) and for the Hz fields are ($1x10^{-4}$ A/m). The colour range is limited to create comparable scales for all plots.

structure. In order to provide an understanding as to the reason out of phase electric fields signify optimal coupling we consider the top and bottom surfaces as an electrical circuit. The incident electric field induces a motion of charge in the substrate. As with an electrical circuit two poles of opposite polarity must be coupled in order for charge to flow. The thicker Au film facilitates strong coupling between the top and bottom surface allowing a flow of charge between these two surfaces. Hence, the top and bottom surface Ez fields must have equivalent spatial distributions and opposite polarity i.e. out of phase electric fields. The in phase nature of the top and bottom surface Hz fields is predominantly

attributed to the extension of the intense top surface Hz component towards the bottom surface.

Hence, considering the reflectance data in section 4.2.3 and the EM field simulations for thin film and thick film TPSs we can now rationalise the effect of electric/magnetic coupling in the substrate. Thin film (≤30nm) TPSs possess low levels of electric/magnetic coupling which means the Ez and Hz fields of the solid/inverse structures are not related. This weak coupling generates low levels of interference between the bright/dark modes of the shuriken producing a Fano resonance. In contrast, Au films ≥40nm generate strong electric/magnetic coupling resulting in the Ez and Hz fields of the solid/inverse structures having a related phase/spatial distribution. This strong coupling gives rise to large levels of bright/dark mode interference producing an EIT effect in the reflectance spectra.

4.2.5 Au Thickness Dependence of TPS Chirality and Optical Activity

In addition to controlling the reflectance lineshape, increasing the Au thickness also changes the lineshape and intensity of the shuriken ORD spectra (figure 4.05b). Thin film (Au ≤30nm) substrates display a weak ORD wherein the spectrum possesses a single peak. In contrast, for films with Au ≥40nm the ORD is increasingly more intense and displays a bisignate profile. This dependence of ORD lineshape and intensity on Au thickness means that the strength of the electric/magnetic coupling also controls the optical activity of the substrate.

In order to explain this thickness dependent behaviour, we assume the optical activity in the TPS to be analogous to that of molecular systems. Moscowitz et al classified natural optical activity of a chromophore in molecular systems in terms of two limiting types[15]: the inherently chiral chromophore in which the electronic states are delocalized over a chiral nuclear framework so that parallel components of electric and magnetic dipole moments are fully allowed for all transitions and may be pictured as a single helical oscillator (SHO); and the inherently achiral chromophore which requires coupling with the chiral environment. For an achiral chromophore there are two distinct coupling mechanisms: dynamic coupling and static coupling. The dynamic coupling mechanism can be interpreted as an exciton model in the case of degenerate transitions on two identical chromophores whereby the electrodynamic fields of one chromophore excited by incident radiation perturbs the second chromophore. In plasmonic metamaterials this can be described as a

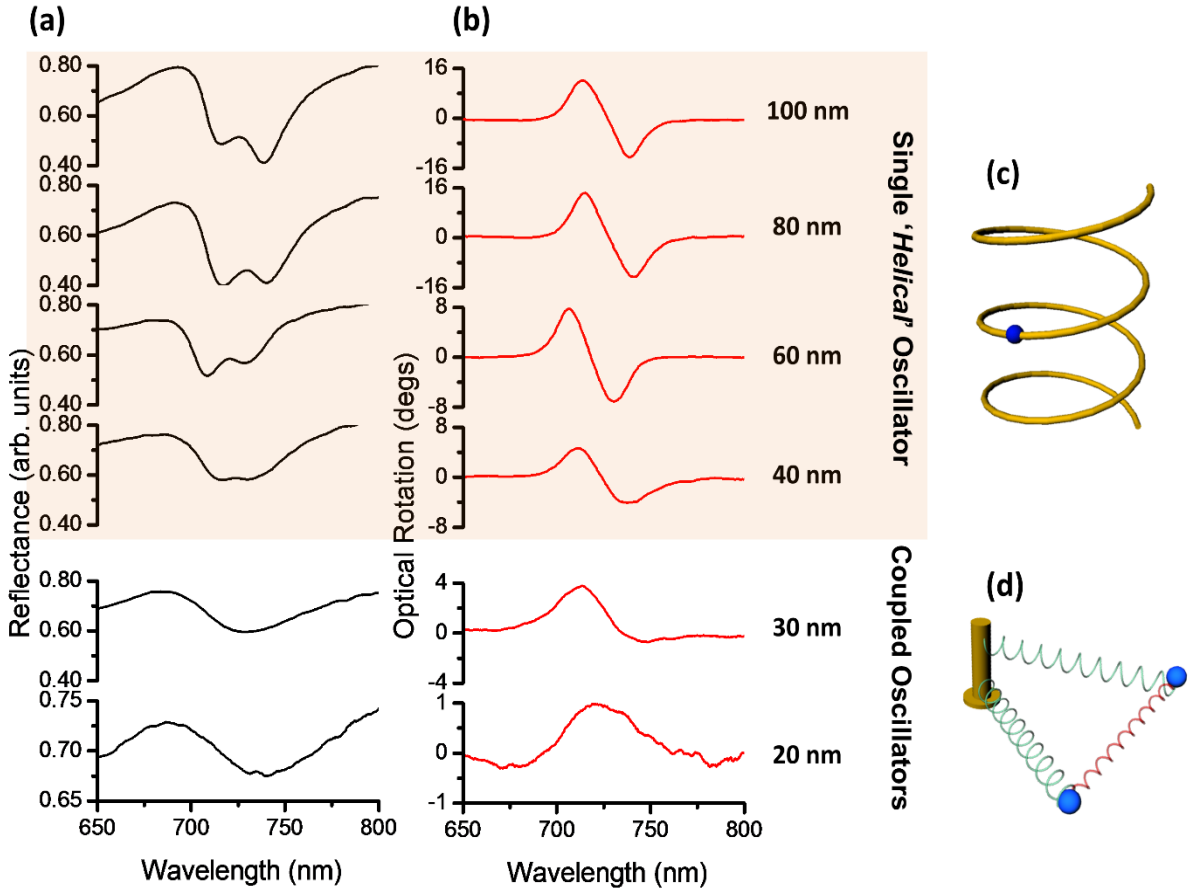

Figure 4.07: Effect of Au thickness on reflectance **(a)** and ORD **(b)** collected from LH TPS shurikens immersed in 10mM tris buffer. Graphic representation of **(c)** SHO and **(d)** Born-Kuhn (coupled oscillator) models of chirality. Pink highlighted region corresponds to ORD lineshapes typical of the Kauzman model and non-highlighted region relate to ORD lineshapes associated with Born-Kuhn model.

plasmonic realization of the Born-Kuhn model of chirality (section 2.1.3). The second coupling mechanism is "static coupling" whereby mixing of electric and magnetic transition dipole moments on the same inherently achiral chromophore arise due to perturbations from electrostatic fields of other groups in the chiral environment. This coupling mechanism is related to the Kauzman model of chirality (section 2.1.3.) and similar to the inherently chiral chromophore may be pictured as a SHO.

The ORD lineshape displayed by thin film (Au ≤30nm) TPSs is characteristic of the Born-Kuhn model [16] which is consistent with the aforementioned weak electric/magnetic coupling of these systems. In this weakly coupled system, the spatial distributions and phase of the Ez and Hz fields on the top and bottom surface (figure 4.06) are unrelated therefore the ORD displays a lineshape typically associated with two separate dynamically coupled achiral

chromophores (figure 4.07). TPS with greater electric/magnetic coupling (Au ≥40nm) display ORD lineshapes associated with static coupling or an inherently chiral chromophore [16], the latter of which is more likely due to the considerable intensity of the ORD which is typical of chiral chromophores. The distribution of the Ez and Hz fields of the top and bottom surface agree with this assignment as they possess the same spatial distributions and distinct phase relationships. In other words, the Ez and Hz fields are related over the entire solid-inverse system analogous to the delocalization of parallel electric and magnetic transition dipole moments in an inherently chiral chromophore.

This optical activity in TPS shurikens arises due to the generation of evanescent fields around the nanostructure which possess a chiral asymmetry. These fields are generated by scattering of linearly polarised light by the TPS nanostructures which create spatially overlapping electric and magnetic fields with components parallel to each other at the Au surface. In section 2.1.4., we introduced function 9 first proposed by Tang et al [17] in order to parameterise the asymmetry of chiral EM fields. We have employed this chiral asymmetry parameter to model the chirality of evanescent fields generated around the hybrid structure for both the strongly coupled (100nm Au) and weakly coupled (30nm Au) solid-inverse system (figure 4.08a-d). Both cases are similar in that fields with chirality greater than that observed for circularly polarised light (C >1) are generated predominantly along the length of the arms and between the gaps of adjacent arms. The fields with the greatest chirality are situated at the top surface around the shuriken void whereas the chirality of fields associated with the solid structure at the bottom surface is weaker. This difference in chirality between the top and bottom surface is explained by looking at the relative Ez and Hz field strengths. The top surface facilitates the presence of intense Ez and Hz fields resulting in strong overlap between these components generating EM fields with a large chiral asymmetry. However, the intensity of the Ez and Hz fields associated with the bottom surface is significantly weaker. This results in a weaker interaction between Ez and Hz at the lower surface which accounts for the reduced chirality. Similarly, the relative strengths of the Ez and Hz components account for the discrepancies in chirality between the 30nm and 100nm Au nanostructures. In this case the increased strength of the Ez and Hz fields in the 100nm TPS compared with the 30nm Au TPS is responsible for the overall larger chirality of evanescent fields in the thicker films. It is important to note that fields with

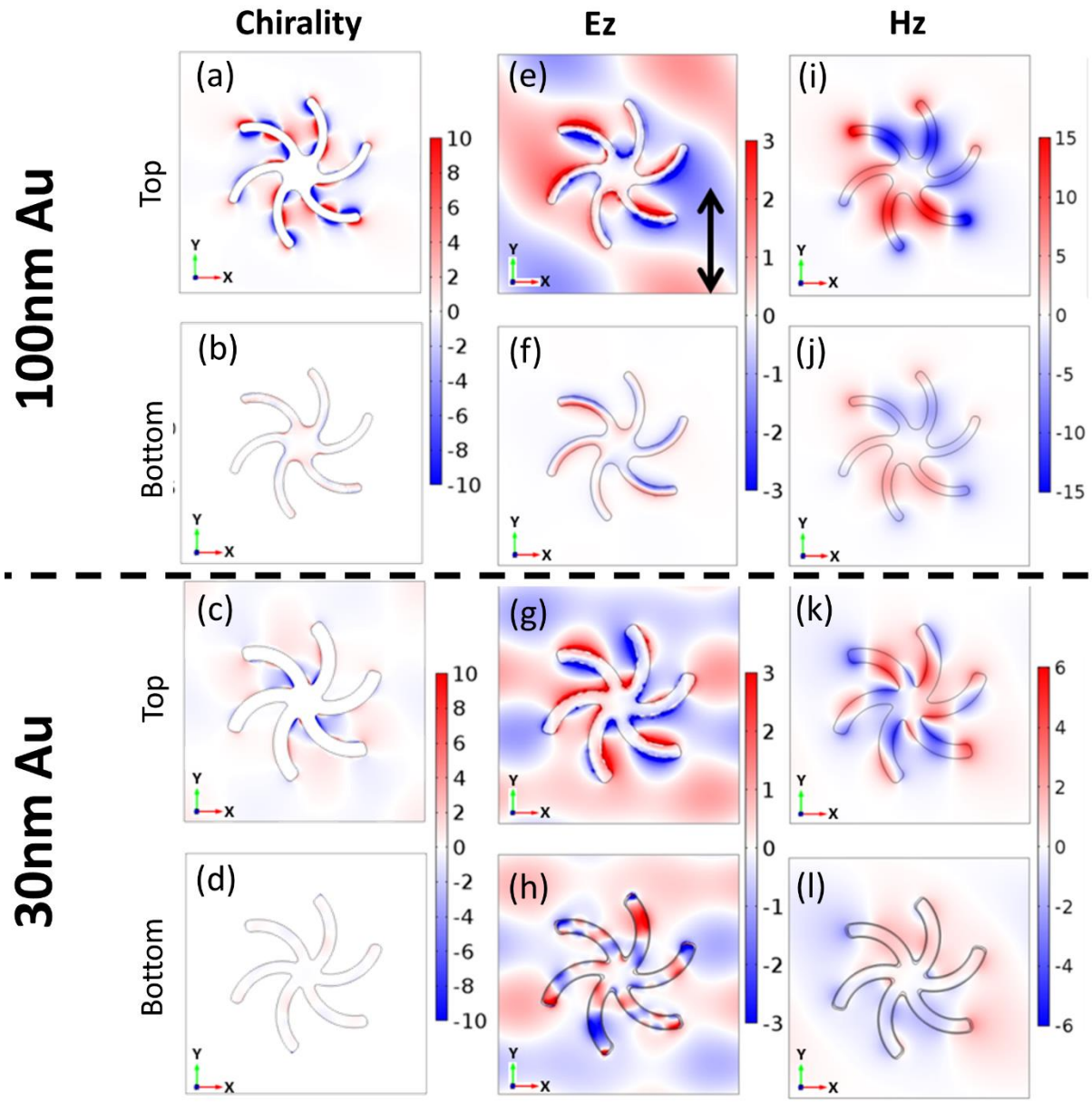

Figure 4.08: Simulation of chirality of z component of EM field **(a-d)** and associated Ez **(e-h)** and Hz **(i-l)** field strength and distribution of top and bottom surfaces. The upper half contains plots for 100nm Au TPS shurikens and the lower half corresponds to 30nm Au TPS shurikens. Scale of chirality normalized to values of circularly polarised light, units for the Ez fields are (MV/m) and for the Hz fields are ($1x10^{-4}$ A/m). The black arrow in (A) indicates electric field polarisation of incident EM wave for all plots. The colour range is limited to create comparable scales for all plots.

opposite chirality are observed on the same nanostructure due to a variation in the phase of Ez and Hz across the system. However, there is an excess of one field handedness which means there remains an overall net chirality associated with the shuriken which results in the observed optical activity.

These differences in ORD lineshape and magnitude of C imply that the optical activity and model of chirality in injection moulded nanostructures can be manipulated through simply varying the thickness of the Au film. Hence, the strength of coupling between the electric/magnetic modes modulates the optical activity in the system from two dynamically coupled electric dipole transition moments to an inherently chiral system wherein electric and magnetic dipole transition moments overlap. This simple process of varying the Au film thickness represents a significant advantage over other nanostructure fabrication methods which require complex geometrical iterations in order to modify the optical behaviour[14, 18].

4.2.6 Hybridisation Scheme

As we have discussed, the optical properties of the TPS shurikens are influenced by the Au thickness which controls the coupling of the electric/magnetic modes. Consequently, this coupling of electric/magnetic modes leads to the generation of hybrid plasmonic modes. In order to provide a simple, intuitive understanding of the hybridisation and structural tunability of the plasmonic system it is necessary to construct a hybridiation scheme (figure 4.09) in a manner analogous to molecular orbital hybridisation [19]. As with molecular hybridisation, the basis of a plasmonic hybridisation scheme is found in the symmetry of the system. Hence, we conduct a symmetry analysis of the solid/inverse structures and their associated modes. The solid and inverse structures have the same shape therefore the electric and magnetic modes are symmetry equivalent (C_6 symmetry) and belong to the C_6 point group. Using the C_6 character table (Appendix 4.4.1) we calculate the irreducible representation for the electric and magnetic modes. We find that the electric and magnetic modes of the solid/inverse structure belong to the A, B, E_1 and E_2 symmetry species. In molecular orbital hybridisation the basis functions associated with each symmetry species directly relate the symmetry of molecular orbitals and their interaction with EM radiation. This concept may be applied to the excitation of the electric/magnetic modes of the shuriken. From the C_6 character table we find that the A and E_1 symmetry species contain linear basis functions which correspond to dipolar modes rendering them optically bright. The A mode may only be excited by vertical components of the incident field (Ez and Hz) however these are not accessible in the normal incidence experimental geometry of the polarisation microscope. Hence, the bright mode is the E_1 mode and is excited by linearly

polarised components in the xy plane or circularly polarised components of the incident field. The B and E_2 modes are both optically dark i.e. an incident EM field does not induce a dipole oscillation for these symmetry species. The lowest energy dark mode is the E_2 mode as this possesses a quadrupolar basis function whereas the B mode may only be excited by higher order multipoles. As a result of this symmetry analysis, we find that the solid/inverse structures each possess a bright dipolar mode with E_1 symmetry and a dark quadrupolar mode with E_2 symmetry.

As discussed, the consequence of the solid/inverse structures having equivalent symmetry is that the electric dipole (quadrupole) and magnetic dipole (quadrupole) modes can hybridise. This is illustrated using a hybridisation scheme (figure 4.09). Hybridisation of electric/magnetic modes generates both in-phase (bonding) and out-of-phase (antibonding) hybrid modes with the former having the lowest energy. The in-phase and out-of-phase dipole hybrid modes are referred to as $D_{(E+M)}$ and $D_{(E-M)}$ respectively. Similarly, the in-phase and out-of-phase quadrupolar hybrid modes are labelled $Q_{(E+M)}$ and $Q_{(E-M)}$. From this we find that the Fano resonance/EIT phenomena reported in section 4.2.3 arises due to the

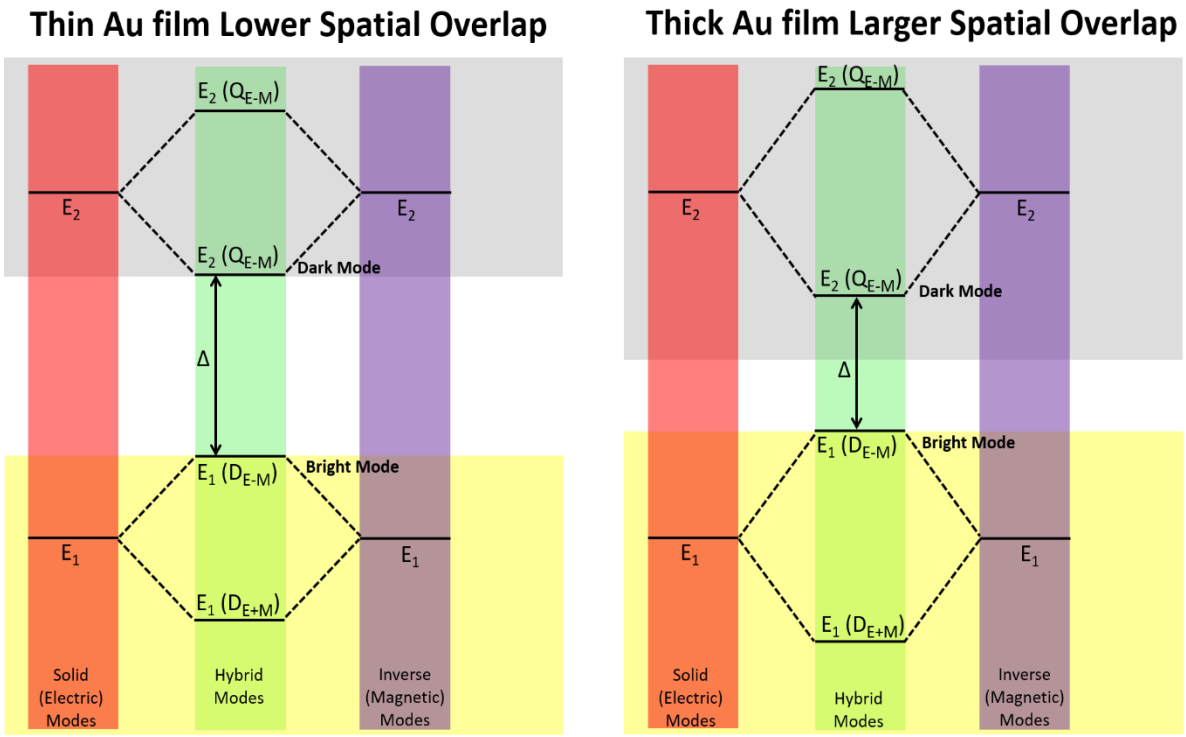

Figure 4.09: Qualitative representation of effect due to varying the Au thickness on hybridisation between electric modes (red) and magnetic modes (purple). Δ is the energy separation between the bright and dark modes.

interference between a bright out-of-phase dipolar hybrid mode ($D_{(E-M)}$) and a dark in-phase quadrupolar hybrid mode ($Q_{(E+M)}$). The assignment of ($D_{(E-M)}$) as the bright mode agrees with the EM modelling of the electric fields generated at the top and bottom surfaces (figure 4.06) which display anti-phase electric field distributions around the shuriken arms.

To summarise, the Au thickness controls the coupling (hybridisation) between the electric/magnetic modes. This in turn modulates the splitting of the in-phase and out-of-phase dipolar/quadrupolar hybrid modes which determines the extent of the interference between ($D_{(E-M)}$) and ($Q_{(E+M)}$), in other words, the magnitude of the energy gap (Δ). In addition, reflectance lineshape variations occur concurrently with changes in the ORD as the level of chirality associated with the shuriken also depends on the coupling of the electric and magnetic modes.

The molecular approach to the hybridisation of plasmonic systems has only been performed for relatively simple structures such as rods and nanospheres. The fields generated around solid/inverse shurikens are significantly more complex. We provide a simplistic view of the symmetry of the bright and dark modes by representing each shuriken arm as a dipole (figure 4.10). Figure 4.10a is derived from the modelling in figure 4.06e-f whereby opposite ends of the shuriken arms are of opposite polarity whilst the central region contains both

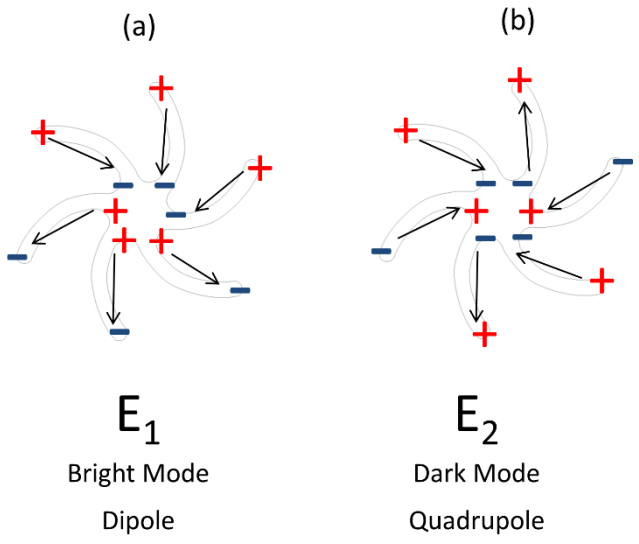

Figure 4.10: Illustration representing the distribution of individual dipoles of the shuriken for **(a)** the E_1 dipolar mode and **(b)** the E_2 quadrupole mode.

polarities. Using the C_6 character table we have ascertained that this representation is the bright E_1 mode as a rotation of the C_2 axis leads to an inversion of the polarities of each arm. Furthermore, this observation corroborates with the EM modelling of the electric fields for solid and inverse structures in figure 4.06 whereby a C_2 rotation results in the inversion of polarity of the EM fields situated on the shuriken arms. Figure 4.10b represents the dark quadrupolar E_2 mode of the shuriken as a C_2 rotation does not result in an inversion of polarity as dictated by the character table.

Nanostructures are arranged periodically therefore it remains a possibility that the observed optical properties of the TPS arise due to this arrangement. The shurikens are arranged in a square lattice which ordinarily belongs to the C_4 point group. However, the presence of the six fold symmetric structures reduces the symmetry of the extended lattice to C_2 (appendix 4.5.2). If we conduct a symmetry analysis for the C_2 symmetry of the array we find that the associated symmetry elements are A and B which are both dipole active. This means excitation of a Fano resonance/EIT would not be possible as there is an absence of a dark mode excitation. As a result, we attribute the chiroptical properties of our nanostructure arrays to the excitation of modes associated with the individual nanostructures themselves.

At this point, it is important to note that the aforementioned bright/dark mode coupling model requires further theoretical analysis before it may be confirmed. Thus, it cannot be discounted that the EIT-like splitting of the two small peaks at ~740nm for Au films ≥40nm may infact arise due to the coupling of two bright shuriken modes ($D_{(E-M)}$ and $D_{(E+M)}$). In order to confirm our proposed Fano/EIT model, it is necessary to perform curve fitting of the resonance to the coupled oscillator model outlined in section 2.2.7; however, this is beyond the scope of this thesis.

4.2.7 Comparison with Lithographically Fabricated Structures

The optical activity of 100nm Au TPS shurikens is compared with that of lithographic 100nm Au shurikens of the same dimensions and periodicity fabricated on a silicon wafer (figure 4.11). The fundamental difference between these substrates is that injection moulded nanostructures are imprinted into the surface producing a solid-inverse system whilst lithographic shurikens are purely solid structures which are protruding from the Si surface. It is clear that the intensity of the ORD for lithographic structures (~1°) is an order of

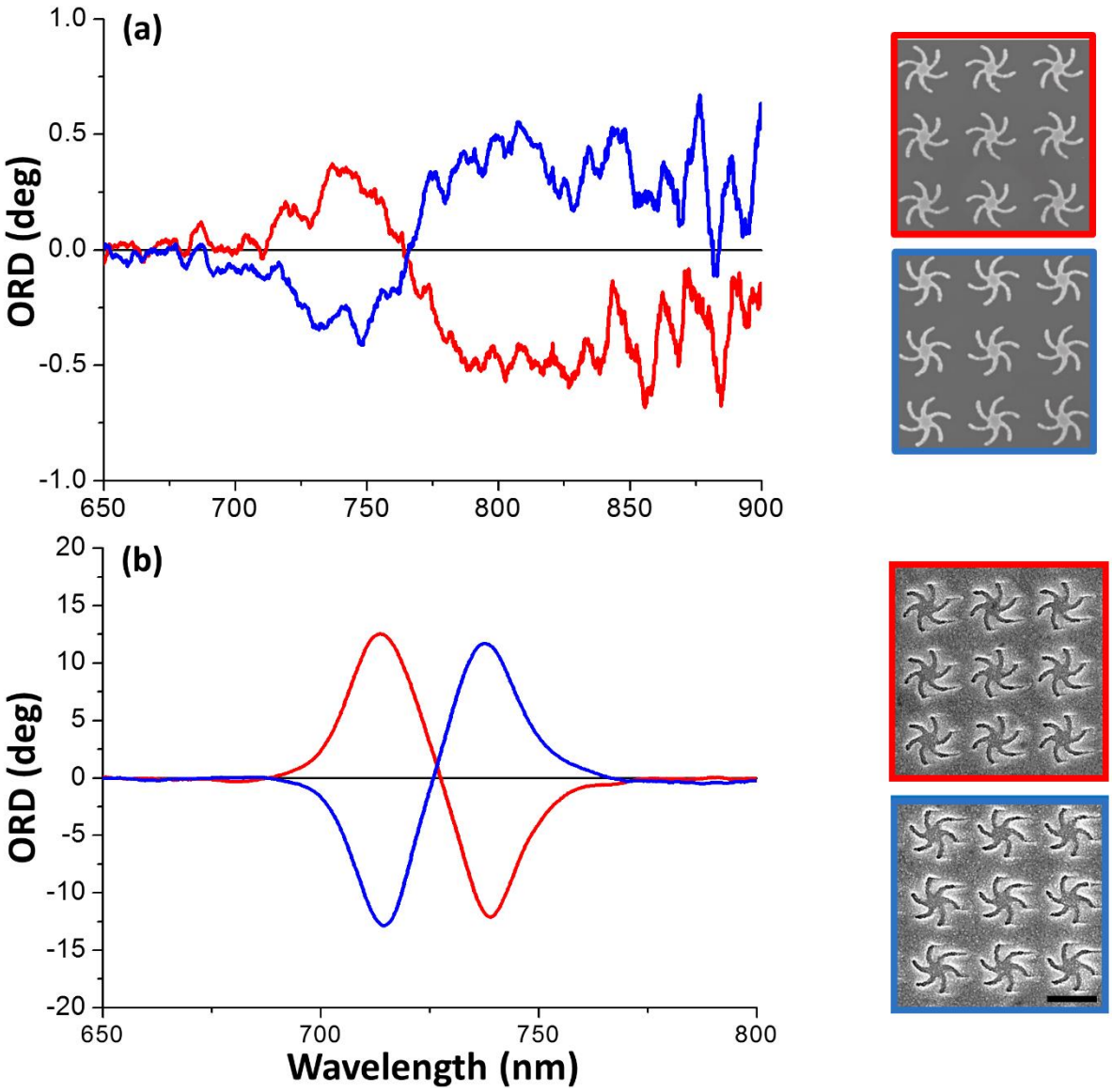

Figure 4.11: ORD spectra and corresponding SEM images for RH (blue) and LH (red) shurikens fabricated using **(a)** electron beam lithography and **(b)** injection moulding. ORD spectra are recorded in 10mM tris buffer. The scale bar for SEM images is 500nm in length.

magnitude smaller than that of the TPS shurikens (~15°). Furthermore, the lineshape is only very slightly bisignate; therefore, this lithographic structure displays low levels of optical activity and is associated with the coupled oscillator model of chirality. In contrast, the 100nm Au TPS displays large levels of chirality associated with a SHO model of chirality due to strong overlap between parallel components of the nanostructure electric and magnetic fields. This comparison reveals that in addition to possessing simpler methods for fabrication and post-fabrication manipulation of optical properties, strongly coupled TPS nanostructures display significantly larger levels of optical activity. These large levels of optical activity displayed by the shuriken suggest that TPS substrates are potentially an

incisive probe of chirality and protein structure; therefore, in the following section we evaluate the TPS biosensing properties.

4.2.8 Protein Spectroscopy using TPS Nanostructures

The ultimate objective of this study into TPS nanostructures is to investigate the viability of such structures for the ultrasensitive spectroscopy of biomolecules. For chiral shurikens the scattering of light from the nanostructures results in the generation of chiral evanescent fields. These fields are more inherently chiral than circularly polarised light (CPL) as seen from the chirality modelling in figure 4.08. Hence, they may be a more incisive probe of biological structure than CPL. In order to exploit the presence of these fields we employ a novel form of plasmonic spectroscopy using TPS nanostructures referred to as "plasmonic polarimetry" (section 3.4.2).

Firstly, it is necessary to calibrate the experimental set up through measurement of an achiral solution. The resonance shift induced by salt solutions of increasing refractive index is found in figure 4.12a. As expected, the gradient of the resonance shifts for RH and LH 100nm Au structures are equivalent as the dielectric properties of the solution are isotropic meaning it has the same refractive index in both RH and LH chiral evanescent fields. This generates the negligible $\Delta\Delta\lambda$ values (4.12b) displayed for different salt solution concentrations. The refractive index sensitivity of the shurikens is found to be approximately 492.5nm/RIU. The refractive index sensitivity values of plasmonic

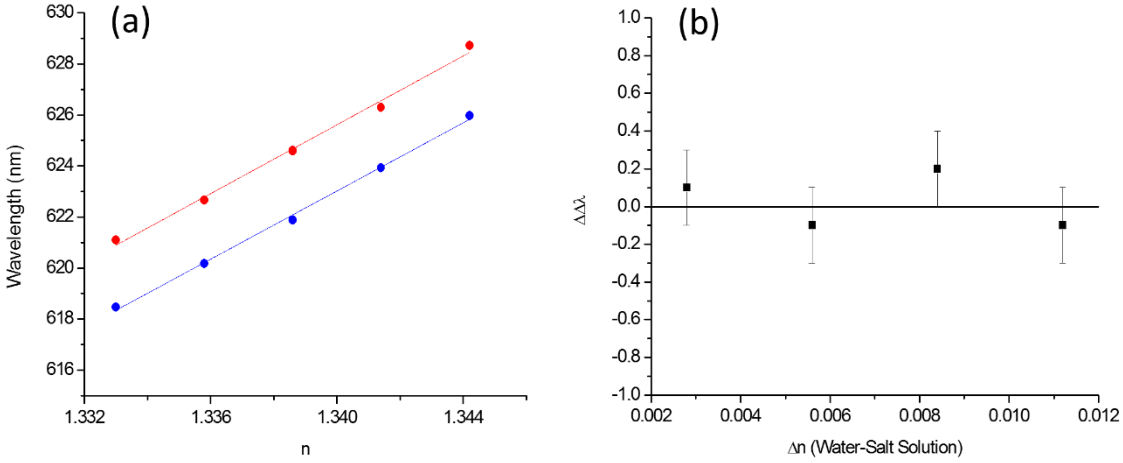

Figure 4.12: (a) Resonant wavelength as a function of increasing refractive index for RH (blue) and LH (red) shurikens. **(b)** $\Delta\Delta\lambda$ values for shurikens as a function of increasing difference in refractive index between salt solution and water.

metamaterials reported in other studies range from 100 nm/RIU to values as high as 1000nm/RIU for nanomaterials designed specifically for SPR measurements[20]. Thus, refractive index sensitivity of TPS substrates is in the middle of the established range; however, what distinguishes these nanomaterials is their ability to detect protein structure.

Previous spectroscopic measurements of biomolecules using chiral EM fields generated in the near field of lithographic plasmonic nanostructures displayed heightened sensitivity to proteins with large β-sheet content[1]. This sensitivity to β-sheet structures arises due to the anisotropic arrangement of this motif in the protein with respect to the sample surface.

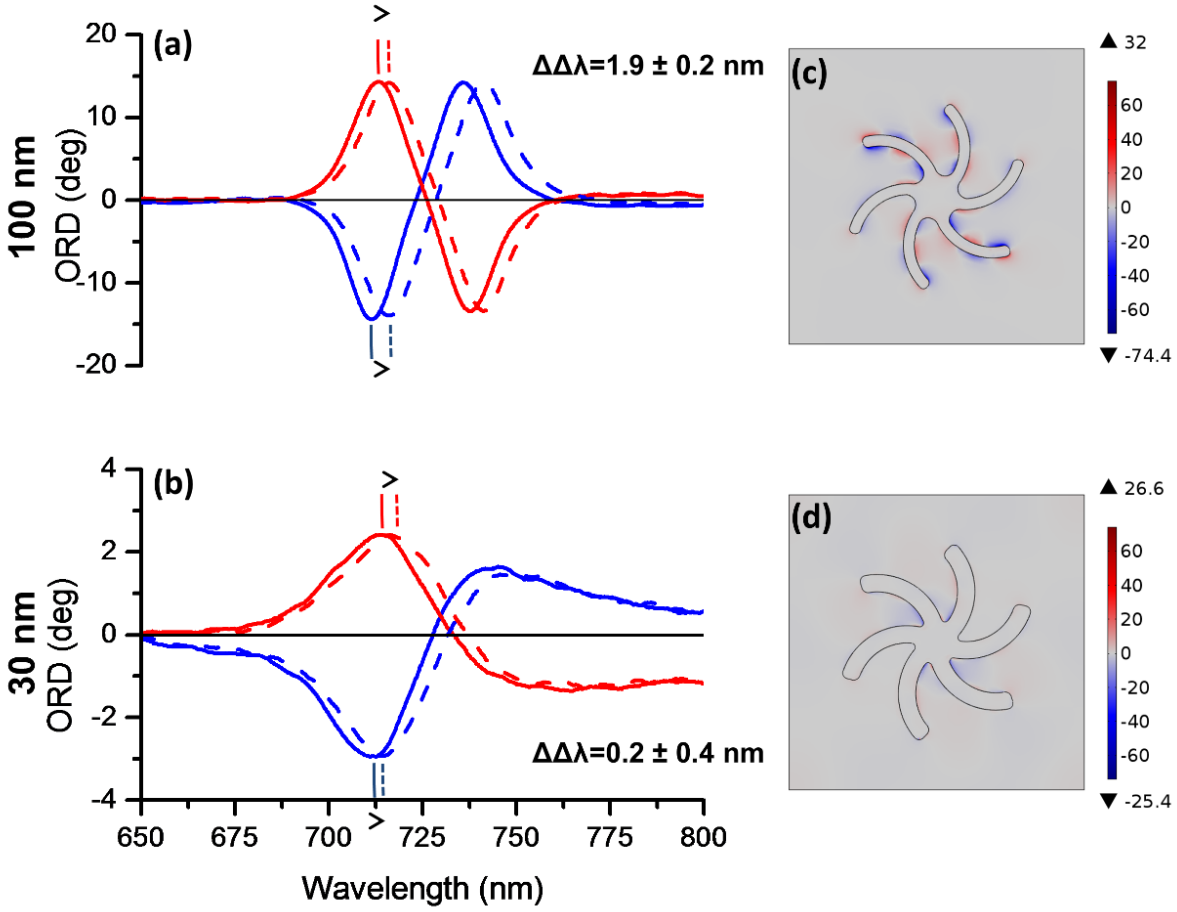

Figure 4.13: ORD spectra for **(a)** 100nm Au TPS and **(b)** 30nm Au TPS. Red lines correspond to LH shurikens and blue lines correspond to RH shurikens. The solid lines are measurements taken in 10mM tris buffer and dotted lines are measured when the sample is immersed in 1mg/ml Con A solution. The solid vertical bars highlight the position of measurement for the buffer and dotted vertical bars are the position for the Con A. ΔΔλ values are also given. EM modelling of the optical chirality of the top and bottom surface combined for **(c)** 100nm and **(d)** 30nm Au films are given for the wavelengths indicated in figure 4.06. Chirality values have been normalised to those of LH circularly polarised light.

The steep field gradients in the nanostructure near-field enhance the quadrupolar contributions to optical activity for anisotropic β-sheet structures[21] whilst quadrupole contributions are averaged to zero for proteins with large α-helical content due to the isotropic arrangement of this motif in biomolecules with respect to the Au surface. This results in a large spectroscopic fingerprint for β-sheet proteins and insensitivity to α-helical proteins. Thus, spectroscopic measurements using chiral plasmonic nanostructures indirectly measure the secondary structure through the isotropic/anisotropic orientation of these motifs with respect to the Au surface[2]. Following this, we investigate the effect of adsorption of the predominantly β-sheet protein, Concanavalin A, on the nanostructure spectroscopic response. The ORD spectra and $\Delta\Delta\lambda$ values upon Con A adsorption to 100nm Au TPS are found in figure 4.13a. The $\Delta\Delta\lambda$ value for Con A is significantly outside experimental error (+1.9± 0.2) which confirms that similar to previous measurements [1]; TPS shurikens are sensitive to the adsorption of β-sheet secondary structure motifs. The sensitivity limits of TPS shurikens also compare favourably with previous spectroscopic measurements using lithographic nanostructures. Previous SPR measurements reveal that $1281x10^{-6}pg\mu m^{-2}$ of Con A adsorbs on a bare Au substrate[1]. The area of the nanostructure array is $90{,}000um^2$ therefore we estimate that 115pg of Con A is adsorbed onto the surface which corresponds to a molar concentration of ~1 femtomole.

In addition to undertaking measurements using substrates with 100nm Au films (figure 4.13a) we also test the performance of the 30nm shurikens through adsorption of Con A (figure 4.13b). These weakly coupled substrates show a lack of asymmetry as the $\Delta\Delta\lambda$ value is 0.2±0.4. The explanation for this reduced sensitivity of the thin film substrate originates from the nature of the coupling between the electric/magnetic modes of the system. As discussed, optical activity of nanostructures in the linear regime requires the overlap of parallel components of the electric and magnetic field in order to generate chiral evanescent fields in the near field of the nanostructure. Thin film substrates have poor mixing of electric and magnetic modes hence the chirality of EM fields associated with the structure is significantly reduced compared to the strongly coupled 100nm Au films. As a result, there is a much weaker chiroptical interaction between adsorbed biomolecules and chiral EM fields in the thin film substrates which results in observation of the negligible plasmonic polarimetry response.

4.3 Conclusions

In this chapter we have introduced a hybrid solid-inverse nanostructured Au metafilm fabricated using a high through-put injection moulding procedure. The linear optical properties of these templated plasmonic substrates (TPS) are investigated through measurement of the reflectance and ORD whilst EM field simulations are employed to visualize electric and magnetic field intensities and distributions as well as the EM field chirality associated with the various surfaces. The lineshape of the reflectance spectra displays strong variations as a function of Au film thickness. The thickness of the Au film is found to control the coupling between the electric modes of the solid structure and the magnetic modes of the inverse structure. As the Au thickness increases, coupling between these modes increases and the reflectance dip lineshape changes from that of a Fano resonance (Au ≤30nm) to an EIT-like effect (Au≥40nm).

The effect of electric/magnetic coupling was also found to control the optical activity of the hybrid system, the effect of which is apparent in the lineshape of the nanostructure ORD spectra. As the coupling of the electric and magnetic modes increases the chirality of the EM fields associated with the nanostructure increases. This accounts for the change from a "coupled oscillator" model of chirality for weakly coupled thin films (Au≤30nm) to a "single helical oscillator" for TPS shurikens with strong electric/magnetic mixing. These changes in the chiroptical response of the substrate agree with the observed reflectance lineshape changes wherein Au films ≤30nm display behaviour typical of a weakly coupled system whilst thicker films (Au≥40nm) show characteristics associated with strong coupling. Consequently, this study reveals that in order to design nanostructures with enhanced optical activity it is necessary to optimize the coupling between electric and magnetic modes which allows the system to behave as an inherently chiral chromophore via the single helical oscillator model of chirality. Control of this coupling through simply varying the thickness of the Au film represents a significant improvement over nanoscale systems wherein the coupling may only be controlled through the time and cost consuming process of manipulating the sample geometry.

The coupling of electric/magnetic modes leads to the generation of hybrid plasmonic modes. To provide a qualitative overview of this electric/magnetic hybridisation we construct a hybridisation scheme analogous to molecular orbital hybridisation. From the Fano/EIT dip in

the reflectance spectra we suggest that interference between a bright and dark mode associated with the nanostructure occurs. Using a symmetry analysis, the optically bright mode is found to be an out-of-phase dipolar hybrid mode with E_1 symmetry ($D_{(E-M)}$) whilst the dark mode is a quadrupolar hybrid mode with E_2 symmetry($Q_{(E+M)}$). Simulations of the Ez fields associated with the top and bottom surfaces also support this assignment. Thus overall, increasing the Au film thickness results in greater coupling (hybridisation) of electric/magnetic modes which increases the splitting of in-phase and out-of-phase dipolar (quadrupolar) hybrid modes facilitating greater interference between $D_{(E-M)}$ and $Q_{(E+M)}$.

The potential of TPS nanostructures for spectroscopic measurements of biomolecules was investigated by introducing the newly developed technique of plasmonic polarimetry. This technique is analogous to conventional optical rotation in that the differential refractive index of chiral molecules in LH and RH chiral evanescent fields is measured. We find that similar to previous measurements with lithographic nanostructures TPS shurikens are sensitive to the adsorption of proteins with β-sheet secondary structures. Considering the cheap, high-throughput nature of the fabrication process, the ease of which their optical properties can be manipulated and their sensitivity to biological structure TPS nanostructures can be considered a prime candidate for the commercial exploitation of nanomaterials on an industrial scale.

4.4 References

1. E. Hendry, T.C., L. D. Barron, J. Johnston, N. Gadegaard,M. Popland, M. Kadodwala, *Ultrasensitive detection and characterization of biomolecules using superchiral field.* Nature Nanotechnology, 2010. **5**: p. 783-787.
2. R. Tullius, A.S.K., M. Rodier, B. Fitzpatrick, N. Gadegaard, L. D. Barron, V. M. Rotello, G. Cooke, A. Lapthorn, M. Kadodwala, *"Superchiral" spectroscopy: Detection of protein higher order hierarchical structure with chiral plasmonic nanostructures.* Journal of American Chemical Society, 2015. **137**: p. 8380-8383.
3. V. R. Manfrinato, L.Z., D. Su, H. Duan, R. G. Hobbs, E. A. Stach,K. K. Berggren, *Resolution Limits of Electron-Beam Lithography toward the Atomic Scale.* Nano Letters, 2013. **13**: p. 1555-1558.
4. Broers, A.N., *Resolution limits for electron-beam lithography.* IBM Journal of Research and Development, 2010. **32**(4): p. 502 - 513.
5. Altissimo, M., *E-beam lithography for micro-/nanofabrication.* Biomicrofluidics, 2010. **4**: p. 025603.
6. A.B. Christiansen, J.S.C., N. Asger Mortensen, A. Kristensen, *Injection moulding antireflective nanostructures.* Microelectronic Engineering, 2014. **121**: p. 47-50.
7. Gale, M.T., *Replication techniques for diffractive optical elements.* Microelectronic Engineering, 1997. **34**(3-4): p. 321-339.

8. N. Gadegaard, S.M., N.B. Larsen, *Biomimetic Polymer Nanostructures by Injection Molding.* Macromolecular Materials and Engineering, 2003. **288**: p. 76-83.
9. J.M. Stormonth-Darling, R.H.P., C. How, N. Gadegaard, *Injection moulding of ultra high aspect ratio nanostructures using coated polymer tooling.* Journal of Micromechanics and Microengineering, 2014. **24**(7): p. 075019.
10. Viana, J.C., *Development of the skin layer in injection moulding: phenomenological model.* Polymer, 2004. **45**: p. 993.
11. J. Bekesi, J.J.J.K., W. Michaeli, F. Klaiber, M. Schoengart, J. Ihlemann, P. Simon, *Fast fabrication of super-hydrophobic surfaces on polypropylene by replication of short-pulse laser structured molds.* Applied Physics A, 2010. **99**: p. 691-695.
12. K. Park, S.L., *Localized mold heating with the aid of selective induction for injection molding of high aspect ratio micro-features.* Journal of Micromechanics and Microengineering. **20**(3): p. 035002.
13. S.H. Yoon, N.G.C., J.S. Lee, J.G. Park, D.J. Carter, J.L. Mead, C.M.F. Barry, *Effect of Processing Parameters, Antistiction Coatings and Polymer Type when Injection Molding Microfeatures.* POLYMER ENGINEERING AND SCIENCE, 2007. **50**: p. 411-419.
14. M. Hentschel, T.W., S. Bagheri, H. Giessen, *Babinet to the half: Coupling of solid and inverse plasmonic structures.* Nano Letters, 2013. **13**: p. 4428-4433.
15. C.W. Deutsche, D.A.L., R.W. Woody, A. Moscowitz, *Optical Activity* Annual Review of Physical Chemistry, 1969. **20**: p. 407-448.
16. Barron, L.D., *Molecular Light Scattering and Optical Activity*. 2nd ed. 2004, Cambridge U.K.: Cambirdge University Press.
17. Cohen, Y.T.a.A.E., *Optical chirality and its interaction with matter.* Physical Review Letters, 2010. **104**: p. 163901.
18. N. Liu, T.W., M. Mesch, L. Langguth, U. Eigenthaler, M. Hirscher, C. Sonnichsen, H. Giessen, *Planar metamaterial analogue of electromagnetically induced transparency for plasmonic sensing.* Nano Letters, 2010. **10**: p. 1103-1107.
19. E. Prodan, C.R., N. J. Halas, P. Nordlander, *A hybridization model for the plasmon response of complex nanostructures.* Science, 2003. **302**: p. 419-422.
20. T. Chung , S.-Y.L., E. Y. Song, H. Chun,B. Lee, *Plasmonic nanostructures for nano-scale bio-sensing.* Sensors, 2011. **11**: p. 10907-10929.
21. Efrima, A., *Raman optical activity of molecules absrobed on metal surfaces: theory.* Journal of Chemical Physics, 1985. **83**: p. 1356-1362.

4.5 Appendix

C_6	E	C_6	C_3	C_2	$(C_3)^2$	$(C_6)^5$	Linear functions, rotations	Quadratic functions	Cubic functions
A	+1	+1	+1	+1	+1	+1	z, Rz	X^2+y^2, z^2	z^3, $z(x^2+y^2)$
B	+1	-1	+1	-1	+1	-1	-	-	$Y(3x^2-y^2)$, $x(x^2-3y^2)$
E_1	+1 +1	+ε +ε*	-ε* -ε	-1 -1	-ε -ε*	+ε* +ε	x+iy; Rx+iRy x-iy; Rx-iRy	(xz, yz)	(xz^2-yz^2) [x(x2+y2), y(x2+y2)]
E_2	+1 +1	-ε* -ε	-ε -ε*	+1 +1	-ε* -ε	-ε -ε*	-	(x^2-y^2, xy)	[xyz, $z(x^2-y^2)$]

Appendix 4.5.1: C_6 character table

C_2	E	C_2	Linear functions, rotations	Quadratic functions	Cubic functions
A	+1	+1	z, Rz	X^2, y^2, z^2, xy	z^3, xyz, y^2z, x^2z
B	+1	-1	x, y, Rx, Ry	yz, xz	xz^2, yz^2, x^2y, xy^2, x^3, y^3

Appendix 4.5.2: C_2 character table

Chapter 5: Nanoscale Control of TPS Surface Chemistry through Nanolocalised Water Heating

5.1. Introduction

The enhanced performance of photonic nanostructures in areas such as photovoltaics[1] and refractive index sensing[2] primarily arises due to an increase in the light-matter interaction at particular regions of the nanostructure. In the case of sensing it is preferable to place the analyte in nanoscale regions where the electromagnetic (EM) fields possess the desired properties. One of the most common methods to achieve this nanoscale control is manipulation of the nanostructure surface chemistry. Spatially controlled chemical functionalisation is performed in a number of ways using techniques such as dip pen lithography[3], ink jet printing[4] and direct laser patterning[5]. However, these "top down" techniques are inherently limited as they involve a direct patterning step whereby each individual nanoscale area is functionalised separately. This renders the process extremely time consuming resulting in a low through-put whilst the resolution is limited to ~50nm.

In this chapter we propose a high through-put "bottom up" procedure to achieve nanoscale control of surface chemistry on a templated plasmonic nanostructure (TPS). This technique exploits the thermal behaviour of TPSs and the surrounding water upon nanosecond pulsed laser irradiation to modify the structure of a thermally responsive polymer bound to the surface. Firstly, the thermal behaviour of TPS shurikens and the surrounding dielectric upon nanosecond pulsed laser irradiation was simulated by colleagues from Ohio University. Thermal calculations confirm the absence of nanolocalised temperature gradients within the metal nanostructures upon irradiation with such pulses. However, significant thermal gradients are found to exist in the water surrounding the shurikens. The water in the shuriken arms is found to be at a higher temperature than the water in the central region. We subsequently exploit these nanoscale thermal gradients in the surrounding water to generate a high-throughput method for nanoscale chemical functionalisation. This method is analogous to the protection/deprotection approach commonly employed in organic synthesis. The protection step simply involves the adsorption of a thermally responsive polymer onto the Au surface which inhibits the binding of biomaterial. Subsequently, the deprotection step exploits the nanoscale temperature gradients generated in the water surrounding the arms and central region. These localised thermal gradients are used to

selectively modify the structure of the thermally responsive polymer in the shuriken arms. This structural modification subsequently allows biomaterial to be adsorbed in the shuriken arms which possess electromagnetic fields with the desired properties. Finally, the effect on TPS biosensing capabilities after this nanoscale chemical functionalisation is investigated.

5.1.1 Sub-Micron Control of Chemical Functionalisation

Nanoscale chemical functionalisation can be described in terms of two limiting types: “top down” and “bottom up”. The most widely reported techniques are those belonging to the former category whereby specific nanoscale regions of a chemical layer are etched away to produce the desired functionalised surface. For “bottom up” techniques the functionalised surface is built up layer by layer from the substrate surface however due to the difficulties of designing molecules which spontaneously assemble into complex patterns and structures this method remains in the early stages of development.

Consequently, top down functionalisation methods have been the focus of most studies. One of the most common top down techniques used to deliver molecules to desired regions of a surface involves the generation of a polymer self-assembled monolayer (SAM) onto the surface. Analogous to electron beam lithography, a pattern can be directly written into the surface using either a beam of electrons[5] or photons[6, 7]. Exposure to the electron/photon beam results in the modification/desorption of the SAM on the surface creating a nano scale functionalised surface. These direct writing techniques enable surface functionalisation down to a resolution of tens of nanometres. Another method for the direct placement of molecular species with nanoscale precision is dip-pen lithography. Unlike electron/photon beam lithography of SAMs, dip-pen lithography involves the direct placement of molecules on the surface. This is achieved by coating an AFM tip with a molecular species (commonly alkane thiolates) that adsorbs onto the surface as the tip moves across it. In simple terms, the AFM tip acts as the “pen”, the molecular species is the “ink” and the substrate is the “paper” onto which the pattern is traced. The resolution limits of these direct writing techniques have been optimised down to tens of nanometres[8]. A more recent development in nanoscale spatial control of surface chemistry has allowed the functionalisation of nanostructured surfaces containing highly complex geometries which combines both a top down and bottom up approach known as MACE:ID (Molecular Assembly Controlled by Electron beam Induced Deposition). This technique involves direct

writing of SiO nanostructures onto the surface through electron beam induced deposition. The nanostructure is then immersed in a silane solution that selectively binds to the hydroxyl groups at the nanostructure surface thus generating a silane SAM which may be further functionalised with dye molecules or nanoparticles. The significant advantage of this technique is that bottom up chemical functionalisation of the nanostructure surface is achieved through simply immersing the substrate in an aqueous silane solution. Hence, modification of the SAM is not required.

Despite the nanoscale accuracy in functionalisation of the aforementioned techniques, these methods are inherently limited as they require the direct writing of a pattern or direct placement of molecules onto the surface. In other words, each nanoscale area has to be functionalised individually and this involves complex alignment procedures which renders these techniques extremely time consuming. This means current nanoscale functionalisation techniques possess an extremely low through-put making them unsuited for commercial applications therefore they remain thoroughly confined to small scale laboratory use. Hence, there is a great need for the development of a simple, high-throughput method for the nanoscale chemical functionalisation of nanostructured surfaces.

5.2 Results and Discussion

5.2.1 TPS Shuriken Chiroptical Properties

The nanoscale chemical functionalisation method outlined in this chapter is performed using the 100nm Au TPS shurikens introduced in chapter 4. Details of the the geometric and optical/chiroptical properties of these substrates can be found in section 4.2. Recall that strong overlap of parallel electric and magnetic fields generates intense EM fields in the near field surrounding the TPS structure which possess chirality i.e. a sense of twist. Using the optical chirality parameter [C] introduced by Tang and Cohen [9], the chirality of fields associated with the top and bottom surface were modelled (chapter 4, figure 4.08). Shurikens were found to support the generation of fields of opposite chirality on both surfaces. In order to gauge the overall net chirality, the field chirality is integrated over the top and bottom surface of the substrate (integrated optical chirality, IOC). For LH shurikens chiral fields generated on the Au film around the void on the top surface have an IOC of -362, whilst this value is +316 for chiral fields in the solid nanostructure at the bottom surface. Considering the system as a whole the TPS has a net IOC of -46. For RH shurikens

these IOC values will be the inverse of LH values. Evidently, the opposite IOC values of the top and bottom surface results in a reduction of the overall net chirality of the system. This reduction in net chirality of the substrate may reduce the sensitivity of TPS chiroptical measurements. Thus, we have subsequently developed a novel "bottom up" nanoscale chemical protection/deprotection strategy to allow selective placement of biomaterial in areas of high net chirality in order to enhance the sensitivity of spectroscopic measurements.

5.2.2 Simulations of TPS Shuriken Thermal Behaviour

The nanoscale control of TPS shuriken chemical functionalisation depends on the thermal behaviour of the substrates and the surrounding water upon irradiation with a nanosecond pulsed laser. As part of this investigation collaborators at Ohio University have modelled the temporal thermal behaviour of shurikens and the surrounding water in which they are immersed upon various irradiation conditions. These simulations are of great importance as they allow the later experimental observations during the chemical protection/deprotection process to be rationalised. For all simulations, nanostructures are irradiated through the back face at an incident wavelength of 1064nm which mimics the experimental conditions described in section 5.2.4 and results in the excitation of a shuriken plasmonic mode. The geometry of the sample and incident beam in the simulations is also set to reproduce the experimental set-up.

As discussed throughout this thesis, plasmonic modes associated with nanostructures are highly dependent on the sample geometry. Excitation of a plasmonic resonance by an EM wave of the appropriate frequency results in the concentration of EM energy in specific regions of the nanostructure. These regions of high current density can act as heat sources [10] and may result in the generation of nanoscale sources of heat depending on the dielectric properties and geometry of the metamaterial[11, 12]. The estimated time for thermal diffusion between the central and arm regions of the TPS shuriken is described by the following relationship[13]:

$$t \cong L^2/D_t \qquad (1)$$

The distance between the central region and end of the arms (L) is 250nm. The thermal diffusivity of the metal is calculated from the thermal conductivity, the density and specific

heat capacity (appendix 5.5.1) which gives a (D_t) value of 1.27x10^{-4} m^{2}s^{-1}. Therefore, using equation 1, t is estimated to be ≈0.5ns. This value is used as a rough estimation of the time required for the shuriken Au film to reach thermal equilibrium.

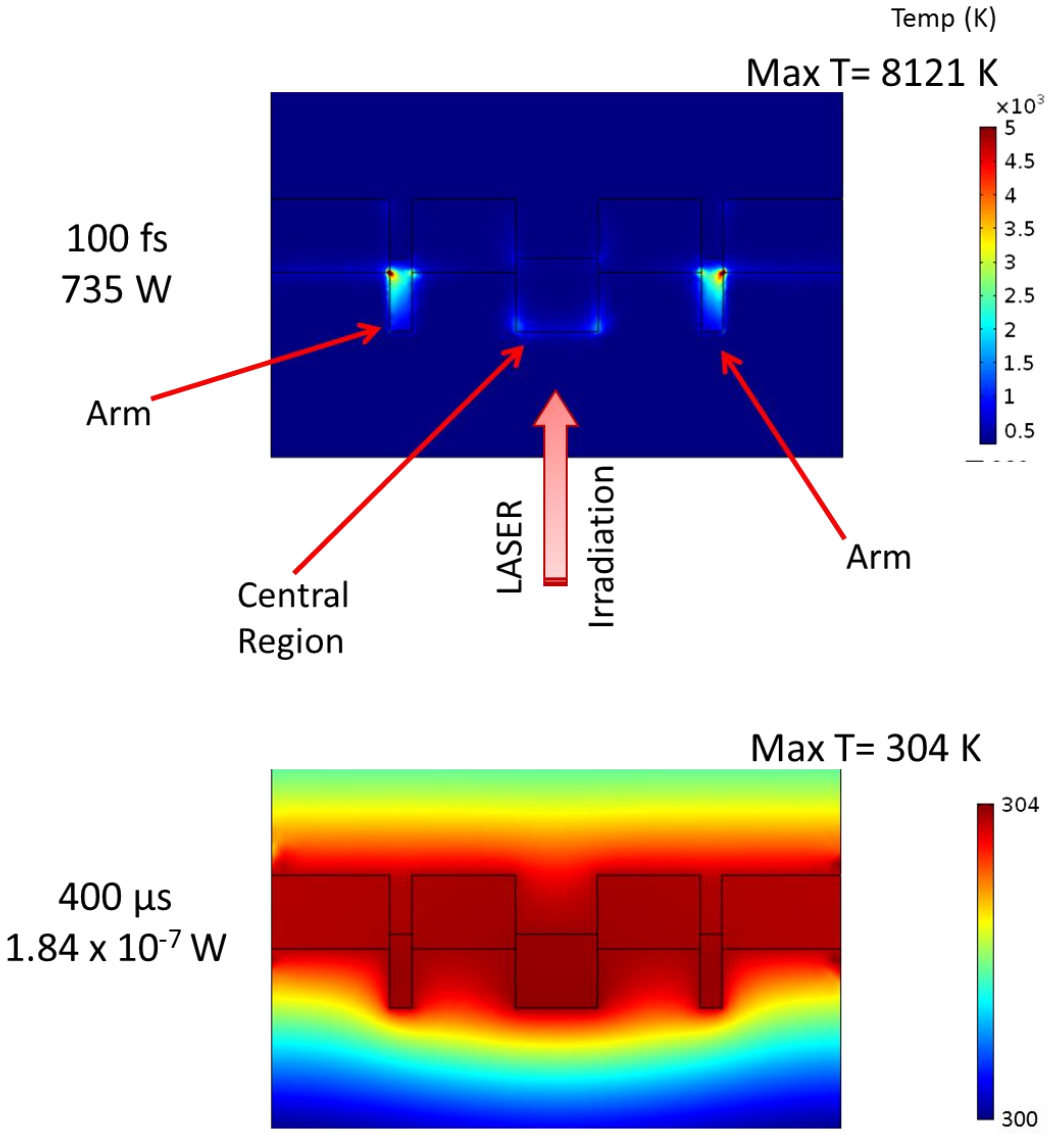

Figure 5.01: Plots of temperature gradients at the pulse end generated in TPS shurikens upon irradiation with an incident beam of different pulse widths. In both cases the fluence of the incident beam is 15mJcm^{-2}.

The thermal behaviour of shurikens upon excitation of a plasmonic mode using a laser of different pulse widths is displayed in figure 5.01. For the 100fs pulse the temperature of the metal at the edge of the shuriken arms approaches several thousand Kelvin whilst the temperature in the central region is at least an order of magnitude cooler. Thus, significant thermal gradients exist in the metal film between this small area of the arms and the central region. For such pulse widths highly localised thermal gradients may arise since the

timescale for heat generation in the metal (~100fs) is significantly shorter than the timescale required for the electron gas to thermalize with the metallic ions throughout the lattice (electron-phonon interactions, ~100ps). This observation of intense nanolocalised thermal gradients in the metal upon femtosecond irradiation is also consistent with previous thermoplasmonic studies[14]. Despite the presence of these large nanoscale thermal gradients, spatially localised chemistry on individual nanostructures cannot be achieved. This is attributed to the large thermal diffusion of noble metals[15] which leads to a uniform temperature distribution throughout the structure over a sub nanosecond timescale. Consequently, the temperature distribution across the metal surface where absorbed chemical species are bound will be homogenous which results in an absence of spatial localisation for thermally activated chemical/physical processes.

In contrast to femtosecond irradiation, the temperature moving from the shuriken arms to the central region is invariant upon irradiation with a 400µs pulse. This homogenous nanostructure temperature is due to the large thermal conductivity of noble metals[15]. Whilst heat generation remains restricted to regions of concentrated EM energy (hotspots), the high thermal conductivity of Au results in a uniform temperature increase throughout the structure[11, 15, 16]. The observation of a homogenous temperature distribution also agrees with the calculated thermal diffusion time for shuriken (0.5ns) which is significantly shorter than the 400µs pulse width. Hence, generation of significant thermal gradients within the shuriken metal film is only achieved using pulsed lasers of width ~100fs; however it is not possible to exploit these thermal hotspots for the control of nanostructure surface chemistry.

The laser used to perform experimental measurements in later sections has a pulse width of 8ns therefore the thermal behaviour of the shuriken and surrounding dielectric is modelled upon irradiation with this light source. EM simulations highlight that a significant discrepancy exists between the water temperature surrounding different regions of the nanostructure upon 8ns pulse irradiation (figure 5.02). It is found that the temperature of the surrounding water displays a variation in three distinct regions. The water at the top surface has a low temperature (≈315K) and is invariant at all points. The water in the central region is at a high temperature (335-345K) close to the bottom surface and markedly decreases (≈25K) approaching the top surface. In contrast, the temperature of the water in

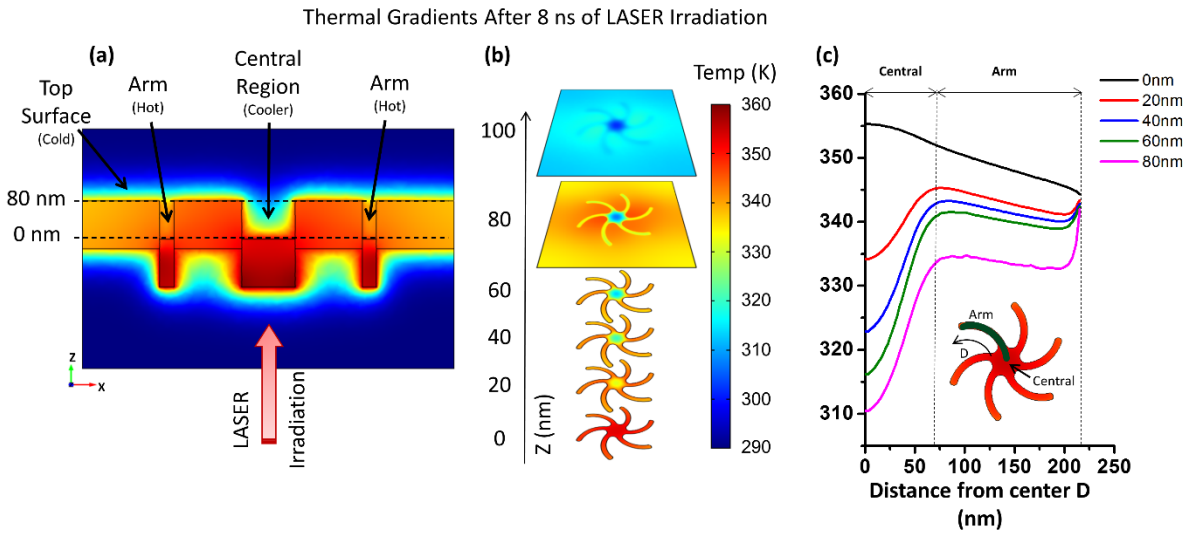

Figure 5.02: (a) Side view of surface plot of the thermal gradients generated in the Au and water upon pulse end (8ns). Labels denote the temperature of the surrounding water. **(b)** Stacked surface plots of water temperature within the shuriken moving up the z axis. **(c)** Graph following the temperature of water moving from the central region to the tips of the arms at different heights of the substrate.

the shuriken arms is large at the bottom surface (345K) and displays only a slight decrease (≈10K) approaching the top surface. Thus, at heights above z=20nm a significant thermal gradient exists between the water in the shuriken arms and central region which increases moving up the z axis to a maximum of ≈20K at z=80nm.

The reason for the non-uniform distribution of thermal energy in the surrounding water is due to the considerably smaller thermal diffusivity of water than Au. The thermal diffusivity (D_t) of water is calculated to be 1.44X10^{-7} m^{2}s^{-1} which is three orders of magnitude lower than that of Au. This accounts for the decreasing temperature of the water at heights above z=20nm in the central region. Water molecules in this region are furthest from the edges of the Au film (i.e. the heat source) therefore the low value of (D_t) means thermal energy is not transferred to these regions within the 8ns time frame of the laser pulse. In contrast, the near uniform distribution of heat in the water of the shuriken arms may be explained by considering the reduced size of these regions relative to the central region. The narrow shape of the arms means the effective distance of the water from the heat source (the Au film) at heights above z=20nm is significantly smaller than at an equivalent height in the central region. From equation 1 we know that the time for thermal diffusion (t) varies with

L^2 therefore this reduced distance allows the rapid distribution of thermal energy to the water in all areas of the arm within the pulse width time frame.

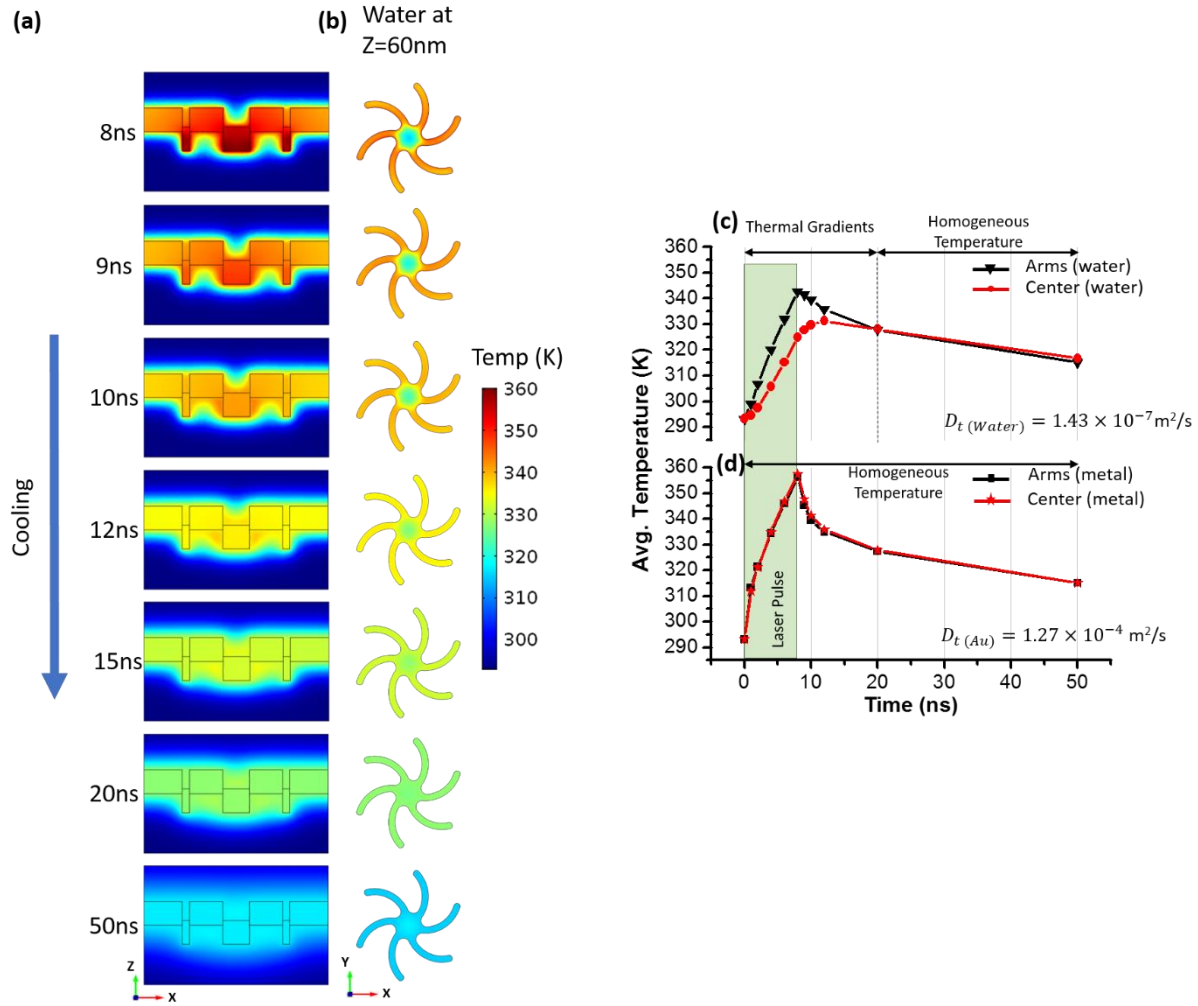

Figure 5.03: (a) Modelling of the temporal thermal behaviour of the nanostructure and surrounding water for various time intervals after the pulse end. **(b)** Surface plots of water temperature in the shuriken at a height of z=60nm after the pulse end. Graph of average temperature of water in arms and central region for 10nm<z≤70nm **(c)** and average temperature in Au nanostructure for z<0nm **(d)**. D_t is the thermal diffusivity of water and Au.

In order to gain an understanding of the post-irradiation thermal behaviour of the system, the spatially resolved temperature dynamics at various time intervals after 8ns were simulated (figure 5.03). From figure 5.03a and 5.03b significant thermal gradients in the water for a time up to 12ns after the pulse end are observed. In other words, the water in the shuriken arms is still significantly hotter along the whole length of the arm than the water in the central region at heights above z=20nm. Figure 5.03c displays plots of the average temperature along the full length of the arms and the central region between z=10-

70nm. At 8ns the average temperature of the water in the arms is 342 K and decreases to 335K after 12ns. In contrast, the average temperature of the water in the central region increases from 324K to 331K in this time period. This temperature increase in the central region and temperature decrease in the arms results in a significant reduction of the thermal gradient between these two regions as highlighted by the gradual overlap of the two profiles in figure 5.03c. The difference in thermal energy is at a maximum of 18K at 8ns and decreases to 4K after 12ns. Thermal equilibrium between the water in the arms and central region is attained after approximately 15ns.

Considering figures 5.02-5.03 thermal modelling signifies the existence of thermal gradients between the water surrounding the arms and the water in the central region at heights above z=20nm upon irradiation with an 8ns pulse laser. The average water temperature in the arms is significantly hotter than in the central region(~20K). The temperature difference is at a maximum after 8ns and a considerable disparity remains until 12ns. In the following sections we use these thermal simulations conducted by colleagues at Ohio University to rationalise the observed experimental behaviour of TPS shurikens during the spatially selective chemical functionalisation of the nanostructure surface.

5.2.3 Chemical Functionalisation of TPS Shuriken Surface

As discussed, we aim to manipulate the surface chemistry in nanoscale regions of the TPS by exploiting the presence of nanolocalised thermal gradients in the surrounding water to allow selective placement of biomolecules in areas of high net chirality. This is achieved using a protection/deprotection strategy similar to that commonly employed in organic synthesis. The first step is the chemical protection of the nanostructure in order to inhibit the binding of biomaterial across all Au surfaces. The protection step involves the generation of a self-assembled monolayer (SAM) of a 6kDa polyethylene glycol methyl ether thiol (PEG-thiol) across the substrate, these substrates will hereby be referred to as PEG-TPS. The macromolecular structure and thermally dependent behaviour of this polymer has been extensively investigated. The structure depends on the conformation of the –(-CH_2-CH_2-O-)– subunits which can adopt either a gauche or trans conformation as illustrated in figure 5.04. At low temperatures or in polar environments a gauche conformation is preferred. The stability of the gauche conformation in H_2O is most likely due to the formation of a hydration layer[17] which facilitates strong hydrogen bonding between

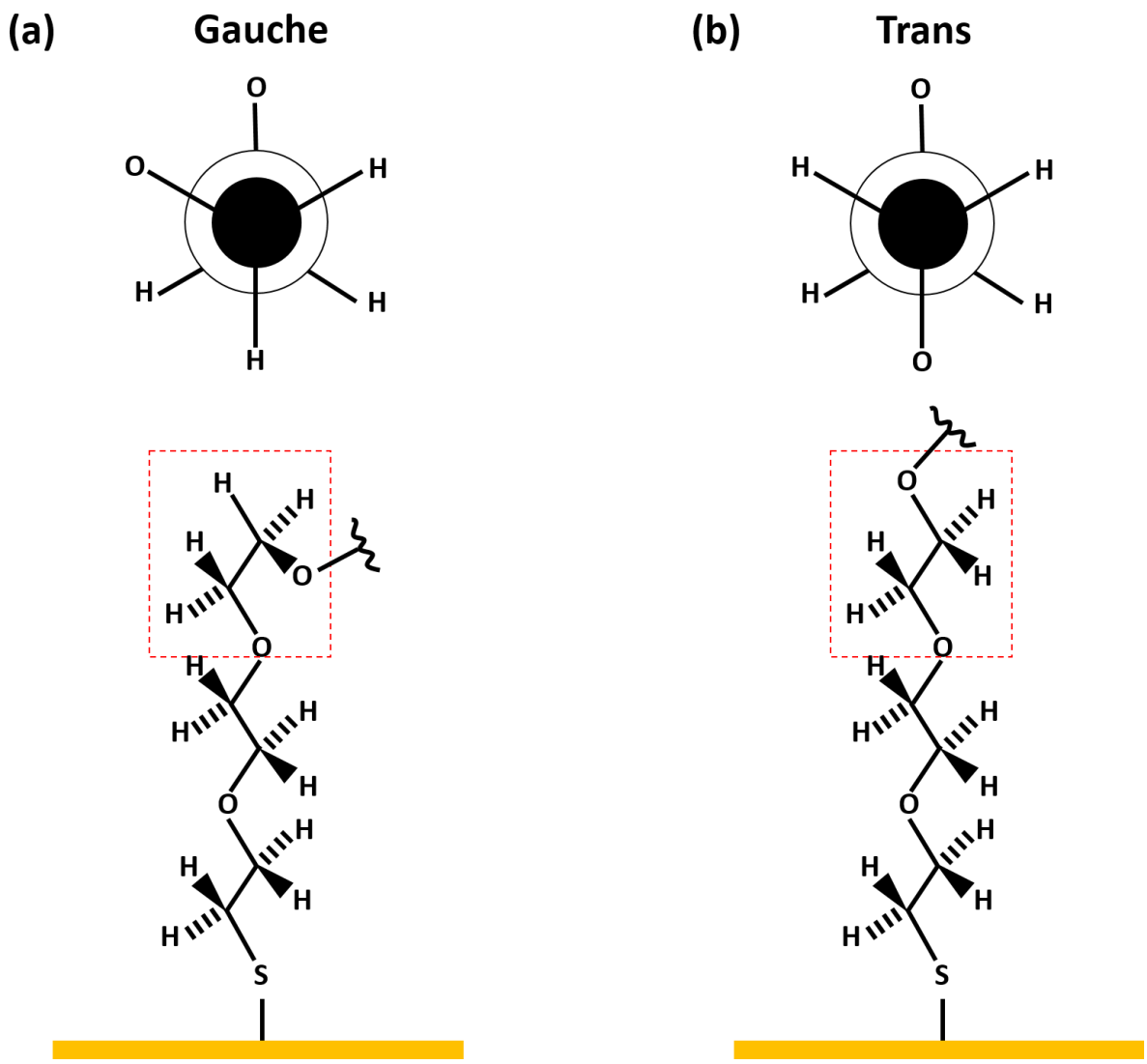

Figure 5.04: Molecular structure and corresponding Newman projection of **(a)** gauche and **(b)** trans conformation of polyethylene glycol methyl ether thiol (PEG-thiol). Red highlighted area represents the section of the molecule displayed in the Newman projection.

solvent molecules and glycol oxygens[18, 19]. In these conditions PEG-SAMs are known to inhibit the binding of biomaterial to the surface due to the compact, ordered, helical structure of the gauche conformation which forms a ~13nm thick SAM[17]. The resistance of this PEG conformation to the adsorption of protein is primarily attributed to steric effects[20]. At higher temperatures or non-polar environments, the trans conformation is adopted. Decreasing polarity of the solvent reduces the number of solvent molecules available for stabilizing hydrogen bond interactions whilst an increase in thermal energy leads to a disruption in such interactions due to increased molecular motion. The temperature that the gauche-trans conformational change occurs has been measured as

~330K [21]. Moreover, this temperature must be achieved along the entire length of the elongated polymer chain (~35nm) in order for the PEG thiol to adopt this conformation[17]. This structural transformation produces less compact packing of the SAM which reduces the steric hindrance experienced by a protein approaching the surface hence biomaterial is able to adsorb [22]. In the protection step the PEG-TPS are immersed in 10mM tris buffer at room temperature therefore the PEG-SAM is in the helical gauche conformation and biomolecules cannot bind to the surface.

5.2.4 Sample Geometry During Irradiation

Following the production of the PEG-TPS in the protection step, we move to the deprotection step which aims to selectively modify the structure of the thermally responsive PEG-SAM in particular nanoscale regions of the shuriken. In order to achieve this, we exploit the aforementioned novel thermoplasmonic phenomenon whereby nanolocalised heating of water surrounding the structure is achieved through irradiation of the TPS with an 8ns

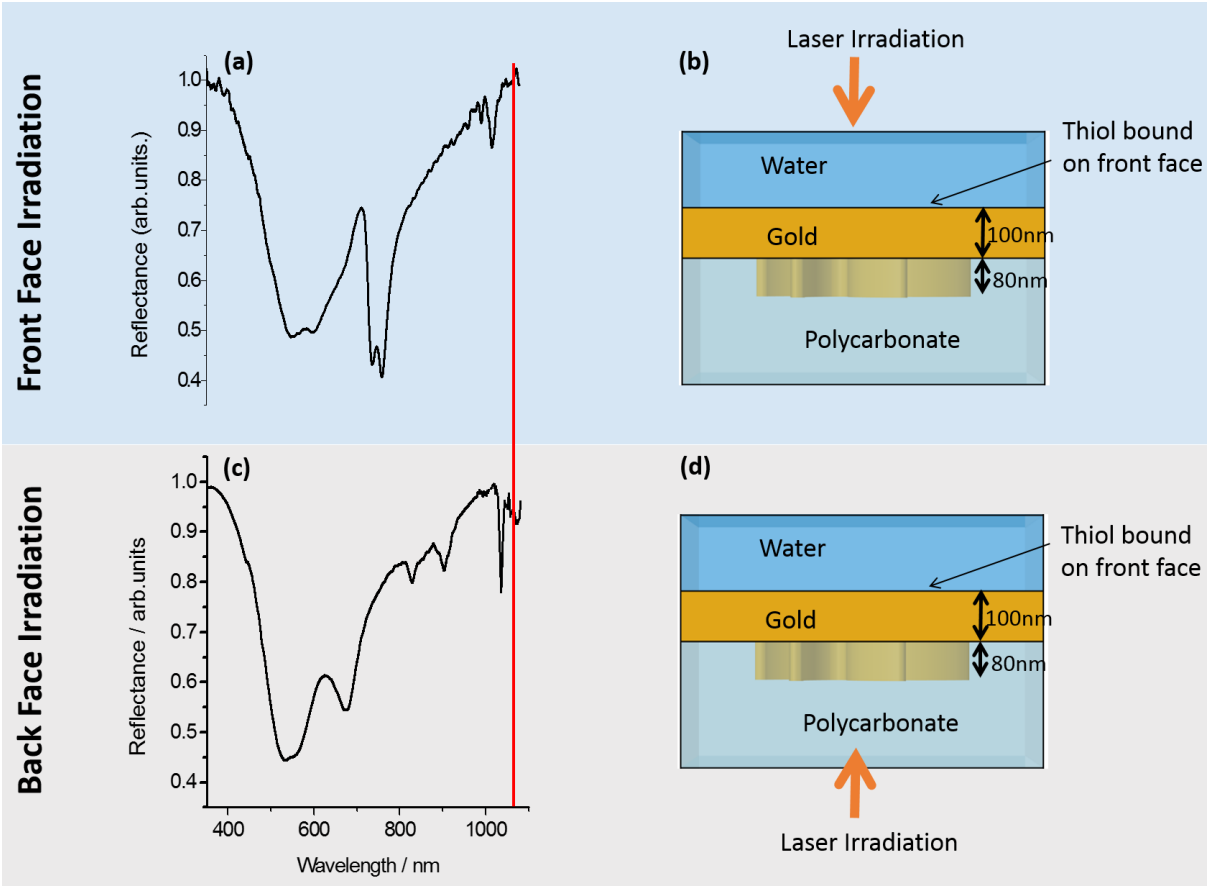

Figure 5.05: Reflectance spectra and corresponding experimental geometry for TPS irradiation from **(a,b)** the front face and **(c,d)** the back face. The red line in the reflectance spectra corresponds to the bandwidth of the 8ns pulse 1064 Nd:YAG laser.

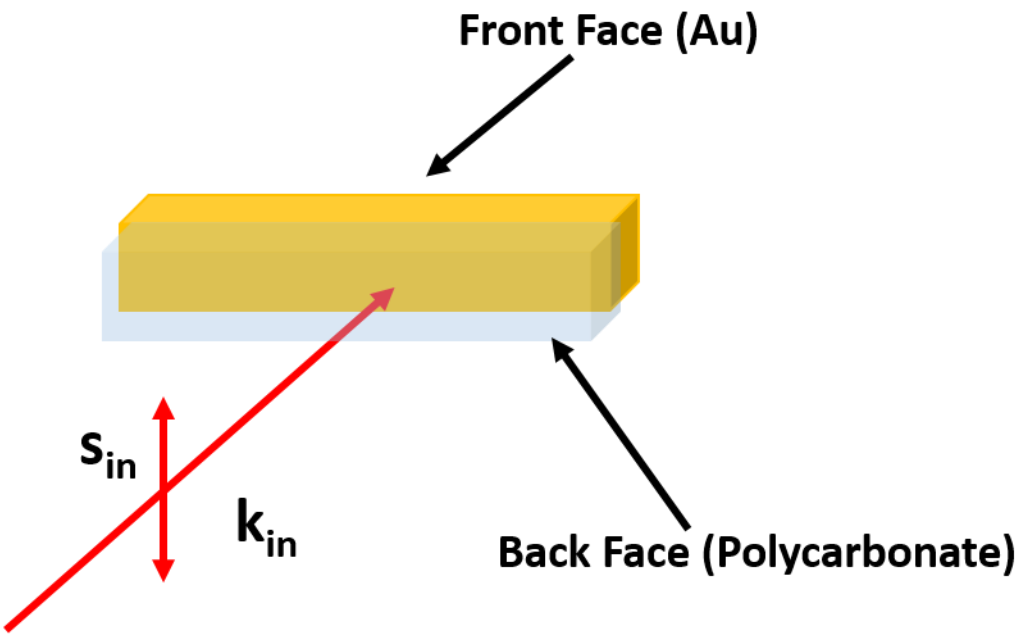

Figure 5.06: Experimental geometry during irradiation of nanostructures with nanosecond pulsed laser.

nanosecond pulsed laser (section 5.2.2). This phenomenon requires excitation of a plasmonic resonance to generate spatial regions with high current density that will act as heat sources[10] (section 5.2.2). Thus, it is necessary to characterise the reflectance spectra measured through the front and back face of the nanostructures in order to ascertain the resonance frequencies of nanostructure plasmonic modes (figure 5.05). Reflectance spectra recorded from the front and back face both display several asymmetric resonances (Fano resonances) in the visible and near infra-red (NIR) which are primarily associated with the excitation of a plasmonic resonance. The dielectric at the interface for the front face measurements is water (n=1.33) whereas the back face dielectric is polycarbonate (n=1.58). From chapter 4.2 we know that the refractive index sensitivity of TPS shurikens is 490nm/RIU from the front face. Hence, measurements through the back face (figure 5.05c-d) correspond to an increase in the refractive index of 0.25 and should result in a red shift for all resonances of approximately 120±20nm relative to the front face (figure 5.05a-b). The reflectance spectra broadly agree with this predicted behaviour therefore we confirm the front and back face resonances correspond to excitation of the same plasmonic modes. The back face NIR resonance displays a slight resonant overlap with the 1064nm laser employed in this study whereas front face modes are off resonance. As a result of this resonant excitation, irradiation of the sample is conducted with the laser beam incident on the back

face of the TPS (figure 5.05d). The experimental geometry during this deprotection step is illustrated in figure 5.06.

5.2.5 Sensitivity to PEG-TPS Surface Chemistry

The deprotection step exploits the presence of nanolocalised thermal gradients between the water surrounding the arms and central region of the TPS shuriken upon 8ns pulse irradiation. In order to monitor the effect of this nanolocalised water heating on the PEG-SAM structure we measure the shuriken optical rotatory dispersion (ORD) from the front face before and after irradiation. From chapter 4 we know that the wavelength of this ORD peak is highly dependent on the refractive index of the surrounding dielectric. Therefore, the magnitude and direction of the resonance shifts are used to infer information about the chemical environment at the Au surface. The PEG-TPS is immersed in 10mM tris buffer before and during irradiation. In this polar solvent at room temperature the PEG-thiol is in the gauche conformation. Unwinding of the PEG-SAM from the tightly packed gauche to the elongated trans form would result in an increase in the thickness of the SAM layer from 13nm to 35nm. This conformational change will result in a red shift of the ORD spectrum since the resonant wavelength of a plasmonic mode increases with the thickness of the molecular layer (d) (equation 2.27).

Before performing nanolocalised water heating we confirm the sensitivity of ORD measurements to the SAM conformational changes at the Au surface. Figure 5.07 displays the changes in the LH ORD spectra of PEG-TPS shurikens upon various solvent and heating conditions. Immersion of the PEG-TPS in water at a temperature of 358K or in the non-polar solvent Butan-1-ol at 293K (figure 5.07a and 5.07b) induces a large red shift of ~5nm ±0.2nm in the ORD spectra. This increase in resonant wavelength is due to an increase in the thickness of the molecular layer as the PEG thiol undergoes a conformational change from the helical gauche to elongated trans form. The PEG-TPS immersed in water at a temperature of 323K does not display a resonance shift (figure 5.07c). This is due to the water temperature being below the critical temperature (330K) at which the gauche-trans transformation occurs. From figure 5.07d we find that heating the PEG-TPS to ~358 K in the absence of water does not induce a red shift in the ORD. The SAM conformational change is therefore a water mediated process which agrees with a previous study of polyethylene glycol systems[22].

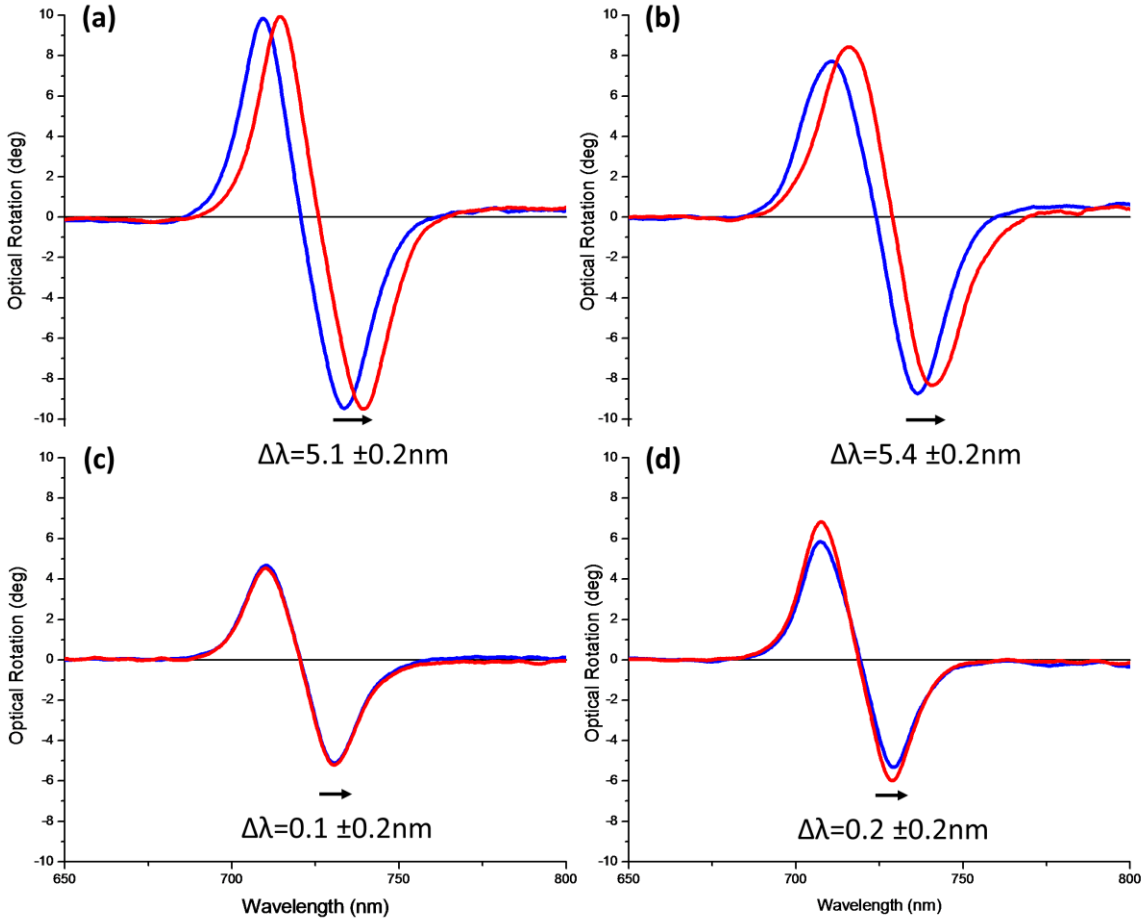

Figure 5.07: ORD spectra of a LH Peg-TPS after: **(a)** heating to 358K in water; **(b)** washing with Butan-1-ol at 293K; **(c)** heating to 323K in water and **(d)** heating to 358K in air. Magnitude and direction of the resonance shifts are given. The blue line corresponds to the PEG-TPS ORD before modification and the red line is the subsequent ORD. All ORD spectra are measured in 10mM tris buffer.

The conformational change was also found to be irreversible. In figure 5.07b the initial measurement is recorded in buffer (polar solvent) before being washed with butan-1-ol (non-polar solvent) after which the ORD is again measured in buffer. If the PEG-thiol adopted the gauche conformation again after re-immersion in buffer, we would not observe a resonance shift. Likewise, both spectra in figure 5.07a are recorded at ~293K, if the thermally induced unwinding of the SAM was reversible a resonance shift would not be observed. Hence, the irreversible nature of the conformational change is confirmed. We suggest that the irreversibility of this process upon the SAM adopting the trans conformation is due to kinetic effects that occur when the SAM is heated above 330K. The main kinetic effect is believed to be lateral interactions between the long, unfolded polymer

branches which leads to intertwining of neighbouring branches inhibiting the reformation of the helical gauche form.

The measurements in figure 5.07 provide a useful insight into the thermal behaviour of the PEG thiol and the effect of surface functionalisation on the optical properties of the shuriken. Our observations are consistent with previously reported PEG-thiol thermal behaviour whereby the irreversible gauche-trans SAM conformational change only occurs at temperatures above 330K and is also a water mediated process. However, in the aforementioned experimental conditions the helical-elongated SAM transformation will occur over all surfaces of the nanostructure and the unstructured Au film since the thermal energy is distributed evenly throughout the system. Hence, we now investigate the effect of nanolocalised water heating on the PEG-SAM conformation upon 8ns pulsed laser irradiation.

5.2.6 Manipulation of Surface Chemistry using Nanolocalised Water Heating

Figure 5.08a displays the ORD resonance shift after irradiation of a PEG-TPS at a fluence of 15mJcm^{-2}. The ORD displays a red shift of 1nm ±0.2nm suggesting that a small amount of the PEG-SAM has undergone a trans-gauche conformational change. The dependence of this effect on the irradiation time is shown in figure 5.08b wherein the level of red-shift saturates after 60s and further irradiation does not elicit any discernible difference in the ORD. We assume that the 5nm red shift upon immersion of a PEG-TPS in water at 358K (figure 5.07a) is due to the elongation of the PEG-SAM over the whole nanostructure. As the laser induced resonance shift in figure 5.08a is 20% of this value we estimate that only 20% of the PEG-thiol on the nanostructure surface has undergone a gauche-trans conformational change. The reduction in the extent of this structural transformation is in agreement with the prediction of nanoscale thermal gradients in the surrounding water generated upon irradiation with an 8ns pulsed light source (section 5.2.2).

Recall from the thermal modelling of water surrounding TPS shurikens that three distinct temperature regions are generated: the top surface; the central region of the shuriken and the shuriken arms. The temperature at the top surface does not exceed 330K therefore insufficient thermal energy is available to induce the gauche-trans conformational change. This means the PEG-SAM will maintain the tightly packed helical structure and will not contribute to the red shift. Figure 5.08c is derived from the thermal modelling in section

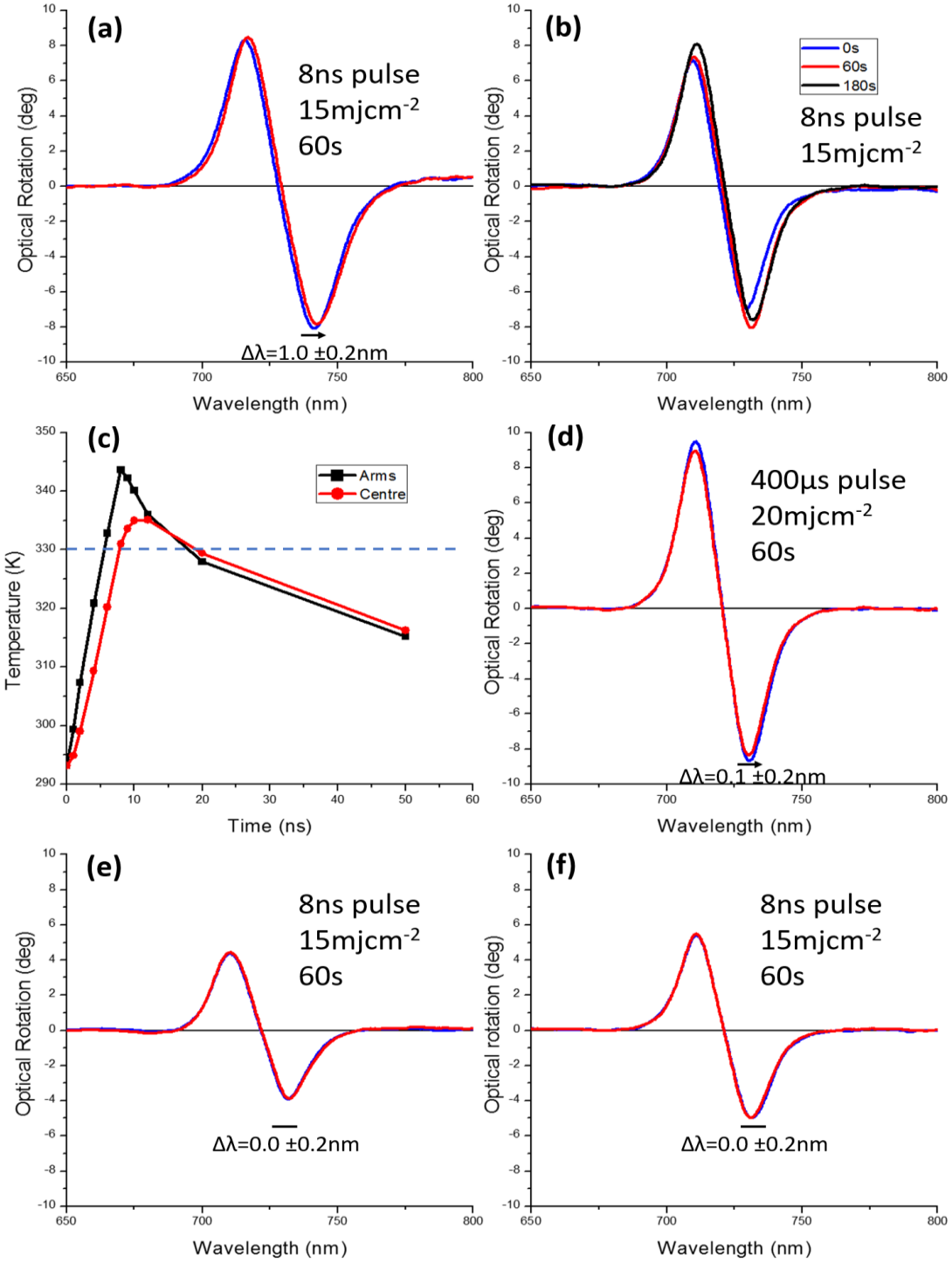

Figure 5.08: ORD spectra of LH shuriken after **(a)** irradiation of a PEG-TPS in water with an 8ns pulsed 1064nm laser at 15mJcm^{-2} for 60s and **(b)** varying time durations of laser irradiation. **(c)** Modelled average temperature of the surrounding water between z=20 and z=30 in the shuriken arms and central region after 60s irradiation at 15mJcm^{-2}. Effect on the LH shuriken ORD spectra after: **(d)** irradiation of a PEG-TPS in water with a 400 µs pulsed laser at 20mJcm-2 for 60s; **(e)** irradiation of a plain TPS in water with an 8ns pulsed laser at 15mJcm^{-2} for 60s and **(f)** irradiation of a PEG-TPS in air with an 8ns pulsed laser at 15mJcm^{-2} for 60s. In all ORD spectra the blue line is the ORD measured before irradiation and the red line is the ORD post irradiation. The magnitude and direction of resonance shifts are indicated below each spectrum.

5.2.2 and displays the average temperature of the surrounding water in the central region and the arms between z=20-30nm during 8ns irradiation and for a subsequent 50ns after the pulse. This height range is particularly relevant as this is the region into which the trans PEG-thiol extends. The critical temperature (330K) for the gauche-trans conformational change is highlighted and from this we find that the surrounding water in both the central region and the arms have several data points above this line. The water temperature in the central region very slightly exceeds the threshold (~4K) for ~3ns. In contrast, the water surrounding the arms reaches temperatures as high as 345K and remains above the threshold for ~8ns. This large divergence between the thermal behaviour of the central and arm region has significant consequences for the surface chemistry of the PEG-SAM. From figure 5.07a-b we know that the gauche-trans conformational change is a kinetically limited, irreversible process due to the intertwining of polymer chains which prevents the reformation of the helical SAM. Earlier studies into the dynamic relaxation of polymers of a similar molecular weight have shown that PEG chains must be above the temperature threshold for a time period of ~5-10ns[23] in order for intertwining to occur. In the cooler central region, the surrounding water only exceeds this temperature for ~3ns therefore the elongated PEG-SAM will not remain above this critical temperature for a long enough time period and will reform the helical, gauche conformation. However, the water of the shuriken arms experiences a significantly higher temperature above the threshold for ~8ns. This timescale is sufficient to allow the irreversible intertwining of the trans PEG-thiol chains hence only in the shuriken arms does the PEG-SAM form the elongated trans conformation. This regionally selective unfolding of the PEG-SAM gauche conformation in the shuriken arms is ultimately responsible for the significantly reduced red shift in the ORD spectra.

Irradiation of the substrate with a 400µs pulse up to a fluence of 20mJcm^{-2} does not induce a shift in the ORD spectra indicating that a gauche-trans conformational change is absent (figure 5.08d). This observation agrees with the modelling of the thermal behaviour of the TPS and surrounding water upon irradiation with such microsecond pulses (figure 5.01). The metal film and the water surrounding all regions of the shuriken are in thermal equilibrium at the end of the pulse and possess a temperature of ~304K. This temperature is significantly below the trans-gauche critical temperature (~330K) therefore the PEG-SAM conformational change does not occur. Figure 5.08e displays the ORD shift upon 8ns pulse

irradiation at 15mJcm^{-2} of a TPS substrate immersed in water without a PEG-thiol SAM generated on the surface. The ORD is invariant between the pre-irradiated substrate and the 8ns pulse irradiated substrate. This invariance allows us to discount thermally induced geometric distortions of the nanostructure as the source of the resonance shifts. The ORD shift is also measured for a PEG-TPS upon 8ns pulse irradiation at 15mJcm^{-2} in air (figure 5.08f). Again we find that the resonance shift is negligible which is commensurate with the gauche-trans conformational change being a water mediated process.

The magnitude of the red-shift hence the surface extent of the trans-gauche conformational change increases as a function of increasing laser fluence up to a saturation point of 20mJcm^{-2} (figure 5.09a). The step-wise nature of this fluence dependency is typical of a thermally driven process as opposed to a hot electron mediated process. In simplistic terms, a hot electron is an electron with a large amount of kinetic energy that is excited from occupied energy levels to an energy above the Fermi level[24]. The generation of hot electrons in plasmonic systems may result in localised heating within the nanostructure or photodesorption/photochemistry of chemical species on the metal surface. Hot electron mediated surface chemistry is highly dependent on the time integrated total flux of hot electrons in the system. This total flux is controlled in part by the rate of energy input to the system (i.e. the pulse width) relative to the rate of electron energy loss to the lattice (electron-phonon relaxation). For femtosecond pulses the energy input to the electronic

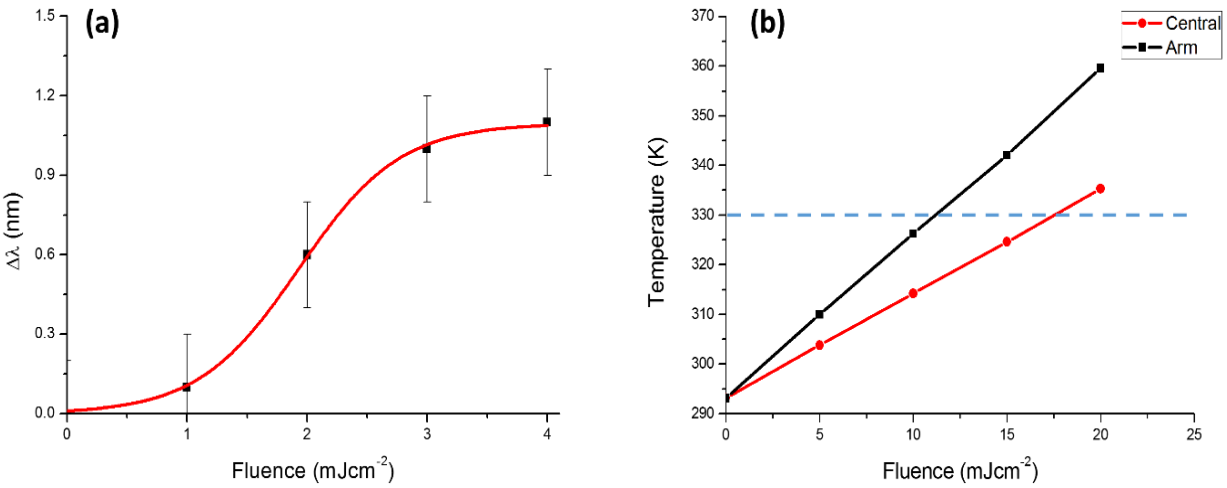

Figure 5.09: (a) Magnitude of the LH shuriken ORD shift as a function of increasing laser fluence. **(b)** Modelled average temperature of the water in the shuriken arms and central region with increasing fluence.

system exceeds the rate of energy loss to the lattice (~100ps), therefore the time integrated total flux of electrons is highly dependent on the pulse width in this time domain. However, for nanosecond pulse widths and below the EM radiation is effectively continuous as these time scales are significantly longer than the electron-phonon relaxation time[25]. This means that despite the lower EM field intensities for microsecond pulses, the total hot electron flux will be the same as for a nanosecond pulsed beam since the lower intensity EM fields exist over a longer time scale. Hence, for a hot electron driven effect the system will display no dependency on the micro/nanosecond pulse duration and a linear dependency on fluence[26]. Evidently, the behaviour of the shuriken PEG-SAM upon 8ns pulse irradiation does not conform with the hot electron model due to the step-wise fluence dependency and reliance on the pulse width. Thus, SAM modification must occur through conductive thermal energy transfer from the Au to the surrounding water.

The dependency of the resonance shift on the laser fluence broadly agrees with figure 5.09b wherein the average temperature within the nanostructure arms and central region has been modelled. The modelled average temperature in the shuriken arms exceeds the threshold temperature for the PEG-SAM conformational change at 12mJcm^{-2} which is close to the 10mJcm^{-2} fluence at which the ORD spectra begins to red shift. As we subsequently increase the laser fluence the temperature in the arms rises up to a value of 340-360K which is commensurate with the measured increase in the red shift of the ORD spectra at these higher energies. The temperature in the central region only exceeds the threshold by ~5K at a fluence of ~20mjcm^{-2} therefore minimal transformation of the PEG-SAM will occur in this region. This correlation between the fluence dependency of the resonance shift magnitude and fluence dependence of the shuriken arm/central region water temperature re-enforces the notion that the we are able to control the surface chemistry of the PEG-SAM with nanoscale precision.

As discussed, the nanoscale modification of the PEG-SAM structure creates a PEG-TPS with two distinct surface functionalisations: the helical, gauche, PEG-SAM on the top surface and in the central region and the elongated, trans, PEG-SAM in the shuriken arms. It is known that a significant height difference ~22nm exists between the helical and elongated forms of the PEG-SAM. Using atomic force microscopy (AFM), it is possible to measure this height difference and distinguish between these PEG-SAM conformations in nanoscale regions of

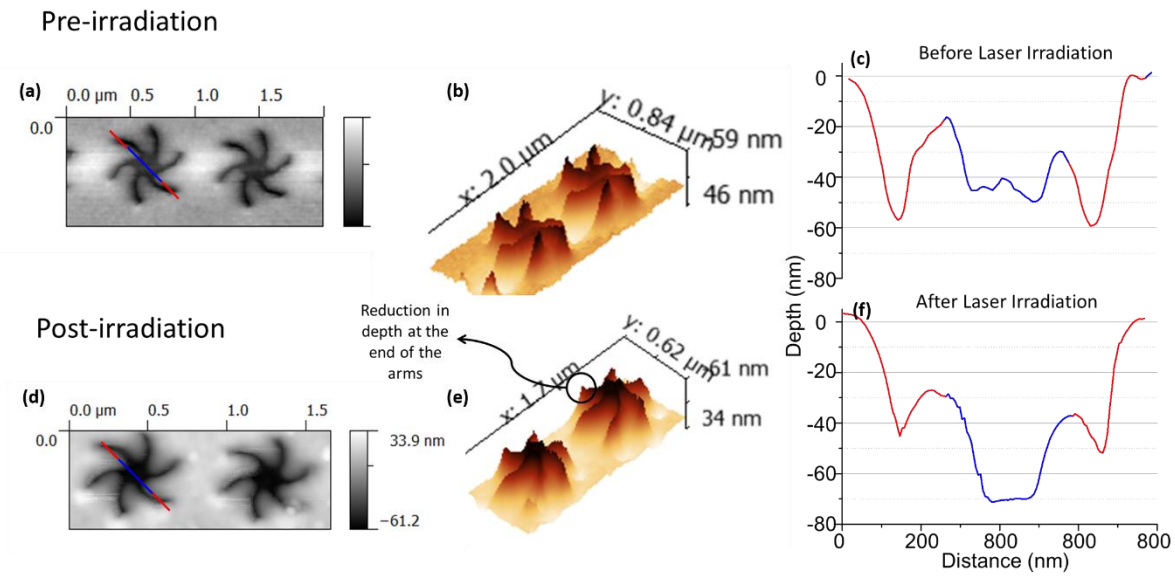

Figure 5.10: SEM images collected for a plain and PEG-TPS before irradiation **(a-c)** and after irradiation with an 8ns laser **(b-d)**.

the TPS. Figure 5.10 displays AFM images and the corresponding height profiles for a PEG-TPS before irradiation (5.10a-c) and a PEG-TPS irradiated with an 8ns pulse for 60s at a fluence of 15mJcm^{-2} (5.10d-f). Comparison of the pre-irradiated and post-irradiated substrates reveal that the depth at the end of the shuriken arms has reduced on average by 20-30nm. This overall reduction in depth agrees with the expected change in SAM thickness upon transformation from the gauche to trans conformation (13nm-35nm). Hence, AFM is able to detect the nanoscale variations in PEG-TPS surface chemistry which provides further confirmation that we can control the conformation of the PEG-SAM through the generation of nanolocalised thermal gradients in the surrounding water. In the following section we will investigate the effects of this nanoscale chemical functionalisation on the biosensing properties of TPS shurikens

5.2.7 Influence of Nanoscale Chemical Functionalisation on Biosensing

PEG-SAMS are often employed in biological measurements to inhibit the binding of biomaterial to a surface. However, it is only when the thiol chains are in the tightly packed helical gauche conformation that inhibition of surface binding occurs[22]. When the PEG-SAM adopts the elongated trans conformation, there are sufficient gaps between adjacent polymer chains to allow binding of molecular species to the surface. Upon irradiation of a PEG-TPS, biomaterial will be unable to bind to the top surface and the central region of the shuriken as the PEG-SAM remains in the gauche conformation at these surfaces. However,

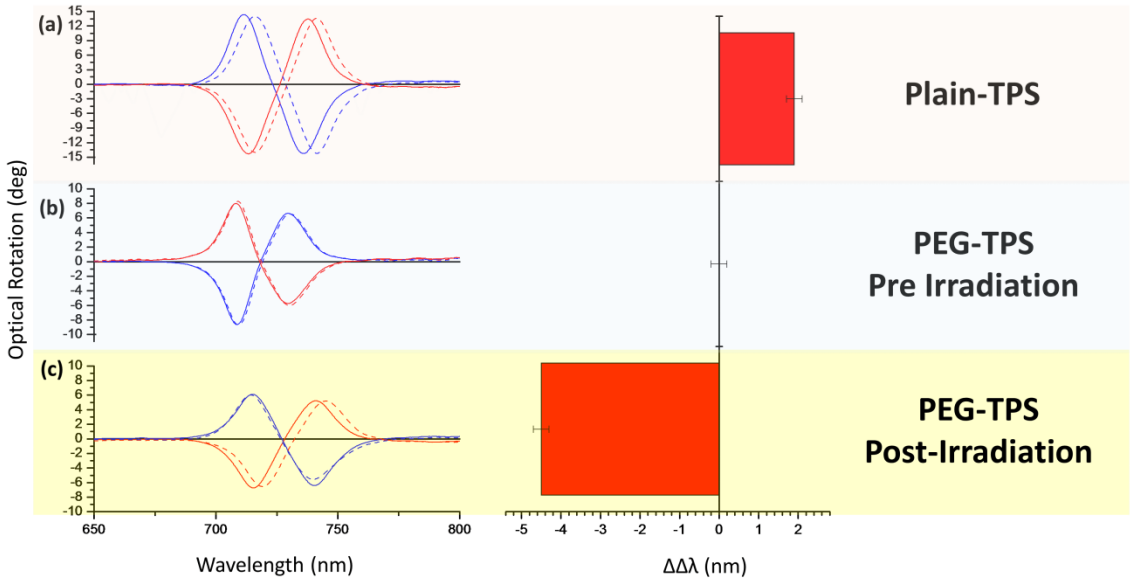

Figure 5.11: RH (blue) and LH (red) shuriken ORD spectra with corresponding asymmetry parameters upon adsorption of Concanavalin A on: a plain TPS **(a)**; a PEG-TPS before irradiation **(b)** and PEG-TPS after irradiation **(c)**. Solid lines are buffer measurements and dashed lines are Concanavalin A measurements.

the increased temperature of the water in the shuriken arms induces the PEG-SAM to adopt the trans conformation which should allow binding of biomolecules in this region.

Similar to chapter 4 the biosensing properties of the TPS and PEG-TPS are investigated through plasmonic polarimetry measurements. Firstly, we investigate the β sheet protein Concanavalin A as from chapter 4 we know this molecule induces a large plasmonic polarimetry response. Figure 5.11 displays the ORD spectra and corresponding asymmetry parameters for the experiment conducted on: a plain TPS; a PEG-TPS before irradiation and a PEG TPS after irradiation with an 8ns pulse for 60s at 15mJcm^{-2}. The Con A induced resonance shift in RH and LH shurikens for the pre irradiation PEG-TPS (5.11b) is negligible whilst the ΔΔλ value is zero. This confirms that the helical PEG-SAM inhibits the binding of the protein to the Au surface. The plain TPS possesses a ΔΔλ value of +1.9nm ±0.2nm (figure 5.11a) whereas the irradiated PEG-TPS has a ΔΔλ value of -4.2nm ±0.2nm (figure 5.11c). The difference in sign and magnitude of the ΔΔλ values between these two substrates can be explained by referring to the chirality of EM fields associated with the top and bottom surfaces. For the plain-TPS, Concanavalin A binds to all available Au surfaces and will experience an overall small, negative net chirality (IOC=-46) due to the cancellation of fields

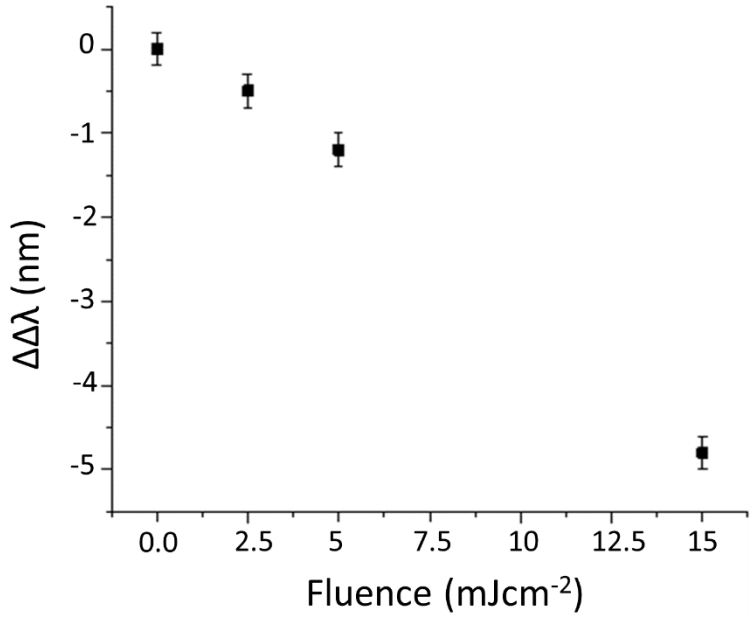

Figure 5.12: Asymmetry parameter (ΔΔλ) for Concanavalin A adsorption on shurikens as a function of increasing laser fluence.

of opposite chirality on the top and bottom surface. In the irradiated PEG-TPS, the protein can only bind to the bottom surface of the shuriken arms, this means overall the molecules will experience a significantly larger positive net chiral field (IOC=+316). Hence, the sign of the asymmetry parameter reverses with the inversion of the net chirality experienced by the molecules. Moreover, the magnitude of this effect increases with an enhancement in the EM field net chirality.

The dependency of ΔΔλ on the laser fluence for irradiated PEG-TPS substrates is displayed in figure 5.12. As the fluence decreases the size of the asymmetry parameter decreases. Reducing the fluence of the incident radiation (i.e. the thermal energy generated in the nanostructure) will lessen the thermal gradients within the surrounding water of the arms and central region. The water in the arms will be at an overall lower temperature therefore smaller areas of the PEG-SAM will undergo the thermally induced gauche-trans conformational change. This means there is a smaller area available for binding of protein to the Au surface meaning fewer molecules will occupy the chiral near fields around the nanostructure. Consequently, the plasmonic polarimetry response will be reduced.

Following the basic proof of principle Concanavalin A measurements, a more complex system involving detection of the Histidine-tagged protein 5-enolpyruvylshikimate-3-

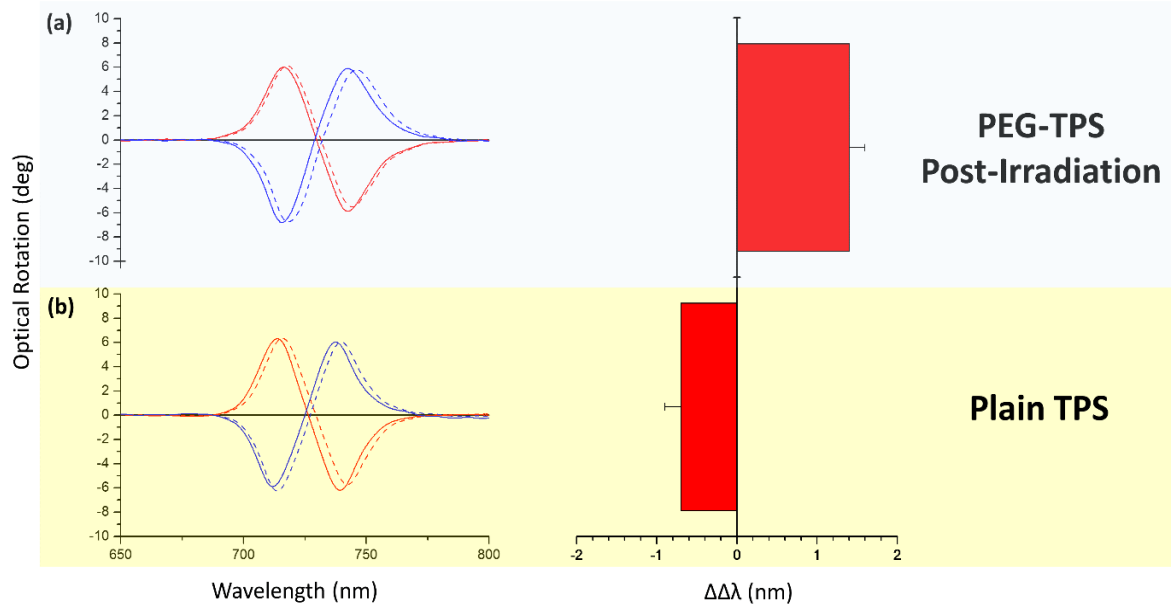

Figure 5.13: RH (blue) and LH (red) shuriken ORD spectra with corresponding asymmetry parameters upon adsorption of EPSP synthase on PEG TPS after irradiation **(a)** and a plain TPS **(b)**. Solid lines are buffer measurements and dashed lines are EPSP synthase measurements.

phosphate (EPSPS) synthase is investigated which requires further functionalisation of the irradiated PEG-TPS. After irradiation of the PEG-TPS, a binding site for the His-tagged EPSP is generated in the shuriken arms by adsorption of a nitrilotriacetic acid (NTA) thiol SAM coordinated to $Ni2^{+}$ and a triethylene glycol mono-11-mercaptoundecyl ether (EG-thiol) spacer unit. The functionalised surface allows the EPSP to selectively bind to the NTA thiol in the shuriken arms due to the high affinity of the His tag to the Ni^{2+} moiety. A detailed description of the functionalisation procedure is outlined in section 3.5.2. For comparison we have also generated an NTA thiol/EG-thiol surface on a plain TPS across the whole nanostructure. The ORD and asymmetry parameter values for the binding of EPSP to NTA thiol for the plain TPS and PEG-TPS are found in figure 5.13. The ΔΔλ values for the PEG-TPS and plain TPS are +1.4nm and -0.7nm respectively. This behaviour is qualitatively the same as the Concanavalin A data. The value of the asymmetry parameter is inverted and enhanced when the protein is selectively bound to the bottom surface of the shuriken arms as opposed to covering the whole nanostructure. Again, we reiterate that this effect arises due to the opposite sign and enhanced net chirality of EM fields in the irradiated PEG-TPS substrates.

The increase in the magnitude of the ΔΔλ values for the PEG-TPS highlights that the spectroscopic response is enhanced when we selectively place molecules in regions of the nanostructure with larger net chirality. Furthermore, the number of molecules responsible for the asymmetric resonance shifts of the PEG-TPS will be significantly smaller as the protein molecules are only able to adsorb to the bottom surface of the shuriken arms. Using a series of simple calculations, we generate an approximation as to the area available for protein binding to the irradiated PEG-TPS surface and the subsequent enhancement of the sensitivity limits using these substrates.

Firstly, we consider the extent of the shuriken arm surface area that is available for protein binding in the irradiated PEG-TPS. The AFM data (figure 5.10) displays a reduction in height only towards the ends of the shuriken arms which suggests the PEG-SAM does not undergo a conformational change across the full arm length. In addition, the ORD data in section 5.2.6 suggests 20% of the PEG-SAM is in the trans conformation however the bottom surface of the six arms constitutes more than 20% of the total shuriken surface area. This provides further evidence that the PEG-SAM is not in the trans conformation along the full length of the arms. Consequently, we suggest that biomolecules cannot bind over the full length of the shuriken arms on the bottom surface. However, it is extremely challenging to gauge what percentage of this surface is available for binding therefore to simplify the following calculations we assume that the PEG-SAM along the full length of all six arms undergoes the gauche-trans conformational change. This renders these calculations an extremely rough estimate with regards to the area available for protein binding and the sensitivity limits of the PEG-TPS. The approximate geometry of individual arms is 150nm x 40nm therefore each arm has an area of 0.006μm^2, giving 0.036 μm^2 per shuriken. The array consists of 430x430 shurikens resulting in 184900 shurikens per array. This gives a total array area of 6.65x$10^3 \mu m^2$ that has undergone the SAM transformation and is available for protein binding in the irradiated PEG-TPS. Conversely, in the plain TPS protein molecules can bind across all surfaces of the array therefore an area 90x$10^3 \mu m^2$ is available for binding. This means the available Au surface area for protein binding in a PEG-TPS is reduced by a factor of ~13.5 relative to the plain TPS.

Using the above estimation for the available Au surface binding area in a PEG-TPS we can now generate approximations for the detection limits of these substrates. From SPR

spectroscopy we know that $1281x10^{-6}pg\mu m^{-2}$ of Con A adsorbs on a bare Au substrate meaning for a plain TPS the total amount of Con A adsorbed on the array is 115.29pg (~1 femtomole). In the case of the PEG-TPS, a total Au surface area of $6.65x10^{3}\mu m^{2}$ is estimated to be available for protein binding. Thus, we calculate that the spectroscopic response arises from only ~8.5pg of Con A adsorbed onto the shuriken arms of these substrates. Concanavalin A is a tetramer at the neutral pH employed in this experiment wherein each subunit has a mass of 26.5 kDa. Assuming a mass of 106kDa per molecule, the molar sensitivity of an irradiated PEG-TPS is ~80 attomoles. This means that nanoscale functionalisation increases the detection limits of shurikens to Con A adsorption from ~1 femtomole to ~80 attomoles which corresponds to an enhancement factor of ~12.5. We will now consider the PEG-TPS sensitivity enhancement for the NTA thiol/EG thiol surface functionalisation and subsequent binding of His-tagged EPSP synthase. The approximate dimensions of a molecule of EPSP synthase is 10nm x 10nm therefore EPSP will occupy an area of $0.0001um^{2}$. For a plain TPS the total number of EPSP molecules will be $9x10^{8}$ molecules. We calculate the mass of 1 EPSP molecule to be $7.6x10^{-20}g$ therefore 70.4pg are bound to the surface which corresponds to 1.5 femtomoles of protein. For an irradiated PEG-TPS whereby the area of the deprotected arms is $6.65x10^{3}\mu m^{2}$, the total number of EPSP synthase moieties will be $6.65x10^{7}$ molecules. The total mass of the surface bound molecules will be 5pg which gives a concentration of 108 attomoles. The concentration of NTA to the spacer molecules is 1:9 meaning a significantly smaller number of EPSP molecules are bound. This means the spectroscopic response is due to 166 attomoles of protein in a plain TPS and 12 attomoles in a PEG-TPS.

From the above estimations it is evident that the sensitivity limits of spectroscopic measurements are enhanced upon nanoscale chemical functionalisation as a larger plasmonic polarimetry response is elicited from a smaller number of molecules when conducting measurements with an irradiated PEG-TPS. This enhancement allows attomoles of biomaterial to be detected which is approaching the upper sensitivity limits for current plasmon enhanced spectroscopies[27].

5.2.8 Nanoscale Spatial Control of TPS Surface Chemical Functionalisation

In summary, a high through-put method for the nanoscale chemical functionalisation of a TPS has been introduced which facilitates an enhancement of the sensitivity limits of TPS

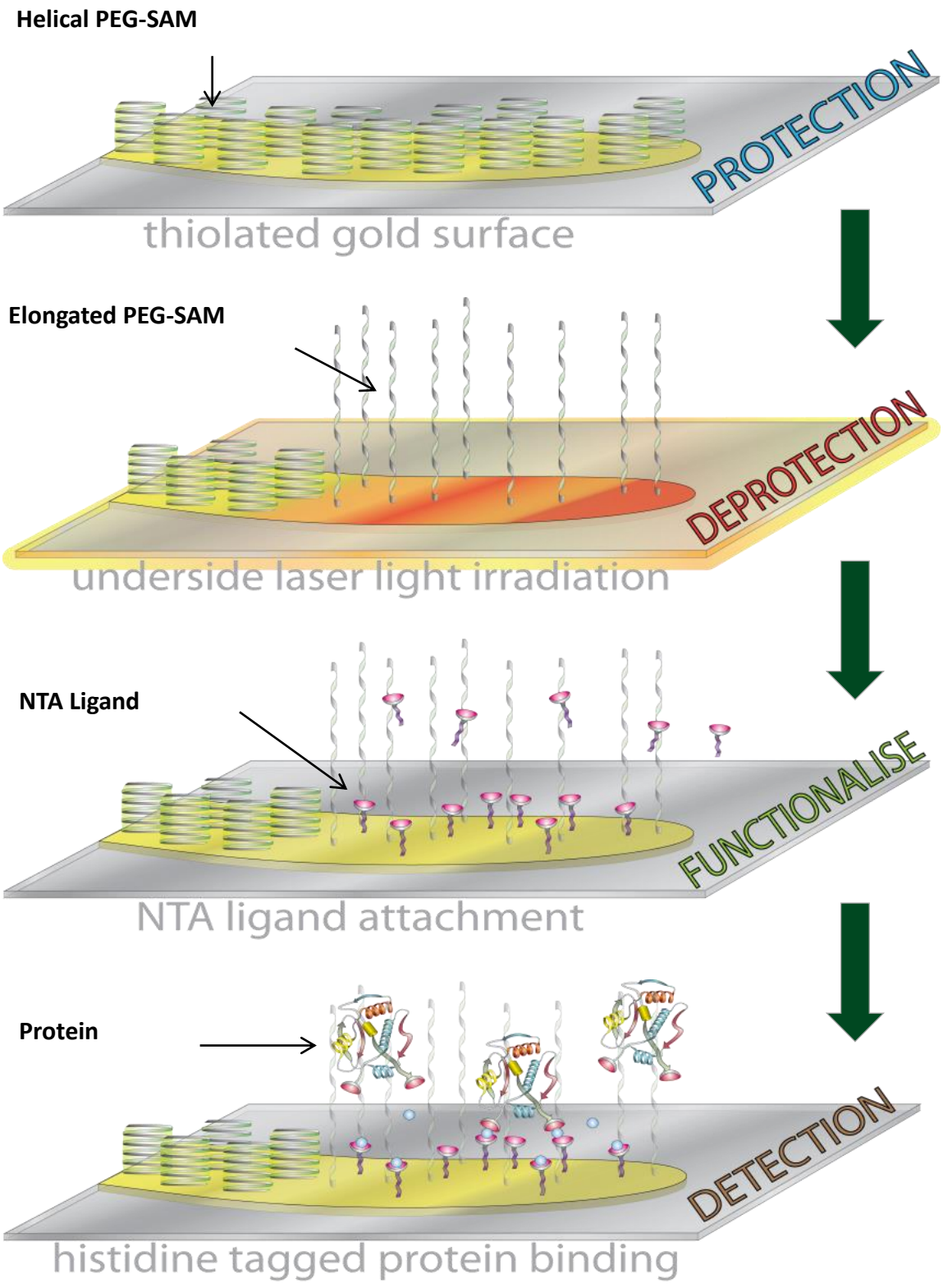

Figure 5.14: Pictorial representation of protection/deprotection strategy and subsequent functionalisation of shuriken nanostructures. The protection step is the formation of a thermally responsive PEG-SAM on the surface. The deprotection step involves irradiation of the PEG-SAM with a ns pulsed laser which generates nanolocalised thermal gradients within the surrounding water. This leads to a conformational change of the PEG-thiol in selective regions of the nanostructure which subsequently facilitates the binding of biomaterial to the surface.

spectroscopic measurements of protein structure. A pictorial overview of this technique is provided in figure 5.14. Thermal simulations, shuriken spectroscopic data and AFM images strongly indicate that the nanolocalised spatial control of surface chemistry is possible through exploiting the thermal gradients in the water surrounding the TPS shuriken upon 8ns pulsed laser irradiation. This method of nanoscale functionalisation represents a significant improvement over the techniques mentioned in section 5.1.2 as it is a rapid, bottom-up approach to the problem of controlling surface chemistry on such a small scale. Furthermore, unlike other techniques this process does not involve a direct writing step and may functionalise large arrays of nanostructures simultaneously. Therefore, due to the high through-put nature of this technique and the simplicity of the overall process chemical functionalisation via nanolocalised water heating has the potential to be expanded beyond small scale laboratory use.

5.3 Conclusion

In this chapter we have introduced a novel protection/deprotection strategy to achieve nanolocalised surface chemical functionalisation of a TPS shuriken in order to allow selective placement of biomaterial in areas of high net chirality. This protection/deprotection strategy is a rapid, bottom up approach which can functionalise large arrays of nanostructures simultaneously (high-throughput). The protection step is adsorption of a thermally responsive PEG-thiol SAM across all Au surfaces of the nanostructure. The polymer chains of the PEG-SAM adopt a tightly packed, helical, gauche conformation at temperatures below 330K which inhibits the binding of biomaterial to the Au surface. If the temperature exceeds 330K along the entire length of the polymer chain for a sufficient time, the PEG-SAM adopts an elongated trans conformation which allows for adsorption of biomaterial. This unwinding process is kinetically limited as the temperature must remain above 330K for ~5ns to allow the irreversible intertwining of polymer chains.

The spatially localised deprotection step exploits a new thermoplasmonic phenomenon whereby thermal gradients are generated in the water surrounding the Au nanostructure upon excitation of a plasmonic resonance with an 8ns pulsed laser. These thermal gradients arise due to the low thermal diffusivity of water compared to Au. From temporal thermal simulations, three regions of distinct thermal behaviour are observed: the top surface; the shuriken central region and the shuriken arms. The PEG-SAM on the top surface remains in

the gauche conformation as the temperature of the surrounding water does not exceed the threshold temperature (330K). The temperature in the central region rapidly decreases moving up the z axis towards the top surface. The PEG-SAM in this region also remains in the gauche conformation as the temperature does not exceed 330K along the entire length of the PEG chain for a sufficient time to allow unwinding and intertwining. In contrast, the temperature in the shuriken arms remains above 330K moving up the z axis. The PEG-SAM is therefore able to undergo the gauche-trans conformational change in this region only. As a result of this thermal behaviour, biomaterial cannot adsorb on the top surface or the central region however adsorption in the shuriken arms is possible.

Experimental investigations of nanolocalised chemical functionalisation in the shuriken arms were primarily performed through measurement of the shuriken ORD. The thermal behaviour of nanostructure plasmonic resonance shifts were consistent with the theory that we are able to control the surface chemistry with nanoscale precision. The importance of pulse width and the dependency of the resonance shift on laser fluence also agreed with the thermal simulations. Furthermore, AFM measurements allow imaging of the nanoscale deprotected regions in the shuriken arms.

This protection/deprotection strategy has allowed us to enhance the biosensing capabilities of shuriken TPSs to Concanavalin A and EPSP down to attomolar quantities. The origin of this enhanced sensitivity lies in the chirality of EM fields associated with the different surfaces of the nanostructure. Using a deprotected PEG-TPS we are able to selectively place biomaterial in regions of the nanostructure that have a larger overall net chirality. This in turn elicits an enhanced spectroscopic response from a significantly reduced number of molecules. Hence the exploitation of thermal gradients in water surrounding nanostructures is a simple and effective method to enhance the performance of plasmonic metamaterials.

5.4 References

1. Tsakalakos, L., *Nanostructures for photovoltaics.* Materials Science and Engineering: Reports, 2008. **62**: p. 175-189.
2. T. Rindzevicius, Y.A., M. Kall, W. A. Murray, W. L. Barnes, *Long-range refractive index sensing using plasmonic nanostructures.* The Journal of Physical Chemistry C, 2007. **111**(32): p. 11806-11810.
3. R. D. Piner, J.Z., F. Xu, S. Hong, C. A. Mirkin, *"Dip-Pen" Nanolithography.* Science, 1999. **238**: p. 661-663.

4. J.U. Park, M.H., S. J. Kang, K. Barton, K. Adair, C. Y. Lee, M. S. Strano, A. G. Alleyne, J. G. Georgidas, P. M. Ferreira, J. A. Rodgers, *High-resolution electrohydrodynamic jet printing.* Nature Materials, 2007. **6**: p. 782-789.
5. C. K. Harnett, K.M.S., H. G. Craighead, *Low-energy electron-beam patterning of amine-functionalized self-assembled monolayers.* Applied Physics Letters, 2000. **76**(17): p. 2466-2468.
6. M. R. Shadnam, S.E.K., R. Fedosejevs, A. Amirfazli, *Thermo-kinetics study of laser-induced desorption of self-assembled monolayers from gold: case of laser micropatterning.* Journal of Physical Chemistry B, 2005. **109**: p. 11996-112002.
7. J. H. Slater , J.S.M., S. S. Yu , J. L. West, *Fabrication of multifaceted micropatterned surfaces with laser scanning lithography.* Advanced Functional Materials, 2011. **21**: p. 2876-2888.
8. T. Miyake, T.T., K. Kato, T. Zako, T. Funatsu, I. Ohdomari, *Selectivity improvement in protein nanopatterning with a hydroxy-terminated self-assembled monolayer template.* Nanotechnology, 2009. **18**(30).
9. Cohen, Y.T.a.A.E., *Optical chirality and its interaction with matter.* Physical Review Letters, 2010. **104**: p. 163901.
10. A.O. Govorov, H.H.R., *Generating heat with metal nanoparticles.* Nanotoday, 2007. **2**(1): p. 30-38.
11. A. Sanchot, G.B., R. Marty, A. Arbouet, R. Quidant, C. Girard, E. Dujardin, *Plasmonic nanoparticle networks for light and heat Concentration.* ACS Nano, 2012. **6**(4): p. 3434-3440.
12. G. Baffou, R.Q., F.J. Garcia de Abajo, *Nanoscale control of optical heating in complex plasmonic systems.* ACS Nano, 2010. **4**(2): p. 709-716.
13. Lee, H.G., *Chemical Thermodynamics for Metals and Materials*. 1999, London: Imperial College Press.
14. L. Liu, P.P., A. Hu, G. Zou, W. W. Duley, Y. N. Zhou, *Highly localized heat generation by femtosecond laser induced plasmon excitation in Ag nanowires.* Applied Physics Letters, 2013. **102**: p. 073107.
15. G. Baffou, C.G., R. Quidant, *Mapping heat origin in plasmonic structures.* Physical Review Letters, 2010. **104**: p. 136805.
16. G. Baffou, R.Q., C. Girard, *Heat generation in plasmonic nanostructures: Influence of morphology.* Applied Physics Letters, 2009. **94**: p. 153109.
17. A. I. Norman, Y.F., D. L. Ho, S. C. Greer, *Folding and unfolding of polymer helices in solution.* Macromolecules, 2007. **40**: p. 2559-2567.
18. H. Matsuura, K.F., *Conformational analysis of poly(oxyethylene) chain in aqueous solution as a hydrophilic moiety of non ionic surfactants* Journal of Molecular Structure, 1985. **126**: p. 251-260.
19. S. Lusse, K.A., *The interaction of poly(ethylene glycol) with water studied by 1H and 2H NMR relaxation time measurements.* Macromolecules, 1996. **29**: p. 4251-4257.
20. S. I. Jeon, J.H.L., J. D. Andrade, P. G. De Gennes, *Protein-surface interactions in the presence of polyethylene oxide.* Journal of Colloid and Interface Science, 1989. **142**(1): p. 149-158.
21. T. Shima, T.M., N. Hoshino,T. Akutagawa,Y. Kobayashi, K. Kinbara, *Thermally driven polymorphic transition prompting a naked-eye-detectable bending and straightening motion of single crystals.* Angewandte Chemie, 2004. **53**: p. 7173-7178.
22. P. Harder, M.G., R. Dahint, G.M. Whitesides, P.E. Laibinis, *Molecular conformation in oligo(ethylene glycol)-terminated self-assembled monolayers on gold and silver surfaces determines their ability to resist protein adsorption.* Journal of Physical Chemistry B, 1998. **102**: p. 426-436.
23. D. R. Bauer, J.I.B., R. Pecora, *Depolarized rayleigh spectroscopy studies of relaxation processes of polystyrenes in solution.* Macromolecules, 1975. **8**(4): p. 443-451.
24. M. L. Brongersma, N.J.H., P. Nordlander, *Plasmon-induced hot carrier science and technology.* Nature Nanotechnology, 2015. **10**: p. 25-34.

25. Gadzuk, J.W., *The road to hot electron photochemistry at surfaces: A personal recollection.* The Journal of Chemical Physics, 2012. **137**: p. 091703.
26. L. Cao, D.N.B., A. R. Guichard, M. L. Brongersma, *Plasmon-assisted local temperature control to pattern individual semiconductor nanowires and carbon nanotube.* Nano letters, 2007. **7**(11): p. 3523-3527.
27. A. D. McFarland, R.P.V.D., *Single silver nanoparticles as real-time optical sensors with zeptomole sensitivity.* Nano Letters, 2003. **3**(8): p. 1057-1062.

5.5 Appendix

	k (W m^{-1} K^{-1})	ρ (kg m^{-3})	C_p (J kg^{-1} K^{-1})
Gold	**318**	**19300**	**129**
Water	**0.6**	**999.9**	**4181.3**
Polycarbonate	**0.2**	**1210**	**1300**

Appendix 5.5.1: Thermal conductivity (k), density (ρ) and specific heat capacity (C_p) values of gold, water and polycarbonate utilised in thermal simulations.

Chapter 6: Mediation of TPS Mode Hybridisation by Protein Secondary Structure

6.1. Introduction

In chapter 4 we introduced a novel nanopatterned substrate composed of symmetry equivalent solid and inverse chiral nanostructures used to perform "plasmonic polarimetry" for the detection of protein secondary structure. The optical properties and biosensing capabilities of these hybrid nanostructures are found to be highly dependent on the hybridisation (coupling) of the electric and magnetic modes associated with the solid and inverse structures respectively. In this chapter we introduce a novel phenomenon whereby the adsorption of biopolymers (proteins and polypeptides) can modulate this hybridisation of electric/magnetic modes in a weakly coupled solid-inverse TPS nanostructure. This modulation of the TPS hybridisation upon adsorption of biomolecules is found to be sensitive to three distinct protein secondary structures and occurs when the sense of twist of the nanostructure chiral evanescent fields matches that of the chiral biomolecule. Unlike previous TPS measurements, this phenomenon does not depend on measuring the effective refractive index of molecules in nanostructure chiral fields and also foregoes the requirement for chiral fields that possess an enhanced chiral asymmetry relative to circularly polarised light. The main benefit of detecting secondary structure through protein mediated mode hybridisation compared with plasmonic polarimetry is that this new technique can unequivocally identify α-helical, β-sheet and disordered protein structures. This enhanced sensitivity to secondary structure motifs is attributed to the electric dipole-magnetic dipole origins of this effect as opposed to the electric quadrupole origins of plasmonic polarimetry. Initial measurements are conducted in the linear regime whereby adsorption of biomolecules results in subtle changes in the nanostructure reflectance lineshape which reflect a change in the TPS hybridisation. The study is then expanded into the nonlinear regime using chirally sensitive second harmonic generation (SHG) measurements. Firstly, we characterise SHG from chiral TPS nanostructures to ascertain the origins of the optical activity in the nonlinear regime. SHG measurements of nanostructures are then conducted upon adsorption of biomaterial whereby the chirally dependent electric dipole SHG term displays a variation due to mediation of the TPS hybridisation by the adsorbed biopolymer.

6.1.1 Hybridisation in Plasmonic Metamaterials

As the framework and functionality of plasmonic metamaterials evolves into ever more complex systems, developing an understanding of the interaction between constituent components within the metamaterial becomes vitally important. In sections 2.2.6 and 2.2.7 we have discussed the coupling between constituent structures in terms of plasmon hybridisation and the interference of bright and dark modes to generate Fano resonances/EIT-like effects. Currently, there are two methods through which this hybridisation of nanostructure plasmonic modes is achieved. Firstly, the work of Geissen et al [1] focussed on manipulation of geometric properties to control coupling between constituent components. This has been achieved using both solid and inverse nanostructures whereby introducing an increasing structural asymmetry in the design of dipole antenna/quadrupole antenna systems modulates the coupling between the bright dipole and dark quadrupole modes [2-4]. Geometric modifications allow the optical properties of the system to be tightly controlled however this method is extremely costly and time consuming due to the requirement for lithographic techniques to modify the geometry. In chapter 4 we introduce a simple alternative to geometric iterations which involves varying the noble metal film thickness of hybrid TPS nanostructures [5]. This modulates the hybridisation (coupling) between the electric/magnetic modes allowing the optical and chiroptical properties to be finely tuned. This represents a significant improvement over changing the sample geometry as varying the Au thickness of a TPS is a simple, cost-effective process. Despite these recent advances, it is clear that the scope for controlling the hybridisation of modes in plasmonic metamaterials remains relatively limited therefore an investigation into the possibility of using molecular species to control this hybridisation within plasmonic metamaterials is extremely relevant.

6.1.2 Nonlinear Optical Activity of Nanostructures

Second harmonic generation (SHG) of chiral plasmonic metamaterials is a potentially more incisive probe of chirality due to the presence of strong chiral χ^2 terms therefore nonlinear chiroptical measurements form an integral part of this study. Plasmonic metamaterials exhibit a strong SHG response as the majority of nanostructure SH studies are conducted under resonant conditions wherein nanostructure plasmonic modes overlap with either the fundamental or SH beam [6]. Strong coupling of an electromagnetic wave with nanostructures results in the generation of intense EM fields in the near field around specific regions of the

structure. This produces an enhanced SH signal since the extent of the nonlinear polarisation increases with the square of the incident electric field intensity[7]. The specific regions of the nanostructures where these intense fields are generated have been imaged through SHG microscopy and were shown to correspond to the excitation of plasmonic modes [8]. Despite enhancing the SH signal, large field gradients surrounding the nanostructures may be a hindrance when studying chiral plasmonic nanostructures. Intense EM fields are known to enhance higher order SH sources (electric quadrupole, magnetic dipole) from the bulk of the achiral metal[9]. These bulk contributions are also strongly dependent on atomic scale defects[10, 11] therefore distinguishing higher order achiral and higher order chiral SH sources is extremely challenging. As a result, the most reliable probe of nanostructure chirality should be the electric dipole SH contribution which arises purely from surface contributions. Preliminary nonlinear investigations into the origin of chiroptical effects in both resonantly and non-resonantly excited plasmonic nanostructures have been conducted wherein optical activity has been found to arise due to electric dipole elements[12] and higher order SH sources[13, 14]. Hence, it is reasonable to expect that nonlinear optical activity in this study may arise due to both these SH sources.

6.2 Results and Discussion

6.2.1 Gammadion Morphology and Hybridisation Scheme

The TPS nanostructures used in the present study consist of arrays of right or left handed (RH/LH) gammadions of length 600 nm with 900nm periodicity which are indented into the surface to a depth of 80nm. Nanostructure arrays cover an area of 300µm x 300µm with 340 gammadions along each side giving a total 115600 gammadions in the RH and LH arrays. Substrates are coated with 100nm Au by evaporation to produce a continuous Au film across the surface. Confirmation of nanostructure dimensions and quality is provided by SEM (figure 6.01a). As with the TPS shuriken nanostructures, the gammadions employed in this study constitute a hybrid solid-inverse system (figure 6.01b) wherein the solid structures are interpreted in terms of electric modes and the inverse structure in terms of magnetic modes[4]. Since the solid and inverse structures are symmetry equivalent and in close proximity, the electric and magnetic modes may hybridise generating in-phase (bonding) and

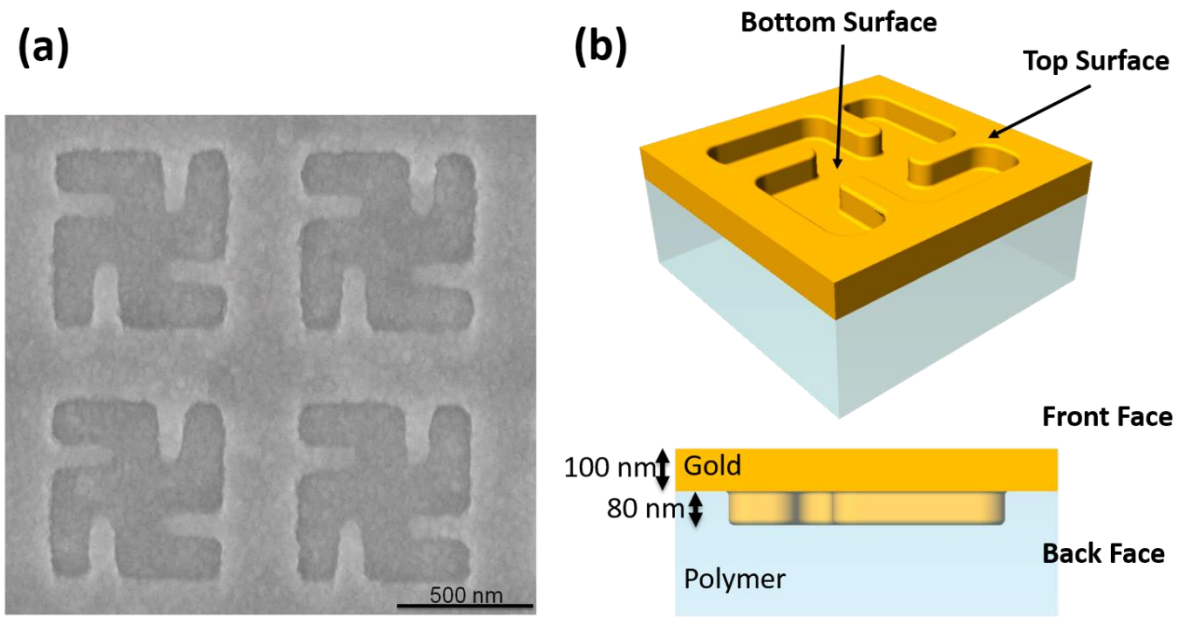

Figure 6.01: **(a)** SEM of gammadions **(b)** Pictorial representation of gammadion geometry and surfaces.

out-of-phase (anti-bonding) hybrid modes with the former having the lowest energy. Analogous to molecular orbital hybridisation a qualitative understanding of this hybridisation is provided by conducting a symmetry analysis of the gammadion (C_4 point group) to produce a hybridisation scheme (figure 6.02). From the C_4 character table (appendix 6.5.1) electric and magnetic modes are found to belong to the A, B and E symmetry species. As with weakly coupled TPS shurikens, the gammadion reflectance spectra (figure 6.03) possess asymmetric Fano resonances indicating the presence of a broad optically bright mode and narrow dark mode. The two optically bright modes are the dipolar A and E species however only E is accessible in the experimental geometry of linear measurements as A corresponds to excitation of field components normal to the sample surface. The remaining B mode does not contain a dipolar function however a quadrupolar term is present hence this must be the dark mode. Consequently, the Fano resonance arises due to the interference between a bright, out-of-phase dipolar hybrid mode (D_{E-M}) and a dark, in-phase quadrupolar hybrid mode (Q_{E+M}). The strength of this interference is governed by the energy separation Δ which is ultimately controlled by the level of hybridisation between the electric/magnetic modes of the system.

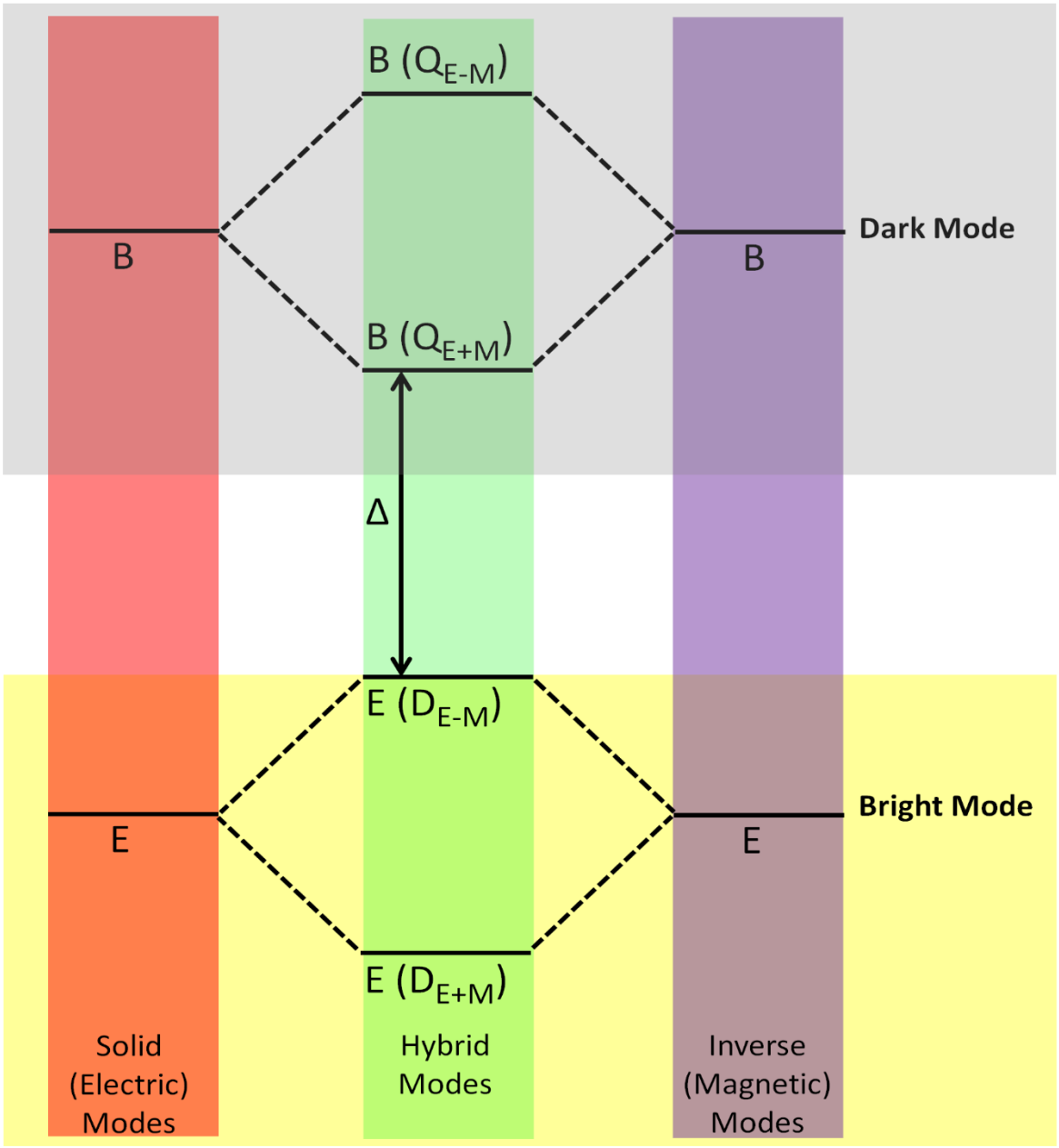

Figure 6.02: Gammadion hybridisation scheme representing a qualitative interpretation of the coupling between electric/magnetic modes. Δ is the energy separation between the bright and dark mode.

6.2.2 Characterisation of Linear Optical Properties

In chapter 4, using Au thickness, we are able to control the hybridisation of the electric/magnetic modes allowing the TPS shuriken reflectance and chiroptical response to be tuned. Strong hybridisation between the electric/magnetic modes results in the appearance of a transmission dip within resonances in the reflectance spectrum (electromagnetically induced transparency, EIT) whilst the ORD displays a lineshape typical of a single helical oscillator (SHO) indicating a large level of chirality. In contrast, weak levels of hybridisation in

TPSs result in the appearance of Fano resonances in the reflectance spectrum whilst the ORD lineshape is typical of a weakly chiral system (coupled oscillator).

RH and LH gammadion linear optical properties are characterized through both the front face (Au/buffer interface) and back face (Au/polycarbonate interface) by measurement of the ORD and reflectance spectra in 10mM tris buffer (figure 6.03). Front face measurements of gammadion enantiomers produce identical visible and Near Infra-Red (NIR) reflectance spectra which possess several sharp, asymmetric reflectance dips typical of Fano resonances indicating weak hybridisation between the electric and magnetic modes. RH and LH

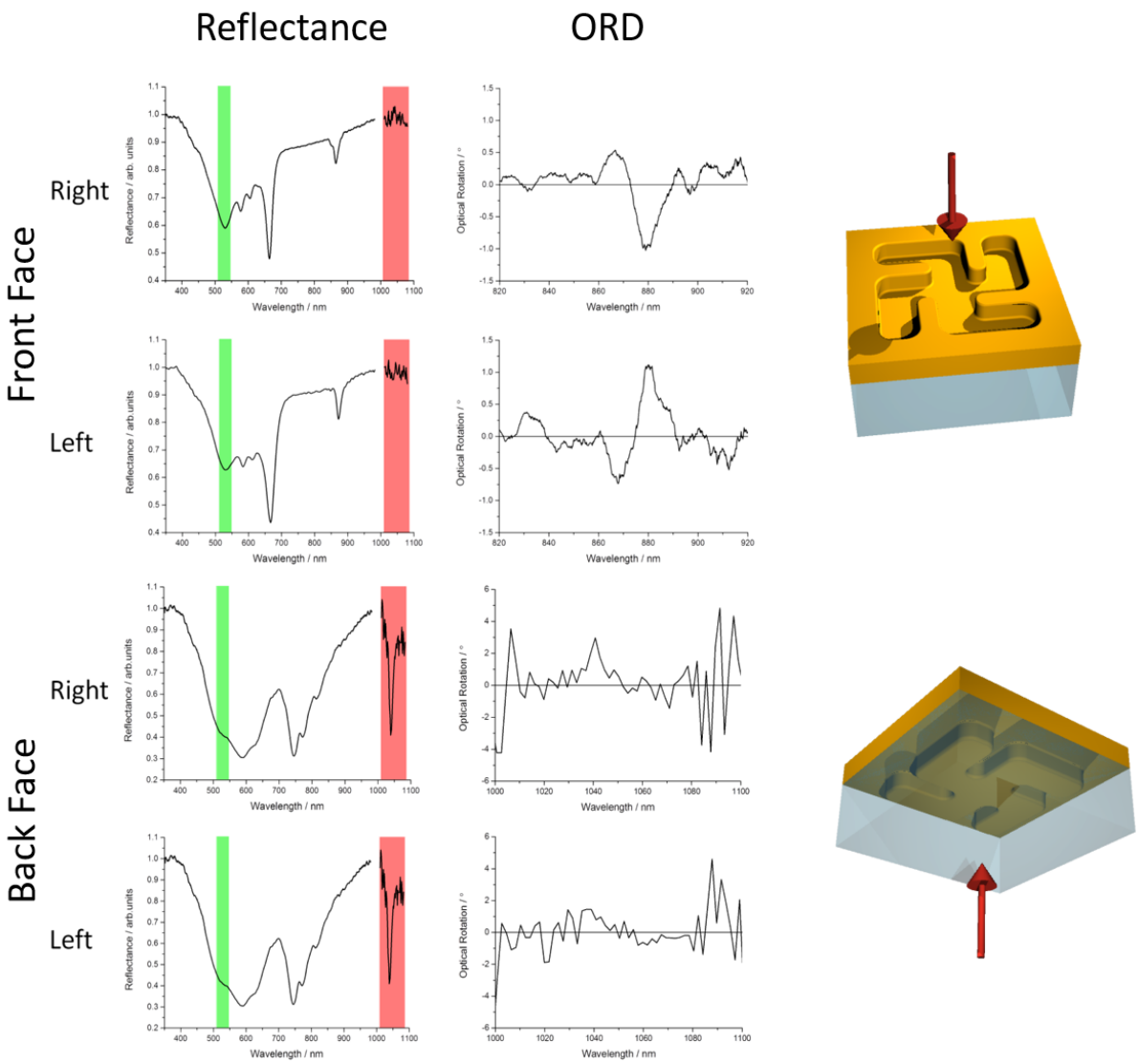

Figure 6.03: Linear reflectance and ORD measurements of RH and LH gammadions in the presence of 10mM tris HCl buffer recorded through the front and back face. For nonlinear measurements the red and green highlighted regions represent the bandwidth of the fundamental and SH beam respectively.

gammadions induce an equal and opposite rotation of linearly polarised light with an ORD intensity of ≈1^{o} which possesses only a single peak. This weak intensity and lineshape of the ORD also suggests low levels of hybridisation between electric and magnetic modes which results in the system displaying low levels of optical activity typical of a coupled oscillator. Similar to the front face, the back face reflectance spectra possess Fano-like resonances indicative of poor hybridisation between electric/magnetic modes. The ORD is below the detectable limit which again suggests poor electric/magnetic hybridisation and the low levels of chirality associated with a coupled oscillator system. Hence, gammadion nanostructures display low levels of hybridisation between electric and magnetic modes meaning the energy gap (Δ) between (D_{E-M}) and (Q_{E+M}) is large. Furthermore, in agreement with this weak hybridisation the system displays low levels of optical activity consistent with a coupled oscillator model of chirality.

In order to rationalise the chiroptical behaviour displayed by TPS gammadions, the reflectance spectra and chirality of the near fields have been modelled upon illumination from both the front and back face (figure 6.04). The simulated reflectance spectra reproduce the main features of the experimental data albeit with a slight red shift which is attributed to nanoscale defects. From chapter 4 we know that scattering of linearly polarised light by chiral TPS nanostructures results in the overlap of parallel electric and magnetic fields generating RH and LH chiral fields in the nanostructure near-field. Beginning with the front face, the chirality of evanescent fields is modelled for both the top and bottom surface at the 930nm resonance excitation wavelength (figure 6.04g-h). As with TPS shurikens, both RH and LH chiral fields are generated at the top surface (inverse structure) and bottom surface (solid structure). However, there is an excess of one field handedness therefore an overall net chirality exists. The magnitude of the chiral asymmetry (C) associated with these fields is > 1 therefore they are more inherently chiral than circularly polarised light (CPL). The field chirality on the top surface is also larger as the excitation wave is initially incident on this surface meaning a larger proportion of the EM energy is absorbed at this surface. Excitation of the resonance at 1060nm through the back face also results in the generation of RH and LH chiral fields at the top and bottom surface (6.04c-d). However, there are some important differences with respect to the front face EM field simulations. The normalised chirality values are < 1 indicating that the chirality of evanescent fields is less than that of CPL, these fields

will be referred to as sub-chiral fields. In addition, the chirality of fields is larger on the bottom surface than the top surface since the excitation beam is initially incident on the solid structure.

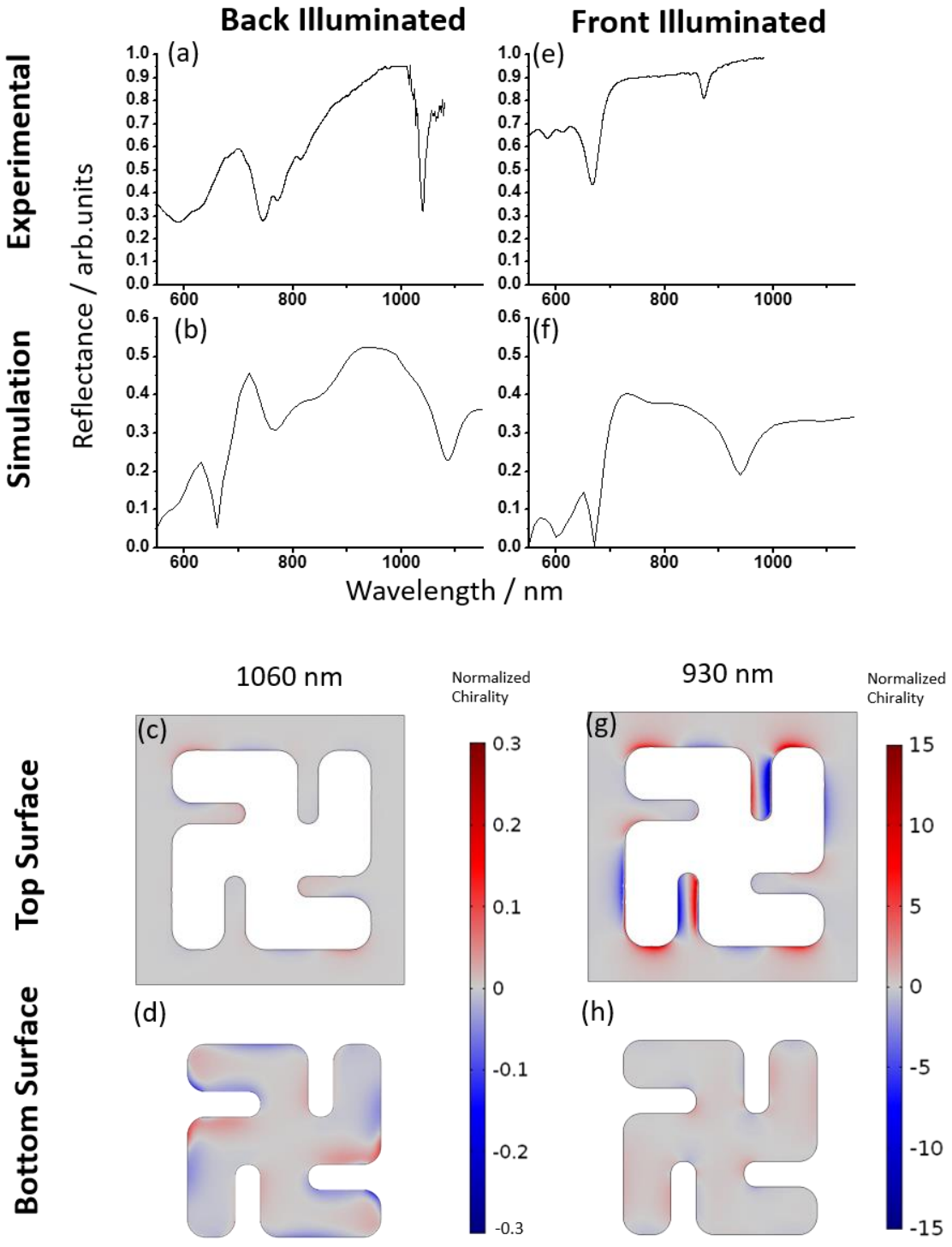

Figure 6.04: Back face illuminated experimental **(a)** and simulated **(b)** reflectance spectra and normalized chirality surface plots for the top **(c)** and bottom surface **(d)**. Front face illuminated experimental **(e)** and simulated **(f)** reflectance spectra and normalized chirality surface plots for the top **(g)** and bottom surface **(h)**.

The ORD intensity and lineshape upon front face and back face illumination indicate excitation of the gammadion in both arrangements results in low levels of chirality. In terms of back face illumination, the EM modelling agrees with this experimental behaviour as the chirality of fields is < 1. In contrast, the chiral EM fields generated upon excitation of the front face resonance possess chirality > 1. Despite this enhanced chiral asymmetry of EM fields, the ORD lineshape is typical of a weakly chiral system. This means the RH and LH chiral fields surrounding the structure must cancel out to a large degree which renders the overall net chirality extremely small. Generation of large net chirality requires strong coupling between electric and magnetic modes [5]. The Fano-like lineshapes in the front face reflectance spectra indicate weak coupling therefore low levels of net chirality for these structures are to be expected. In the next section we will investigate how this low level of chirality affects the gammadion biosensing properties upon adsorption of proteins with different secondary structure motifs on the front face.

6.2.3 Linear Spectroscopic Measurements of Gammadions Upon Adsorption of Biomolecules

In chapter 4 we tested the novel spectroscopic technique of plasmonic polarimetry using strongly coupled and weakly coupled TPS nanostructures whereby only the strongly coupled substrates were sensitive to protein structure. In this section we conduct plasmonic polarimetry measurements using the weakly coupled TPS gammadions upon adsorption of proteins with distinct α-helical (native Bovine Serum Albumin, BSA), β-sheet (Concanavalin A) and unfolded (denatured BSA) protein secondary structures. The front face plasmonic polarimetry response upon adsorption of each protein can be found in appendix 6.5.2. Due to the weak single peak gammadion ORD, this data possesses an extremely poor signal-to-noise therefore it is not possible to accurately gauge the spectral position of the ORD peak. This means we cannot measure any asymmetries in the resonance shift for RH and LH gammadions upon adsorption of biomolecules. As with weakly coupled TPS shurikens, this lack of sensitivity ultimately arises due to the small net chiral asymmetry of the evanescent fields surrounding the nanostructures.

Alternatively, if we neglect refractive index induced shifts, it is evident that protein adsorption has an asymmetric effect on the Fano lineshape of the RH and LH gammadion reflectance spectra upon protein adsorption (figure 6.05). It is most relevant to compare the effect of

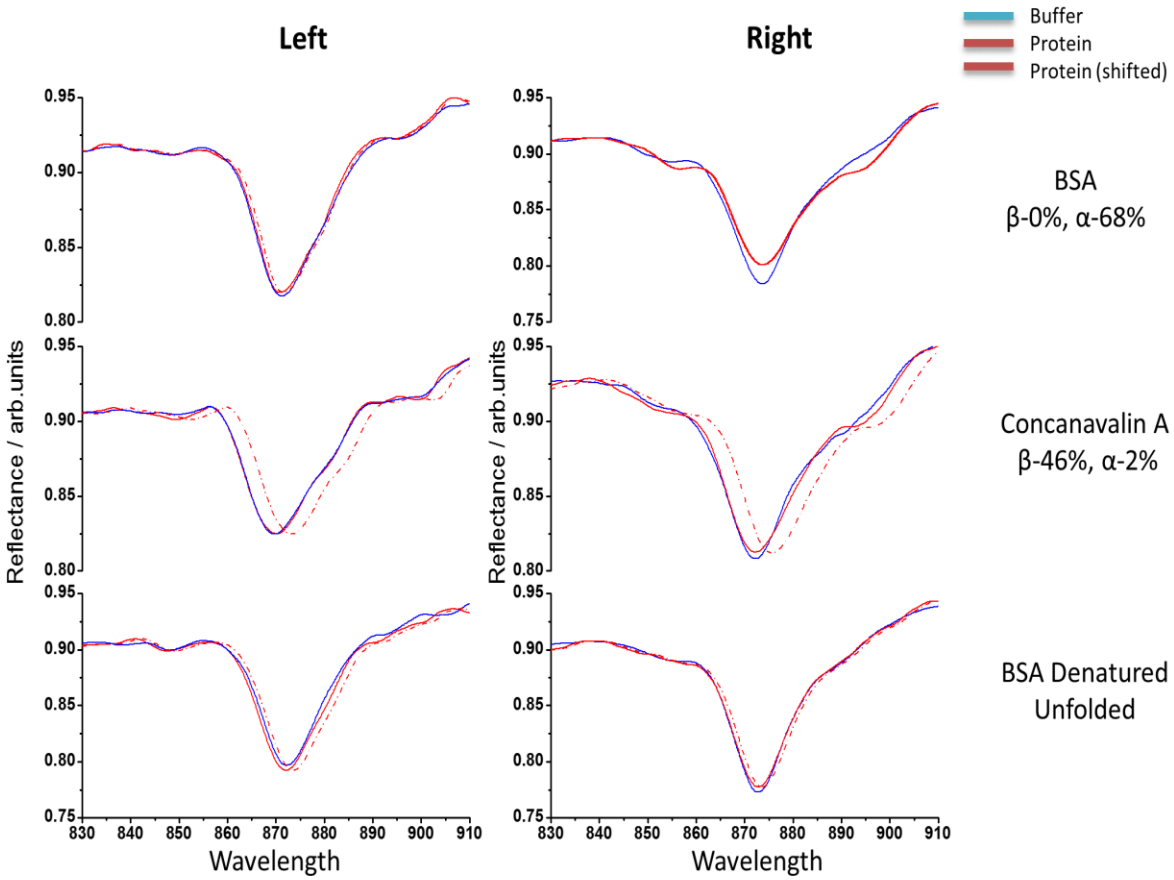

Figure 6.05: Reflectance spectra of RH and LH gammadions for front face protein experiments. Blue lines are for buffer, dotted red show results with protein solutions and the solid red line is the protein solution data blue shifted to overlap with the buffer to allow clearer comparison of lineshapes.

Bovine Serum Albumin (BSA, α-helical) and Concanavalin A (β-sheet) with the denatured BSA (unfolded). The ordered protein structures have a significantly different effect on the resonance lineshape compared with the unfolded structure, specifically for the RH gammadion. Adsorption of BSA and Concanavalin A on RH nanostructures leads to the appearance of a subtle reflectivity dip at ~895nm which results in an overall broadening of the resonance lineshape towards longer wavelengths. In stark contrast the RH reflectance lineshape remains effectively unchanged upon adsorption of denatured BSA indicating that the presence of ordered macromolecular structure is required to elicit a change in the RH gammadion lineshape. For all three proteins the lineshape of LH gammadions is unaffected. The reflectance spectra in figure 6.05 imply that through asymmetric changes in the resonance lineshape between RH and LH structures, TPS gammadions are able to distinguish ordered protein structures (α-helical, β-sheet) from biomolecules that lack macromolecular structure.

The Fano resonance lineshape displayed by a TPS nanostructure depends on the interference between the bright and dark hybrid mode. In chapter 4 this was modulated through changing the thickness of the Au film which resulted in the appearance of a dip in the Fano resonance. This indicates an enhancement in the interference between bright and dark hybrid modes (reduction in Δ) due to increased hybridisation between the electric/magnetic modes of the

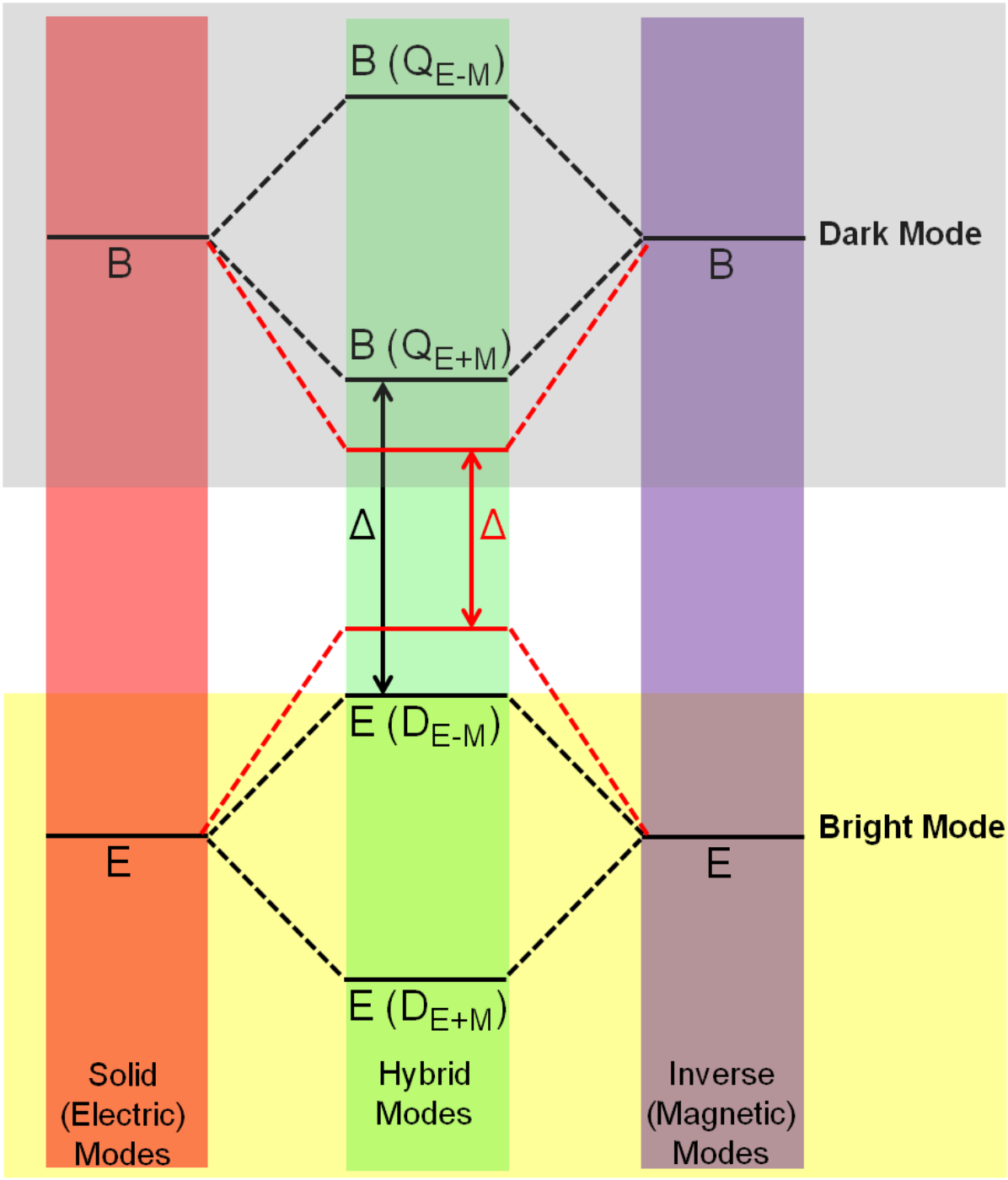

Figure 6.06: Qualitative representation of the changes in hybridisation of the electric and magnetic modes between buffer (black) and upon protein adsorption (red). Δ is the energy separation between the bright and dark modes.

constituent solid/inverse structures. The similar albeit significantly weaker effect observed upon adsorption of BSA and Concanavalin A suggests that the presence of structured proteins can also affect the interference between the bright (D_{E-M}) and dark (Q_{E+M}) hybrid modes of the TPS gammadions. Upon adsorption of structured biomolecules, the energy gap Δ between these modes decreases due to a reduction in the energy of Q_{E+M} and a corresponding increase in D_{E-M} (figure 6.06). This must arise due to a molecular induced increase in the hybridisation of electric and magnetic modes which will also affect the level of chirality in the system. It is important to understand that the sensitivity of this effect to biomolecular structure does not rely on the effective refractive indices of molecules in nanostructure chiral fields. Hence, this new phenomenon of mediating electric/magnetic mode hybridisation using biomolecular species represents an alternative method to refractive index based measurements for the detection of protein structure using TPS nanostructures. Measurements of this new phenomenon through discrete reflectance lineshape variations provide a valuable insight with regards to the physical effect of protein adsorption on the weakly hybridised solid/inverse system. However, due to the relatively weak nature of these effects, linear measurements are not a particularly incisive spectroscopic probe.

6.2.4 Characterisation of Gammadion Nonlinear Optical Properties

An alternative and potentially more sensitive method to investigate protein mediation of TPS mode hybridisation is to conduct measurements in the nonlinear regime through Second Harmonic Generation (SHG). Firstly, it is necessary to characterize the SHG response of nanostructures from the front and back face under two different polarisation conditions. Measurements are recorded upon front and back face illumination in the presence of tris buffer solution through a far-field polarisation analysis of both the s-polarised and p-polarised SH signal intensity (figure 6.07). Comparing the shape of the polar plots for gammadions and a flat Au surface we find that a chirally sensitive nonlinear response is observed for s and p-polarised SHG only when the TPS nanostructures are irradiated through the back face.

The sensitivity to gammadion chirality displayed by s and p-polarised SH measurements recorded through the back face can be explained by referring to linear reflectivity measurements. From figure 6.04 we find that RH and LH back face reflectance spectra possess a sharp, asymmetric Fano resonance centred at 1040nm which overlaps with the bandwidth of the 1050nm fundamental whilst the SH beam around 525nm overlaps a broad resonance.

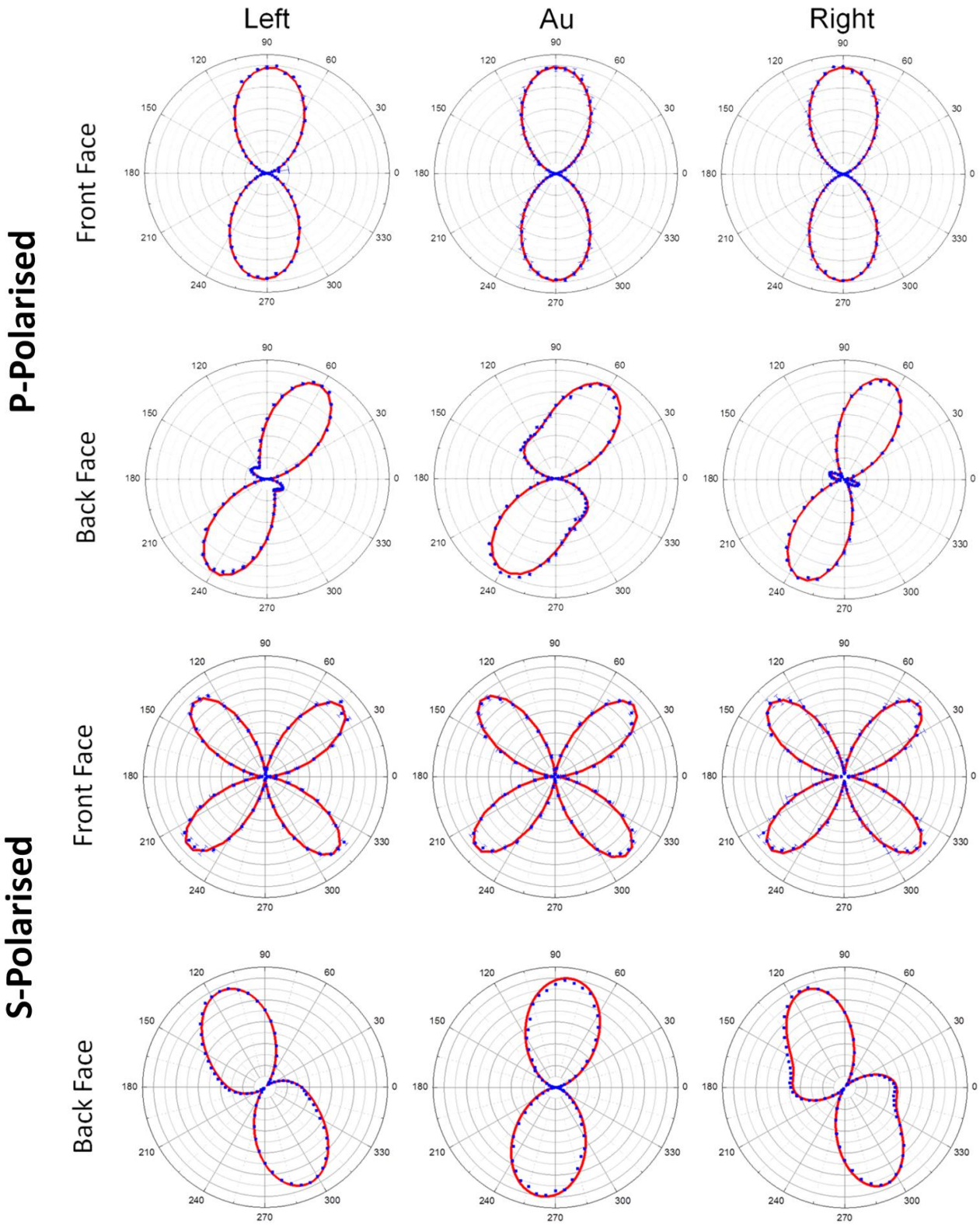

Figure 6.07: Normalised s and p-polarised SHG profiles of 100nm Au TPS gammadions and a flat Au surface measured from the front and back face in the presence of 10mM tris buffer. Blue squares are experimental data and the red solid line is the fit to equation 2.62 in chapter 2.

In the case of front face measurements, the reflectance spectra do not possess a resonance which overlaps with the 1050nm fundamental beam however a broad resonance does coincide with the SH beam. Since only the back face measurements display nonlinear optical activity it is evident that excitation of a Fano resonance by the fundamental beam is required to elicit a chiral SH response from TPS nanostructures.

To quantify the nature of the nanostructure SH response we follow the theoretical framework outlined in chapter 2 and fit experimental polarisation dependent data to equation 2.62. This fitting procedure allows us to quantify the magnitude of the relevant electric dipole, magnetic dipole, electric quadrupole and other higher order contributions to the SH signal. It is important to remember that for the s-polarised SH signal α is the electric dipole contribution and γ is the magnetic dipole element and vice versa for the p-polarised SH signal. Fitting parameters for the p and s-polarised SH signal from the front and back faces are listed in tables 6.01-6.04.

In agreement with the polar plots in figure 6.07, front face fitting parameters are invariant within experimental error between gammadions and Au for both the s and p-polarised SH signals. P-polarised data are dominated by an electric dipole whilst slight contributions from the two higher order terms (δ, ε) and the electric quadrupole are present. The predominant s-polarised fitting parameter is the electric quadrupole (β) which accounts for the four lobed appearance of the polar plot whilst small values of the higher order δ, ε contributions are also observed.

As we have seen from the polar plots in figure 6.07, the p and s-polarised SH response from the back face differs between gammadion enantiomers and flat Au. For p-polarised profiles the fitting coefficients that are sensitive to chirality (different for RH and LH gammadions) are the β, γ and δ terms. The chirally sensitive term which has the most significant effect on the shape of the SH profile is γ which accounts for the electric dipole contribution in the p-polarised SH signal. For s-polarised SH measurements sensitivity to the chirality of gammadion nanostructures is derived primarily from the relative strength of three coefficients: α, β and δ. Consistent with p-polarised data the term primarily responsible for the disparity between RH and LH SH profiles is the electric dipole contribution (α) whereas

Front Face (P-Pol)	α	β	γ	δ	ε
Right	0.01 ± 0.02	0.41 ± 0.07	0.95 ± 0.02	0.10 ± 0.06	0.48 ± 0.08
Left	0.03 ± 0.02	0.50 ± 0.07	0.94 ± 0.02	0.15 ± 0.06	0.51 ± 0.08
Au	0.01 ± 0.02	0.47 ± 0.07	0.95 ± 0.02	0.12 ± 0.06	0.47 ± 0.08

Table 6.01: Fitting coefficients to equation 2.62 for p-polarised SH emission from the front face in the presence of tris buffer. Errors are derived from a standard deviation of four measurements.

Back Face (P-Pol)	α	β	γ	δ	ε
Right	0.04 ± 0.02	0.47 ± 0.07	0.62 ± 0.02	-0.17± 0.06	1.46 ± 0.08
Left	0.02 ± 0.02	1.42 ± 0.07	0.53 ± 0.02	0.04 ± 0.06	1.30 ± 0.08
Au	0.02 ± 0.02	1.82 ± 0.07	0.65 ± 0.02	0.11 ±0.06	0.79 ± 0.08

Table 6.02: Fitting coefficients to equation 2.62 for p-polarised SH emission from the back face in the presence of tris buffer. Errors are derived from a standard deviation of four measurements.

Front Face (S-Pol)	α	β	γ	δ	ε
Right	0.05 ± 0.02	3.67 ± 0.07	0.03 ± 0.02	0.21 ± 0.06	-0.18 ± 0.08
Left	0.04 ± 0.02	3.67 ± 0.07	0.02 ± 0.02	0.29 ± 0.06	-0.28 ± 0.08
Au	0.04 ± 0.02	3.77 ± 0.07	0.02 ± 0.02	0.29 ± 0.06	-0.30 ± 0.08

Table 6.03: Fitting coefficients to equation 2.62 for s-polarised SH emission from the front face in the presence of tris buffer. Errors are derived from a standard deviation of four measurements.

Back Face (S-Pol)	α	β	γ	δ	ε
Right	0.45 ± 0.02	0.40 ± 0.07	0.70 ± 0.02	-0.11 ± 0.06	-1.17 ± 0.08
Left	0.34 ± 0.02	0.63 ± 0.07	0.70 ± 0.02	-0.41 ± 0.06	-1.12 ± 0.08
Au	0.01 ± 0.02	0.59 ± 0.07	0.98 ± 0.02	0.05 ± 0.06	0.36 ± 0.08

Table 6.04: Fitting coefficients to equation 2.62 for s-polarised SH emission from the back face in the presence of tris buffer. Errors are derived from a standard deviation of four measurements.

variations in the β and δ terms have a negligible effect on the overall shape. The chiroptical behaviour of back face s-polarised and p-polarised SH measurements are in general agreement with previous discussion of SHG from chiral plasmonic metamaterials in section 6.1.2. The electric dipole term is the most sensitive to the chirality of the surface which is commensurate with the fact that this term arises purely from surface contributions. The weak chiral sensitivity of β and δ is attributed to the fact that in plasmonic nanostructures these terms may arise from both the achiral bulk Au and the chiral metal surface. From the polar plots and fitting parameters it is evident that the s-polarised data display a larger discrepancy between RH and LH gammadions therefore subsequent spectroscopic measurements of gammadions upon protein adsorption will use this SH polarisation state.

6.2.5 Nonlinear Spectroscopic Measurements of Gammadions Upon Adsorption of Biomolecules

SHG measurements of gammadions upon adsorption of biomolecules are conducted through illumination of the back face of the TPS with the protein solutions absorbed on the front face. The skin depth of Au at the fundamental wavelength is ~ 15nm [15] therefore the surface/bulk sources of the SH signal from the back face are not in direct contact with the adsorbed species at the front face. Thus, the biomolecules cannot directly influence the optical/chiroptical properties of the TPS when illuminated from the back face. Consequently, any protein induced changes in the SH response must arise due to an indirect interaction between the biomolecules and the substrate. Furthermore, as the substrate is illuminated through the

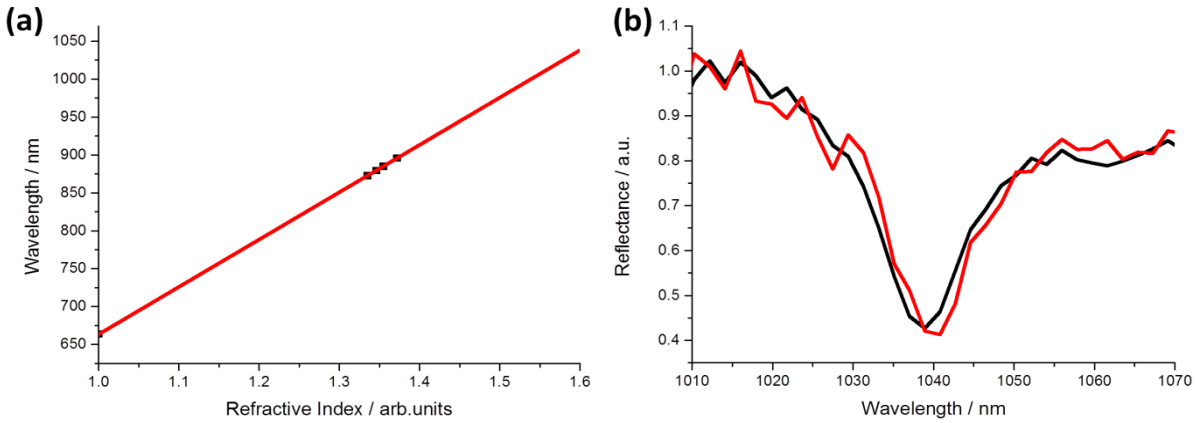

Figure 6.08: (a) Relationship between resonance position and refractive index for reflectance spectra recorded through the front face. **(b)** Reflectance spectra measured through the back face in the presence of air (n=1.00) and 8M guanidine hydrochloride (n=1.48).

back face in nonlinear measurements this indirect interaction must occur via sub-chiral fields (figure 6.04).

Linear measurements confirm that the refractive index of the dielectric at the front face has an extremely small effect on the optical properties of TPS gammadions upon back face illumination. The refractive index sensitivity when measured through the back face at the 1040nm resonance is 3.37nm/RIU (figure 6.08b) which is two orders of magnitude smaller than the front face resonance at 870nm (373nm/RIU) (figure 6.08a). These observations are in agreement with EM field modelling whereby the field intensities and chirality at the fundamental and SH wavelength for back face illumination are invariant upon large refractive index variations (appendix 6.5.3). Consequently, the presence of protein solution will induce a negligible shift in the wavelength of the back face resonance as the refractive index change relative to buffer is extremely small ($\Delta n \sim 0.01$). This means we can discount a wavelength shift of the 1040nm resonance as the source of any observed changes in the gammadion SH signal upon protein adsorption. We confirm the invariance of the back face gammadion SHG response upon adsorption of an achiral dielectric at the front face by performing polarisation dependent measurements (figure 6.09). RH and LH gammadion profiles and their corresponding fitting parameters are found to be identical going from air (n=1.00) through buffer (n=1.33) to guanidine hydrochloride (n=1.47). As discussed in section 6.2.3, detection of biopolymer structure by mediation of TPS mode hybridisation is not a refractive index based technique. Hence, we suggest that the SHG changes reported in the following section are the result of biopolymer molecules mediating the coupling between the electric and magnetic modes of the TPS.

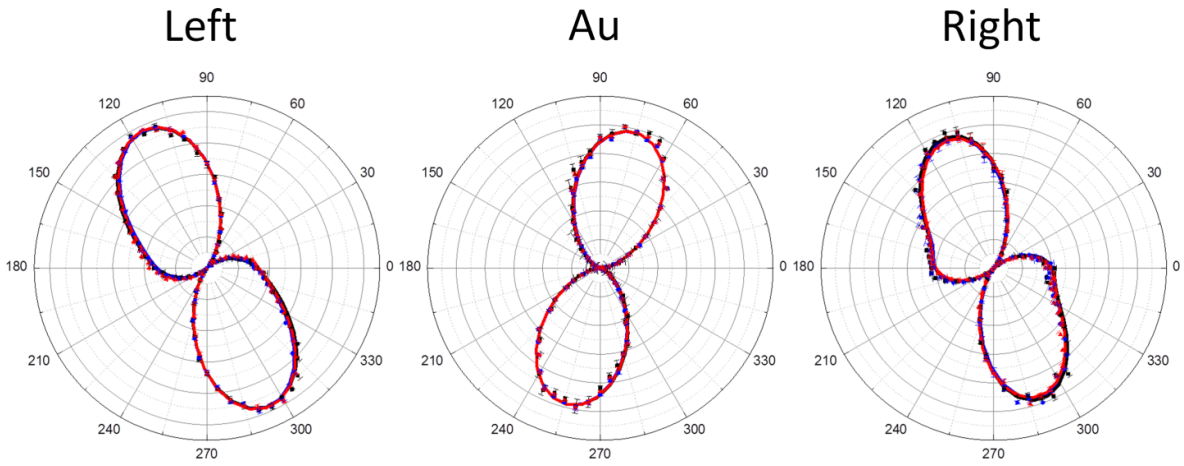

Figure 6.09: Normalised back face s-polarised SH profiles for gammadions and Au collected in the presence of air, (black) 10mM tris buffer (blue) and 8M Guanidine Hydrochloride (red). Zero degrees in the polar plots corresponds to s-polarised incident light.

Au	α	β	γ	δ	ε
Air	0.04 ± 0.02	0.76 ± 0.07	0.82 ± 0.02	0.22 ± 0.06	0.88 ± 0.08
Buffer	0.03 ± 0.02	0.73 ± 0.07	0.81 ± 0.02	0.24 ± 0.06	0.91 ± 0.08
Guanidine	0.03 ± 0.02	0.75 ± 0.07	0.81 ± 0.02	0.23 ± 0.06	0.90 ± 0.08

Table 6.05: Fitting parameters to equation 2.62 for the s-polarised SH signal generated from Au in the presence of air, 10mM tris buffer and 8M Guanidine Hydrochloride.

Left	α	β	γ	δ	ε
Air	0.32 ± 0.02	0.68 ± 0.07	0.67 ± 0.02	-0.38 ± 0.06	-1.20 ± 0.08
Buffer	0.32 ± 0.02	0.62 ± 0.07	0.67 ± 0.02	-0.30 ± 0.06	-1.24 ± 0.08
Guanidine	0.33 ± 0.02	0.66 ± 0.07	0.67 ± 0.02	-0.29 ± 0.06	-1.25 ± 0.08

Table 6.06: Fitting parameters to equation 2.62 for the s-polarised SH signal generated from LH gammadions in the presence of air, 10mM tris buffer and 8M Guanidine Hydrochloride.

Right	α	β	γ	δ	ε
Air	0.40 ± 0.02	0.29 ± 0.07	0.76 ± 0.02	-0.21 ± 0.06	-1.17 ± 0.08
Buffer	0.40 ± 0.02	0.25 ± 0.07	0.76 ± 0.02	-0.24 ± 0.06	-1.11 ± 0.08
Guanidine	0.41 ± 0.02	0.25 ± 0.07	0.76 ± 0.02	-0.19 ± 0.06	-1.16 ± 0.08

Table 6.07: Fitting parameters to equation 2.62 for the s-polarised SH signal generated from RH gammadions in the presence of air, 10mM tris buffer and 8M Guanidine Hydrochloride.

The sensitivity to protein structure in the nonlinear regime is investigated by measuring the TPS gammadion SH response upon adsorption of a range of biopolymers (proteins and polypeptides). We begin by investigating the effect of protein secondary structure on the RH and LH gammadion SHG response. The structural moieties used are naturally occurring α-helical (BSA, Haemoglobin), β-sheet (Concanavalin A, β-Lactoglobulin, IgG) and unfolded protein structures (Denatured BSA). The fitted and experimental data for RH and LH gammadions upon adsorption of these proteins are found in figure 6.10. The values of the fitting coefficients for all buffer and protein experiments are found in appendix 6.5.4 and 6.5.5. As mentioned prior, there are three elements (α, β, δ) that display sensitivity to nanostructure chirality for the s-polarised SH signal. Adsorption of ordered protein structure only induces a change in the magnitude of the gammadion electric dipole (α) SH contribution which is consistent with the previous buffer nonlinear measurements whereby α was found

to be the most sensitive element to chirality. The coloured lobes at 0° and 180° in figure 6.10 correspond to the magnitude of the gammadion electric dipole (α) SH contribution obtained from the fit to equation 2.62 allowing a graphical representation of the protein induced variation. The effect is quantified by calculating the α coefficient asymmetry parameter $\varsigma = \left(\frac{(\text{Analyte}-\text{Buffer})}{(\text{Buffer})}\right)$ for both gammadion enantiomers, Table 6.08.

Adsorption of proteins with a high α-helical content (BSA and Haemoglobin) causes the magnitude of the RH gammadion electric dipole (α) SH element to markedly increase relative to measurements in buffer resulting in a positive value of ς. Conversely, adsorption of the β-sheet proteins Concanavalin A, β-Lactoglobulin and IgG results in a large reduction in the RH gammadion α lobe magnitude compared with buffer producing negative ς values. As with

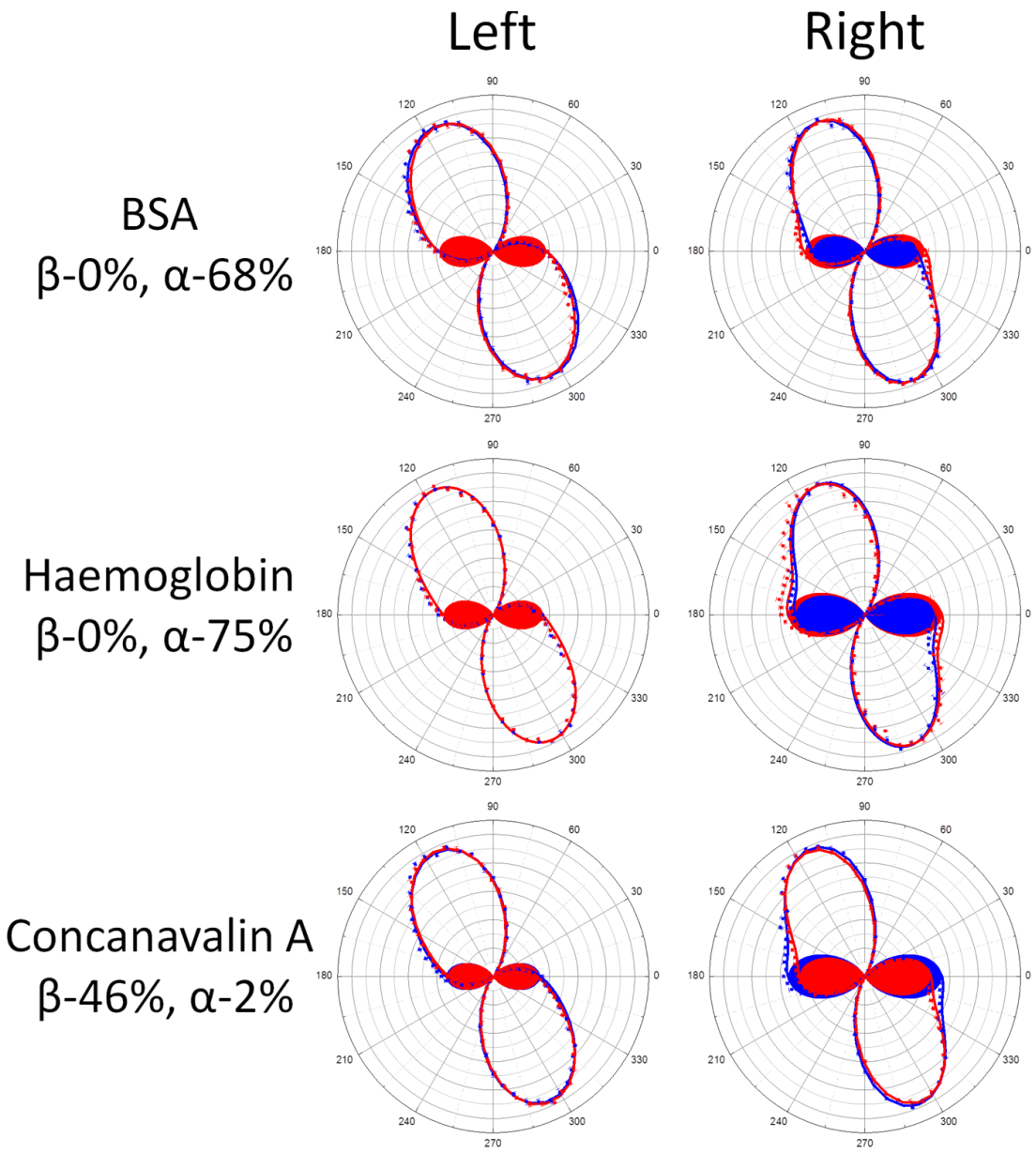

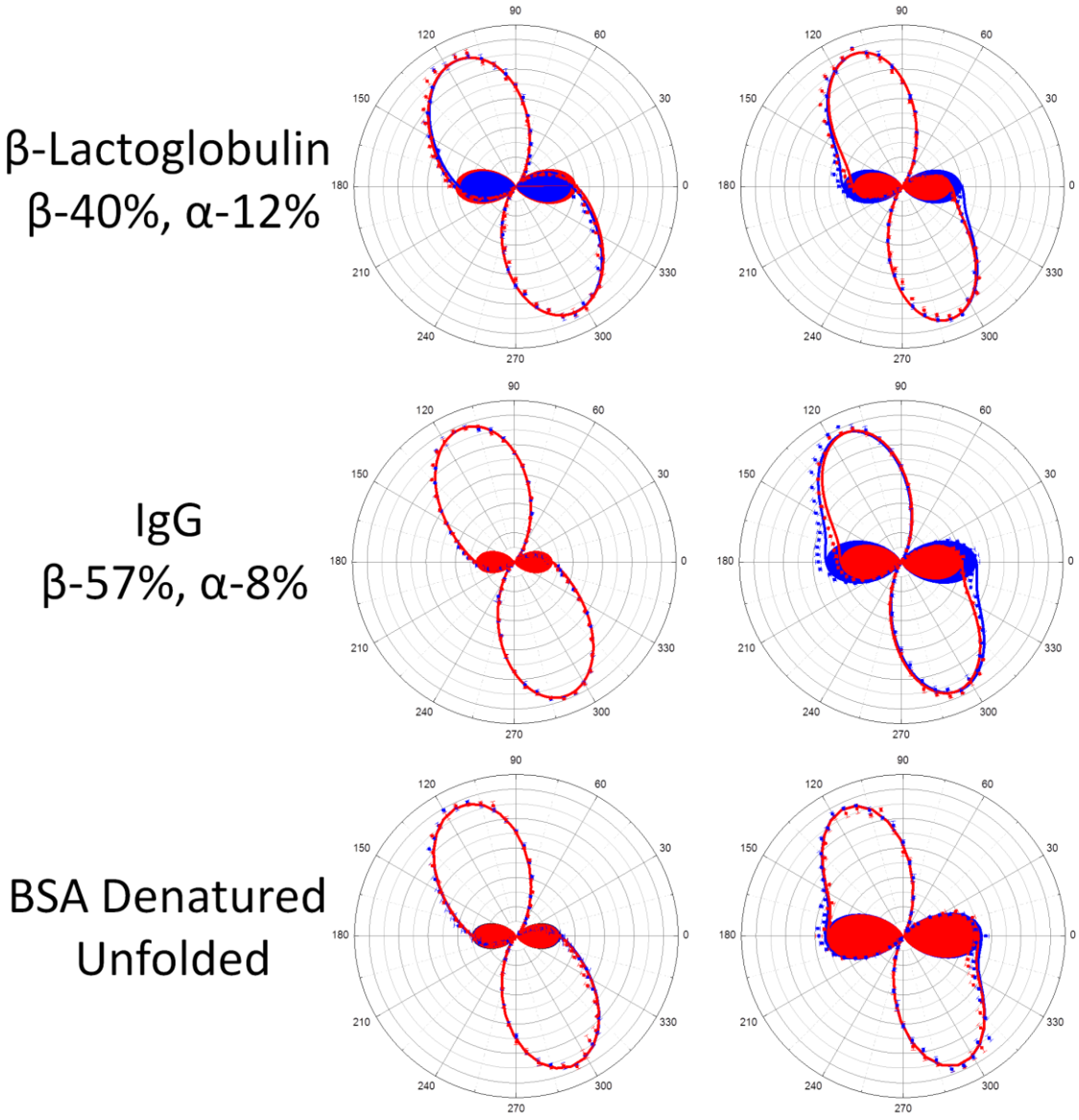

Figure 6.10: Normalised intensity of S-polarised SH signal as a function of the incident polarisation angle (θ) for arrays of right and left handed gammadions in the presence of tris buffer (blue) and protein solution(red). Squares represent the measured experimental data; solid lines are the fit to equation (2.62); blue and red shaded lobes correspond to the fit of only the dipolar term (α) of equation (2.62). Zero degrees in the polar plots corresponds to s-polarised incident light.

linear measurements protein adsorption is found to influence the SH response of only the RH gammadion whilst the LH nanostructure α lobe is unaffected for all proteins and $\varsigma = 0$. In order to confirm that the observed effects arise due to protein secondary structure we measure the SH response upon binding of denatured BSA to the surface. BSA was denatured using 8M Guanidine Hydrochloride which induces unfolding of the protein macromolecular structure through the disruption of non-covalent interactions between peptide chains[16]. Adsorption of denatured BSA does not induce a significant change in the α lobe magnitude

	ζ	
	Right	Left
Poly D-Lysine	0.04 ± 0.03	0.26 ± 0.03
Poly L-Lysine	0.25 ± 0.03	0.00 ± 0.03
BSA	0.22 ± 0.03	0.02 ± 0.03
Haemoglobin	0.14 ± 0.03	0.00 ± 0.03
Concanavalin A	-0.20 ± 0.03	-0.06 ± 0.03
B- Lactoglobulin	-0.18 ± 0.03	0.06 ± 0.03
IgG	-0.20 ± 0.03	0.00 ± 0.03
BSA Denatured	-0.04 ± 0.03	-0.04 ± 0.03

Table 6.08: Values of ζ for RH and LH gammadions upon adsorption of biomolecules. The α-helical biopolymers are highlighted purple, red and blue; β-sheet structures are highlighted peach colour and the disordered structure is highlighted green.

for RH or LH gammadions meaning ζ is negligible for both structures. Therefore, we confirm that through SHG studies of protein adsorption on TPS gammadions we are able to unequivocally identify α-helical, β-sheet and unfolded protein secondary structures.

Following the behaviour of linear spectroscopic measurements, we find that adsorption of ordered protein structures only induces a change in the optical response of the RH gammadion. This specificity of RH gammadions for structural detection in naturally occurring proteins suggests that the system is also sensitive to the handedness of the secondary structure which is controlled by the underlying molecular chirality of the constituent amino acids. This phenomenon was investigated through the adsorption of poly D/L-Lysine at pH 11.5 wherein the molecules form model α-helices. The handedness of the helix in poly L-Lysine is the same as that found in naturally occurring proteins whilst poly D-Lysine represents the unnatural form. The structural integrity and handedness of the poly-Lysine helices was

confirmed through CD spectroscopy (appendix 6.5.7). Fitted and experimental data for RH and LH gammadions immersed in distilled water (pH 11.5) and D or L poly-Lysine solutions are found in figure 6.11. L-Lysine adsorption results in an increase of the α lobes (ζ=+ve) for the RH gammadion and LH structures remain unchanged (ζ=0). D-Lysine displays an equal but opposite effect whereby α lobes for RH structures are unchanged (ζ=0) whilst LH α lobes increase (ζ=+ve). The secondary structure sensitivity is in agreement with the previous nonlinear measurements of naturally occurring proteins whereby the adsorption of molecules with a primarily α-helical secondary structure results in an increase of the α lobes and a positive value of ζ. Sensitivity to the handedness of the helix and hence the underlying molecular chirality of the poly D/L-Lysine is also apparent. Poly L-Lysine adsorption induces a change in the RH gammadions and leaves the left handed structures unaffected which corroborates with the protein data since all naturally occurring protein molecules are formed

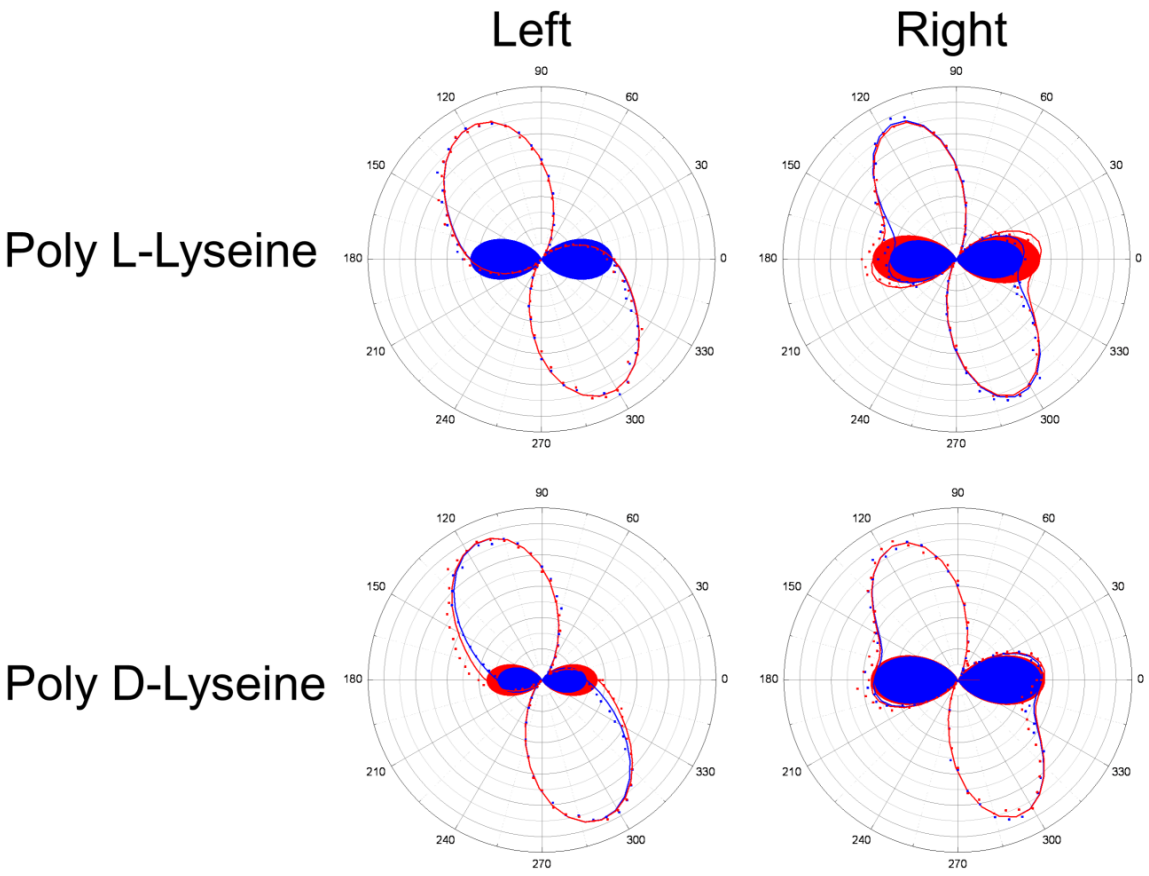

Figure 6.11: Normalised intensity of S-polarised SH signal as a function of the incident polarisation angle (θ) for arrays of right and left handed gammadions in the presence of tris buffer (blue) and Lysine solution(red). Squares represent the measured experimental data; solid lines are the fit to equation (2.62); blue and red shaded lobes correspond to the fit of only the dipolar term (α) of equation (2.62).

from L-amino acids. As expected, the poly D-Lysine α-helices induce an equal but opposite effect whereby the LH gammadion displays the variation in α and the SH response of the RH enantiomer is invariant.

Finally, in order to discount the possibility of the observed effects arising due to errors within the experimental system, biological measurements are also conducted on the unstructured Au surface during the same experimental session as the RH and LH nanostructure data is recorded. The SH profiles and fitting parameters collected from the unstructured surface in the presence of tris buffer and protein can be found in appendix 6.5.10 and 6.5.11. The invariance in the SH response for all protein Au measurements confirms the accuracy of the experimental set up and allows us to discount Au annealing effects or laser alignment errors as sources of the SH profile variation.

6.2.6 Molecular Mediation of TPS Mode Hybridisation to Detect Protein Structure

The commensurate behaviour of linear reflectance and nonlinear SHG measurements upon protein adsorption supports the hypothesis that the presence of ordered biopolymers can modulate the hybridisation between the electric and magnetic modes of the solid-inverse TPS gammadions. In linear measurements this phenomenon is manifested through the appearance of a distinct shoulder in the Fano resonance lineshape which we know reflects an increase in the interference between the bright and dark hybrid modes as a result of an increase in hybridisation between electric/magnetic modes. Furthermore, variations in hybridisation also modify the level of chirality in the TPS[5]. This protein induced modulation of the TPS hybridisation is apparent to a greater degree in nonlinear spectroscopic measurements. As opposed to inducing subtle changes in the spectroscopic lineshape, protein adsorption at the front face results in a significant change in the nature of the back face SHG response, specifically for the chirally sensitive α term. The negligible sensitivity of back face linear/nonlinear measurements to refractive index variations at the front face allows us to discount resonance shifts as a source of these SHG changes. This means the variation in α is not due to a direct interaction between the nanostructure SH sources and the biomolecule, hence, it must occur via an indirect interaction. Through EM field modelling it is shown that an achiral dielectric adsorbed on the front face does not affect the intensity/chirality of EM fields surrounding the nanostructure when illuminated from the back

face. However, we know that the chirality of these evanescent fields is influenced by the hybridisation of electric/magnetic modes and linear measurements in section 6.2.2. show this hybridisation can be modulated by the adsorption of chiral molecules. Thus, for SHG measurements we conclude that adsorption of structured biopolymers modulates the electric/magnetic coupling which affects the chirality of EM fields associated with the substrate. This change in the level of chirality in the TPS is manifested through a variation in the chirally sensitive α SHG contribution. This effect is dependent on the handedness of the nanostructure, the secondary structure of the biomolecule and the handedness of the secondary structure motif which is dictated by the molecular chirality of the constituent amino acids. Hence, molecular mediation of TPS mode hybridisation only occurs when the handedness of the nanostructure chiral evanescent fields matches that of the ordered biomacromolecular structure.

Aside from being independent of the effective refractive index of proteins in nanostructure chiral fields, this novel phenomenon for the detection of biomolecular structure is fundamentally different from plasmonic polarimetry in several other ways. From chapter 4 we know that plasmonic polarimetry requires the presence of evanescent fields with a large net chirality to elicit a measureable asymmetric resonance shift. In contrast, the evanescent fields associated with the gammadion nanostructures have a weak net chirality when illuminated from the front face and are sub-chiral when illuminated from the back face. This dictates that the generation of large levels of chirality in the nanostructure near-fields is not a prerequisite for molecular mediation of TPS hybridisation. This is advantageous as it relieves the engineering constraint of designing nanostructures with large net chirality for use in chiroptical spectroscopy.

The second major difference is that unlike previously reported plasmonic polarimetry measurements [17, 18], the novel spectroscopic technique reported in this chapter is sensitive to three distinct protein secondary structures (α-helical, β-sheet and unfolded). This arises due to the different physical mechanisms through which the nanostructure and molecules interact. Plasmonic polarimetry does not directly measure the secondary structure content of proteins but is instead sensitive to the structural anisotropy of these motifs. In plasmonic metamaterials the steep field gradients present around nanostructures can dramatically enhance the electric quadrupole contributions (E_2) to the optical activity.

Proteins with a high β-sheet content facilitate an enhancement of this contribution as the β-sheets are arranged anisotropically in the protein with respect to the Au surface resulting in a large chiroptical response. In contrast, α-helices in proteins are oriented isotropically with respect to the Au surface therefore the quadrupolar contributions average to zero leading to a negligible plasmonic polarimetry response. The sensitivity of molecular mediated TPS mode hybridisation to isotropically arranged α-helices, means this effect is not quadrupolar in origin. The modulation of hybridisation between electric/magnetic modes in the TPS by chiral molecules must therefore arise due to an electric dipole-magnetic dipole interaction(E_1M_1). As discussed in section 2.1.3 it is the interaction of parallel components of these terms that give rise to chiroptical effects such as circular dichroism and optical rotation in isotropic media. This interaction displays greater sensitivity to a range of chiral structures than the electric quadrupole term as evidenced by the sensitivity of chiroptical spectroscopies to protein secondary and tertiary structure. This increased structural sensitivity of electric dipole-magnetic dipole terms compared with quadrupolar terms is consistent with the relative structural sensitivities of molecular mediation of TPS mode hybridisation (E_1M_1 mechanism) and plasmonic polarimetry (E_2 mechanism).

6.3 Conclusion

We have developed a novel chiroptical biosensing technique using weakly hybridised TPS nanostructures in both the linear and nonlinear regime that can identify three distinct protein secondary structures. In addition, these measurements are also sensitive to the handedness of ordered protein structures which is dictated by the molecular chirality of the constituent amino acids. This technique introduces a novel effect whereby the adsorbed molecules mediate the hybridisation between electric/magnetic modes in a weakly coupled hybrid nanostructure affecting the optical and chiroptical properties of the system. This effect is significantly different to previous chiroptical measurements using TPS nanostructures as it does not depend on the effective refractive index of molecules in chiral fields nor must these fields possess an enhanced chiral asymmetry compared with CPL. Firstly, we perform a symmetry analysis of the substrate which reveals that the optical properties depend on the interference between a bright dipolar hybrid mode and a dark quadrupolar hybrid mode. Linear spectroscopic measurements were employed to characterise the strength of interference between these modes and the model of chirality in the system. The substrate

was found to display reflectance and ORD spectra typical of a weakly hybridised system with low levels of chirality.

Plasmonic polarimetry measurements using TPS gammadions to detect three distinct protein secondary structures were not possible due to the low levels of chirality associated with the nanostructure. Despite this, detection of ordered protein structure was possible by monitoring the subtle changes in reflectance lineshape upon adsorption of α-helical, β-sheet and unfolded proteins. In chapter 4, changes in reflectance lineshape were shown to correspond to changes in the hybridisation of the electric/magnetic modes. We therefore attribute this protein induced lineshape variation to a new phenomenon whereby biomolecules can influence the electric/magnetic mode hybridisation within the TPS. This modifies the interference of the bright and dark mode resulting in changes in the structure of the Fano resonance lineshape. Measurement of this novel biosensing technique in the linear regime is adequate in providing a physical explanation as to the origins of this phenomenon however linear measurements are not an especially incisive probe.

Having proposed a physical mechanism to explain protein induced effects on the TPS hybridisation, we then conduct similar measurements in the nonlinear regime through polarisation dependent SHG of nanostructures. Nonlinear measurements must be conducted through the reverse face in order to elicit a chiral SH response as it is only in this sample geometry that a Fano resonance associated with the nanostructures may be excited by the incident beam. Sensitivity to nanostructure chirality is manifested in several ways however the most significant element is the differential electric dipole contribution to the RH and LH gammadion SH response. The adsorption of protein molecules was found to influence this electric dipole element of the gammadion SHG and changes were characterized through an asymmetry parameter ς. Nonlinear measurements allowed for the clear distinction between α-helical, β-sheet and disordered proteins. Adsorption of an α-helical protein resulted in a positive ς, β-sheet proteins gave a negative ς and disordered proteins yielded a ς of zero. Sensitivity to the handedness of secondary structure motifs which is dictated by the underlying amino acid molecular chirality was confirmed using α-helical poly D and poly L-Lysine. Due to the back face illumination of the substrate in nonlinear measurements, the biomolecules are not in direct contact with the SH sources therefore the observed protein induced changes must occur via an indirect interaction. The mechanism for this interaction is

the same as that observed for linear measurements whereby chiral molecules mediate the hybridisation between the TPS electric/magnetic modes which influences the chirality of the evanescent fields. Consequently, changes in the magnitude of the chirally sensitive SHG α term reflect this modification of evanescent field chirality.

Detection of biomolecular structure through protein induced coupling modulation is found to be fundamentally different from the previously reported plasmonic polarimetry measurements. This novel technique does not require the generation of nanostructure evanescent fields of enhanced chirality, indeed the fields surrounding gammadions for the SHG measurements have a lower level of chirality than circularly polarised light. The other significant difference is that through measuring protein mediated TPS mode hybridisation we can unequivocally distinguish between three distinct secondary structure motifs. The physical reason for this enhanced sensitivity is found to lie in the electric dipole-magnetic dipole origin of the light matter interaction which is known to be a more incisive probe of protein structure than the electric quadrupole term which determines the sensitivity of plasmonic polarimetry.

6.4 References

1. B. Tang, L.D., C. Jiang, *Electromagnetically induced transparency in hybrid plasmonic-dielectric system.* Optics Express, 2011. **19**(2): p. 628-637.
2. Na Liu, L.L., T. Weiss, J. Kästel, M. Fleischhauer, T. Pfau, H. Giessen, *Plasmonic analogue of electromagnetically induced transparency at the Drude damping limit.* Nature Materials, 2009. **8**: p. 758.
3. Na Liu, T.W., M. Mesch, L. Langguth, U. Eigenthaler,M. Hirscher, C. Sonnichsen, H. Giessen, *Planar metamaterial analogue of electromagnetically induced transparency for plasmonic sensing.* Nano Letters, 2010. **10**: p. 1103.
4. M. Hentschel, T.W., S. Bagheri, H. Giessen, *Babinet to the half: Coupling of solid and inverse plasmonic structures.* Nano Letters, 2013. **13**: p. 4428-4433.
5. A. S. Karimullah, C.J., R. Tullius, V. M. Rotello, G. Cooke, N. Gadegaard , L. D. Barron , M. Kadodwala, *Disposable plasmonics: plastic templated plasmonic metamaterials with tunable chirality.* Advanced Materials, 2015.
6. M. L. Sandrock, C.D.P., F. M. Geiger, C. A. Foss, *Synthesis and second-harmonic generation studies of noncentrosymmetric gold nanostructures.* Journal of Physical CHemistry B, 1999. **103**: p. 2668-2673.
7. A. Bouhelier, M.B., A. Hartschuh, L. Novotny, *Near-field second harmonic generation induced by local field enhancement.* Physical Review Letters. **90**(1): p. 013903.
8. V. K. Valev, N.S., A. V. Silhanek, B. De Clercq, W. Gillijns, M. Ameloot, V. V. Moshchalkov, T. Verbiest, *Plasmonic Ratchet Wheels: Switching circular dichroism by arranging chiral nanostructures.* Nano Letters, 2009. **9**(11): p. 3945-3948.
9. F. X. Wang, F.J.R., W.M. Albers, R. Ahorinta, J. E. Sipe, M. Kauranen, *Surface and bulk contributions to the second-order nonlinear optical response of a gold film.* Physical Review B, 2009. **80**: p. 233402.

10. S. Kujala, B.K.C., M. Kauranen, Y. Svirko, J. Turunen, *Multipole interference in the second-Harmonic optical radiation from gold Nanoparticles.* Physical Review Letters, 2007. **98**(167403): p. 167403-1.
11. S. Kujala, B.K.C., M. Kauranen, Y. Svirk, J. Turunen, *Multipolar analysis of second-harmonic radiation fromgold nanoparticles.* Optics Express, 2008. **16**(22): p. 17196-17208.
12. N. Abdulrahman, C.D.S., C. Jack, A. Karimullah, L. D. Barron, N. Gadegaard, M. Kadodwala, *The origin of off-resonance non-linear optical activity of a gold chiral nanomaterial.* Nanoscale, 2013. **5**: p. 12651.
13. V. K. Valev, A.V.S., N. Verellen, W. Gillijns, P. Van Dorpe, O. A. Aktsipetrov, G. A. E. Vandenbosch, V.V. Moshchalkov, T. Verbiest, *Asymmetric optical second-harmonic generation from chiral G-shaped gold nanostructures.* Physical Review Letters, 2010. **104**: p. 127401.
14. V. K. Valev, J.J.B., B. De Clercq, N. Braz, X. Zheng, E. J. Osley, S. Vandendriessche, M. Hojeij, C. Blejean, J. Mertens, C. G. Biris, V. Volskiy, M. Ameloot, Y. Ekinci, G. A. E. Vandenbosch, P. A. Warburton, V. V. Moshchalkov, N. C. Panoiu T. Verbiest, *Nonlinear superchiral meta-surfaces: Tuning chirality and disentangling non-reciprocity at the nanoscale.* Advanced Materials, 2014. **26**: p. 4074-4081.
15. C.T. Williams, Y.Y., C.D. Bain, *Total internal reflection sum-frequency spectroscopy: A strategy for studying molecular adsorption on metal surfaces.* Langmuir, 2000. **16**: p. 2343-2350.
16. R. F. Greene, C.N.P., *Urea and guanidine hydrochloride denaturation of ribonuclease, lysozyme, α-chymotrypsin and β-Lactoglobulin.* The Journal of Biological Chemistry, 1974. **249**(17): p. 5388-5394.
17. R. Tullius, A.S.K., M. Rodier, B. Fitzpatrick, N. Gadegaard, L. D. Barron, V. M. Rotello, G. Cooke, A. Lapthorn, M. Kadodwala, *Superchiral" spectroscopy: Detection of protein higher order hierarchical structure with chiral plasmonic nanostructures.* Journal of the American Chemical Society, 2015. **137**: p. 8380-8383.
18. E. Hendry, T.C., J. Johnston, M. Popland, R. V. Mikhaylovskiy, A. J. Lapthorn, S. M. Kelly, L. D. Barron, N. Gadegaard, M. Kadodwala, *Ultrasensitive detection and characterization of biomolecules using superchiral field.* Nature Nanotechnology, 2010. **5**: p. 783-787.

6.5 Appendix

C_4	C_4	E	C_2	$(C_4)^3$	Linear functions, rotations	Quadratic functions	Cubic functions
A	+1	+1	+1	+1	Z, R_z	$X^2 + y^2, Z^2$	z^3, $z(x^2+y^2)$
B	+1	-1	+1	-1	-	$X^2 - y^2$, xy	xyz, $z(x^2-y^2)$
E	+1 +1	+i -i	-1 -1	-i +i	x+iy; $R_x + iR_y$ x-iy; $R_x - iR_y$	(yz, xz)	(xz^2, yz^2), (xy^2, x^2y), (x^3, y^3)

Appendix 6.5.1: C_4 character table

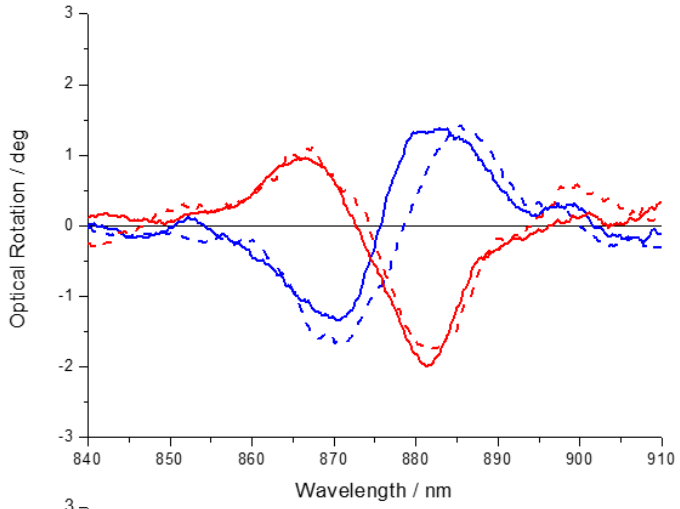

BSA
β-0%, α-68%

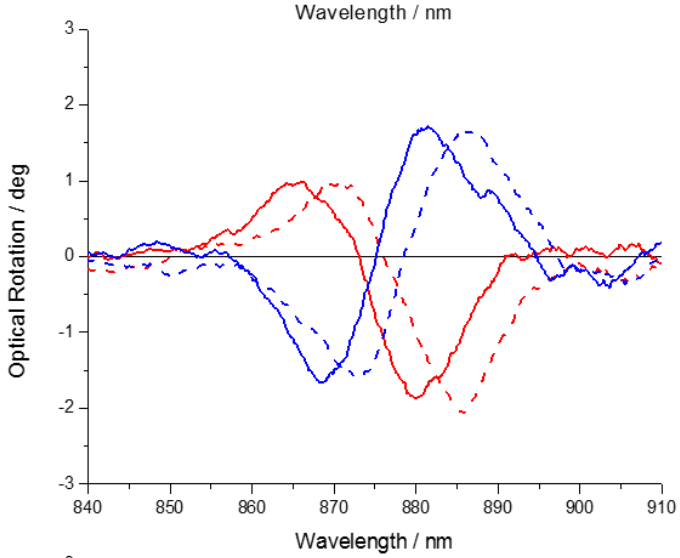

Concanavalin A
β-46%, α-2%

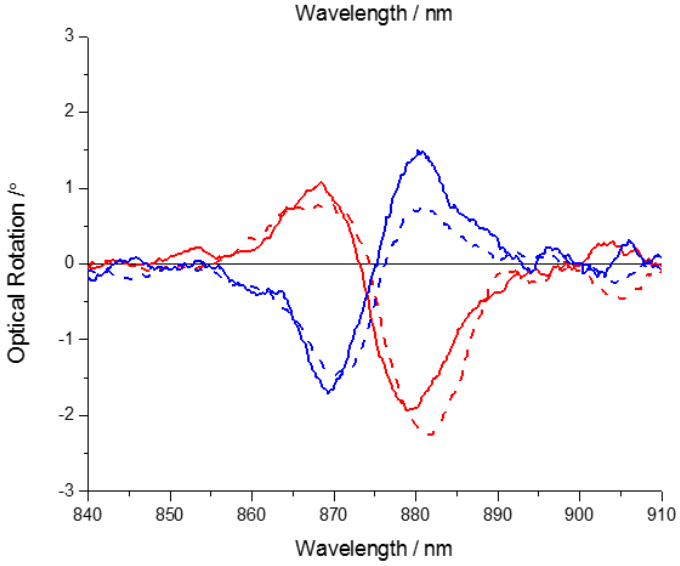

BSA Denatured
Unfolded

Appendix 6.5.2: ORD measurements for RH (blue) and LH (red) 100nm Au TPS gammadions immersed in buffer (solid line) and protein solution (dashed line)

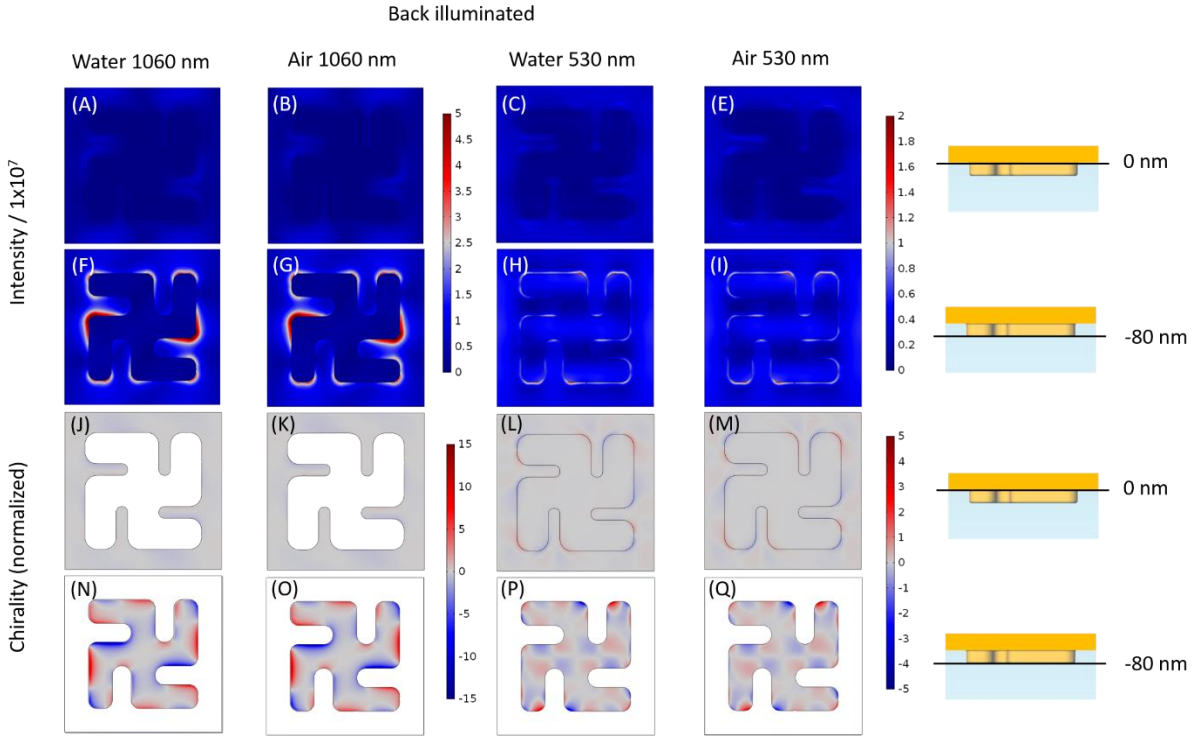

Appendix 6.5.3: EM field Simulations results showing (A-I) normalized electric field intensity and (J-Q) normalized chirality for the fundamental and SH wavelengths in air and water at the front face of the TPS when illuminated through the back. Results are shown for two different points along the z axis, for surfaces in the xy plane.

	Left	α	β	γ	δ	ε
α-helical	Buffer	0.37 ± 0.02	0.65 ± 0.07	0.71 ± 0.02	-0.53 ± 0.02	-1.11 ± 0.08
	BSA	0.38 ± 0.02	0.59 ± 0.07	0.73 ± 0.02	-0.47 ± 0.06	-1.07± 0.08
	Buffer	0.35 ± 0.02	0.71 ± 0.07	0.65 ± 0.02	-0.33 ± 0.06	-1.26 ± 0.08
	Haemoglobin	0.35 ± 0.02	0.70 ± 0.07	0.64± 0.02	-0.33 ± 0.06	-1.26 ± 0.08
β-Sheet	Buffer	0.33 ± 0.02	0.64 ± 0.07	0.69 ± 0.02	-0.44 ± 0.06	-1.15 ± 0.08
	Concanavalin A	0.32 ± 0.02	0.69 ± 0.07	0.67 ± 0.02	-0.37 ± 0.06	-1.21 ± 0.08
	Buffer	0.38 ± 0.02	0.67 ± 0.07	0.68 ± 0.02	-0.45 ± 0.06	-1.10 ± 0.08
	β-Lactoglobulin	0.41 ± 0.02	0.70 ± 0.07	0.66 ± 0.02	-0.40 ± 0.06	-1.18 ± 0.08
	Buffer	0.26 ± 0.02	0.57 ± 0.07	0.75 ± 0.02	-0.34 ± 0.06	-1.11 ± 0.08
	IgG	0.26 ± 0.02	0.57 ± 0.07	0.75 ± 0.02	-0.34 ± 0.06	-1.14 ± 0.08
Unfolded	Buffer	0.26 ± 0.02	0.64 ± 0.07	0.70 ± 0.02	-0.41 ± 0.06	-1.13 ± 0.08
	Denatured BSA	0.27 ± 0.02	0.62 ± 0.07	0.71 ± 0.02	-0.37 ± 0.06	-1.13 ± 0.08

Appendix 6.5.4: Fitting parameters to equation 2.62 for LH gammadions for all buffer and protein experiments.

	Right	α	β	γ	δ	ε
α-helical	Buffer	0.37 ± 0.02	0.38 ± 0.07	0.76 ± 0.02	-0.26 ± 0.02	-1.16 ± 0.08
	BSA	0.42 ± 0.02	0.25 ± 0.07	0.79 ± 0.02	-0.29 ± 0.06	-1.09 ± 0.08
	Buffer	0.49 ± 0.02	0.21 ± 0.07	0.76 ± 0.02	-0.20 ± 0.06	-1.20 ± 0.08
	Haemoglobin	0.55 ± 0.02	0.36 ± 0.07	0.70 ± 0.02	-0.15 ± 0.06	-1.33 ± 0.08
β-Sheet	Buffer	0.54 ± 0.02	0.40 ± 0.07	0.69 ± 0.02	-0.18 ± 0.06	-1.34 ± 0.08
	Concanavalin A	0.46 ± 0.02	0.57 ± 0.07	0.64 ± 0.02	-0.13 ± 0.06	-1.36 ± 0.08
	Buffer	0.40 ± 0.02	0.30 ± 0.07	0.75 ± 0.02	-0.19 ± 0.06	-1.17 ± 0.08
	β-Lactoglobulin	0.32 ± 0.02	0.45 ± 0.07	0.72 ± 0.02	-0.25 ± 0.06	-1.16 ± 0.08
	Buffer	0.52 ± 0.02	0.56 ± 0.07	0.64 ± 0.02	-0.10 ± 0.06	-1.39 ± 0.08
	IgG	0.43 ± 0.02	0.54 ± 0.07	0.66 ± 0.02	-0.12 ± 0.06	-1.38 ± 0.08
Unfolded	Buffer	0.28 ± 0.02	0.36 ± 0.07	0.73 ± 0.02	-0.09 ± 0.06	-1.21 ± 0.08
	Denatured BSA	0.29 ± 0.02	0.42 ± 0.07	0.73 ± 0.02	-0.08 ± 0.06	-1.25 ± 0.08

Appendix 6.5.5: Fitting parameters to equation 2.62 for RH gammadions for all buffer and protein experiments.

Right	α	β	γ	δ	ε
Buffer	0.53 ± 0.02	0.57 ± 0.07	0.60 ± 0.02	0.09 ± 0.02	-1.40 ± 0.08
Poly D-Lyseine	0.55 ± 0.02	0.56 ± 0.07	0.62 ± 0.02	0.15 ± 0.06	-1.37 ± 0.08
Buffer	0.42 ± 0.02	0.52 ± 0.07	0.62 ± 0.02	0.14 ± 0.06	-1.39 ± 0.08
Poly L-Lyseine	0.50 ± 0.02	0.62 ± 0.07	0.62 ± 0.02	0.17 ± 0.06	-1.39 ± 0.08

Appendix 6.5.6: Fitting parameters to equation 2.62 for RH gammadions for all buffer and poly Lysine experiments.

Left	α	β	γ	δ	ε
Buffer	0.26 ± 0.02	0.68 ± 0.07	0.71 ± 0.02	-0.39 ± 0.02	-1.12 ± 0.08
Poly D-Lyseine	0.42 ± 0.02	0.80 ± 0.07	0.62 ± 0.02	-0.46 ± 0.06	-1.19 ± 0.08
Buffer	0.35 ± 0.02	0.69 ± 0.07	0.64 ± 0.02	-0.44 ± 0.06	-1.21 ± 0.08
Poly L-Lyseine	0.35 ± 0.02	0.75 ± 0.07	0.61 ± 0.02	-0.43 ± 0.06	-1.22 ± 0.08

Appendix 6.5.7: Fitting parameters to equation 2.62 for LH gammadions for all buffer and poly Lysine experiments.

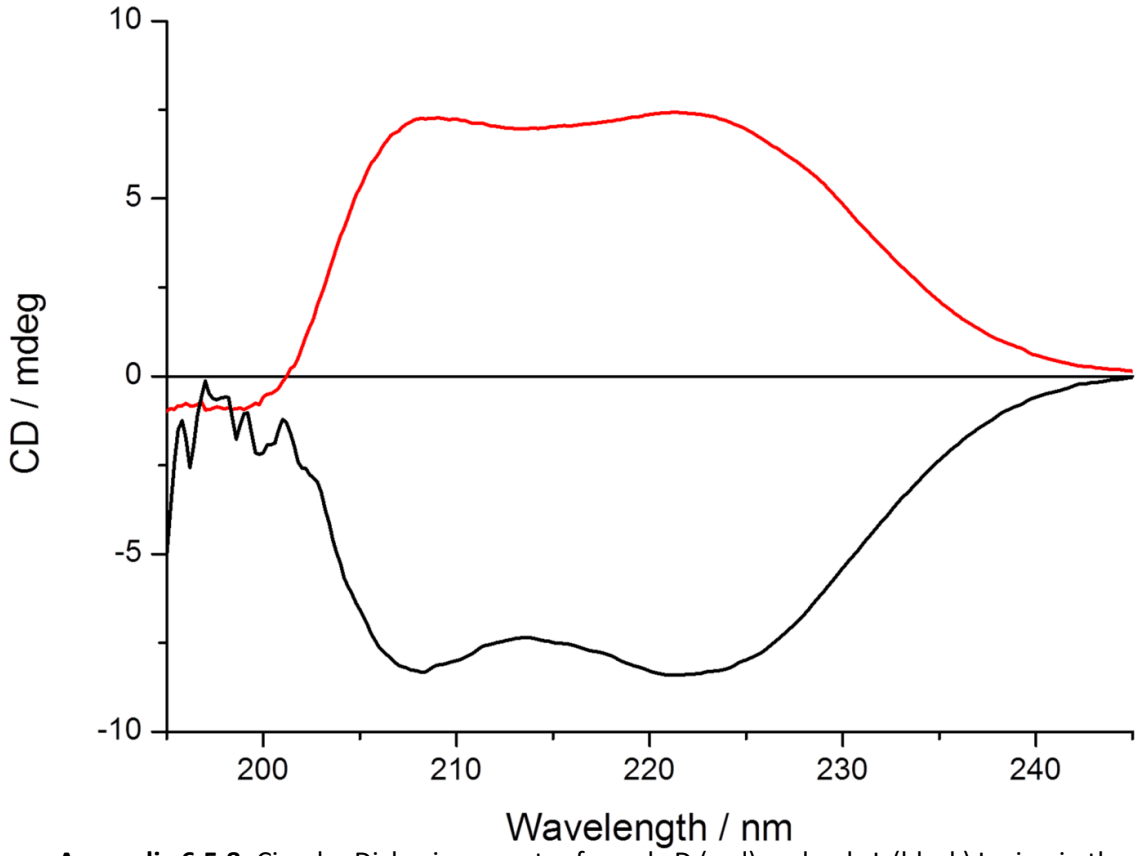

Appendix 6.5.8: Circular Dichroism spectra for poly D (red) and poly L (black) Lysine in the α conformation measured in distilled water at pH 11.5.

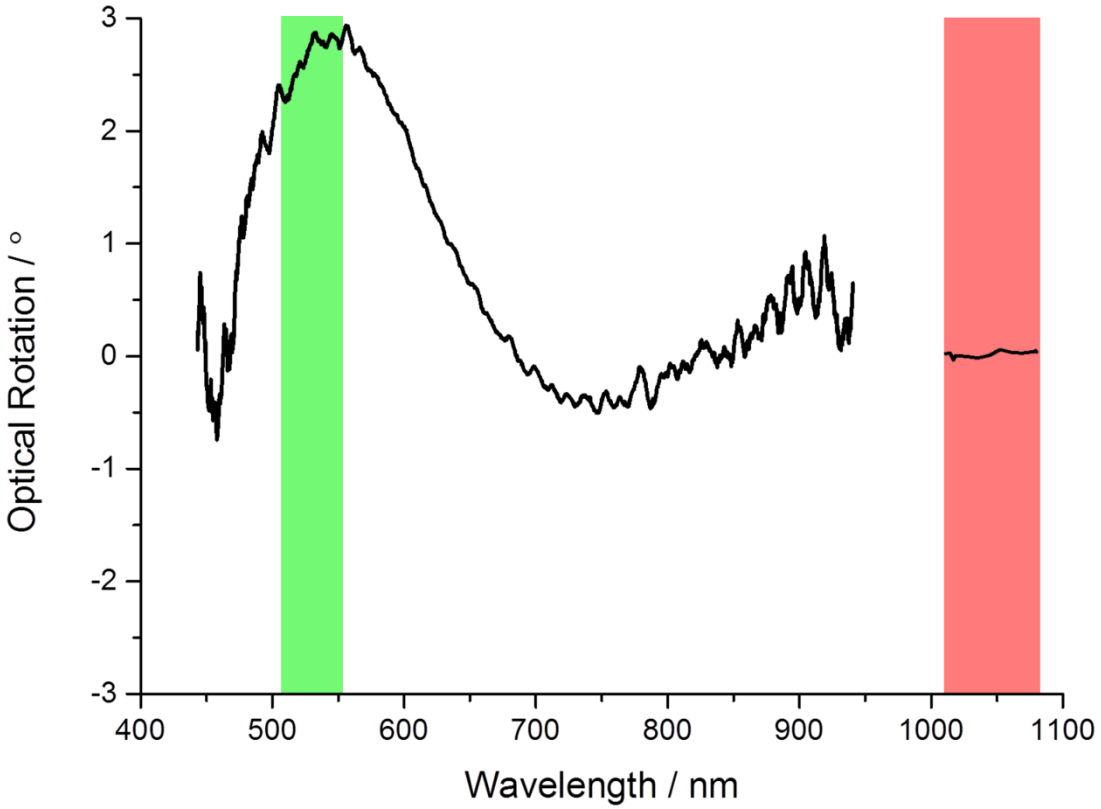

Appendix 6.5.9: Optical rotatory dispersion from flat Au measured through the back face.

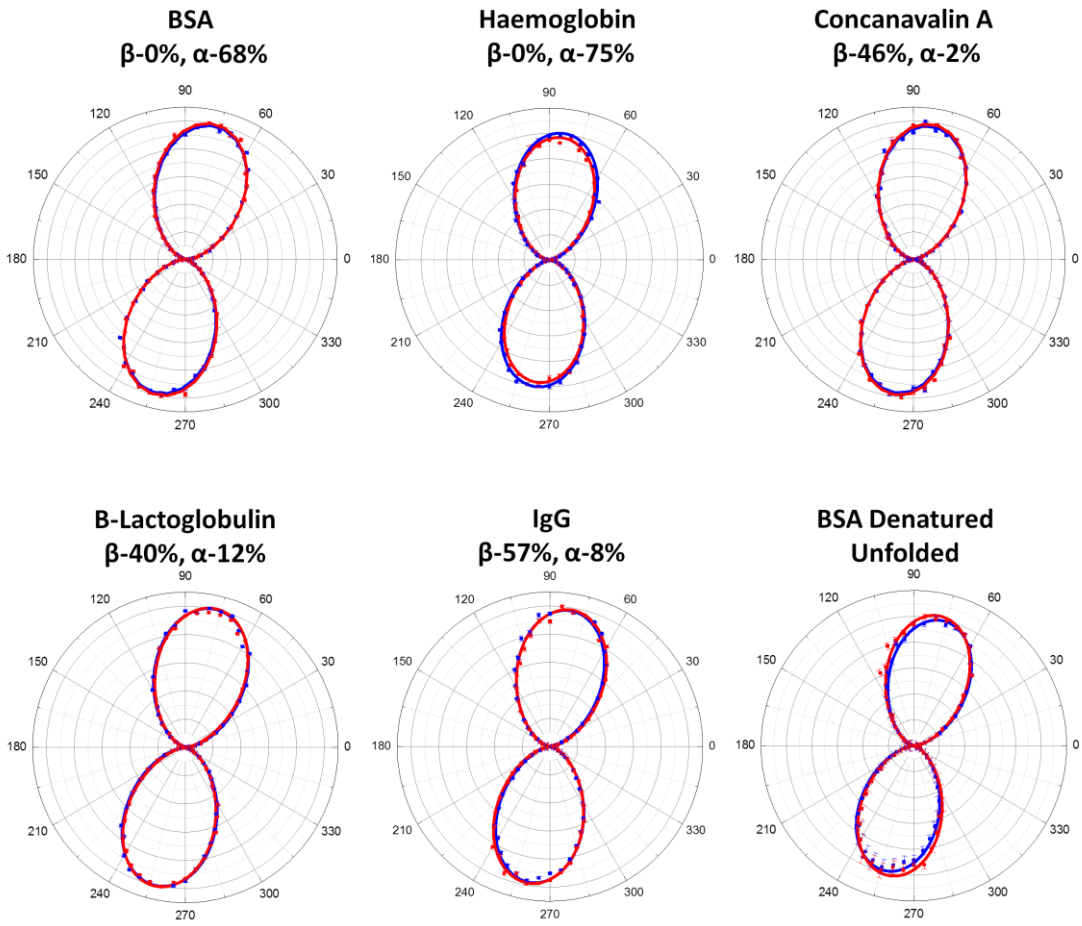

Appendix 6.5.10: Normalised s-polarised SH polar plots from the Au surface measured through the back face in the presence of 10mM tris buffer (blue) and protein (red). Squares are the experimental data and solid lines are the fits to equation 2.62.

	Au	α	β	γ	δ	ε
α-helical	Buffer	0.06 ± 0.02	0.95 ± 0.07	0.74 ± 0.02	0.41 ± 0.02	1.00 ± 0.08
	BSA	0.06 ± 0.02	0.95 ± 0.07	0.74 ± 0.02	0.41 ± 0.06	1.00 ± 0.08
	Buffer	0.01 ± 0.02	0.67 ± 0.07	0.92 ± 0.02	0.08 ± 0.06	0.67 ± 0.08
	Haemoglobin	0.01 ± 0.02	0.59 ± 0.07	0.90 ± 0.02	0.07 ± 0.06	0.63 ± 0.08
B-Sheet	Buffer	0.04 ± 0.02	0.77 ± 0.07	0.81 ± 0.02	0.24 ± 0.06	0.94 ± 0.08
	Concanavalin A	0.04 ± 0.02	0.77 ± 0.07	0.81 ± 0.02	0.24 ± 0.06	0.94 ± 0.08
	Buffer	0.04 ± 0.02	0.79 ± 0.07	0.84 ± 0.02	0.34 ± 0.06	0.84 ± 0.08
	β-Lactoglobulin	0.01 ± 0.02	0.67 ± 0.07	0.93 ± 0.02	0.10 ± 0.06	0.64 ± 0.08
	Buffer	0.01 ± 0.02	0.71 ± 0.07	0.87 ± 0.02	0.17 ± 0.06	0.75 ± 0.08
	IgG	0.02 ± 0.02	0.68 ± 0.07	0.90 ± 0.02	0.16 ± 0.06	0.67 ± 0.08
Unfolded	Buffer	0.05 ± 0.02	0.76 ± 0.07	0.96 ± 0.02	0.36 ± 0.06	0.97 ± 0.08
	Denatured BSA	0.08 ± 0.02	0.88 ± 0.07	0.93 ± 0.02	0.29 ± 0.06	0.90 ± 0.08

Appendix 6.5.11: Fitting parameters to equation 2.62 for flat Au for all buffer and protein experiments.

Chapter 7: Detection of Mesoscale Biological Structure using Chiral Plasmonic Nanostructures

7.1. Introduction

In this chapter we present a preliminary investigation into the viability of lithographically fabricated chiral gammadions for the detection of mesoscale biological structure. Using gammadions of the same periodicity but different Au thickness (65nm, 75nm, 100nm ,150nm), the mesoscale biological structure we aim detect is the helical pitch of insulin amyloid fibrils. The mesoscale is typically defined as the intermediate region which encompasses lengthscales larger than individual molecular arrangements (a few tens of nanometres) but no larger than the size of a cell (tens of microns). The size of the fibril helical pitch is known to be 70-120nm which is towards the lower end of the mesoscale. In order to gauge the sensitivity of nanostructures to the helical pitch we use two distinct forms of insulin amyloid fibrils in solution: spherulites fibrils and fragmented fibrils. The spherulite fibrils, provided by the MacPhee group at the University of Edinburgh, form when fibrils aggregate into large scale spherical structures whereby individual fibrils emanate out radially from a central core. Bundles of fragmented fibrils are produced through sonication of spherulites which shatters this large structure. An important difference between these two fibril arrangements is the nature through which the individual fibrils bind to the Au/quartz surface of the substrate. When aggregated into spherulites, fibrils bind with their long axis perpendicular to the surface whilst fragmented fibrils bind with their long axis parallel to the surface. This differential surface binding is fundamental for the detection of the fibril helical pitch.

Spectroscopic measurements are performed by measuring the asymmetry between the right handed (RH) and left handed (LH) gammadion CD response upon adsorption of spherulite fibrils and fragmented fibrils. This asymmetry is rationalised through calculation of an asymmetry parameter whereby we find that an asymmetric CD response only arises upon adsorption of spherulite fibrils on the 75nm and 100nm Au substrates. We subsequently propose a preliminary hypothetical model to explain these observations in which gammadion sensitivity to the helical pitch depends on the fibril being oriented perpendicular to the Au surface and the vertical height of the gammadion matching the lengthscale of the fibril helical pitch.

7.1.1 Formation and Structural Characterisation of Amyloid Fibrils

The function and properties of a protein are highly dependent on the folding and arrangement of the amino acid backbone and subunits. Given the complexity of this folding process it is not uncommon for a protein to misfold into an abnormal conformation which may be highly toxic to cell function. These misfolded proteins are known as amyloids and are typically insoluble, protease resistant molecules that aggregate resulting in cell death within the organs or tissues in which they are deposited [1]. Misfolded protein aggregates may form long, twisted, unbranched filaments known as amyloid fibrils [2]. These structures possess diameters between 70-140 Å and lengths ranging from tens of nm to several microns [3, 4]. The length over which the fibril twists is typically around 70-120nm (figure 7.01b) [5]. In section 7.2 it is this mesoscale fibril twist that we aim to detect using CD measurements of gammadions.

Studies into the mesoscale helical pitch of fibrillar biomolecules requires the use of microscopy techniques. The most common method is atomic force microscopy (AFM) whereby the sensitivity of this technique to sub-nanometre variations in the fibril surface allows an accurate description of the structural properties[5, 6]. Recent studies have also combined the use of Cryo-transmission electron microscopy (TEM) with x-ray fiber diffraction and nuclear magnetic resonance (NMR) spectroscopy to provide a structural description of the fibril helix from the molecular scale to the mesoscale [7]. However, whilst employing microscopy techniques for fibril structural analysis allows high resolution imaging of the mesoscale structure, these techniques are time consuming and require costly equipment as well as extremely competent operators to obtain detailed images. Furthermore, for microscopy techniques, fibrils must be removed from solution which may cause fracturing in the fibril structure. Thus, there is a need for a simple spectroscopic method to characterise fibril mesoscale structure.

On the atomic level, the structure of amyloid fibrils has been partially elucidated through X-ray fiber diffraction to reveal a cross-β composition [8]. This cross-β structure is built from strands of parallel or anti-parallel β sheets spaced 4.8 Å apart in a helical arrangement which gives rise to the twist of the overall fibril structure (figure 7.01c) [9]. The constituent β sheets are aligned perpendicular to the long axis of the fibril and interact with neighbouring sheets via hydrogen bonds [10]. The irreversible formation of this structure is typical for all

amyloid fibrils regardless of the structure of the native soluble protein suggesting amyloid fibril formation is a generic property of all polypeptide chains [11, 12].

7.1.2 Formation and Structure of Amyloid Fibril Spherulites

A key aspect of this study into detecting the fibril helical pitch using nanostructure chiral fields requires the aggregation of amyloid fibrils into large scale spherical assemblies known as spherulites (figure 7.01a) [12]. Previous electron microscopy studies of insulin amyloid fibril spherulites reveal this spherical aggregate consists of three distinct regions [13]. Firstly, the central core is formed through aggregation of randomly oriented amyloid material. The diameter of this core is determined in vitro by a variety of environmental factors such as pH, temperature and salt concentration [14]. These randomly oriented fibrillar aggregates act as nucleation sites for the generation of further amyloid fibrils. The fibrils formed at this surface emanate out radially from the central core forming the spherulite "corona". The outer surface of the spherulite is irregular and composed of amyloid fibrils protruding out from the corona which then fold over back onto the corona surface. In this study the spherulite diameter ranged from 10µm to 130µm with a mean value of 30µm. Finally, spectroscopic measurements are also performed on amyloid fibrils that are not aggregated into spherulites. This is achieved by sonicating the amyloid fibril spherulite solution which shatters the spherulite structure to yield bundles of amyloid fibril fragments (figure 7.08a)

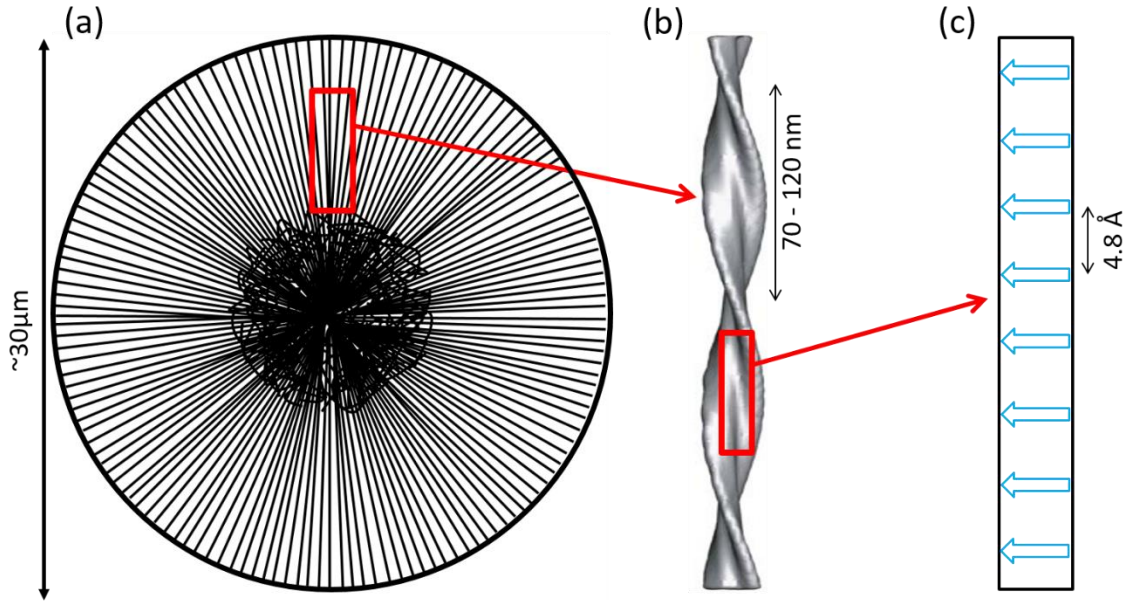

Figure 7.01: (a) Schematic diagram of spherulite with a disordered core at the centre, radially oriented fibrils emanating from the core and a thin outer layer formed by the ends of fibrils that fold back onto the structure. **(b)** Representation of individual amyloid fibril with a nanometre scale helical pitch and **(c)** layout of constituent cross β strands**.**

7.2 Results and Discussion

7.2.1 Polarised Optical Microscopy of Insulin Amyloid Fibril Spherulites

The insulin amyloid fibril spherulites used in this study were grown in vitro by the MacPhee group at the University of Edinburgh. Before gammadion spectroscopic measurements can be performed we must confirm the structural integrity of insulin amyloid fibril spherulites and also the destruction of this spherulite structure after sonication. The simplest and most common method for the structural analysis of spherulites is through polarised optical microscopy[12-15]. Hence, we employ this technique to probe the presence/absence of fibril spherulite structure.

The insulin amyloid fibril spherulites are adsorbed onto the gammadion surface then observed under a cross polarised microscope in transmission (figure 7.02). Further experimental details can be found in section 3.7. The spherulites are found to generate a typical “Maltese cross” extinction pattern (figure 7.02a). This extinction pattern consists of a dark central region with four bright quadrants surrounding the core and arises due to the radial orientation of the amyloid fibrils emanating from the central core[15]. Amyloid fibrils have two different refractive indices depending on whether the incident ray is polarised parallel or perpendicular to the long axis of the fibril. This causes incident rays with different polarisations to refract by different amounts, in other words, the radially oriented fibrils are

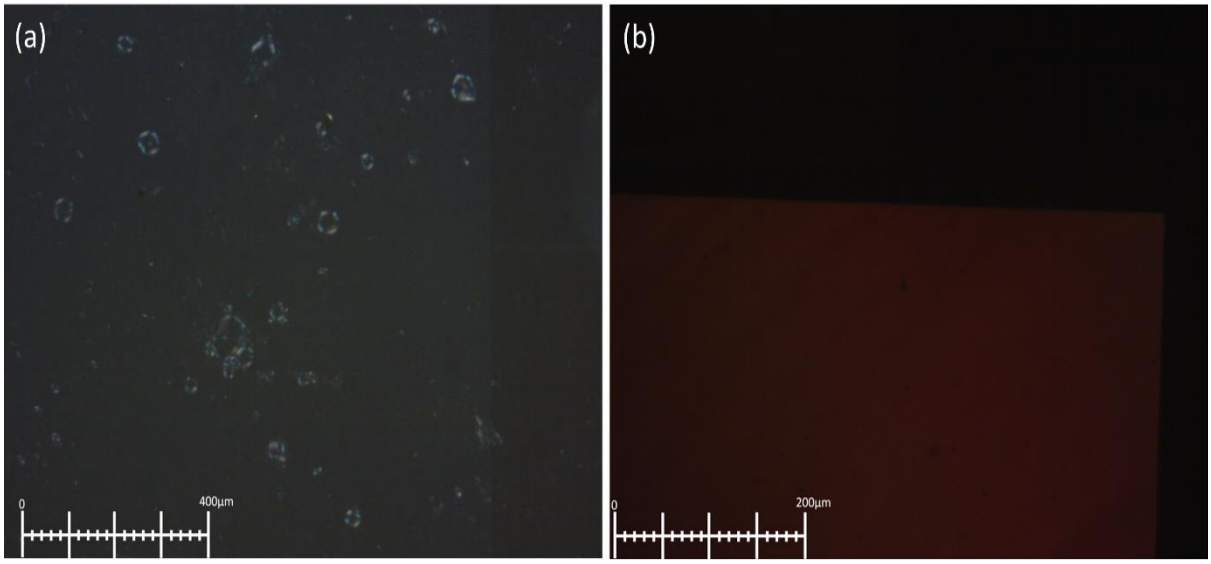

Figure 7.02: Cross polarised microscope images of **(a)** insulin amyloid fibril spherulites and **(b)** sonicated insulin amyloid fibril spherulites. The biomaterial is adsorbed onto the surface of gammadions in both images. The lighter green area in **(a)** is the gammadion Au surface and the orange area in **(b)** corresponds to the gammadion Au surface.

birefringent. Hence, the interference of rays of different polarisation exiting the spherulite results in the characteristic Maltese cross pattern[15]. The amyloid fibrils in the central core are randomly oriented therefore this region is not birefringent and remains dark in the cross polarised images. Comparison of cross polarised optical microscopy images before and after sonication of the spherulite fibril solution are used to confirm the destruction of the spherulite structure (figure 7.02b). The fibrils are now arranged into bundles of amyloid fibril fragments (figure 7.08a) therefore the spherulite structure is absent and the Maltese cross birefringence effects are not observed.

7.2.2 Gammadion Geometry and CD Spectra

Chiral Au gammadions with the same periodicity but differing heights are employed to detect the helical pitch of fibrils. These nanostructures consist of right handed or left handed (RH/LH) gammadions of length 400nm and periodicity 800nm lithographically fabricated on quartz. Gammadion height was controlled by varying the Au film thickness during the fabrication process producing separate substrates with heights ranging from 65nm to 150nm on top of a 5nm chromium layer to aid adhesion. Figure 7.03 displays an SEM image of 100nm Au gammadions.

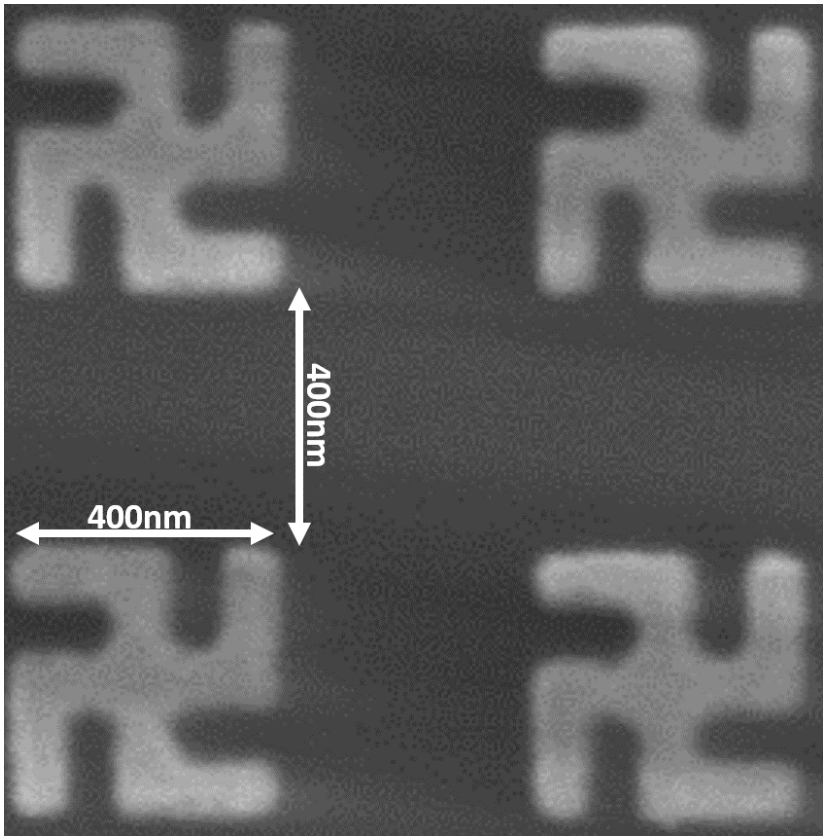

Figure 7.03: SEM image of 100nm Au LH gammadions.

The chiroptical properties of gammadions are probed through UV/Visible Circular Dichroism (CD) spectroscopy in order to measure their differential absorption of left and right circularly polarised light (CPL). Further experimental details may be found in section 3.4.4. Initial CD spectra are recorded in the presence of 10mM tris HCl buffer for each gammadion handedness and height (figure 7.04). RH and LH gammadion CD spectra possess peaks of varying intensity and lineshape in the visible region. Such peaks arise due to the excitation

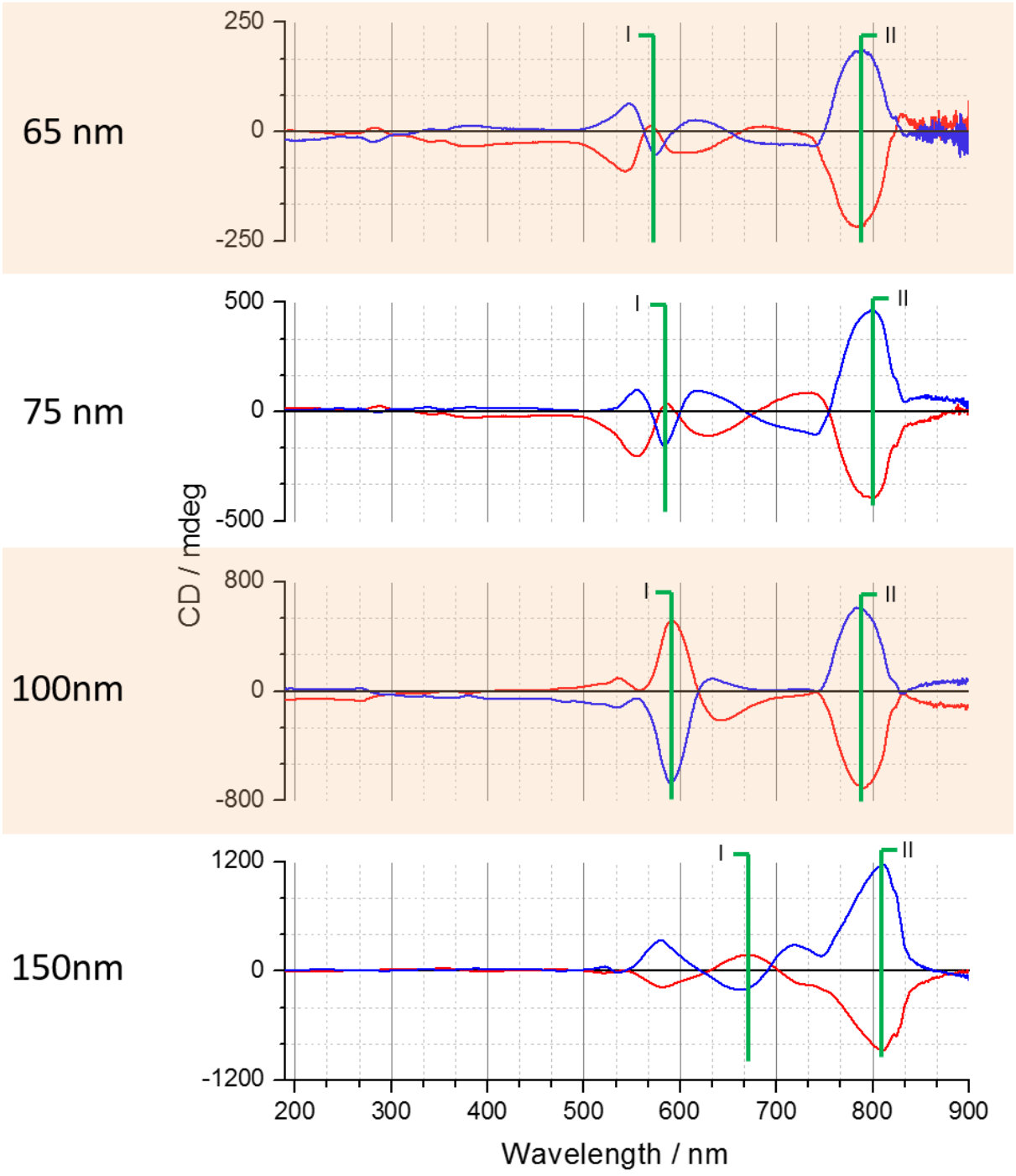

Figure 7.04: CD spectra of RH (blue) and LH (red) gammadions of varying Au thickness recorded in the presence of 10mM tris buffer.

of Localized Surface Plasmon Resonance (LSPRs) associated with the gammadion nanostructure. CD spectra for each Au thickness follow a similar trend wherein there exists two main LSPR modes as highlighted in figure 7.04. A strong, broad resonance exists around ~800nm and a weaker narrow resonance is found at ~600nm. As expected, RH and LH gammadion CD spectra of the same Au thickness are mirror images with small differences in resonance positions and peak intensities attributed to nanoscale defects incurred during the fabrication process. Neglecting the difference in magnitude, the CD lineshape at the main LSPR modes is the same for gammadions of all Au thickness therefore we confirm that these modes are associated with the geometry of the nanostructure.

From the gammadion CD measurements upon deposition of insulin amyloid fibrils (section 7.2.3 and 7.2.4) we find that the most significant changes in the CD occur at the region around mode I (500nm-700nm). This observation is in agreement with previous protein spectroscopic measurements carried out at the University of Glasgow using 100nm Au gammadions of the same dimensions[16]. Thus, in the following gammadion spectroscopic measurements of amyloid fibrils we will focus around this spectral range.

7.2.3 Spectroscopic Measurements of Insulin Amyloid Fibril Spherulites

As discussed, the mesoscale structure we aim to detect is the helical pitch of insulin amyloid fibrils which measures 70-120nm. Gauging the sensitivity of gammadions to this fibril helical pitch involves determining the asymmetry between the RH and LH gammadion CD response upon deposition of insulin amyloid fibrils in two distinct structural arrangements. Firstly, the gammadion CD spectra is measured upon adsorption of insulin amyloid fibril spherulites. Following this, we repeat the CD measurements with sonicated spherulites that form bundles of amyloid fibril fragments. Gammadion spectroscopic measurements are performed using these two distinct fibril arrangements as the orientation of fibril strands with respect to the Au/quartz surface is significantly different in each case. As will be revealed, this difference in the nature of fibril surface binding has a significant effect on the gammadion CD response and sensitivity to the helical pitch.

Before discussing the gammadion CD measurements of fibril spherulites we consider the binding of the constituent fibrils to the Au surface when assembled into these spherical aggregates. The polarised optical microscopy image of spherulites deposited onto

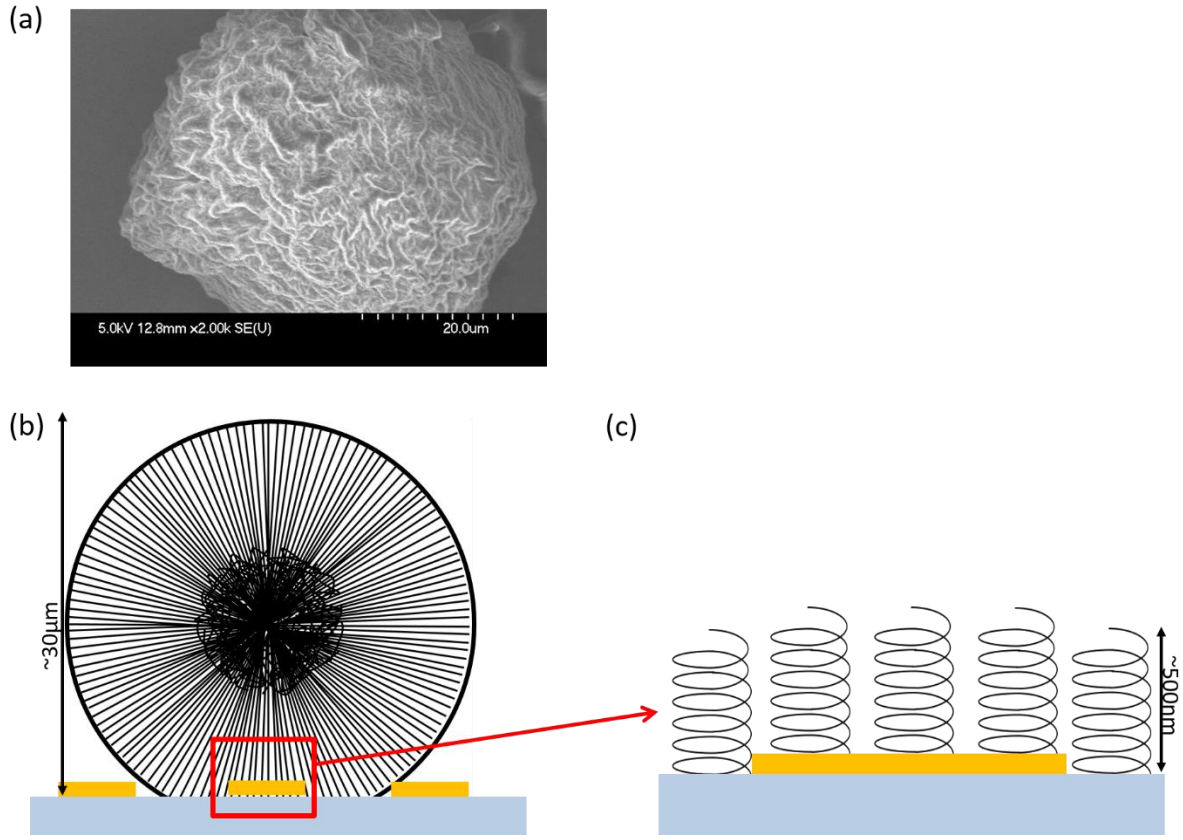

Figure 7.05: (a) SEM image of an insulin amyloid fibril spherulite. **(b)** Pictorial representation of a spherulite bound to the substrate surface. **(c)** Magnified view of spherulite fibrils bound with their long axis perpendicular to the sample surface. The relative size of the gammadions and spherulite are not to scale.

gammadions (figure 7.02a) confirms that the fibril spherulite structure is maintained upon binding to the Au/quartz surface. Due to the large size of the spherulites (~30µm) compared with the gammadions (400nm), only a small number of the constituent fibrils on the underside of the structure will bind to the surface. Fundamental to this study, the long axis of these surface bound fibrils will be aligned perpendicular to the sample surface. Figure 7.05b-c is a pictorial representation of this spherulite fibril binding whereby the gammadion is effectively embedded in the chiral helical dielectric with the long axis of the fibrils aligned perpendicular to the Au/quartz surface.

Spectroscopic measurements are performed by recording the gammadion CD spectra in buffer before repeating the measurements with the nanostructures immersed in insulin amyloid fibril spherulite solution (figure 7.06). Confirmation of fibril adsorption to the surface is provided by the appearance of a CD dip at ~220nm which has the typical lineshape displayed by β-sheet proteins due to the cross-β structure of the fibrils. The magnitude of

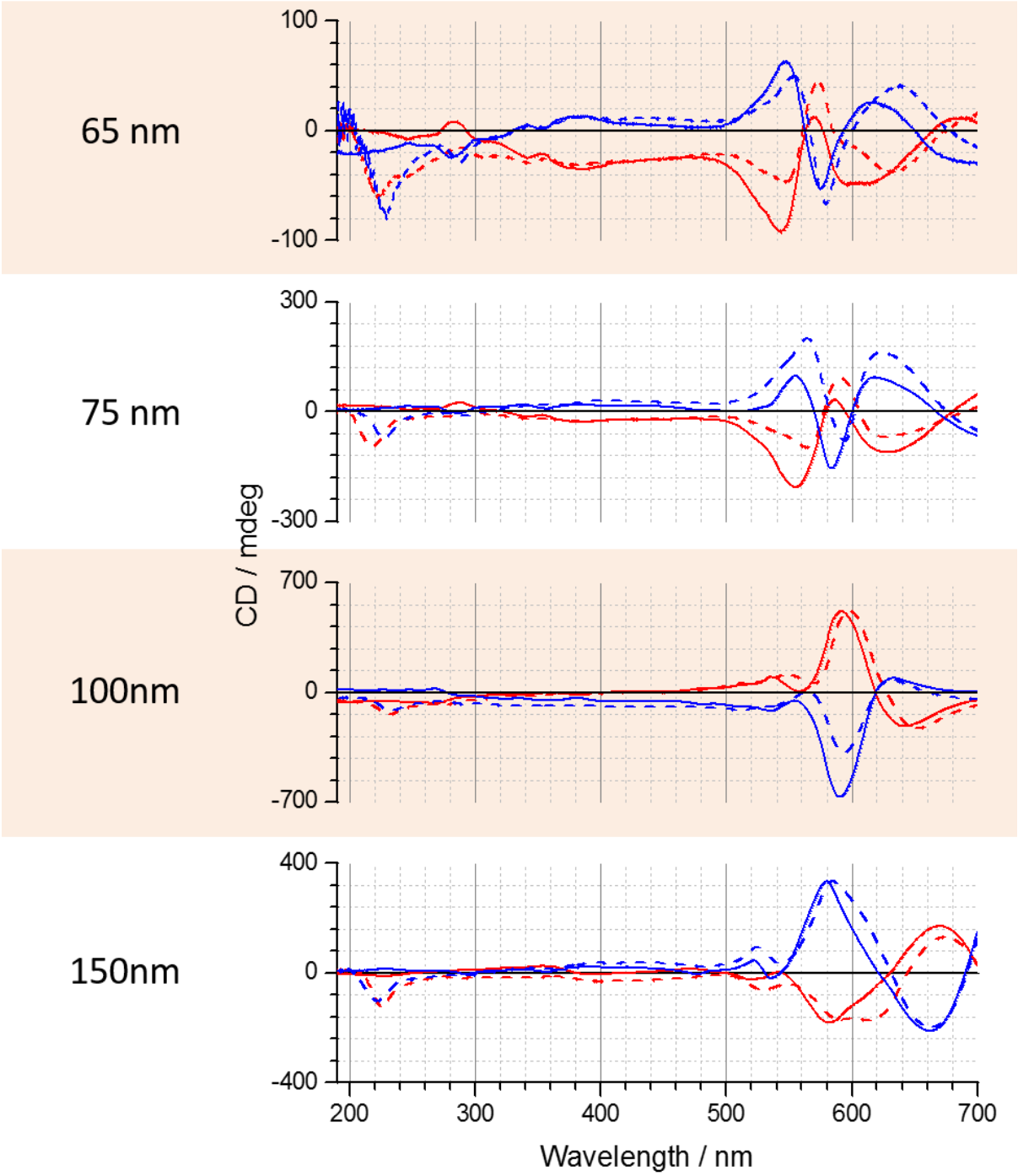

Figure 7.06: CD spectra of RH (blue) and LH (red) gammadions of varying Au thickness recorded in the presence of 10mM tris buffer (solid) and insulin amyloid fibril spherulite solution (dashed).

this dip is approximately the same in each spectrum (~100mdeg) indicating similar levels of adsorption. Therefore, any difference in the CD response between substrates upon spherulite fibril adsorption cannot be attributed to differential surface concentrations. As expected, adsorption of biomaterial results in a red shift of the LSPR peaks for both RH and LH gammadions of all Au thicknesses. At this point, it is important to emphasise that the

changes in the gammadion CD spectra are only due to the fibrils bound at the substrate surface and not the overall spherulite structure. Unlike previous gammadion CD studies [16], we cannot compare the differential wavelength shifts between RH and LH gammadions at particular resonance peaks to probe biological structure. This is due to considerable variations in the CD lineshape around the resonance of interest upon spherulite fibril adsorption which renders this resonance shift comparison an extremely inaccurate method of analysis.

An alternative and more reliable method to scrutinise the disparity between the RH and LH gammadion CD response is to generate a difference spectrum by subtracting the buffer CD spectrum from the spherulite fibril CD spectrum for each enantiomer. If the response of RH and LH gammadions is equivalent upon fibril adsorption, the RH and LH difference spectra will be mirror images about the x-axis (ΔCD for enantiomers will have opposite sign and equal magnitude). An inequivalent response from the RH and LH structures will generate difference spectra with dissimilar lineshapes. The CD difference spectra for all Au thicknesses upon adsorption of insulin amyloid fibril spherulites is displayed in figure 7.07. As discussed for gammadions, the spectroscopic region of interest is around 500-700nm which corresponds to mode I in the CD spectrum. Adsorption of spherulite fibrils on gammadions of thickness 65nm and 150 nm Au produces RH and LH CD difference spectra that are almost perfect mirror images about the x-axis. These mirror image difference spectra indicate that adsorption of spherulite fibrils induce an identical response in the CD for both gammadion enantiomers.

Unlike the 65nm and 150nm profiles, RH and LH CD difference spectra for 75nm and 100nm gammadions are distinctly asymmetric about the x-axis. In the case of 75nm gammadions, the LH difference spectrum has a positive ΔCD value for all wavelengths whilst the ΔCD for RH gammadions is also predominantly positive. The most significant deviations from mirror image difference spectra arise around 550-630nm which corresponds to the position of LSPR mode I. A similar effect is reflected in the 100nm Au data wherein the RH profile has a positive ΔCD value for all wavelengths whilst the LH profile has both positive and negative ΔCD values. Again the most noticeable deviation from mirror image profiles arises around 550-630nm. The asymmetries between RH and LH difference spectra arise due to a

combination of differences in the magnitude of the wavelength shifts and CD intensity variations between RH and LH gammadions upon spherulite adsorption.

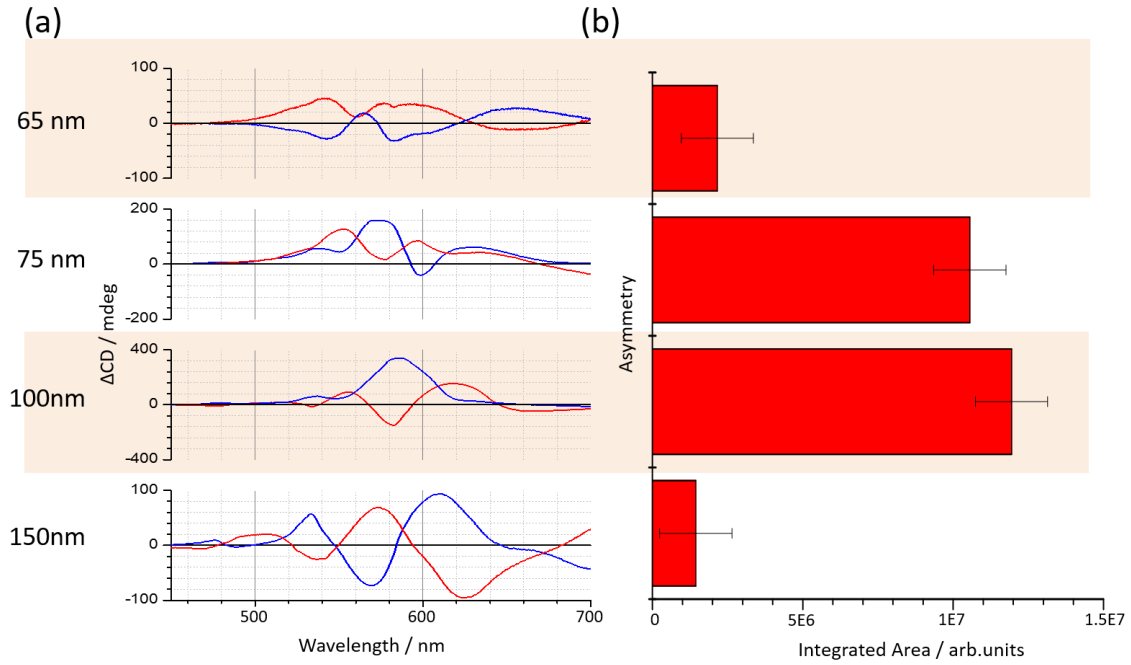

Figure 7.07: (a) Calculated difference spectra upon adsorption of insulin amyloid fibril spherulites for RH (blue) and LH (red) gammadions of varying Au thickness. **(b)** Values of the asymmetry calculated using equation 1.

To provide a clearer interpretation of the observed difference spectra asymmetries we calculate an asymmetry parameter (figure 7.07b). This is achieved through summation of the RH and LH difference spectra and integrating the resultant profile between 450nm and 700nm:

$$Asymmetry = \int (RH\ Difference\ Spectrum + LH\ Difference\ Spectrum) \quad (1)$$

If the difference spectra are perfect mirror images they will cancel out and the resultant spectrum will be a flat line with an integrated area of zero. However, if the difference spectra are asymmetric, the resultant profile will not perfectly cancel but possess peak/trough features and the integrated area will be non-zero. From figure 7.07b we find that the 75nm and 100nm gammadions display a large value for the asymmetry parameter whilst the value for the 65nm and 150nm gammadions is within experimental error. This trend is in agreement with the observed difference spectra lineshapes whereby a significant asymmetry between RH and LH profiles is only observed for the 75nm and 100nm

substrates. Hence, the asymmetry parameter and difference spectra confirm that insulin amyloid fibrils bound with their long axis perpendicular to the Au surface only induce an asymmetric CD response in the 75nm and 100nm Au gammadions.

7.2.4 Spectroscopic Measurements of Fragmented Insulin Amyloid Fibrils

Following CD measurements of insulin amyloid fibrils aggregated into spherulites, we now evaluate the gammadion CD response upon adsorption of fragmented insulin amyloid fibrils. The nature of fibril binding to the Au surface is significantly different for this structural arrangement compared with spherulite fibrils. Figure 7.08a displays an SEM image of these fragmented fibrils adsorbed onto a metal surface. In this form, individual fibrils bind with their long axis parallel to the surface plane (figure 7.08b). The gammadions are now embedded in the helical chiral dielectric with the fibril long axis parallel to the surface which is in stark contrast to the perpendicular alignment for spherulite fibrils.

Identical to spherulite fibril measurements in section 7.2.3, gammadion CD measurements are first recorded in buffer then measured upon adsorption of fragmented insulin amyloid fibrils for each Au thickness (figure 7.09). The intensity of the β-sheet dip at ~220nm is on a similar level to that observed in spherulite measurements therefore differences between the spherulite fibril and fragmented fibril data cannot be attributed to differential protein surface concentrations. As with spherulite fibrils, fragmented fibril adsorption results in the modification of the resonance lineshape rendering comparison of RH and LH resonance shifts inaccurate. CD difference spectra and the magnitude of the corresponding asymmetry parameter are therefore calculated for each Au thickness (figure 7.10).

(a) (b)

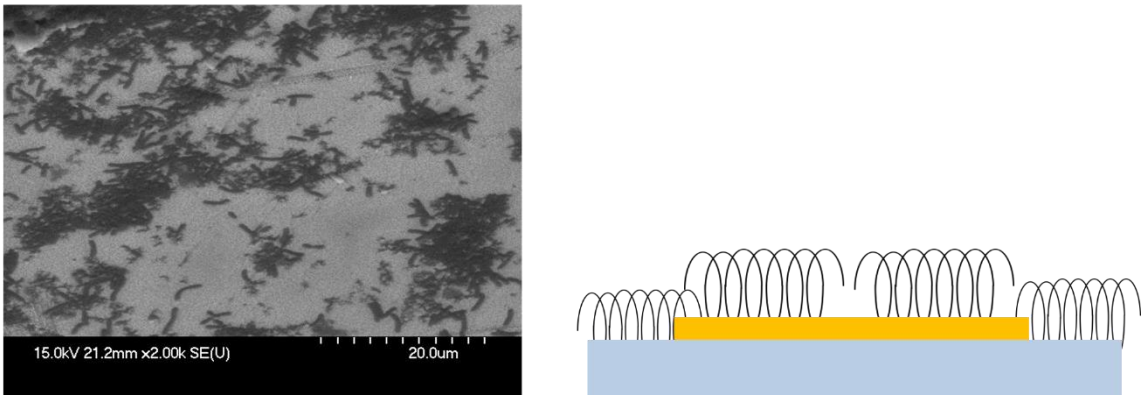

Figure 7.08: (a) SEM image of sonicated spherulites on a metal surface. **(b)** Pictorial representation of fragmented insulin amyloid fibrils bound to the sample surface where the long axis of the fibril is parallel to the surface.

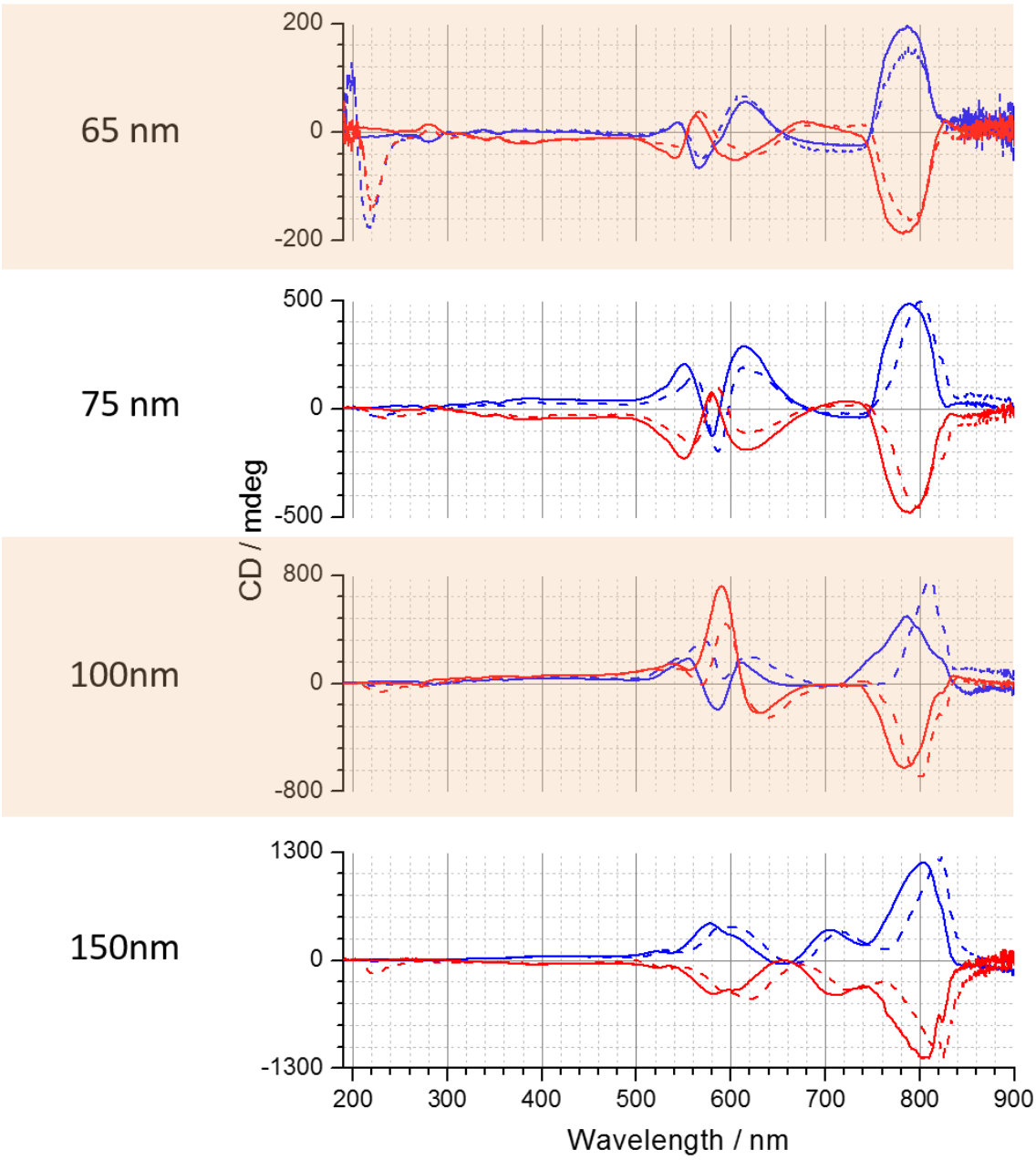

Figure 7.09: CD spectra of RH (blue) and LH (red) gammadions of varying Au thickness recorded in the presence of 10mM tris buffer (solid) and fragmented insulin amyloid fibrils(dashed).

The RH and LH difference spectra for the 65nm and 150nm gammadions display mirror image lineshapes. However, in contrast to the spherulite fibril data, the difference spectra for 75nm and 100nm gammadions are also mirror images. The magnitude of the asymmetry parameter agrees with this observation as the values of this parameter for each Au thickness are negligible. Hence, we confirm that for all Au thicknesses there is an absence of asymmetry between the RH and LH gammadion CD response when insulin amyloid fibrils bind with their long axis parallel to the surface plane.

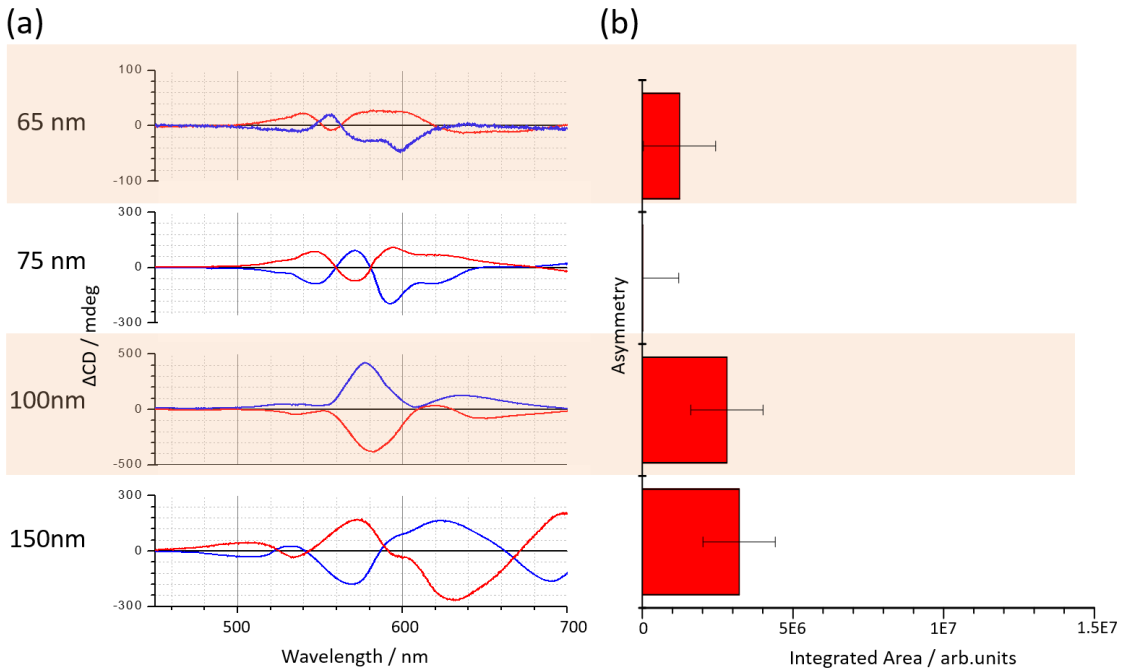

Figure 7.10: (a) Calculated difference spectra upon adsorption of fragmented insulin amyloid fibrils for RH (blue) and LH (red) gammadions of varying Au thickness. **(b)** Values of the asymmetry calculated using equation 1.

7.2.5 Detection of Fibril Helical Pitch

The CD data reveals that an asymmetric gammadion response is highly dependent on two factors: the orientation of the fibril at the surface and the Au thickness of the gammadion. A comprehensive understanding of the CD data is not possible without extensive modelling of the chirality, intensity and distribution of electromagnetic fields in the near-field of the structure. Such calculations have yet to be completed however it is possible to speculate as to the origins of the CD behaviour.

Firstly, the spherulite fibril and fragmented fibril CD data demonstrate that detection of the fibril helical pitch requires the long axis of the fibril to be perpendicular to the Au/quartz surface. The fibril helix precesses around the long axis (figure 7.01), therefore in the perpendicularly aligned spherulite fibrils the helical pitch will be normal to the surface whilst in the fragmented fibrils the long axis and hence the helical pitch is in the surface plane. Thus, the asymmetry in the spherulite fibril data indicates that the gammadion chiral evanescent fields may only detect the fibril twist when this structural element lies along the surface normal.

Following this dependence of the gammadion CD on the orientation of the fibril helical pitch, we now focus on the variation of the CD response with gammadion Au thickness. This thickness dependency is only evident upon adsorption of spherulite fibrils which agrees with the premise that the fibril helical pitch must be aligned perpendicular to the Au/quartz surface in order to facilitate a chiroptical interaction. We find that unlike the 75nm and 100nm Au substrates, adsorption of spherulite fibrils on the 65nm and 150nm Au gammadions does not elicit an asymmetric CD response. The Au thickness is therefore an extremely important parameter for the detection of the spherulite fibril helical pitch.

As illustrated in figure 7.05, upon deposition of spherulite fibrils the gammadions are embedded in a helical chiral dielectric whereby perpendicularly oriented fibrils are bound to the Au surface and the quartz substrate surrounding the gammadion. We suggest a model to account for the thickness dependence whereby it is the helical pitch of the surrounding fibrils bound to the quartz surface that the gammadion chiral fields are able to detect. Whilst these fibrils are not directly bound to the gammadion Au surface, they remain within the nanostructure near-field therefore a chiroptical interaction may still occur. Recall that the twist of amyloid fibrils extends over a distance of 70-120nm whilst the gammadions that display an asymmetric CD response upon spherulite fibril adsorption have an Au thickness of 75nm and 100nm. These closely matching lengthscales suggest that gammadions are only sensitive to the fibril helical pitch when this structural property corresponds to the vertical height of the nanostructures. However, this matching of the gammadion height and fibril helical pitch can only occur when the fibril is adjacent to the nanostructure. Thus, it is not the fibrils bound directly to the Au surface that facilitate detection of the helical pitch, rather it is the fibrils that are bound to the quartz surface surrounding the nanostructure. Further expansion of this model is not possible without extensive EM field modelling therefore this model remains purely speculative at this stage.

The dependence of the asymmetric CD response on the vertical height of the gammadions relative to the fibril helical pitch results in the gammadions effectively acting as a “plasmonic ruler”. Plasmonic rulers have recently evolved into an incisive method to measure nanoscale distances in molecular and biological species[17-19]. This technique relies on the distance dependence of coupling between nanoparticles attached to molecular species to reveal the dynamics of molecular interactions[20]. As nanoparticles approach

each other the coupling increases which modulates the light scattering which is then used to infer information about molecular distances. However, instead of using coupling between nanoparticles to measure molecular distances we use the gammadion Au thickness. In this study, detection of the fibril helical pitch relies on the gammadion vertical height matching the size of this structural element. Thus, our measurements suggest it is possible to identify the size of chiral mesoscale biological structure by measuring the asymmetric CD response using gammadions with a known Au thickness.

In summary, we propose a preliminary model to explain the sensitivity of gammadions to the fibril helical pitch that accounts for several key structural and spectroscopic features of the gammadions and insulin amyloid fibrils. The fibril helix must be aligned along the Au/quartz surface normal to facilitate a chiroptical interaction with the gammadions. Furthermore, this interaction only occurs when the height of the gammadions is on a similar lengthscale to the helical pitch of the adjacent fibrils meaning gammadions may effectively be employed as a "plasmonic ruler". Finally, it is important to emphasize that this model remains purely hypothetical and numerical field simulations of the nanostructure EM field intensity, spatial distribution and chirality is required to provide confirmation.

7.3 Conclusion

We have introduced a preliminary study into the potential of lithographic nanostructures to detect mesoscale biological structure. The mesoscale structure probed in this chapter is the helical pitch of insulin amyloid fibrils which is approximately 70-120nm in length. In order to achieve this, we use insulin amyloid fibrils arranged into two distinct structural forms: fibril spherulites and fragmented fibrils. Spherulites are large scale aggregates of fibrils whereby a central core is surrounded by radially oriented fibrils emanating out from this core. Conversely, fragmented fibrils are not aggregated into the large scale structures and are formed by sonicating spherulite fibrils. We first confirm the structural integrity of these two fibril forms through polarised optical microscopy. Spherulite fibrils display a characteristic "Maltese Cross" extinction pattern due to the birefringence of the spherulite structure which arises from the fibril radial orientation. Fragmented fibrils do not display any birefringence effects due to the lack of spherulite structure.

The use of spherulite fibrils and fragmented fibrils is fundamental to the study of the helical pitch as fibrils in these two forms bind to the Au surface in a significantly different manner. When aggregated into spherulites, the fibrils bound to the Au surface are oriented with their long axis perpendicular to the surface of the substrate. In contrast, fragmented fibrils bind with their long axis parallel to the sample surface. In subsequent spectroscopic measurements this differential surface binding has a significant effect on the gammadion sensitivity to the fibril helical pitch.

Detection of the fibril helical pitch requires measuring the asymmetry induced in the RH and LH CD spectrum of gammadions with the same periodicity but different Au thickness (65nm, 75nm, 100nm, 150nm) upon spherulite fibril/fragmented fibril adsorption. For all Au thicknesses RH and LH CD spectra in buffer are mirror images and possess two distinct LSPR modes. Due to the changes in the CD lineshape upon adsorption of fibril solutions we are unable to measure the asymmetry in the resonance shift of RH and LH gammadion LSPR peaks. Alternatively, we generate a difference spectra and calculate an asymmetry parameter to convey the asymmetry between the RH and LH nanostructure response. Adsorption of spherulite fibrils causes an asymmetric CD response for the 75nm and 100nm Au gammadions whereas no asymmetry is observed for the 65nm and 150nm substrates. In contrast, adsorption of fragmented fibrils does not induce an asymmetric CD response for gammadions of any Au thickness.

We propose a hypothetical model to explain these results whereby the sensitivity of gammadions to the fibril helical pitch depends on the orientation of the helical pitch at the Au/quartz surface and the vertical height of the gammadions. The asymmetry observed for the spherulite fibrils and lack of asymmetry for the fragmented fibrils indicates that gammadion chiral fields can only detect the fibril helical pitch when it is aligned perpendicular to the Au surface. Furthermore, from the thickness dependence we propose that gammadions are only sensitive to the fibrils bound to the quartz surface adjacent to the nanostructures when the height of the gammadion matches the helical pitch (70-120nm) of these fibrils. Thus, using gammadions of different Au thickness we have effectively developed a “plasmonic ruler” to measure mesoscale biological structure.

7.4 References

1. M. Ramirez-Alvarado, J.S.M., L. Regan, *A systematic exploration of the influence of the protein stability on amyloid fibril formation in vitro.* Proceedings of the National academy of Science, 2000. **97**(16): p. 8979-8984.
2. J. Brange, L.A., E.D. Laursen, G. Meyn, E. Rasmussen, *Towards Understanding Insulin Fibrillation.* Journal of Pharmaceutical Sciences, 1997. **86**(5).
3. R. Nelson, D.E., *Structural models of amyloid-like fibrils.* Advances in Protein Chemistry, 2006. **73**: p. 235-272.
4. W.F. Xue, S.W.H., S.E. Radford, *Amyloid fibril length distribution quantified by atomic force microscopy single-particle image analysis.* Protein Engineering, Design and Selection, 2009. **22**(8): p. 489-496.
5. Z. Xu, R.P., M. J. Buehler, *Alzheimer's Ab(1-40) amyloid fibrils feature size-dependent mechanical properties.* Biophysical Journal, 2010. **98**: p. 2053-2062.
6. G. Lee, W.L., H. Lee, C.Y. Lee, K. Eom, T. Kwon, *Self-assembled amyloid fibrils with controllable conformational heterogeneity.* Scientific Reports, 2015. **5**: p. 16220.
7. A.W. P. Fitzpatrick, G.T.D., M.J. Bayro, D.K. Clare, M.A. Caporini, V.S. Bajaj, C.P. Jaronie, L. Wang, V. Ladizhansky, S.A. Müller, C.E. MacPhee, C.A. Waudby, H.R. Mott, A.De Simone,, T.P.J. Knowles, H.R. Saibil, M. Vendruscolo, E.V. Orlova, R.G. Griffin, C.M. Dobson, *Atomic Structure and Hierarchical Assembly of a cross-Beta Amyloid Fibril.* Proceedings of the National Academy of Science, 2013. **110**(14): p. 5468-5473.
8. D. Kirschner, C.A., D. Selkoe, *X-ray diffraction from intraneuronal paired helical ¢laments and extra-neuronal amyloid fibres in Alzheimers disease indicates cross L conformation.* Proceedings of the National Academy of Science, 1986. **83**: p. 503-507.
9. R. Nelson, M.R.S., M. Balbirnie, A. Ø. Madsen, C. Riekel, R. Grothe, D. Eisenberg, *Structure of the cross-beta spine of amyloid-like fibrils.* Nature, 2005. **435**: p. 773-778.
10. Serpell, L.C., *Alzheimers's amyloid fibrils: Structure and assembly.* Biochimica et Biophysica Acta, 2000. **1502**: p. 16-30.
11. C. Sachse, C.X., K. Wieligmann, S. Diekmann, N. Grigorieff, M. Fändrich, *Quaternary structure of a mature amyloid fibril from alzheimer'sAβ(1-40) peptide.* Journal of Molecular Biology, 2006. **362**: p. 347-354.
12. M. R. H. Krebs, C.E.M., A. F. Miller, I. E. Dunlop, C. M. Dobson, A. M. Donald, *The formation of spherulites by amyloid fibrils of bovine insulin.* Proceedings of the National Academy of Science, 2004. **101**(40): p. 14420-14424.
13. M. R. H. Krebs, E.H.C.B., S. S. Rogers, A. M. Donald, *The mechanism of amyloid spherulite formation by bovine insulin.* Biophysical Journal, 2005. **88**: p. 2013-2021.
14. M.I. Smitha, V.F., J.S. Sharpa, C.J. Roberts, A.M. Donald, *Factors affecting the formation of insulin amyloid spherulites.* Colloids and Surfaces B: Biointerfaces, 2012. **89**: p. 216-222.
15. M. I. Smith, J.S.S., C. J. Roberts, *Giant amyloid spherulites reveal their true colours.* Soft Matter 2012. **8**(14): p. 3751-3755.
16. E. Hendry, T.C., J. Johnston, M. Popland, R.V. Mikhaylovskiy, A.J. Lapthorn, S.M. Kelly, L.D. Barron, N. Gadegaard, M. Kadodwala, *Ultrasensitive detection and characterization of biomolecules using superchiral field.* Nature Nanotechnology, 2010. **5**: p. 788-787.
17. N Liu, M.H., T. Weiss, A.P. Alivisatos, H. Giessen, *Three-dimensional plasmon rulers.* Science, 2011. **332**: p. 1407-1410.
18. R.T. Hill, J.J.M., A. Hucknall, S.D. Wolter, N.M. Jokerst, D.R. Smith, A. Chilkoti, *Plasmon ruler with angstrom length resolution.* ACS Nano, 2012. **6**(10): p. 9237-9246.
19. C. Sonnichsen, B.M.R., J. Liphardt, A.P. Alivisatos, *A molecular ruler based on plasmon coupling of single gold and silver nanoparticles.* Nature Biotechnology, 2005. **23**(6): p. 741-745.

20. B.M. Reinhard, S.S., A. Mastroianni, A.P. Alivisatos, J. Liphardt, *Use of plasmon coupling to reveal the dynamics of DNA bending and cleavage by single EcoRV restriction enzymes.* Proceedings of the National Academy of Science, 2007. **104**(8): p. 2667-2772.

Summary and Future Outlook

The content of this thesis focusses on the development of chiral plasmonic nanostructures for use in ultrasensitive spectroscopic measurements of biomolecules. In this section we will provide a brief overview of the results presented in chapters 4-7 and consider the possible future direction of this work for applications across a range of biosensing platforms.

In the initial work presented in chapter 4 we introduce the first example of complex nanostructures fabricated using a cost effective, low through-put fabrication process. This metamaterial is composed of a nanopatterned polycarbonate slide fabricated by injection moulding which is coated in a thin layer of Au to produce a nanopatterned plasmonic film. The optical properties of this templated plasmonic substrate (TPS) are determined by the coupling between the electric and magnetic modes of the constituent solid and inverse structures respectively. This is controlled by varying the thickness of the Au film which allows for the simple modification of the nanostructure optical and chiroptical properties. Thin Au films (Au≤30nm) display Fano-like reflectance dips associated with weak electric/magnetic coupling whilst the optical rotation (OR) is analogous to the optical activity observed for a coupled oscillator model of chirality. In contrast the thicker films display an EIT effect in the reflectance lineshape typical of strongly coupled systems whilst the OR is analogous to the optical activity for an inherently chiral single helical oscillator (SHO). Due to these large levels of chirality we find that only strongly coupled TPSs are sensitive to protein β-sheet structures whilst the sensitivity limits are similar to that observed for previous spectroscopic measurements using lithographically fabricated nanostructures.

This chapter represents a natural progression from previous work in our lab with regards to the fabrication and application of chiral plasmonic nanostructures in ultrasensitive chiroptical spectroscopy. The fundamental limitation of this previous work was the requirement for costly and low through-put lithographically fabricated structures. We have shown for the first time that injection moulded nanostructures are a viable alternative to lithographically fabricated samples. Hence, future work with these new substrates will now focus on expanding the range of biological systems to which they can be applied whilst also fostering a deeper understanding as to the physical mechanisms that govern these new hybrid nanostructures. Finally, due to the simplicity with which the optical properties can be

manipulated after fabrication of the polymer slide, investigations into the TPS behaviour upon deposition of different metal films is also a potentially valuable study.

In chapter 5 of this thesis we continue the theme of developing simple, high through-put processes for application in the field of plasmonic metamaterials whereby we develop a process for the nanoscale chemical functionalisation of the TPS surface. This allows selective placement of biomolecules in areas of high net chirality which further enhances the TPS biosensing properties. This work was conducted in collaboration with colleagues at the University of Ohio. Thermal modelling of the TPS and surrounding water reveals that the water surrounding specific regions of the TPS is significantly hotter than other regions. This effectively generates localised thermal hotspots surrounding the TPS surface. We exploit the presence of these hotspots to control the chemical functionalisation of the surface using a protection/deprotection strategy. Firstly, the protection step involves adsorption of a thermally responsive polymer to inhibit protein binding. The deprotection step then exploits the presence of nanolocalised hotspots in the surrounding water to modify the conformation of the polymer in nanoscale regions of the TPS surface. This enables biomaterial to be selectively placed in these regions which possess high net chirality resulting in an enhancement of the sensitivity of the TPS chiroptical measurements compared with the results reported in chapter 5.

Nanoscale chemical functionalisation conducted using this novel phenomenon of nanoscale plasmonic water heating is a significant improvement compared with previously reported functionalisation techniques. This technique represents a real alternative for a high through-put chemical functionalisation process and may potentially allow for the development of advanced functionalised nanomaterials. Moreover, thermoplasmonic phenomena are often limited due to the large diffusivity of thermal energy in noble metals which inhibits the formation of thermal hotspots. The development of nanolocalised water heating may be exploited to overcome this fundamental limitation and opens the door for a wide range of novel applications in thermoplasmonics.

In chapter 6 we continue our study into the biosensing capabilities of TPS nanostructures by introducing an alternative chiroptical technique for the detection of protein secondary structure. In contrast to chapters 5 and 6 this technique is not based on measuring effective refractive indices of biomolecules in RH and LH chiral fields. Alternatively, protein secondary

structures are detected through monitoring the effect protein adsorption has on the strength of coupling between the electric/magnetic modes of a weakly coupled TPS nanostructure. This technique represents an improvement over previous measurements as it is able to unequivocally identify three distinct secondary structure motifs whilst it does not require fields of enhanced chirality. In the linear regime this protein mediation of TPS mode coupling is manifested through subtle changes in the reflectance lineshape whilst in the nonlinear regime protein adsorption results in changes in the electric dipole contribution to the nanostructure SHG response. Finally, the enhanced sensitivity of this technique is found to arise due to the electric dipole-magnetic dipole origins of this effect.

The basis of all previous studies of plasmonic nanostructures for biosensing has focussed on measuring the refractive index of biomolecules in the presence of plasmonic fields. The results presented in this chapter signify a dramatic shift away from this refractive index based sensing and exploit an as yet unreported phenomenon. The discovery of protein mediation of TPS coupling for the detection of protein secondary structure has the potential to significantly expand the applicability of TPS nanostructures. Hence, subsequent work will focus on investigating the possibility of detecting higher orders of protein structure using this technique whilst also expanding the design toolbox of metamaterials through modifying the optical properties by adsorption of various molecular species.

In the final results chapter, a preliminary investigation into the possibility of sensing mesoscale biological structure is performed. This lengthscale is important as it is occupied by species such as viruses and amyloid plaques associated with various diseases. The mesoscale structure studied in this chapter is the helical pitch of insulin amyloid fibrils. Unlike previous chapters, spectroscopic measurements are performed by monitoring the changes in the CD spectrum of lithographically fabricated gammadions of different Au thicknesses upon adsorption of spherulite fibrils and fragmented fibrils. It is found that an asymmetric CD response only occurs for gammadions of thickness 75nm and 100nm Au upon adsorption of spherulite fibrils. In the absence of electromagnetic field simulations, we propose a hypothetical model to account for the observed CD changes. This model suggests that detection of the fibril helical pitch depends on the fibril being aligned perpendicular to the nanostructure surface whilst the vertical height of the gammadion must be similar to that of the fibril helical pitch (70-120nm).

These preliminary results presented in chapter 7 illustrate the potential of chiral plasmonic nanostructures to detect biological structure across vastly different lengthscales. Previous chapters have proven the sensitivity of such structures to nanoscale protein structure however it is increasingly important to probe the structure of biological species beyond this domain. The natural progression of this study is to determine whether TPS nanostructures are also able to detect mesoscale biological structure. In addition, we will focus on the detection of larger structural motifs such as the overall structure of viruses with the ultimate objective of developing a cheap high through-put nanotechnology for use in clinical diagnostics.